Monitoring cell metabolism with NAD(P)H fluorescence lifetime imaging

Thomas Stephen Blacker

A thesis submitted for the degree of

Doctor of Philosophy

of

University College London.

Centre for Mathematics and Physics in the Life Sciences and Experimental Biology

Research Department of Cell and Developmental Biology

&

Department of Physics and Astronomy

I, Thomas Stephen Blacker, confirm that the work presented in this thesis is my own. Where information has been derived from other sources, I confirm that this has been indicated within.

July 8, 2013

Abstract

In live tissues, alterations in metabolism induce changes in the fluorescence decay of the spectrally identical redox carriers NADH and NADPH. The biochemical pathways and photophysical mechanisms that contribute to these changes are largely unknown. This work combined ultrafast laser spectroscopy and live-cell imaging to investigate these phenomena.

Time-resolved spectroscopy of NADH and NADPH was performed using single-photon and two-photon excitation. In solution, the fluorescence lifetimes of the two cofactors were identical. The anisotropy decay dynamics of both molecules indicated that distinct molecular configurations caused the presence of two emitting states, perhaps involving alternate cis/trans geometries of the amide group. Using a range of water/glycerol mixtures as solvents, the viscosity dependence of the non-radiative decay of NAD(P)H was shown to be well described by Kramers and Kramers-Hubbard models of activated barrier crossing. This suggested that variations in the fluorescence lifetimes of the cofactors when bound to different enzymes result from differing levels of conformational restriction of the nicotinamide ring in the binding site.

Despite identical fluorescence lifetimes in solution, studies on genetically modified cell lines in which NAD kinase was overexpressed or knocked down indicated that intracellular NADPH was associated with a significantly larger fluorescence lifetime when bound to enzymes (~4.4 ns) than enzyme-bound NADH (~1.5 ns). This suggested that variations in the NAD(P)H fluorescence decay upon metabolic perturbation by pharmacological or pathological means, reported both in this work and in the literature, result from changes in the relative concentrations of NADH and NADPH.

NAD(P)H FLIM was used to observe elevated NADPH concentrations in the support cells of the mammalian cochlea, highlighting the potential of the technique as a label-free method for monitoring the metabolic state of complex tissue preparations.

Acknowledgements

Although I'm the one who got to join the dots, the results contained in this thesis arose from the combined skills of a large number of talented people.

In the Bain lab, I thank Dr. Daven Armoogum for showing me the TCSPC ropes back in the 2008/09 season and for the teaching-lab overtime that kept my bank balance above the x-axis while I wrote this work up. I am also grateful for the assistance of Dr. Nick Nicolaou in ensuring that I channeled the inevitable rage induced by the early days of PhD research onto the football pitches of South Wimbledon rather than the lasers. The days spent without natural light underneath the Students' Union were made bearable by the good company of my fellow PhD students Ellie Bailey and Siân Culley. In recognition of his expertise across all of the equipment used in chapters 3 and 4 of this work, I thank Dr. Richard Marsh. Acquiring 1% of his technical ability alone would have made the last four years worthwhile.

This thesis has been shaped by the insight and advice of Prof. Peter Rich from the UCL Department of Structural and Molecular Biology, Prof. David Whitmore from the UCL Department of Cell and Developmental Biology, Dr. Jonathan Gale from the UCL Ear Institute, Dr. Sean Davidson from the Hatter Cardiovascular Institute and Dr. Gyuri Szabadkai from down the corridor. I am indebted to Jonathan and Dr. Paromita Majumder for preparing the cochlea explant cultures studied in chapter 6 of this work and for spending time showing me how to image them. It is the nature of the live-cell microscopy part of this work that many other collaborators have my gratitude for their generosity, in particular Prof. Mathias Ziegler from the University of Bergen, Dr. Juanma Funes from the UCL Cancer Institute and Dr. Philippe Behe from the UCL Centre for Molecular Medicine.

Back when I didn't know an aspirator from an Eppendorf, past members of the Duchen and Szabadkai labs to whom I am grateful for helping me to find my feet are too many to name individually here. However, Dr. Fabrice Ivanes deserves mention for showing his

now legendary patience when successfully teaching me the art of cell culture. Thanks to those who, over the course of my PhD, demonstrated that the most informative discussions about mitochondrial biology are followed by a trip home on the N155. For frequently going beyond the call of duty to keep the lab running smoothly, Sam Ranasinghe deserves special praise.

UCL CoMPLEX has provided an ideal postgraduate education. I remain grateful to Dr. Guy Moss, Prof. Andrew Pomiankowski and Prof. Rob Seymour for accepting me into the department five years ago, giving me the opportunity to pursue such a unique programme of study and acquire such a varied skill set. I thank the EPSRC for funding my time here and Abi Espie and Chris Langridge in the admin office for always knowing the answer.

Finally, and most importantly, I thank my supervisors, Prof. Michael Duchen and Dr. Angus Bain, not only for their knowledge, guidance and constructive criticism while I performed the research, but for their encouragement, patience and support over the time I was writing it up. I have enjoyed my time working in your labs, and I hope I've done the project justice.

This work is dedicated to

HOLLY WEBBER

10th April 1986 — 30th August 2012

"...though I'm past one hundred thousand miles,

I'm feeling very still..."

Contents

List of Figures

List of Tables

List of Abbreviations

ADP	adenosine diphosphate
ATP	adenosine triphosphate
BRENDA	Braunschweig Enzyme Database
CFD	constant fraction discriminator
DAPI	4',6-diamidino-2-phenylindole
DMEM	Dulbecco's modified Eagle's medium
DMSO	dimethyl sulfoxide
DNA	deoxyribonucleic acid
DRBIO	Developmental Resource for Biophysical Imaging Optoelectronics
EGCG	epigallocatechin gallate
FBS	foetal bovine serum
FCCP	carbonyl cyanide 4-(trifluoromethoxy)phenylhydrazone
FLIM	fluorescence lifetime imaging microscopy
FWHM	full width at half maximum
HBSS	Hank's balanced salt solution
HEPES	4-(2-hydroxyethyl)-1-piperazineethanesulfonic acid
HOMO	highest occupied molecular orbital
HPLC	high-performance liquid chromatography
IRF	instrument response function
KDP	potassium dihydrogen phosphate
LUMO	lowest unoccupied molecular orbital
MCP-PMT	micro channel plate photomultiplier tube
MOPED	Model Organism Protein Expression Database
NA	numerical aperture
NAD	nicotinamide adenine dinucleotide (oxidised)
NADH	nicotinamide adenine dinucleotide (reduced)
NADK	NAD kinase
NADP	nicotinamide adenine dinucleotide phosphate (oxidised)
NADPH	nicotinamide adenine dinucleotide phosphate (reduced)
NAD(P)H	combined NADH and NADPH fluorescence
PCI	peripheral component interconnect
PMT	photomultiplier tube
RCSB	Research Collaboratory for Structural Bioinformatics
RNA	ribonucleic acid
TAC	time to amplitude converter
TCSPC	time correlated single photon counting
TMRM	tetramethylrhodamine, methyl ester
UV	ultraviolet

Chapter 1

Introduction

Living systems require the constant input of energy to maintain their characteristic order. In the cell, this energy is extracted from the chemical bonds between atoms in molecular substrates such as carbohydrates and fatty acids. The controlled breakdown of large biological molecules into smaller ones to release energy is known as catabolism. Conversely, the cell can join together simple molecular units to produce more complex ones. This is known as anabolism. The anabolic and catabolic biochemical processes used to keep a cell alive are collectively known as metabolism.

Substrates can be channeled through different sets of metabolic reactions depending on the needs and circumstances of the cell. For example, when oxygen supplies are limited, the cell can produce usable energy from glucose using the process of glycolysis. When oxygen is available, more energy can be yielded from a single glucose molecule by employing the process of oxidative phosphorylation. The particular sets of reactions utilised at a particular time can be described as the metabolic state of the cell.

This thesis describes the development of a biophotonic method for monitoring the metabolic state of live cells and tissues based on the natural fluorescence of two molecules crucial to cell metabolism; reduced nicotinamide adenine dinucleotide (NADH) and reduced nicotinamide adenine dinucleotide phosphate (NADPH). This chapter details the biochemical pathways relevant to the thesis and introduces the physical process of fluorescence. This discussion includes the concept of the fluorescence lifetime; the optical property central to this work.

1.1 ATP: life's universal energy currency

Catabolic reactions convert the chemical potential energy in the bonds of molecules taken in as food into a form that the cell can readily use. This universal form is adenosine triphos-

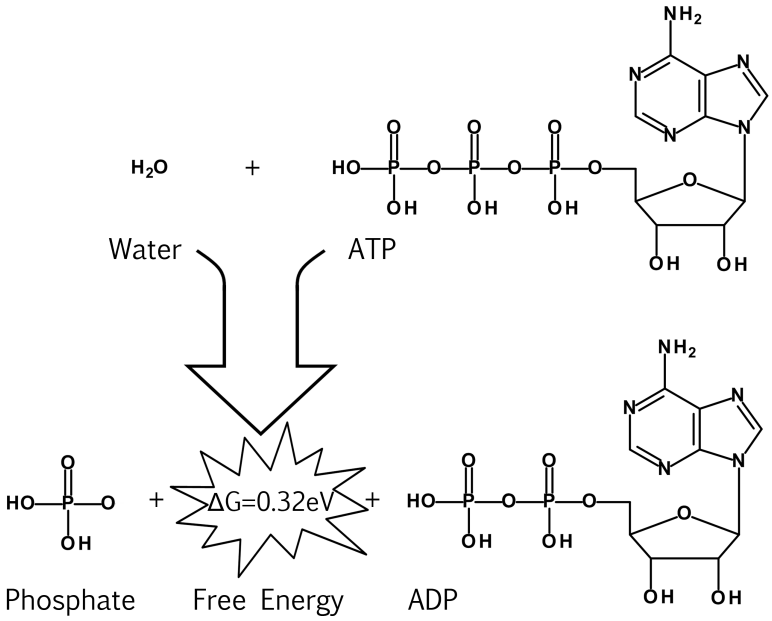

Figure 1.1: The release of free energy by the hydrolysis of ATP.

phate (ATP), common to all cellular life from bacteria to humans (Alberts et al., 2007).

ATP consists of an adenine base attached to a ribose sugar, itself attached to a chain of three phosphate units. When the outermost phosphate unit is removed from the ATP molecule, turning the adenosine triphosphate into adenosine diphosphate (ADP), 0.32 eV of energy are released (Berg et al., 2011). A water molecule donates an oxygen atom to the removed portion to form a free phosphate molecule so the overall reaction, shown in figure 1.1, is termed ATP hydrolysis.

In figure 1.1, ΔG is the change in Gibbs free energy between the reactants (ATP and H_2O) and the products (ADP and P_i) of the ATP hydrolysis reaction. ΔG depends on the concentrations of the reactants and products present as well as their precise molecular structures (Schroeder, 2000). A negative Gibbs free energy change represents an amount of "usable" energy that can be extracted from the reaction. This portion is denoted usable because it takes account of the energy lost to increasing the entropy of the surroundings, as required by the second law of thermodynamics (Nelson et al., 2007).

A reaction producing usable energy ($\Delta G < 0$) is denoted an exergonic reaction. In contrast, an endergonic reaction ($\Delta G > 0$) can only proceed by consuming energy. An endergonic reaction can take place by supplying it with energy using an exergonic reaction, such that the overall free energy change of the reaction is negative. This coupling is common in the cell with ATP hydrolysis the primary energy supply (Berg et al., 2011). ATP provides the energy for a wide range of processes from the contraction of muscle to the

transport of molecules into and out of the cell (Alberts et al., 2007). A human will turnover its own body weight in ATP in a day, such is its ubiquity as an energy provider (Rich, 2003).

1.2 Enzymes and metabolic pathways

Exergonic reactions are characterised by a decrease in free energy between products and reactants, often leading to these reactions being described as "spontaneous" (Berg et al., 2011). However, this does not imply that all exergonic reactions can proceed without stimulus. Frequently, an energy barrier must be overcome in order to convert the reactants into the products. This barrier corresponds to an energetically unfavourable molecular state that must be passed in order to form the product from the reactant. The energy required to overcome this transition state barrier is known as the activation energy of the reaction (Nelson et al., 2007). The energy to overcome this barrier can be provided by the thermal jostling of the surrounding molecules in the cell, provided that the average thermal energy available from the environment is greater than the activation energy. The magnitude of this thermal energy is approximately $k_B T$, where T is the temperature and k_B is the Boltzmann constant (Schroeder, 2000). If the activation energy is sufficiently higher than this value, the products of the reaction cannot spontaneously form from the reactants. The presence of an activation barrier ensures, for example, that ATP cannot uncontrollably decay into ADP, despite the negative free energy change of this process.

In order for a reaction to proceed, such as harnessing the free energy stored in an ATP molecule, the activation barrier must be overcome. The cell achieves this using enzymes. These are catalytic proteins that hold reactants in such a configuration as to make entry into the transition state more probable, lowering the activation energy to an extent whereby the thermal jostling of the surroundings can force the reaction to form the products (Nelson et al., 2007). Energy surfaces displaying this process are shown in figure 1.2.

Each enzyme produced and used by the cell is specific to a particular reaction or set of similar reactions (Berg et al., 2011). The reactants assigned to a particular enzyme are known as its substrates. This substrate specificity requires that a huge range of different enzymes are employed by the cell to perform its vast number of metabolic functions. For example, the metabolism of the simple bacterium *Escherichia coli* is a network of over 1000 different reactions (Berg et al., 2011). Sets of different enzymes map out well-defined routes for the transformation of substrate molecules into particular products. These routes are the metabolic pathways of the cell.

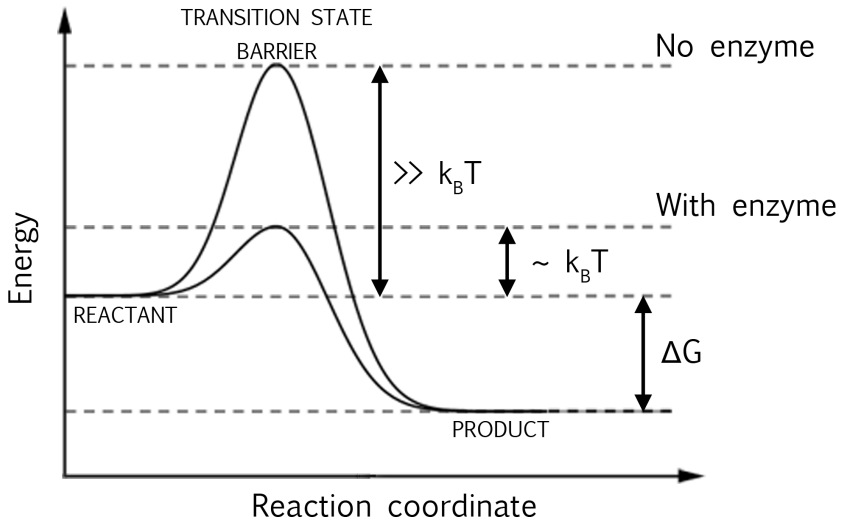

Figure 1.2: Enzymes catalyse biochemical reactions by reducing the size of the transition state barrier such that it can be crossed using the thermal energy of the surroundings.

Metabolic pathways can be blocked by molecules that inhibit the function of their enzymes (Zollner, 1999). Inhibitors can be externally applied, such as pharmaceuticals, or can themselves be the products of a particular pathway. Some enzymes require the presence of additional molecules, known as cofactors, to catalyse their particular reaction. Other enzymes can reverse the direction of the reaction they catalyse if the products far outweigh the reactants (Berg et al., 2011). These features of metabolic pathways allow their procession to be regulated, forming a complex network that allows the pathways to be activated or deactivated in response to the metabolic needs of the cell (Kitano, 2002).

1.3 Production of ATP and NADH by glycolysis

The primary energy source of most cells is glucose (Rose, 1999). The most primitive metabolic pathway for the production of usable energy, in the form of ATP, from glucose is glycolysis. Glycolysis does not require oxygen, making it likely that it evolved at least 3 billion years ago, before oxygen was a major component of the Earth's atmosphere (Lane, 2002; Alberts et al., 2007). While it is not fully accepted that glycolysis was used by the last common ancestor of all life on Earth today (Lane et al., 2010), versions of this pathway occur in the metabolism of all three of life's domains; archaea, bacteria and eukaryotes (Romano and Conway, 1996). Eukaryotes perform the canonical version of the glycolytic pathway shown in figure 1.3 (Berg et al., 2011).

Transporter proteins in the cell membrane aid the entry of glucose into the cell (Thorens and Mueckler, 2010). Once inside, the first step of glycolysis uses an ATP molecule

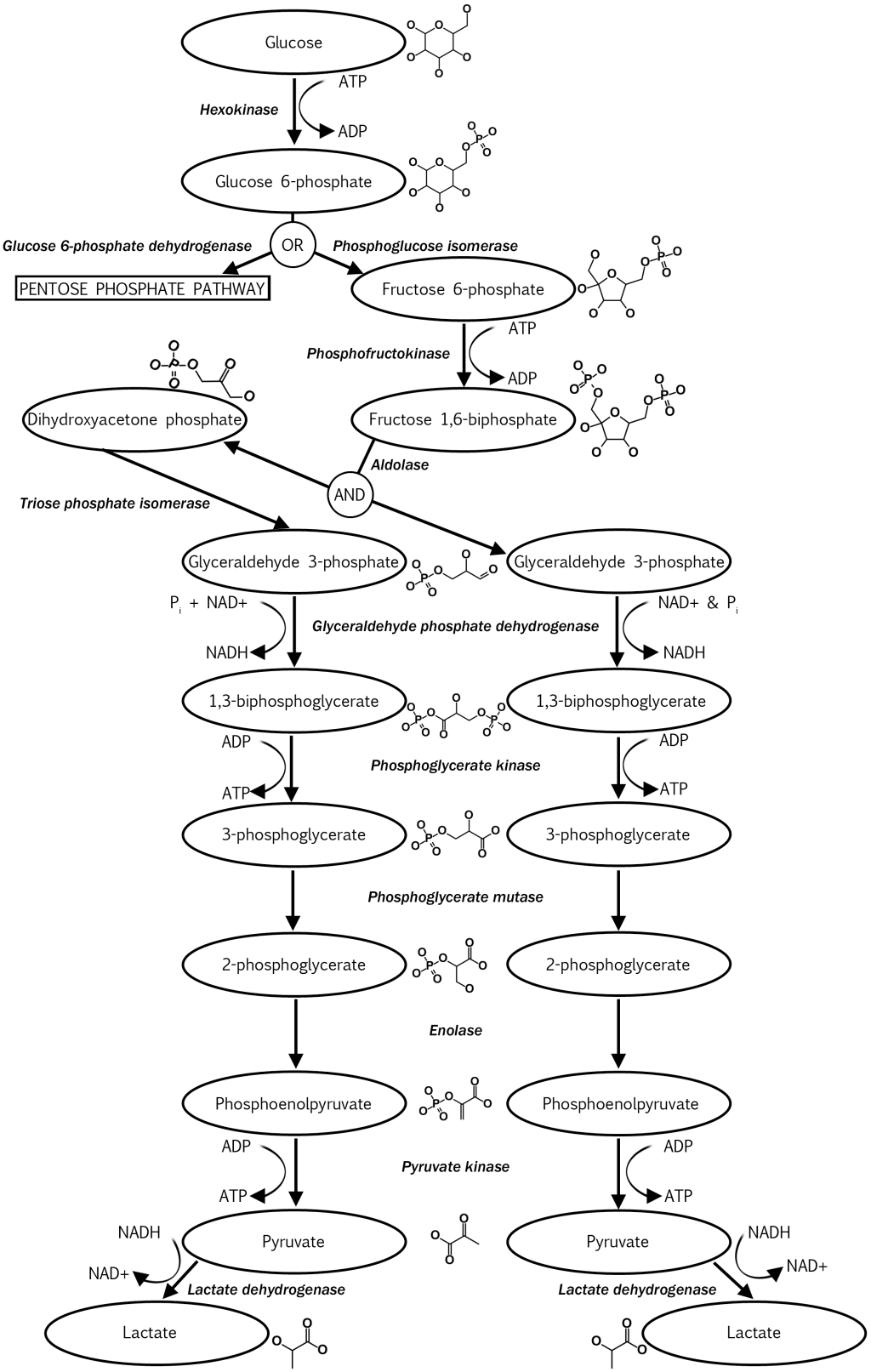

Figure 1.3: The anaerobic breakdown of glucose by glycolysis to produce ATP and NADH, adapted from (Berg et al., 2011).

to phosphorylate glucose into glucose 6-phosphate. This reaction is catalysed by the enzyme hexokinase. Two further enzymatic steps convert the glucose 6-phosphate into fructose 1,6-biphosphate, using another ATP molecule in the process. The fructose 1,6-biphosphate is then split in half by the enzyme aldolase, forming dihydroxyacetone phosphate and glyceraldehyde 3-phosphate. The dihydroxyacetone phosphate is then converted into a second molecule of glyceraldehyde 3-phosphate by the enzyme triose phosphate isomerase (Berg et al., 2011).

This first section of glycolysis represents an "energy investment" stage with the consumption of two ATP molecules to produce two glyceraldehyde 3-phosphate molecules from one glucose molecule. Five further reactions occur to convert glyceraldehyde 3-phosphate into pyruvate, two of which output energy in the form of an ATP molecule each (Alberts et al., 2007). As two molecules of glyceraldehyde 3-phosphate are produced from one molecule of glucose in the first stage of glycolysis, this "energy generation" stage produces four molecules of ATP in total. This means a net gain of two ATP molecules per molecule of glucose entering the glycolytic pathway.

ATP is not the only molecule that carries energy away from glycolysis. The first reaction in the energy generation stage, the conversion of glyceraldehyde 3-phosphate into 1,3-biphosphoglycerate, involves the oxidation of glyceraldehyde 3-phosphate. While oxidation reactions can refer to those in which oxygen is transferred between reactants, the reactions of glycolysis do not involve oxygen. Formally, an oxidation reaction refers to any reaction in which electrons are transferred between the reactants (Atkins and De Paula, 2010). The reactant with a net loss of electrons has been oxidised. The reactant with a net gain of electrons is said to have been reduced. As reactions such as this always involve one reactant being oxidised while another is reduced, they are generally referred to as redox reactions (Alberts et al., 2007). In the redox reaction in the energy generation stage of glycolysis, glyceraldehyde 3-phosphate is oxidised while the molecule that is reduced is NADH. For this reason, NADH is often described as an electron-carrier molecule.

The tendency of a molecule to acquire electrons is characterised by its redox potential E^0_{red} (Berg et al., 2011). This quantity can be positive or negative, with increasingly positive values indicating greater electron affinity. The redox potential of NADH is –320 mV (Nicholls and Ferguson, 2013), highlighting its role in ferrying electrons between intracellular redox reactions. The change in Gibbs free energy upon the reduction of NAD^+

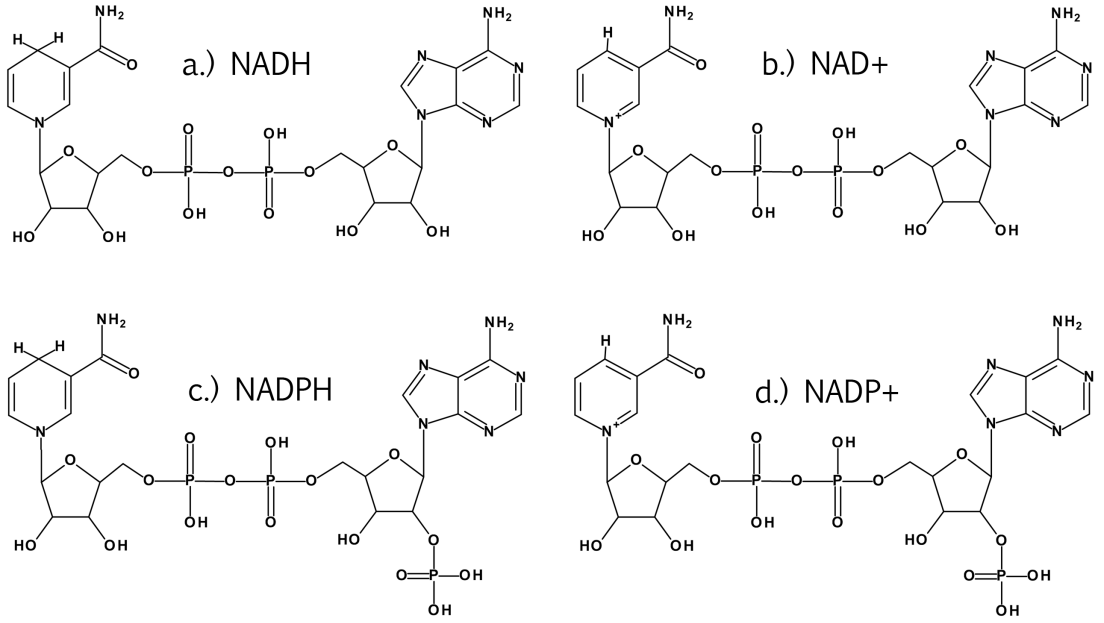

Figure 1.4: The chemical structures of the reduced NADH and NADPH and the oxidised NAD^+ and $NADP^+$. NADH and NAD^+ differ from NADPH and $NADP^+$ by the presence of a phosphate group attached to the ribose at the adenine end of the molecule.

is related to this redox potential by,

$$\Delta G = -2FE^0_{\text{red}} + N_A k_B T \ln\left(\frac{[\text{NAD}^+]}{[\text{NADH}]}\right) \tag{1.1}$$

where F is the Faraday constant and N_A is the Avogadro constant (Nicholls and Ferguson, 2013). ΔG will therefore be positive in physiological conditions (NAD^+/NADH $\approx$ 0.01, Sun et al., 2012), demonstrating the transit of energy, in addition to electrons, by NADH.

The structure of NADH is shown next to its oxidised form NAD^+ in figure 1.4 (Berg et al., 2011). NADH consists of two ribose sugars joined by a pair of phosphate groups. Attached to one ribose sugar is an adenine moiety. Attached to the other is a nicotinamide ring. It is this nicotinamide ring that carries electrons, in the form of a hydride ion, away from redox reactions such as that catalysed by glyceraldehyde 3-phosphate dehydrogenase in glycolysis (De Ruyck et al., 2007). A hydride ion is removed from glyceraldehyde 3-phosphate and transferred to the nicotinamide ring of NAD^+, incorporated in the manner shown in figure 1.4, forming NADH (Alberts et al., 2007).

The progress of glycolysis is reliant on there being sufficient oxidised NAD^+ available to accept a hydride ion during the oxidation of glyceraldehyde 3-phosphate and produce NADH. Glycolysis would grind to a halt if no method were available to regenerate NAD^+

from NADH (Berg et al., 2011). The cell avoids this problem by providing a pathway for the reduction of pyruvate, the end product of glycolysis, into lactate. The enzyme lactate dehydrogenase catalyses this reaction, transferring hydride from NADH to perform the reduction of pyruvate, thus restoring the NAD^+ pool and allowing glycolysis to continue. In this way, the ratio of NAD^+ to NADH in the cytosol can be kept high, between 20 and 100 (Sun et al., 2012).

1.4 NADPH via the pentose phosphate pathway

The removal of electrons by NADH during the breakdown of a substrate is an example of a catabolic redox reaction. The cell also utilises redox reactions in anabolic pathways, with an electron-carrier required to donate a reducing equivalent for the formation of larger molecules. However, if anabolic and catabolic pathways shared the same electron-carriers, anabolism and catabolism would compete for the carriers to be in a reduced or oxidised state, respectively. The cell bypasses this problem by employing the molecule NADPH as the electron-carrier in anabolic reactions, allowing anabolism and catabolism to be regulated independently (Alberts et al., 2007).

NADPH and its oxidised form $NADP^+$ are structurally identical to their catabolic analogues NADH and NAD^+, apart from the presence of a phosphate group attached to the ribose sugar of the adenine moiety (Alberts et al., 2007), as shown in figure 1.4. This small difference allows the binding sites on redox enzymes to be specific to their particular electron-carrier (Scrutton et al., 1990) and allows separate pathways to exist for maintaining the NADH and NADPH pools in separate redox states. The main pathway for the reduction of NADPH is the pentose phosphate pathway (Ying, 2008). In this pathway the primary NADPH-producing enzyme, glucose 6-phosphate dehydrogenase, has a 1000-times higher affinity for $NADP^+$ than NAD^+. This allows the ratio of $NADP^+$ to NADPH in the cytosol to be maintained low, independently of the NADH pool redox ratio, in a ratio of around one to 100 (Berg et al., 2011).

The pentose phosphate pathway takes glucose 6-phosphate, produced from glucose by hexokinase in the first step of glycolysis, as its starting point. A series of three reactions converts glucose 6-phosphate into ribulose 5-phosphate. Two of these reactions, catalysed by glucose 6-phosphate dehydrogenase and 6-phosphogluconate dehydrogenase respectively, are oxidations in which $NADP^+$ is reduced to NADPH. NADPH carries reducing equivalents to the redox reactions performed during anabolism such as fatty acid and nucleotide syn-

thesis (Berg et al., 2011). While the pentose phosphate pathway is the primary method of NADPH production, two other cytosolic NADPH-producing enzymes exist in mammalian cells: isocitrate dehydrogenase and malic enzyme (Pollak et al., 2007a; Ying, 2008).

The ribulose 5-phosphate produced by the pentose phosphate pathway can be converted into various glycolytic intermediates by a network of enzymes. Phosphopentose isomerase and phosphopentose epimerase are able to convert ribulose 5-phosphate into ribose 5-phosphate and xylulose 5-phosphate, respectively. The enzymes transketolase and transaldolase can then take these molecules, along with each other's products, to form glyceraldehyde 3-phosphate and fructose 6-phosphate (Berg et al., 2011), as shown in figure 1.5. Thus, after branching off from glycolysis by initiating from glucose 6-phosphate, the NADPH-producing pentose phosphate pathway can feed its products back into the NADH-producing glycolysis.

1.5 Controlling the fate of glucose

The molecule ribose 5-phosphate, produced by the pentose phosphate pathway, is not only useful to the cell for being a precursor for the production of glycolytic intermediates. As can be seen in figures 1.1 and 1.4, the ribose sugar forms part of the "skeleton" onto which the ATP, NADH and NADPH molecules are built (Alberts et al., 2007). Ribose is also used in forming the backbones of ribonucleic acid (RNA) and deoxyribonucleic acid (DNA), the transport and storage molecules of genetic information respectively (Rose, 1999).

If large amounts of ribose 5-phosphate are required by the cell, glucose can be sent through the energy investment stage of glycolysis and, using the glyceraldehyde 3-phosphate and fructose 6-phosphate produced, the pentose phosphate pathway reactions catalysed by transketolase and transaldolase can be reversed to produce six molecules of ribose 5-phosphate per five molecules of glucose (Clasquin et al., 2011). However, no NADH or NADPH is produced this way, represented as A→B→D in figure 1.6. Had the same amount of glucose been passed through the pentose phosphate pathway, 10 molecules of NADPH would have been produced alongside five molecules of ribose 5-phosphate (A→D). The former method can therefore be used by the cell when large amounts of ribose 5-phosphate but no NADPH is required, whereas the latter method can be used when ribose 5-phosphate and NADPH requirements are balanced (Alberts et al., 2007).

If large amounts of NADPH are required by the cell but ribose 5-phosphate is not necessary, 60 molecules of NADPH can be produced by the complete oxidation of 5 glucose

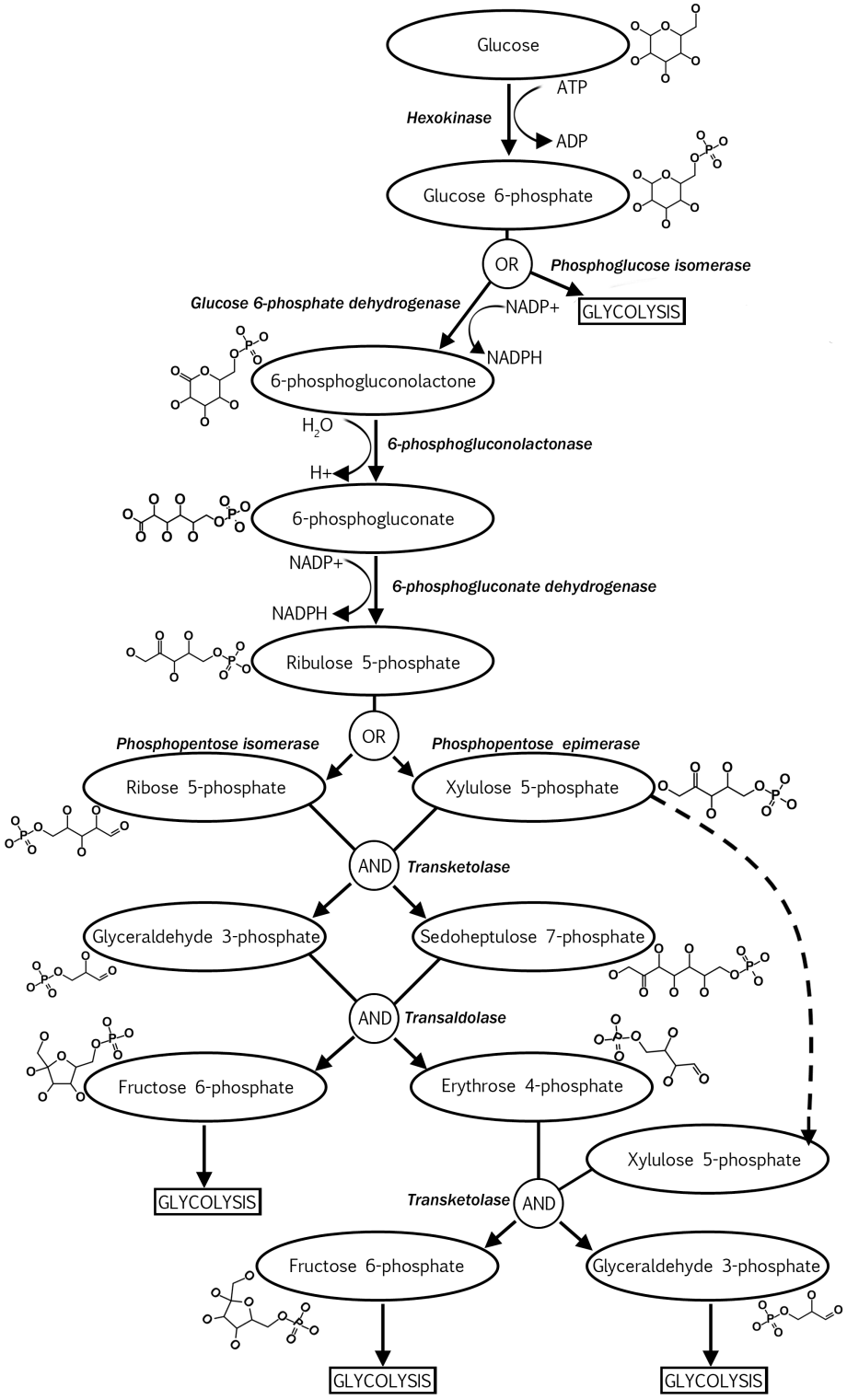

Figure 1.5: The anaerobic breakdown of glucose by the pentose phosphate pathway to produce NADPH, adapted from (Berg et al., 2011). The fructose 6-phosphate and glyceraldehyde 3-phosphate produced can be further metabolised by glycolysis.

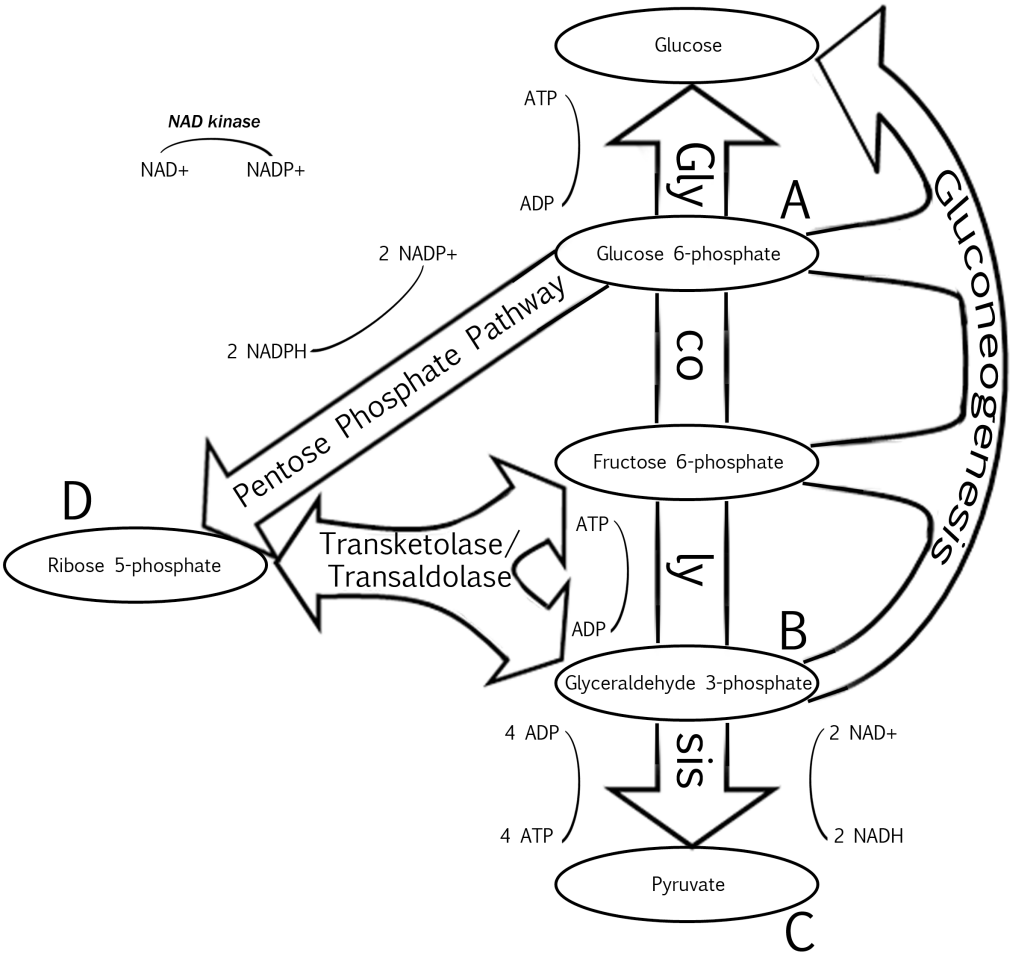

Figure 1.6: The network of options available for the metabolism of glucose (Alberts et al., 2007).

molecules via the pentose phosphate pathway. This is achieved by repeatedly breaking down the ribose 5-phosphate produced by each pass of the pentose phosphate pathway into the glycolytic intermediates glyceraldehyde 3-phosphate and fructose 6-phosphate, then sending these through a set of enzymes that catalyse the reverse of the energy investment stage of glycolysis, known as gluconeogenesis, to reproduce glucose 6-phosphate (A→D→B→A) to send back through the pentose phosphate pathway (Berg et al., 2011).

Rather than sending glyceraldehyde 3-phosphate and fructose 6-phosphate through gluconeogenesis, completing their metabolism after the pentose phosphate pathway using the energy generation stage of glycolysis (A→D→B→C) produces six NADPH molecules, five NADH molecules and five ATP molecules per three glucose molecules entered (Berg et al., 2011). This route yields both ATP and NADPH. If NADPH is not required, simply sending the same amount of glucose through glycolysis (A→B→C) would produce six ATP molecules and six molecules of NADH (Alberts et al., 2007).

As seen in figure 1.6, various pathways are available for glucose metabolism by combining glycolysis, gluconeogenesis, the reversible action of the transketolase and transaldolase enzymes and the pentose phosphate pathway. However, the extent to which the pentose phosphate pathway can be utilised depends solely on the concentration of $NADP^+$ in the cell. With no available $NADP^+$, no electron-carrier is available to be reduced during the oxidation of glucose 6-phosphate or 6-phosphogluconate. The particular metabolic pathway for glucose that the cell employs from the complex network available is therefore a consequence of the availability of $NADP^+$ in addition to the proportions of ATP, NADH, NADPH and ribose 5-phosphate required by the cell (Berg et al., 2011).

The sole method for producing $NADP^+$ in the cell is the phosphorylation of NAD^+ (Berger et al., 2004). This reaction is catalysed by the enzyme NAD kinase. As NADPH levels are determined by the availability of $NADP^+$ for reduction by the pentose phosphate pathway, NAD kinase plays the central role in controlling the concentration of NADPH present in the cell (Pollak et al., 2007b).

1.6 Mitochondrial metabolism

The appearance of significant levels of oxygen in the atmosphere around 2 billion years ago allowed organisms to pass electrons removed during the oxidation of substrates to oxygen molecules, reducing the oxygen to water (Lane, 2002). Oxygen has a high affinity for electrons. An electron added to an oxygen atom will therefore become tightly bound, releasing large amounts of energy (Atkins and De Paula, 2010). The process of oxidative phosphorylation couples this large energy release to ATP production, allowing more ATP to be produced per substrate molecule than by the non-oxidative pathway of glycolysis. While the anaerobic oxidation of glucose to pyruvate in glycolysis produces two ATP molecules, the subsequent passage of pyruvate through the aerobic pathway gives an approximate yield of 28 further ATP molecules (Alberts et al., 2007).

Aerobic respiration takes place in the mitochondria. These are cylindrical organelles, located in the cytosol of eukaryotic cells, enclosed by a double membrane. The distribution of the mitochondrial network varies with the function and metabolic state of the cell (Osellame et al., 2012). For example, in muscle, large numbers of mitochondria are packed between the contracting filaments to provide the ATP necessary for movement, whereas in cultured cell lines the mitochondrial network is more diffuse (Duchen, 2004). The inner mitochondrial membrane encloses the mitochondrial matrix with the gap between the in-

ner and outer mitochondrial membranes referred to as the intermembrane space (Alberts et al., 2007).

Aerobic respiration takes pyruvate, the end product of anaerobic glycolysis, as its starting point. Pyruvate is imported into the mitochondrial matrix (Herzig et al., 2012) where the pyruvate dehydrogenase complex, a set of three enzymes, oxidises and decarboxylates pyruvate into acetyl CoA, producing CO_2 and NADH in the process. The enzyme citrate synthase joins the two-carbon acetyl group of acetyl CoA to the four-carbon molecule oxaloacetate, forming citrate (Berg et al., 2011). This citrate then enters a series of seven enzyme-catalysed reactions known as the citric acid cycle.

In the citric acid cycle, the six-carbon citrate is oxidised back to four-carbon oxaloacetate. The two carbon atoms lost are carried away as carbon dioxide. Three molecules of NADH are produced in the full cycle, with energy also being carried away by one molecule of ATP (Berg et al., 2011). The resulting oxaloacetate is then joined to another molecule of acetyl CoA and the reactions of the citric acid cycle, shown in figure 1.7, can be repeated.

The citric acid cycle harvests electrons from substrate molecules, the final fate of which is in the reduction of oxygen to water with the energy released used for the synthesis of ATP in oxidative phosphorylation. In addition to the pyruvate dehydrogenase complex providing the route for sugars, in the form of pyruvate, to provide the energy for this process, pathways also exist for the conversion of fats and amino acids into acetyl CoA, the citric acid cycle's starting point (Berg et al., 2011). As such, the mitochondria represent the site for the universal conversion of all types of fuel substrate into energy of a useable form.

The reduction of NADH removes energy from the substrates of the citric acid cycle. The conversion of the energy carried by NADH into ATP begins with the electron transport or respiratory chain, a group of multisubunit protein complexes located on the inner mitochondrial membrane. NADH molecules carry electrons to the first complex in the chain, NADH dehydrogenase or complex I (Efremov et al., 2010). Upon oxidation of NADH to NAD^+, the electrons are passed down the electron transport chain, ending at complex IV: cytochrome c oxidase. Here, four electrons are passed to an oxygen molecule and combined with four protons, producing two molecules of water (Osellame et al., 2012).

The electron-affinity of the redox-carrying units of the respiratory chain complexes increases along the chain (Alberts et al., 2007). Electrons become more tightly bound as they move down the chain, meaning energy is released as they progress. The protein complexes

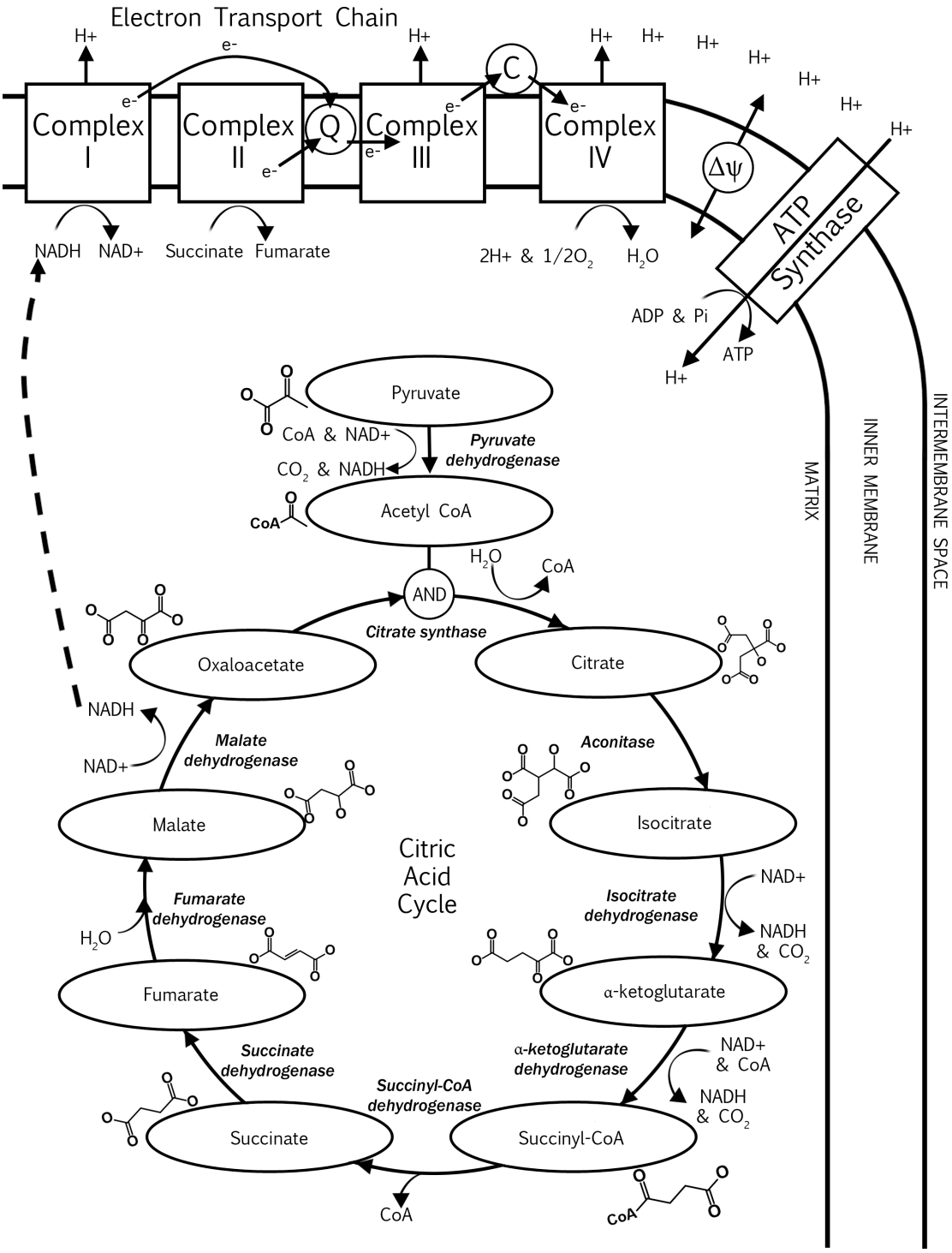

Figure 1.7: Aerobic metabolism in the mitochondria, consisting of the citric acid cycle, electron transport chain and ATP synthase enzyme.

of the electron transport chain use this energy to pump protons from the mitochondrial matrix into the intermembrane space (Osellame et al., 2012). The passage of electrons along the respiratory chain, shown in figure 1.7, therefore produces an electrochemical gradient across the inner mitochondrial membrane. Akin to a battery, this potential gradient provides the energy source for ATP synthesis (Mitchell, 1961).

ATP synthase is the enzyme responsible for converting the energy stored in the proton gradient across the inner mitochondrial membrane, or membrane potential, into ATP. This enzyme consists of a static complex attached to the inner mitochondrial membrane, containing binding sites for ADP and phosphate, and a rotating transmembrane complex containing a proton channel (Berg et al., 2011). A stalk attached to the rotor protrudes inside the static complex. Passage of protons through the transmembrane portion of the enzyme forces its rotation. The movement of the rotor inside the stator, powered by the membrane potential, provides the energy necessary to combine ADP with phosphate and release ATP into the mitochondrial matrix (Nakamoto et al., 2008).

Sufficient reducing equivalents are supplied to the respiratory chain by the oxidation of one molecule of pyruvate in the citric acid cycle to pump around 50 protons across the inner mitochondrial membrane (Osellame et al., 2012). Estimates of how many protons must pass through ATP synthase in order to produce a single ATP molecule vary between two and five (Ferguson, 2010).

The electrons carried by the two molecules of NADH produced during glycolysis can also contribute to the electron transport chain by being imported into the mitochondria by the malate-aspartate shuttle (LaNoue and Williamson, 1971). Here, cytosolic NADH is used to reduce cytosolic oxaloacetate to malate. The malate then enters the mitochondria via a specific inner-membrane carrier where it is oxidised back to oxaloacetate, reducing an NADH molecule inside the mitochondrial matrix in the process. The oxaloacetate returns to the cytosol indirectly, by gaining an amino group from glutamate to form α-ketoglutarate and aspartate, which then exit through inner-membrane carrier proteins. Oxaloacetate can be restored in the cytosol by the reverse of this reaction (Berg et al., 2011). The net result is the indirect transfer of reduced NADH between the cytosol and mitochondria, supplying reducing equivalents to the electron transport chain for ATP synthesis and aiding the maintenance of the cytosolic NAD^+/NADH pool in a largely oxidised state.

1.7 Mitochondria in disease

The efficient production of large amounts of ATP by the mitochondria is critical in providing the energy required to maintain complex life (Lane and Martin, 2010). For this reason, the mitochondria are frequently referred to as the cell's "powerhouses" (Alberts et al., 2007). Due to their crucial role in energy supply, mitochondrial dysfunction is a hallmark of a large number of pathologies, from cancer and diabetes to Alzheimer's and Parkinson's diseases (Duchen, 2004).

In so-called mitochondrial disorders, such as Leigh syndrome, dysfunction results directly from mutations in the mitochondria's own small genome (Osellame et al., 2012), retained as an artefact from the organelle's evolutionary origins as symbiotic bacteria (Gray, 2012). Impaired functioning of the mitochondria can also result from the dysregulation of mitochondrial pathways, such as in the improper handling of mitochondrial calcium, used as a regulatory signal for increased citric acid cycle activity (Osellame et al., 2012). The increased production of reactive oxygen species is also a hallmark of faulty mitochondria. Also known as free radicals, these are formed when single electrons are allowed to leak from the respiratory chain directly to oxygen, producing superoxide; reduced molecular oxygen containing a single unpaired electron (Murphy, 2009). Superoxide is highly reactive, imparting oxidative stress on the cell, damaging membranes, proteins and DNA (Brand et al., 2004). The cell is able to protect itself from reactive oxygen species to some extent using the antioxidant glutathione. Reduced glutathione can donate an electron to a free radical to stabilise it. The enzyme glutathione reductase restores the reduced glutathione supply using NADPH as the redox carrier (Berg et al., 2011).

Typically, disease-states are associated with defects in a variety of the functional and regulatory mitochondrial mechanisms (Duchen, 2004). For example, both increased oxidative stress and modified calcium signalling have been observed in cancer cells (Carew and Huang, 2002; Capiod et al., 2007). The requirement for the development of cancerous tumours is the imbalance between cell proliferation and cell death (Alberts et al., 2007). Mitochondria are often described as the poison cabinets of the cell for their role in the initiation of the cell's pathway for programmed cell death, apoptosis (Osellame et al., 2012). As such, impaired control of apoptosis by the mitochondria is also able to contribute to cancer development (Carew and Huang, 2002).

The earliest indication that mitochondrial function is altered in cancer cells was de-

scribed by Otto Warburg in 1924. The Warburg effect states that cancer cells display the exaggerated glucose uptake and increased levels of lactate release indicative of an excessive rate of glycolysis, even in the presence of sufficient oxygen to support oxidative phosphorylation (Vander Heiden et al., 2009). This so-called aerobic glycolysis is utilised for diagnostic imaging. The radioactive glucose analogue fluorodeoxyglucose is more readily taken up by cancer cells than normal cells, allowing the localisation of tumours using positron emission tomography (Alberts et al., 2007).

1.8 Fluorescence monitoring of redox state

In 1962, Britton Chance showed that light with a peak emission wavelength of around 460nm is emitted by live tissue when light of wavelength 366nm is incident upon it (Chance et al., 1962). Removing the oxygen supply to the tissue caused the intensity of this emission to increase, returning back to its initial value when the oxygen supply was restored. The molecule in the tissue responsible for this effect was shown to be NADH, absorbing light in the ultraviolet portion of the electromagnetic spectrum and emitting blue light as fluorescence.

When oxygen supply is removed from live tissue, the electron transport chain halts and NADH oxidation in the mitochondria by complex I stops, while the citric acid cycle continues to reduce NAD^+ to NADH. The oxidised NAD^+ does not absorb the 366nm incident light (De Ruyck et al., 2007), causing the intensity of the light emitted from the tissue to increase as the NAD^+ is reduced to the fluorescent NADH. Restoration of the oxygen supply to the tissue allows the electron transport chain to proceed, oxidising the NADH produced by the citric acid cycle back to the non-fluorescent NAD^+, decreasing the intensity of emission back to the initial value. The steady-state intensity of the light emitted by NADH will be determined by the balance of reduction by the citric acid cycle and oxidation by the electron transport chain (Duchen et al., 2003).

By applying drug treatments chosen to maximally reduce or maximally oxidise mitochondrial NADH, the redox ratio of the mitochondrial NADH pool in live cells and tissues can be estimated (Duchen et al., 2003). Rotenone is an inhibitor of complex I of the electron transport chain (Li et al., 2003). Treatment of cells with this compound will cause the maximal reduction of mitochondrial NADH as complex I can no longer oxidise the reduced NADH being produced by the citric acid cycle. In contrast, application of the compound carbonyl cyanide 4-(trifluoromethoxy)phenylhydrazone (FCCP) will maximally oxidise the

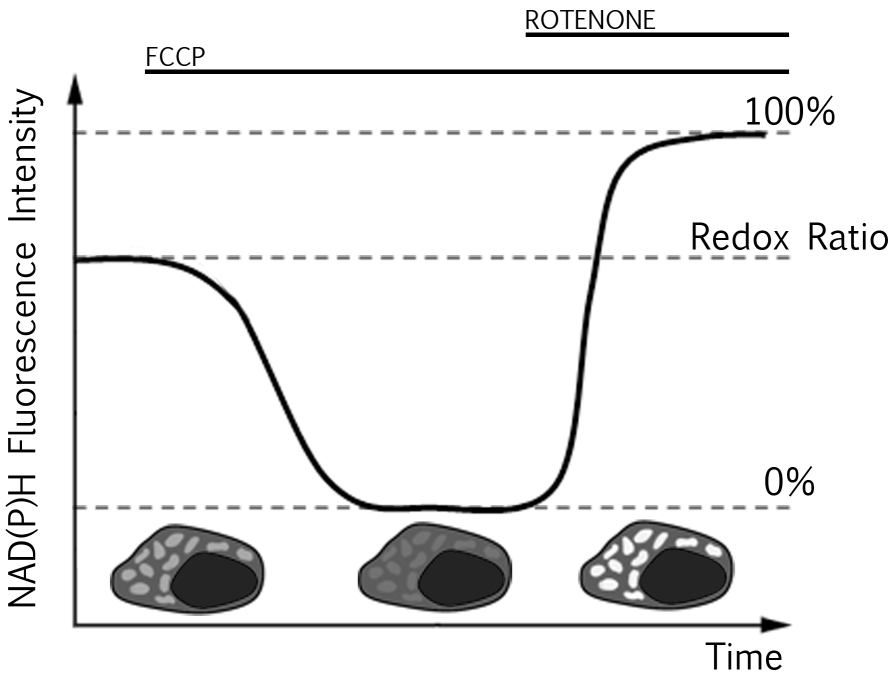

Figure 1.8: A technique for measuring the redox ratio of the NAD^+/NADH pool in the mitochondria using the intensity of NAD(P)H fluorescence in the presence of FCCP and rotenone to define the dynamic range upon which to compare the resting fluorescence level.

mitochondrial NADH pool. FCCP uncouples the mitochondrial membrane potential from ATP synthesis by providing an alternative route to ATP synthase for the passage of protons across the inner membrane (Duchen, 2004). The energy lost by the protons as they pass across the inner membrane via FCCP is dissipated as heat (Osellame et al., 2012). With the membrane potential disrupted, the rate of electron transport chain activity will increase to restore the proton gradient, increasing the rate of NADH oxidation. The intensity of NAD(P)H fluorescence observed under FCCP then rotenone treatment defines a dynamic range for the comparison of the emission intensity under the initial untreated conditions, as illustrated in figure 1.8. This resting intensity can be normalised and scaled between the minimum and maximum values obtained with the drug treatments to give an approximate value of the redox ratio of the mitochondrial NAD^+/NADH pool.

The approach described above provides an estimate of the ratio of NAD^+ to NADH in the mitochondria alone. Emission from cytosolic NADH, such as that produced by glycolysis, will not contribute to the result obtained as it is subtracted from the steady state intensity with the FCCP-treated measurement. In addition, this technique cannot differentiate the fluorescence arising from NADH and that arising from NADPH. This is because the spectral characteristics of these two electron-carriers are identical (Patterson et al., 2000).

1.9 Fluorescence properties of NAD(P)H

In any molecule, the distribution of electrons about its structure are known as its molecular orbitals. Mathematically, a molecular orbital describes the probability of an electron occupying it being found at a given position in the molecule (Atkins and Friedman, 2010). To each molecular orbital corresponds an energy that an electron occupying it will possess. These energies are quantised, meaning the molecular orbitals form a discrete set of energy levels available to the electrons within a molecule. The electrons will fill these orbitals from the lowest energy upwards, with only two electrons with opposite spins permitted in each orbital, in accordance with the Pauli exclusion principle. The molecular orbital with the highest energy that is occupied by an electron is known as the highest occupied molecular orbital, or HOMO (Valeur, 2001).

The next energy level above the HOMO is known as the LUMO, the lowest unoccupied molecular orbital. The electron occupying the HOMO can be excited into the LUMO upon the absorption of a photon with energy equal to the difference between the initial HOMO energy level, the so-called ground state, and the LUMO excited state (Lakowicz, 2006). The energy of a photon, E is related to its wavelength, λ, by the Planck relation,

$$E = \frac{hc}{\lambda} \tag{1.2}$$

where h is Planck's constant and c is the speed of light (Young and Freedman, 2004). Shorter wavelength photons therefore carry more energy than longer wavelength photons. While individual atoms will absorb light only at the sharply-defined wavelengths corresponding to the precise energy differences between the available electronic states, molecules will absorb light over a range of wavelengths either side of the HOMO to LUMO energy gap. This is because the complex structure of a molecule provides a large number of vibrational degrees of freedom (Lakowicz, 2006). Each possible molecular motion is therefore part of a discrete set of vibrational energy levels available to the molecule at each electronic energy level. This drastically increases the range of possible photon energies that can be absorbed by the molecule. As such, the wavelengths at which a molecule will absorb light is a distribution known as its absorption spectrum.

The absorption spectra of NADH and NADPH are identical, peaking at 340 nm with a full width at half maximum (FWHM) of 60 nm (Patterson et al., 2000), as shown in figure 1.9. The molecular orbitals involved in this excitation are localised to the nicotinamide

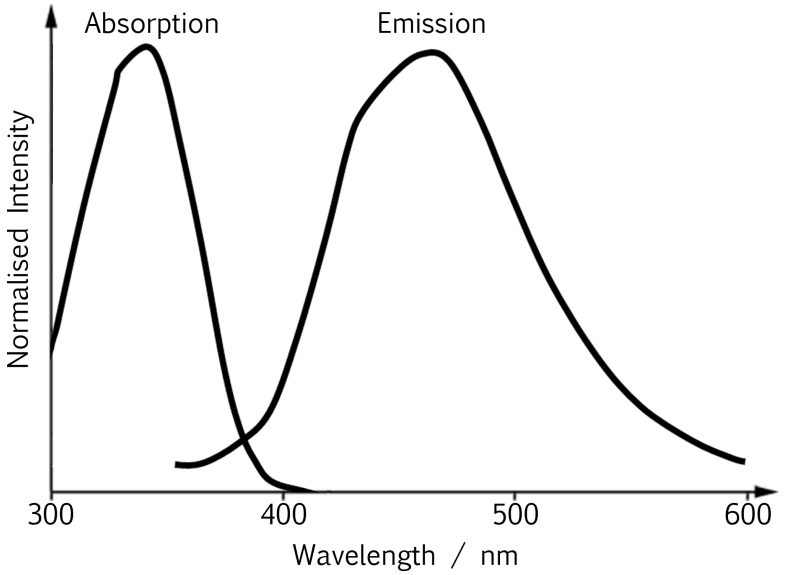

Figure 1.9: Absorption and emission spectra of NAD(P)H, from Patterson et al. (2000). The spectral characteristics of NADH and NADPH are identical.

ring of the molecule (Kierdaszuk et al., 1996), the redox-active region. Quantum chemical calculations (De Ruyck et al., 2007) have shown that removal of the hydride ion carried by NADH or NADPH, forming NAD^+ or $NADP^+$, causes the energy of the HOMO to decrease by 2.96 eV. However, the energy of the LUMO decreases by only 1.99 eV, meaning the energy difference between these states is 0.97 eV larger than that of the electron-carrier in its reduced form. As a result, HOMO to LUMO excitation requires more energy in the oxidised cofactors and the absorption is blue-shifted, with its spectrum peaking at around 220nm (De Ruyck et al., 2007).

At room temperature, the Boltzmann distribution dictates that the majority of molecules will occupy their lowest vibrational energy levels in the ground state (Schroeder, 2000). These intramolecular motions take place at a much slower time scale than electronic transitions, typically tens of picoseconds compared to femtoseconds (Valeur, 2001). The nuclei of the molecule are therefore effectively stationary during excitation, implying that the most probable vibrational states entered upon excitation to the excited state are ones in which the current position of the nuclei is possible. This is the Franck-Condon principle, illustrated in figure 1.10, and the most probable vibrational state entered upon excitation is the Franck-Condon state (Lakowicz, 2006).

The distribution of electronic charge will be different in the excited state than the ground state. For example, in NADH and NADPH, excitation shifts electron density from the nitrogen of the nicotinamide ring towards the amide group (Kierdaszuk et al., 1996). As

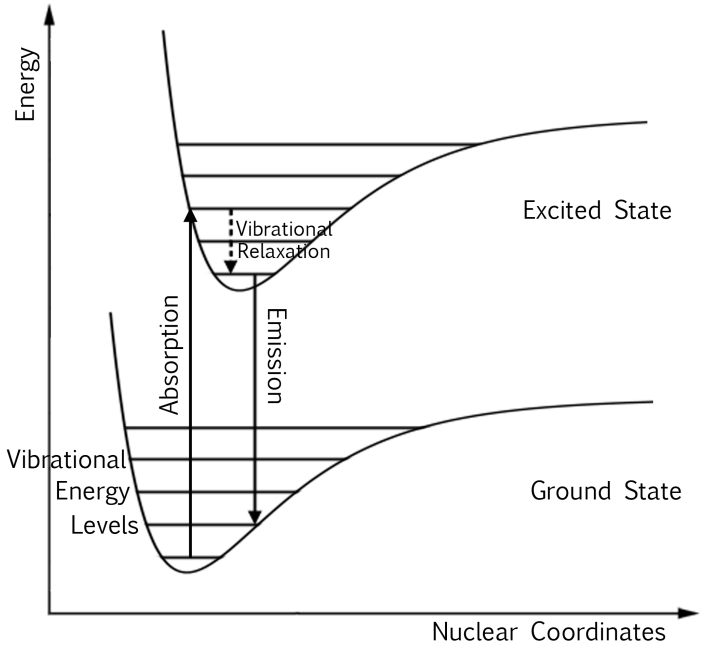

Figure 1.10: The Franck-Condon principle: as electronic excitation takes place at a much faster time scale than nuclear rearrangement, the most probable vibrational energy level entered in the excited state will be one where the nuclear coordinates overlap with the ground state configuration. As bond strengths will be weakened in the excited state, altering the shape of the molecule, this will not necessarily be the same vibrational energy level as in the ground state.

a result, bond strengths may be altered in the excited state. This will cause the geometry of the molecule to change, meaning the Franck-Condon state may not necessarily be the same vibrational state as occupied by the molecule in the ground state (Willock, 2009). However, any additional energy in the Franck-Condon state is rapidly dissipated to the surroundings via collisions over a picosecond time scale (Lakowicz, 2006), taking the molecule into the lowest vibrational energy level of the excited state.

The excited molecule can relax back to the ground state by emitting a photon. This phenomenon is termed fluorescence. Light emitted as fluorescence will be of longer wavelength than the light absorbed due to the vibrational energy lost to the surroundings in the excited state. The spread of wavelengths emitted by a molecule, known as its emission spectrum, is therefore red-shifted relative to the absorption spectrum, an effect known as the Stokes shift (Valeur, 2001). As with the absorption spectra, the emission spectra of NADH and NADPH are identical, peaking at 460 nm with FWHM 100 nm (Patterson et al., 2000), as shown in figure 1.9. The shared absorption and emission properties of the two electron-carriers mean their fluorescence cannot be separated spectrally. As such, the combined signal arising from live tissue is termed NAD(P)H (Duchen et al., 2003).

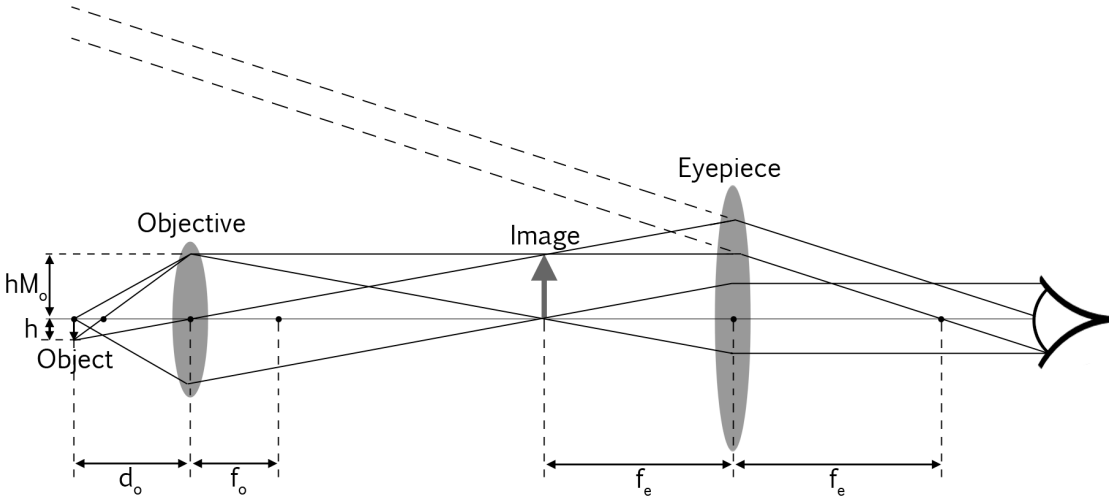

Figure 1.11: A basic compound microscope: a magnified image produced by the objective lens is further magnified by the eyepiece lens.

Not all relaxation from the excited state occurs through the emission of fluorescence. The other, so-called non-radiative, pathways of excited-state decay are discussed in section 1.11. The ratio of photons emitted to photons absorbed by a particular molecule is known as its quantum yield, denoted Φ (Lakowicz, 2006). Tailor-made fluorescence dyes will be designed and synthesised to possess high quantum yields in order to maximise their brightness. For example, the dyes rhodamine 6G and fluorescein have quantum yields of 0.95 and 0.97 respectively (Du et al., 1998). In contrast, the quantum yield of NAD(P)H is 0.02 (Scott et al., 1970), meaning only 2% of the photons absorbed result in emission of fluorescence. Nevertheless, with laser excitation and sensitive detectors, this metabolic cofactor still represents a viable target for fluorescence imaging.

1.10 Fluorescence microscopy

The development of optical instruments to aid the study of microscopic phenomena began in the 17th century (Hecht and Zajac, 1974). Since then, the quality and resolution of images obtainable using a microscope have improved hand-in-hand with advances in the field of optics. However, the very basic principles for creating a magnified image of a sample have remained the same. Figure 1.11 shows the design of the simplest compound microscope. A convex objective lens collects light scattered from an object. The focal length of the objective is short, ensuring that a real, magnified image is formed behind the lens (Pedrotti et al., 1993).

The magnification of the objective lens is given by,

$$M_o = \frac{f_o}{f_o - d_o} \tag{1.3}$$

where d_o is the distance of the object from the objective of focal length f_o. As $d_o > f_o$, the magnification will be negative, indicating that the image will be inverted (Hecht and Zajac, 1974). If the object is of length h, the image will be of length hM_o. This image is then further magnified by the eyepiece. Assuming the eyepiece lens is located at the so-called near point of the eye, 0.25m away, the magnification of the image by the eyepiece is given by (Pedrotti et al., 1993),

$$M_e = \frac{0.25}{f_e} \tag{1.4}$$

The total magnification by this two-lens microscope is then the product of equations 1.3 and 1.4. Using equation 1.4, the magnification of a simple looking-glass of focal length 0.1 m is 2.5. If a crude microscope were constructed from two of these magnifying glasses, based on the design in figure 1.11, and the object was positioned 0.01 m from the focal point of the objective, the total magnification would increase 10-fold to 25. It is through combining a number of lenses that allows the microscope to obtain magnifications far greater than a single lens (Feynman, 1970).

Real lenses are not perfect, suffering from a number of errors that can reduce the quality of the image they produce. For example, light passing close to the centre of a lens can be brought to a different focal point as light passing close to the lens edge. This is known as spherical aberration. In addition, the focal point of a lens can be different for light of different wavelength. This is known as chromatic aberration (Hecht and Zajac, 1974). The introduction of additional optical components to correct for these aberrations increases the complexity of real microscopes compared to the simple system shown in figure 1.11.

The brightness of the image produced by a microscope results from the amount of light that can be collected by the objective lens. This property is described by the numerical aperture of the objective, defined as,

$$\text{N.A.} = n \sin \alpha \tag{1.5}$$

where α is the half-angle through which the lens can accept light emanating from

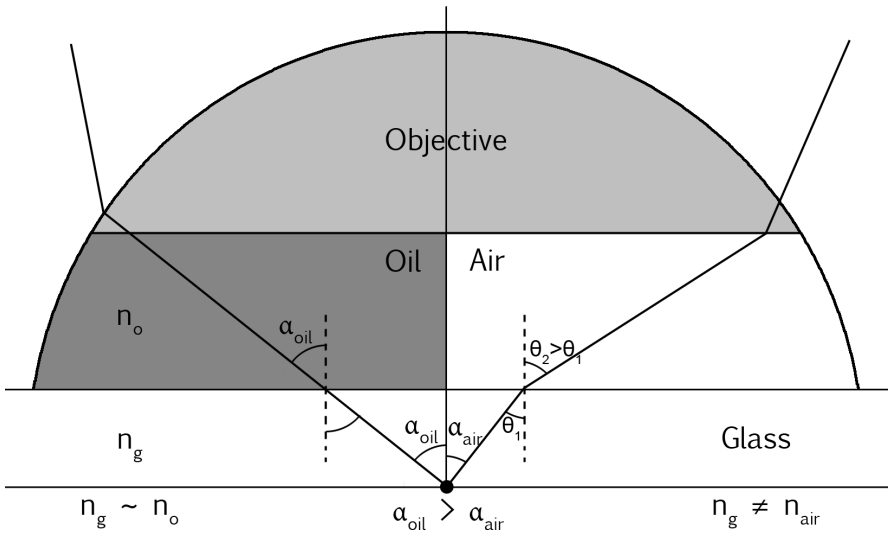

Figure 1.12: The use of an immersion fluid such as oil reduces the refraction of light exiting the cover glass. This allows light to be collected by the objective over a greater angle, increasing its numerical aperture (equation 1.5).

the object and n is the refractive index of the medium in which the objective is operating (Pedrotti et al., 1993). Biological samples are typically imaged through thin cover glass. By filling the region between the cover glass and the objective with a high refractive index fluid, the numerical aperture, and therefore the amount of light collected from the object, can be increased. This occurs because light exiting the cover glass into air will be refracted away from the normal, limiting the range of angles through which light can be collected, as shown in figure 1.12. This effect is reduced by immersing the objective in oil or water, whose refractive indices are closer to that of the cover glass.

Increasing the amount of light incident on a sample will also increase the amount of light captured by the objective. This can be achieved by focussing the light from an external source, such as a lamp, onto the region of the sample being imaged. The lens responsible for this is known as the condenser (Pedrotti et al., 1993). While images obtained using this simple set-up still find use in the biological sciences for day-to-day tasks such as inspection of cell cultures, the molecular era demands more sophisticated techniques for the study of biochemical processes using imaging. These applications are realised by an extensive catalogue of fluorescent dyes designed for staining particular components of the cell (Lichtman and Conchello, 2005). These range from signalling ions and reactive oxygen species to organelles and membranes (Johnson and Spence, 2010).

To obtain an image of the distribution of a fluorescent dye within a biological sample, illumination is provided at a wavelength present in the absorption spectrum of the

fluorophore. Due to their monochromaticity, lasers are typically employed for this purpose (Pawley, 2006). Fluorescence will be emitted by the dye in all directions, whereas the majority of the high-intensity excitation light not absorbed will continue in a straight path. This allows a large portion of the incident light to be removed from the image obtained by using epitaxial illumination, a scheme in which illumination and detection are both made through the objective lens (Lichtman and Conchello, 2005).

A small amount of reflected or backscattered illumination will still be present in the light passing back through the objective. This is filtered out by taking advantage of the Stokes shift of the fluorescent dye, described in section 1.9. A dichroic mirror is placed in the beam path, responsible for reflecting light with a wavelength above a certain threshold and transmitting light with a wavelength below that value (Pawley, 2006). Appropriate choice of a dichroic with a threshold wavelength between the absorption and emission spectra of the dye will separate the fluorescence image from noise caused by residual excitation light. Emission filters can then be placed before the eyepiece to select a specific region of the emission spectrum of the dye. This set-up is known as an epifluorescence microscope (Lichtman and Conchello, 2005).

In an epifluorescence microscope, the entire sample is illuminated. The contrast of the image produced will be decreased by the presence of significant amounts of light entering the objective from outside its focal plane. The image quality can be improved by rejecting this out of focus light using the technique of confocal microscopy (Pawley, 2006). In a confocal microscope, shown in figure 1.13, a pinhole is placed at the rear focal point of the objective such that only the light emanating from the sample at the focal point is allowed through. Only the small focal volume of the objective is imaged at any one time in this technique, requiring the eyepiece to be removed and replaced by a photodetector. The excitation laser light is then raster-scanned across the sample and an image constructed by combining the fluorescence intensities at each point (Pawley, 2006).

As NAD(P)H is fluorescent, images can be produced using confocal laser-scanning microscopy to observe its concentration in different regions of the cell. Using 351 nm excitation from an argon ion laser (UV Enterprise, Coherent), a 40x oil immersion 1.3 N.A. quartz objective lens, a dichroic with a 375 nm cutoff wavelength and a 460($\pm$25) nm bandpass emission filter in a Zeiss LSM510 microscope, images of the HeLa cell line were obtained, displayed in figure 1.14. The punctate regions of intense NAD(P)H fluorescence

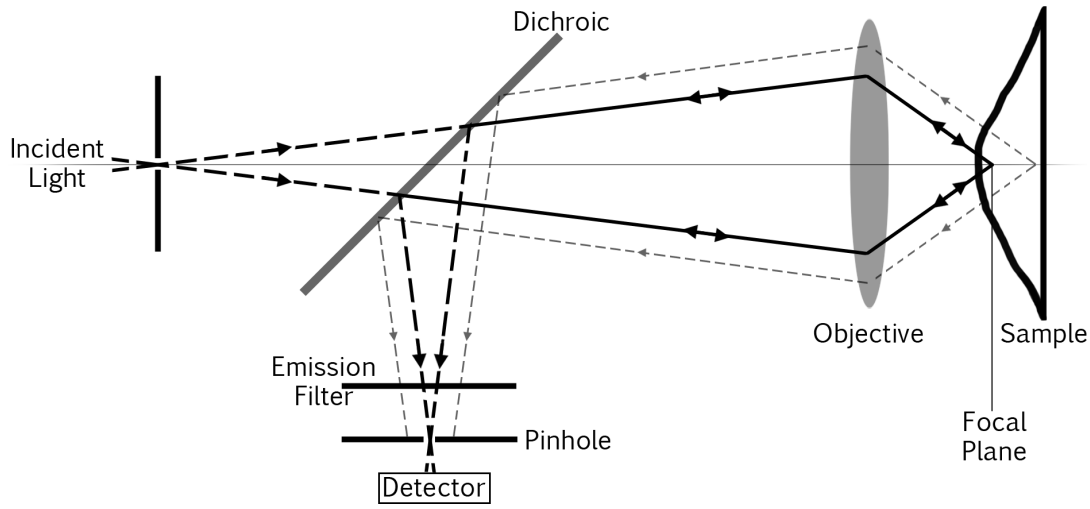

Figure 1.13: The confocal microscope: light emitted from outside the focal plane of the objective is rejected by a pinhole placed in front of the detector.

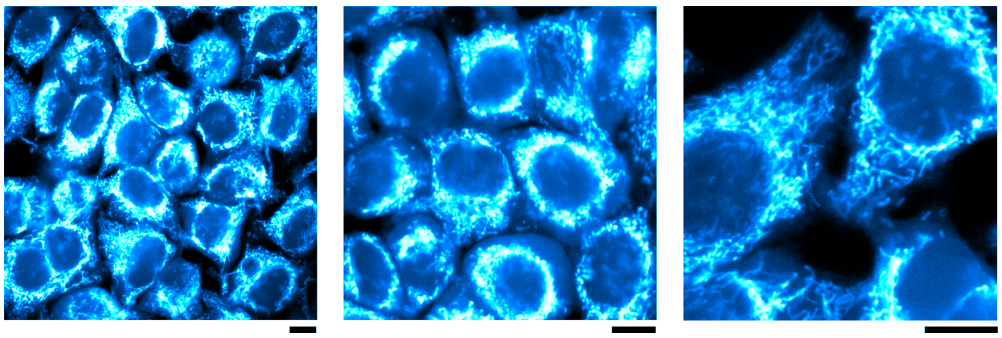

Figure 1.14: NAD(P)H fluorescence in cultured HeLa cells imaged using a confocal microscope. Scale bars are 10 μm.

are the mitochondria.

In confocal microscopy, the smaller the pinhole, the less light either side of the focal plane is allowed through to the detector. This results in a thinner section of the sample contained in the image. This optical sectioning can also be achieved without the use of a confocal pinhole using the technique of two-photon excitation (Denk et al., 1990). Here, rather than one photon providing all the necessary energy to send a fluorophore into the excited state, two lower energy photons are absorbed. Using Heisenberg's uncertainty principle to estimate the existence time of the virtual electronic state entered upon absorption of the first photon, the two photons must be absorbed within approximately 0.5 fs of each other (Helmchen and Denk, 2005). This interval is more than five times shorter than the oscillation period of the excitation light. The absorption of both photons is therefore effectively simultaneous (Larijani et al., 2006).

With one-photon excitation, the amount of light absorbed by a molecule is linearly

proportional to the excitation intensity. However, two-photon absorption is proportional to the excitation intensity squared, with the proportionality constant σ_{2P} defined as the two-photon cross section of the molecule (Lakowicz, 2006). If the cross section of the focal volume of an objective is assumed to be circular with radius r_0, at a distance l away from the focal point along the beam path, the amount of absorption will be approximately reduced by a factor,

$$\frac{\text{Absorption}_{\text{l}}}{\text{Absorption}_{\text{focus}}} = \left(\frac{I_{\text{l}}}{I_{\text{focus}}}\right)^2 = \left(\frac{\text{area}_{\text{focus}}}{\text{area}_{\text{l}}}\right)^2 = \left(\frac{r_0}{r_0 + l\tan\alpha}\right)^4 \tag{1.6}$$

where α is the half angle at which the light is focussed, given by equation 1.5 and shown in figure 1.12. The value of r_0 is related to the numerical aperture of the objective and can be estimated by the Rayleigh criterion for a diffraction limited microscope (Pawley, 2006) as,

$$r_0 \approx \frac{\lambda}{2\text{N.A.}} \tag{1.7}$$

where λ is the wavelength of the incident light. The axial resolution of a confocal microscope is around 1 μm (Pawley, 2006). Based on equation 1.6, therefore, in two-photon excitation microscopy with 700 nm illumination and a 1 N.A. objective, absorption 1 μm from the focal point of the objective will have reduced by 99.7%. The application of two-photon excitation in microscopy therefore provides inherent optical sectioning due to absorption being localised to the femtolitre focal volume of the objective (Helmchen and Denk, 2005).

A simultaneous advantage of two-photon excitation microscopy compared to conventional fluorescence microscopy results from the red-shifted illumination. As longer-wavelength light scatters less in biological tissue, images can be taken at depths up to 1 mm (Helmchen and Denk, 2005). This allows fluorescence imaging to be a viable technique for investigations into the physiology of complex tissue preparations ranging from the intact heart (Davidson et al., 2012) to the inner ear (Griesinger et al., 2005).

1.11 Excited state decay

The techniques of confocal laser-scanning microscopy and two-photon excitation microscopy produce images in which the contrast is derived from the intensity of emission from a fluorophore at each point in a sample. In fluorescence lifetime imaging microscopy

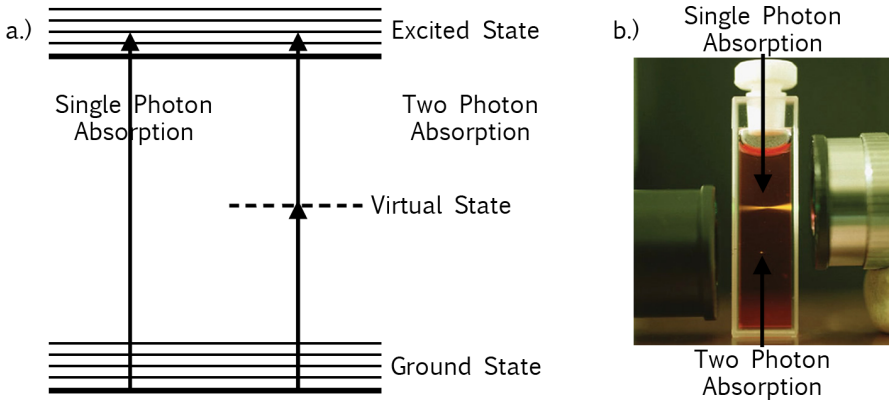

Figure 1.15: (a) Two-photon excitation occurring upon the simultaneous absorption of two photons with half the energy (twice the wavelength) of that required by a single photon to send the molecule into the excited state. As shown in (b), the low probability of this event occurring ensures that significant excitation only occurs in the focal volume of the objective (lower beam), providing inherent optical sectioning not possible with single photon absorption (upper beam; image courtesy Brad Amos, Science Photo Library).

(FLIM), the subject of this thesis, contrast is derived from the rate at which excited fluorophores return to the ground state at each point in a sample (Periasamy and Clegg, 2010).

A molecule in the excited state has a number of options available for returning to the ground state, shown as a Jablonski diagram in figure 1.16. Fluorescence is only one of a number of possible excited state decay routes. The energy of excitation can be transferred during collisions with other molecules or other molecular groups attached to the fluorophore in a process known as quenching (Lakowicz, 2006). Alternatively, if there is overlap between the excited state and ground state vibrational energy levels, the molecule can make the transition between the two states without the emission of a photon. This process is known as internal conversion (Valeur, 2001). Both quenching and internal conversion are examples of non-radiative deexcitation processes.

There exists a finite probability that the spin of an excited electron will flip, moving from a singlet state into a so-called triplet state. This process is known as intersystem crossing (Valeur, 2001). Transitions from the triplet state back to the ground singlet state are forbidden by quantum-mechanics. As such, they still occur but with low probability and therefore at a low rate and slow timescale. The light emitted during this radiative transition is known as phosphorescence (Lakowicz, 2006).

If the rate at which electrons are removed from the excited state via non-radiative pathways, such as quenching and internal conversion, is denoted $k_{\mathrm{non-rad}}$, while the radiative rate of spontaneous emission is denoted k_{rad}, light of a suitable wavelength incident

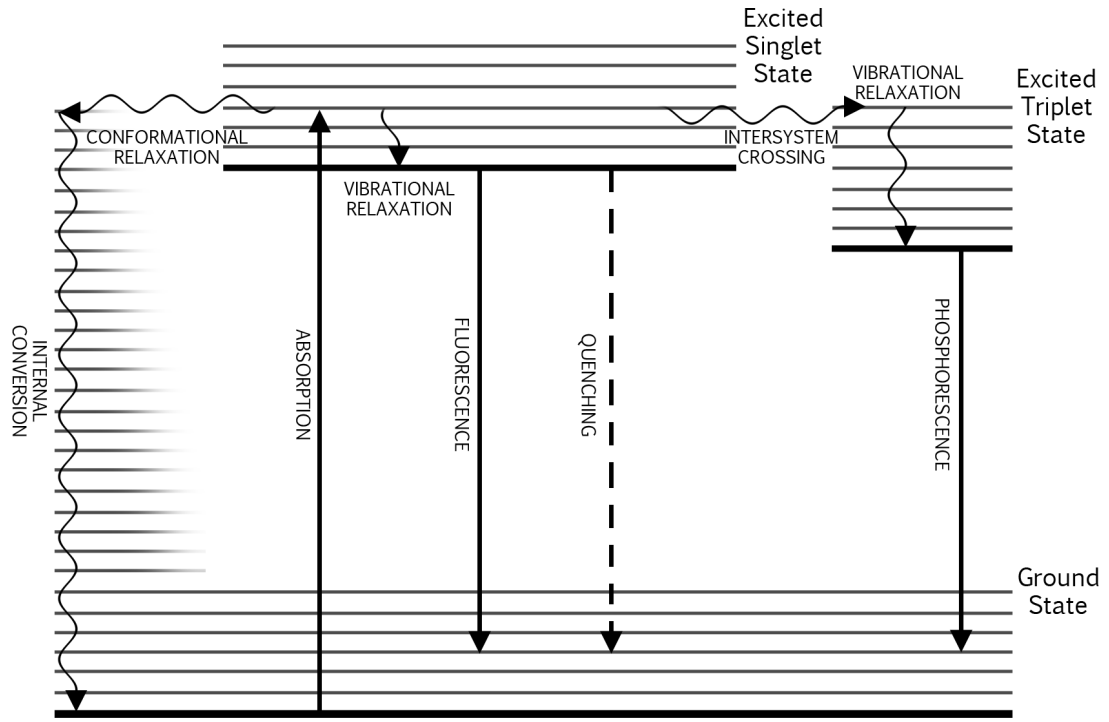

Figure 1.16: A Jablonski diagram demonstrating that emission of fluorescence is but one of a number of paths of relaxation for an excited state molecule. Routes not causing emission of a photon, such as internal conversion and quenching, are termed non-radiative pathways.

on a homogenous population of molecules will cause a number $n(0)$ to enter the excited state with the number of excited-state molecules n decreasing with time t according to the first order rate law,

$$\frac{dn(t)}{dt} = -\left(k_{\text{rad}} + k_{\text{non-rad}}\right) n(t) \tag{1.8}$$

Integration gives the solution of equation 1.8 as,

$$n(t) = n(0) \exp\left(-\left[k_{\text{rad}} + k_{\text{non-rad}}\right] t\right) \tag{1.9}$$

The rate constant k_{rad} is the average number of photons emitted per unit time per excited molecule. Equation 1.9 can therefore be written in terms of the number of photons emitted at time t, $I_{\text{total}}(t)$, by multiplying through by k_{rad},

$$I_{\text{total}}(t) = k_{\text{rad}} n(t) = k_{\text{rad}} n(0) \exp\left(-\left[k_{\text{rad}} + k_{\text{non-rad}}\right] t\right) \tag{1.10}$$

Setting $k_{\text{rad}} n(0) = I(0)$, the intensity of light emitted by the population immediately after excitation, and replacing the sum of decay rates with a time constant τ_f, equation

1.10 can be rewritten as,

$$I_{\text{total}}(t) = I(0)\exp\left(-\frac{t}{\tau_f}\right) \tag{1.11}$$

The time constant of the decay, τ_f, is the fluorescence lifetime of the molecule. It is related to the rates of radiative and non-radiative decay through,

$$\tau_f = \frac{1}{k_{\text{rad}} + k_{\text{non-rad}}} \tag{1.12}$$

The fluorescence lifetime of a molecule is therefore a measure of the magnitude of radiative and non-radiative processes contributing to the depletion of the excited state population. If the rate at which these processes occur increases, the fluorescence lifetime becomes shorter and, according to equation 1.11, the intensity of light emitted from the population of molecules decays more quickly with time.

It is possible to define the fluorescence lifetime in a more intuitive manner. The average amount of time a fluorophore remains in the excited state following excitation can be written (Lakowicz, 2006),

$$\langle t \rangle = \frac{\int_0^\infty t I_{\text{total}}(t)\,dt}{\int_0^\infty I_{\text{total}}(t)\,dt} = \frac{I(0)\int_0^\infty t\exp\left(-\frac{t}{\tau_f}\right)dt}{I(0)\int_0^\infty \exp\left(-\frac{t}{\tau_f}\right)dt} = \tau_f \tag{1.13}$$

Therefore, the fluorescence lifetime of a molecule can be thought of as the average time a molecule remains in the excited state before it returns to the ground state by radiative or non-radiative means. This is a statistical average and, as such, the molecules do not all return to the ground state at a time equal to the lifetime (Lakowicz, 2006); 63.2% of the molecules have returned to the ground state by $t = \tau$ and 36.8% (1/e) return after this time due to the exponential nature of the decay.

k_{rad} is an intrinsic property of the electronic structure of a molecule which, in the absence of non-radiative pathways, is the reciprocal of the fluorescence lifetime (Lakowicz, 2006). The introduction of non-radiative deexcitation pathways will decrease the fluorescence lifetime by increasing the rate of excited state depletion. Processes which contribute to $k_{\text{non-rad}}$, such as quenching and internal conversion, take place within distance scales of the order of 10 nm and occur at time scales around the lifetime of the excited state, typi-

cally of the order of nanoseconds (Valeur, 2001). Lifetime measurements therefore provide a window through which to study intra- and inter-molecular interactions at the "nano" scale.

1.12 NAD(P)H fluorescence lifetimes

As with the absorption and emission spectra, the fluorescence decays of NADH and NADPH in solution are identical (Visser and Hoek, 1981), indicative of the fact that the excited state transition takes place on the nicotinamide ring structure common to both molecules. Rather than being described by a single-exponential as in equation 1.11, the fluorescence decay of NAD(P)H is best described by a sum of two exponentials, one with a lifetime of around 0.3ns and the other with a lifetime of around 0.7ns (Visser and Hoek, 1981). The apparently homogenous solutions of either cofactor must therefore consist of two distinct fluorescent species.

Uncertainty exists in the literature as to the cause of the two observed fluorescence lifetimes of NAD(P)H. It is known that free NAD(P)H can exist in a state in which the nicotinamide and adenine rings are stacked on top of each other (Scott et al., 1970; Tanner et al., 1999). It has therefore been suggested that the two fluorescent species of NAD(P)H correspond to the extended and folded configurations of the cofactor (Visser and Hoek, 1981; Couprie et al., 1994). However, other models have been proposed in which the molecule can undergo an excited state reaction to create a new fluorescent product, thereby adding a separate fluorescent species to the NAD(P)H solution (Krishnamoorthy et al., 1987; Ladokhin and Brand, 1995).

In the 1970's, it was shown that the fluorescence lifetime of NAD(P)H is increased upon binding to an enzyme (Scott et al., 1970). The precise lifetime varies depending on which enzyme NAD(P)H is bound to (Konig et al., 1997; Yu and Heikal, 2009) and whether any substrate molecules are simultaneously present (Brochon et al., 1976). Enzyme-bound NADH and NADPH fluorescence lifetimes of between 1 ns and 6 ns can be found in the literature (Gafni and Brand, 1976; Vishwasrao et al., 2005), summarised in table 1.1. The reported fluorescence decays are frequently multiexponential, with the fraction of NAD(P)H present in the excited state population with lifetime τ_i denoted α_i and the α-weighted mean of the fluorescence lifetimes denoted $\langle\tau\rangle$. NAD(P)H fluorescence lifetimes in mitochondrial suspensions have been reported as large as 6.5 ns (Wakita et al., 1995; Blinova et al., 2005).

Cofactor	Enzyme	Substrate	α_1	τ_1 / ns	τ_2 / ns	$\langle\tau\rangle$ / ns
NADH	Lactate dehydrogenase[1]	-	-	-	-	1.5
NADH	Lactate dehydrogenase[1]	Oxalate	-	-	-	6.5
NADPH	Glutamate dehydrogenase[2]	Glutamate	0.52	1.2	2.6	1.9
NADPH	Glutamate dehydrogenase[2]	GTP	0.75	1.1	3.3	1.7
NADH	Alcohol dehydrogenase[3]	-	-	-	-	2.9
NADH	Alcohol dehydrogenase[4]	Isobutyramide	0.45	2.4	5.8	4.3
NADH	Malate dehydrogenase[5]	-	0.72	0.6	1.3	0.8
NADH	Lactate dehydrogenase[6]	-	0.86	1.1	2.5	1.3
NADH	Malate dehydrogenase[6]	-	0.86	0.8	1.6	0.9

Table 1.1: Published fluorescence lifetimes of NADH or NADPH in solution with various enzymes. Values are taken from [1]Scott et al. (1970), [2]Brochon et al. (1976), [3]Konig et al. (1997), [4]Gafni and Brand (1976), [5]Vishwasrao et al. (2005) and [6]Yu and Heikal (2009).

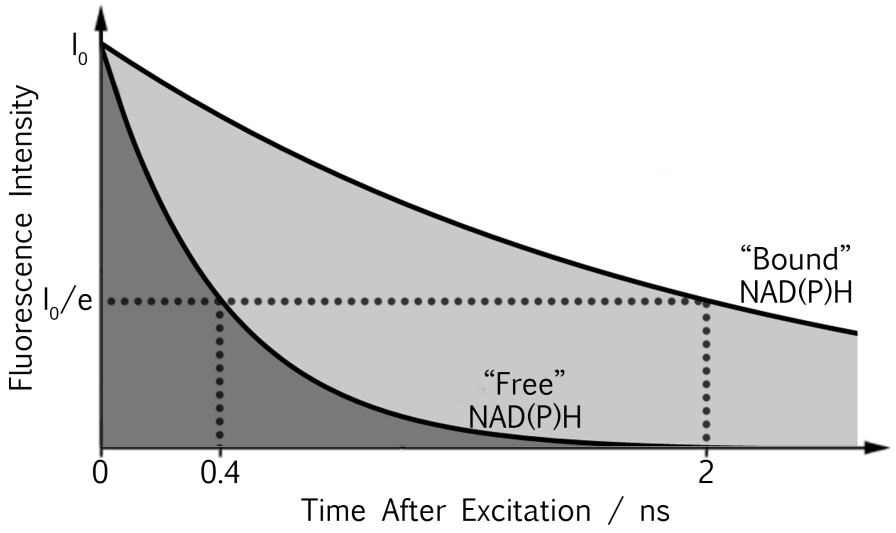

Figure 1.17: The quantum yield of a fluorophore is proportional to the area under its fluorescence decay. A solution of enzyme-bound NAD(P)H will therefore emit more fluorescence than an equimolar solution of NAD(P)H with no enzyme present.

The increase of the fluorescence lifetime of NAD(P)H upon binding to an enzyme has important implications for the NAD(P)H fluorescence intensity studies mentioned in section 1.10. The reason for this is shown in figure 1.17. The number of photons emitted by a fluorophore is proportional to the area under its fluorescence decay curve. A longer lifetime causes a slower decay rate and thus a larger area under the decay curve, assuming equal initial sizes of excited state populations. Bound NADH will therefore emit more photons as fluorescence than an equal concentration of free NADH for a given number of photons absorbed.

Mathematically, the total number of photons emitted by a population of excited fluorophores can be expressed as the integral of equation 1.10,

$$I_{\text{sum}} = k_{\text{rad}} n(0) \int_0^\infty \exp\left(-\frac{t}{\tau_f}\right) dt = k_{\text{rad}} n(0)\, \tau_f \tag{1.14}$$

$n(0)$ gives the number of photons initially absorbed by the population, so the ratio of photons emitted to photons absorbed can be written,

$$\frac{I_{\text{sum}}}{n(0)} = k_{\text{rad}} \tau_f = \Phi \tag{1.15}$$

Φ is the quantum yield of the fluorophore, first introduced in section 1.9 as the ratio of the number of photons emitted to the number of photons absorbed. The radiative rate of NAD(P)H can be assumed to be unaffected by enzyme-binding (Vishwasrao et al., 2005), so the quantum yield of enzyme-bound NAD(P)H is up to 20 times bigger than that of the molecule free in solution. The fluorescence observed during intensity-based imaging of NAD(P)H will therefore be over-represented by enzyme-bound species.

The quantum yield of free NAD(P)H has been measured as 0.02 (Scott et al., 1970). Inputting the average of the lifetimes of the two NAD(P)H species in solution into equation 1.15 gives a radiative rate of 4 x 10^7 s^{-1}. The non-radiative rate of NAD(P)H is therefore calculated, using equation 1.12, as 2 x 10^9 s^{-1}, a value 50 times larger than the radiative rate. The particular processes giving rise to this large rate of non-radiative decay are unknown. As enzyme-binding does not affect the radiative rate (Vishwasrao et al., 2005), the variation in fluorescence lifetimes observed in enzyme-bound species of NAD(P)H must result from binding processes that restrict the non-radiative pathways. For example, an increase in lifetime from 0.3 ns to 2 ns between free and bound NAD(P)H would require the process of enzyme binding to restrict the non-radiative rate of NAD(P)H to around 15% of its unbound value.

1.13 FLIM of NAD(P)H

In 1991, Lakowicz and Berndt described a method for extending fluorescence lifetime measurements into two dimensions. Fluorescence lifetimes at each point of an image were measured by observing the phase-shift between laser light incident on a fluorescent sample and the light arriving at each pixel of a phase-sensitive camera. Although similar lifetime imaging methods had previously been reported (Periasamy and Clegg, 2010), this paper was the first to introduce the acronym FLIM to describe a technique used to acquire “im-

ages in which the contrast is based upon the fluorescence lifetimes rather than upon local probe concentrations or local intensity" (Lakowicz and Berndt, 1991).

A year later, solutions of NADH and NADH bound to malate dehydrogenase were used as a proof of principle of this frequency-domain technique (Lakowicz et al., 1992). In the same year, the fluorescence lifetime of NAD(P)H within live biological samples was first measured by Schneckenburger and Koenig. These measurements were made on suspensions of yeast inside a cuvette and employed the widely-used time-correlated single photon counting (TCSPC) technique, to be described in section 2.2. Multiexponential fluorescence decay kinetics were observed, suggesting a heterogeneous environment for NAD(P)H inside cells.

By 1995, a number of studies had reported spectral differences in the autofluorescence emitted by healthy and diseased tissue (Ramanujam, 2000). Pradhan et al. (1995) extended these studies into time-resolved spectroscopy by comparing the fluorescence decay of NAD(P)H in metastatic and non-metastatic variants of a number of cancer cell lines in suspension. The measured decays were best fit to a sum of two exponential decays. Across all cell lines, the average fluorescence lifetimes of the two decay components were 0.33($\pm$0.06) ns and 3.3($\pm$0.9) ns. Comparison of these values with the photophysical studies available at the time suggested the short component represented freely diffusing NAD(P)H while the longer component arose from enzyme-bound species. Measurements of the rotational correlation times of these components, as determined by their fluorescence anisotropy decays (to be described in section 2.4) have since confirmed that the lifetimes correspond to free and bound species respectively (Vishwasrao et al., 2005; Zheng et al., 2010).

If the two lifetimes present in the fluorescence decay of NAD(P)H in live tissue are denoted τ_{free} and τ_{bound}, with a fraction α_{bound} of the total NAD(P)H population being bound to enzymes, the fluorescence decays $I_{\text{total}}(t)$ are described by,

$$I_{\text{total}}(t) = I(0)\left[\left(1-\alpha_{\text{bound}}\right)\exp\left(-\frac{t}{\tau_{\text{free}}}\right)+\alpha_{\text{bound}}\exp\left(-\frac{t}{\tau_{\text{bound}}}\right)\right]+Z \qquad (1.16)$$

where Z accounts for a constant level of background noise uncorrelated with time. Pradhan et al. observed a general trend for the amplitude-weighted mean lifetime $\left\langle\tau_{\text{NAD(P)H}}\right\rangle$ to be, on average, three times smaller in the metastatic cell lines compared

to their non-metastatic counterparts. This quantity is calculated as,

$$\left\langle \tau_{\mathrm{NAD(P)H}} \right\rangle = \left(1 - \alpha_{\mathrm{bound}}\right) \tau_{\mathrm{free}} + \alpha_{\mathrm{bound}} \tau_{\mathrm{bound}} \tag{1.17}$$

Further functional changes in NAD(P)H fluorescence lifetime characteristics were reported by Paul and Schneckenburger in 1996. Again using yeast cell suspensions, the contribution of fluorescence from free NAD(P)H species was shown to decrease with increasing levels of oxygen, while the bound NAD(P)H fluorescence signal remained relatively constant. This study used a time-gating approach (Periasamy and Clegg, 2010) to compare the free and bound NAD(P)H fluorescence signals, rather than TCSPC, so the specific lifetimes of the two species under varied oxygen concentration were not measured.

With cancer progression known to correlate with changes in metabolism (Warburg, 1956), the initial studies of Pradhan et al. and Paul and Schneckenburger appeared to show that the fluorescence decay of NAD(P)H varied with altered metabolic state. This led to attempts to produce and test clinical diagnosis systems based on the measurement of NAD(P)H lifetimes. For example, in 1998, Mycek et al. produced an endoscope coupled to a time-resolved spectrometer able to differentiate between the autofluorescence arising from adenomatous and non-adenomatous colonic polyps. Subsequently, a number of bespoke NAD(P)H fluorescence lifetime systems were designed for the clinical monitoring of metabolism (Colasanti et al., 2000; Pogue et al., 2001). Time-resolved NAD(P)H fluorescence was suggested to be a viable technique for the diagnosis of cancers of the breast (Tadrous et al., 2003), brain (Butte et al., 2005), oesophagus (Sud et al., 2006), skin (De Beule et al., 2007) and mouth (Sun et al., 2009), as well as for the monitoring of blood glucose levels in diabetes patients (Evans et al., 2005).

Application of fluorescence lifetime imaging of autofluorescence was initially limited to research groups able to construct their own full systems (Cole et al., 2001; Konig and Riemann, 2003; Periasamy and Clegg, 2010). In the early 2000's, FLIM add-ons for conventional laser scanning microscopes were made commercially available (Becker, 2012). With the only other requirement being a pulsed laser source (Periasamy and Clegg, 2010), this increased the ease with which fluorescence lifetime measurement capabilities could be added to existing live-cell microscopy set ups. Bird et al. (2005) used such a system to investigate the effect of cell confluence and electron transport chain inhibition on the observed fluorescence decay characteristics of NAD(P)H in MCF10A breast cells. Again, two fluorescence

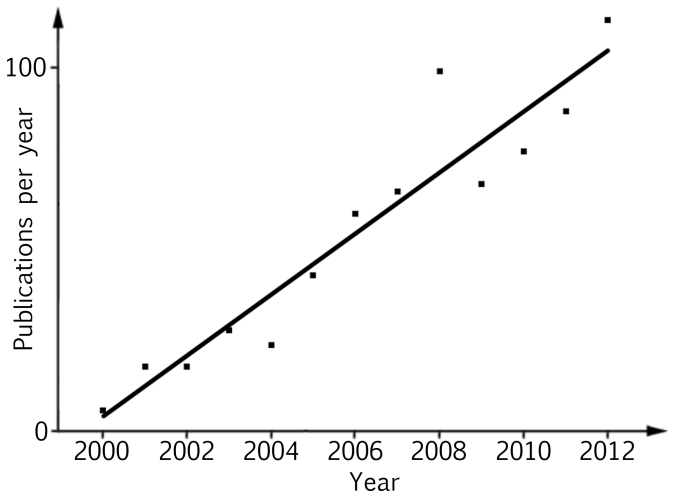

Figure 1.18: The number of papers on the subject of "NADH FLIM" is increasing steadily year-on-year, with more than 100 published in 2012 (Google Scholar). A biochemical interpretation for changes in fluorescence lifetimes measured in an NAD(P)H FLIM experiment has yet to be established.

lifetimes, attributed to free and enzyme-bound NAD(P)H, were resolved at each pixel. The value of τ_{bound} averaged over the cells was observed to decrease with increasing confluency from 3.1(±0.1) ns with 25,000 cells per dish to 1.72(±0.02) ns with 1,000,000 cells per dish. The fraction of bound species α_{bound} also decreased, from 46(±3)% to 27(±2)%. This weighting was further decreased by 8(±5)% upon electron transport chain inhibition with cyanide. Supported by a previous study (Schneckenburger et al., 2004), this led the authors to propose that α_{bound} provides a measure of the NAD^+/NADH redox ratio.

Combining two-photon excitation with laser scanning FLIM allows NAD(P)H fluorescence lifetime images of complex tissue preparations to be produced (Periasamy and Clegg, 2010). For example, Skala et al. (2007a) used this technique to investigate differences in the biexponential fluorescence decay of NAD(P)H between normal and dysplastic tissues in a hamster cheek pouch model of oral carcinogenesis. They observed that the enzyme-bound lifetime component was significantly shorter in cancerous tissue than in healthy tissue, with τ_{bound} decreasing from 2.03(±0.06) ns in control regions to 1.6(±0.3) ns in precancerous regions. The authors then observed that inhibition of oxidative phosphorylation in MCF10A cell cultures using cobalt chloride also caused a significant decrease in τ_{bound}. In contrast, inhibition of glycolysis in the same cells using 3-bromopyruvate caused τ_{bound} to significantly increase. This led Skala et al. to conclude that the decrease in τ_{bound} with neoplasia in the hamster cheek pouch could be caused by the Warburg effect.

The number of studies published per year on the topic of NAD(P)H FLIM has been

increasing steadily since the turn of the millennium, as shown in figure 1.18. The models in which changes in the fluorescence decay of NAD(P)H are observed are many and varied, with recent applications range from wound healing (Gehlsen et al., 2012) to stem cell differentiation (Stringari et al., 2012b) and necrotic deterioration of skin (Sanchez et al., 2010) to staurosporine-induced apoptosis (Wang et al., 2008; Ghukasyan and Kao, 2009; Yu et al., 2011). This highlights the potential of the technique as a non-invasive method for the investigation of metabolism in both a clinical and research setting. Useful application of NAD(P)H FLIM is held back, however, by the lack of a functional understanding of the biochemical and photophysical causes of the measured fluorescence lifetime changes, as discussed in the next section.

1.14 Research aims

Despite the diversity of the models investigated using NAD(P)H FLIM, the literature is consistent in its lack of a systematic underlying mechanism for the changes in fluorescence lifetime measured upon alterations in metabolism. Creating a biochemical hypothesis for the interpretation of the NAD(P)H fluorescence lifetimes measured in live cells and tissues is the primary research aim of this thesis.

To aid the construction of a metabolic framework within which to analyse changes in the fluorescence lifetimes of NAD(P)H *in vivo*, the photophysics of NADH and NADPH will first be investigated. Despite a literature dating back to the 1960's, the cause of the large non-radiative rate in NAD(P)H has largely been ignored. Investigating this phenomenon will allow the mechanism behind the fluorescence lifetime increase upon enzyme binding to be understood. This will assist in the molecular-level interpretation of the NAD(P)H fluorescence lifetimes measured in live cells.

In addition to their single-photon photophysics, the two-photon absorption properties of NADH and NADPH will be characterised. Two-photon excitation is not a requirement for FLIM. However, implementation of the TCSPC technique for measuring fluorescence lifetimes requires a pulsed laser source. Microscopes intended for two-photon imaging typically use a pulsed Ti:sapphire laser, tunable between 680 nm and 1100 nm, as the excitation source. Extending the capabilities of such a two-photon microscope to include FLIM is therefore simple, requiring the addition of a sensitive detector and commercially available photon counting electronics. As a result, two-photon excitation is widely applied in FLIM, as it will be in this work. Two-photon spectroscopy of NAD(P)H will allow its use

as an autofluorescent metabolic marker to be optimised, in addition to providing further information about the electronic structure of these molecules.

As can be seen in table 1.1, the fluorescence lifetime of NAD(P)H varies depending on the enzyme to which it is bound. The large number of NADH and NADPH-binding enzymes inside the cell should therefore be represented by the presence of a large variety of different lifetimes in the fluorescence decay of NAD(P)H measured in live tissue. However, as discussed previously, only two lifetime components are typically observed. The reasons for this will be investigated using a simple computational model. This will allow the effect of changes in the distribution of enzymes present in live tissue on the simplified fluorescence decay of NAD(P)H to be determined prior to their measurement in live cells.

Once these preliminary studies have been performed, a systematic investigation will be made into changes in the NAD(P)H fluorescence decays measured in live cells in response to cellular perturbations with known effects on metabolism. Suggestions are frequently made in the literature that changes in the fluorescence lifetime of NAD(P)H in live tissue reflect changes in the balance between anaerobic metabolism by glycolysis and aerobic metabolism by oxidative phosphorylation. As such, the investigation will initially focus on treatments known to perturb these two processes. The cytosolic and mitochondrial regions of the lifetime images obtained will also be examined to ascertain whether intrinsic differences exist between the decay of NAD(P)H fluorescence arising from these two distinct compartments.

The aforementioned live-cell studies will provide knowledge of how the NAD(P)H fluorescence lifetimes measured *in vivo* vary in response to known alterations of metabolism. The computational studies described will provide an understanding into how changes in the distribution of the different enzymes present in a cell are manifest in the apparently simplified fluorescence decays measured in live cells and tissues. Finally, the photophysical studies will elucidate the non-radiative decay mechanism in NADH and NADPH, allowing changes in their fluorescence lifetime to be interpreted at a molecular level. This should represent sufficient information upon which to build a hypothesis for the interpretation of the fluorescence lifetimes of NAD(P)H in terms of the underlying metabolism of the tissue, allowing the technique of NAD(P)H FLIM to contribute meaningfully to studies of metabolism in both diagnostic and research applications.

Chapter 2

Methods

2.1 Laser sources

Since their invention in 1960's (Hecht and Zajac, 1974), lasers have become the tool of choice for providing excitation in time-resolved fluorescence studies (Lakowicz, 1992). Lasers generate a highly directional monochromatic beam of light and are capable of producing the short (fs), high repetition rate (MHz) pulses (Svelto, 2010) required for the methods of fluorescence lifetime measurement in the time domain applied in this work (Lakowicz, 2006).

Lasers use the phenomenon of stimulated emission to amplify light within an optically resonant cavity (Pedrotti et al., 1993), giving rise to their name (***L***ight ***A***mplification by ***S***timulated ***E***mission of ***R***adiation). Stimulated emission, first proposed theoretically by Einstein in 1916 (Pedrotti et al., 1993), describes the induction of radiative decay in an excited state molecule upon interaction with a photon of sufficient energy (Hecht and Zajac, 1974). In contrast to spontaneous emission, in which the energy released upon stochastic relaxation is emitted as a randomly-directed photon, stimulated emission results in the duplication of the incident photon, producing light identical in phase, polarisation, wavelength and direction to that which caused the transition (Pedrotti et al., 1993). In stimulated emission, the intensity of the incident light is multiplied upon interaction with an excited state molecule. Laser light is therefore produced by the repeated amplification of light in this manner.

A laser design is typically named after the material in which light is amplified, known as the gain medium. This can be solid, liquid or gas (Pedrotti et al., 1993). As in fluorescence, the differences between the electronic energy levels in the gain medium govern the wavelength of light produced. If possessing sufficient energy, the path of a photon

travelling through the gain medium can be perturbed by either absorption or stimulated emission. In thermal equilibrium at room temperature, the vast majority of molecules will be in the ground state, in accordance with the Boltzmann distribution (Young and Freedman, 2004). As such, absorption events will outweigh stimulated emission events. To achieve light amplification, the majority of molecules must be forced to exist in an excited state. This population inversion is accomplished by supplying the gain medium with an external energy source; a process known as pumping (Svelto, 2010).

Gain media are designed such that their excited state lifetime is long (10^{-3} s, Lakowicz, 1992), allowing a population inversion to be maintained. Occasional spontaneous emission in a random direction will produce a photon with the correct energy to cause stimulated emission, beginning the light amplification process. By containing the pumped gain medium between two mirrors, light travelling off-axis will exit the optical cavity, leaving behind a directional beam being repeatedly amplified by stimulated emission during the reflection back and forth. Choosing one mirror to be less than 100% reflective allows part of the beam to escape and become the useful laser output (Pedrotti et al., 1993). The distance between the mirrors, the cavity length L, is set to ensure the constructive interference of light at the operating wavelength λ. This requires that an integer number of half wavelengths, q, fit in the cavity (Prasad, 2004), such that,

$$L = q\frac{\lambda}{2} \tag{2.1}$$

In this work, standard confocal microscopy was performed using excitation from an argon ion laser. Population inversion is achieved in this laser by passing a current through the argon plasma gain medium (Svelto, 2010). The variety of transitions possible in the electronic structure of ionised argon (Bogaerts and Gijbels, 1998) permits emission at a number of wavelengths ranging from ultraviolet to green. The argon ion laser used in this work (Enterprise UV, Coherent) is specifically designed for lasing at the ultraviolet wavelengths, allowing imaging of NAD(P)H to be performed using the 351 nm line.

Only sharply-defined emission wavelengths are possible using an ionised gas as the gain medium. Lasers tunable across a wide continuum of wavelengths can be produced by using a gain medium in which the electronic states are broadened by a distribution of vibrational energy levels. The Ti:sapphire laser is the most widely tunable of these (Svelto, 2010). The gain medium, a sapphire host crystal doped with titanium atoms, is able to lase

from 660 nm to 1180 nm (Wall and Sanchez, 1990).

The wide wavelength range over which light can be amplified in a Ti:sapphire laser is reflected in the large value of its gain bandwidth $\Delta\upsilon_0$ of approximately 100 THz (Svelto, 2010). Based on equation 2.1, the frequency separation of adjacent laser cavity modes is 150 MHz for $L = 1$. A Ti:sapphire laser cavity of one metre in length can therefore support more than 500,000 different modes, allowing interference to take place between them. If the relative phases of the modes are random, the laser output will resemble noise. However, the phase differences of the longitudinal modes can be fixed such that constructive interference occurs between them periodically, as shown in figure 2.1. This situation, known as mode locking, results in a single short pulse of light reflecting back and forth between the mirrors (Coherent, 2013).

In Ti:sapphire lasers, mode locking is achieved by the optical Kerr effect; extremely intense pulses induce the formation of a lens in the gain medium and become slightly focused. Lower power modes cannot induce this transient lens, allowing the insertion of a slit in the cavity to block this light and allow through the narrowed intense pulse. Repeated amplification causes this mode to dominate, forming the output pulse train with a repetition rate governed by the round-trip time of the laser cavity (Svelto, 2010); 150 MHz for a one metre cavity. The temporal width of the pulse can be estimated from Heisenberg's Uncertainty Principle. Based on its gain bandwidth, the Ti:sapphire laser is capable of producing femtosecond pulses, making them more than adequate excitation sources for studies of the pico-to-nanosecond excited state processes in NAD(P)H.

In this work, fluorescence lifetime measurements of NADH and NADPH in solution were performed using excitation from a Mira 900F (Coherent) Ti:sapphire laser. Single photon time-resolved spectroscopy was performed by halving the output wavelength with a frequency-doubling crystal. The operating wavelength of the Mira was selected by manually rotating a birefringent tuning plate and observing the laser emission spectrum using a USB spectrometer (Ocean Optics). Output powers were measured using a Thorlabs optical power meter. These were maximised by rotating a prism to adjust for dispersion inside the laser cavity and by opening the cavity slit as wide as possible while still maintaining modelocking, confirmed by the continuous-wave detector incorporated into the laser design (Coherent, 2013). In the equivalent laser used for two-photon excitation microscopy (Chameleon, Coherent), this tuning and power optimisation process is automated upon se-

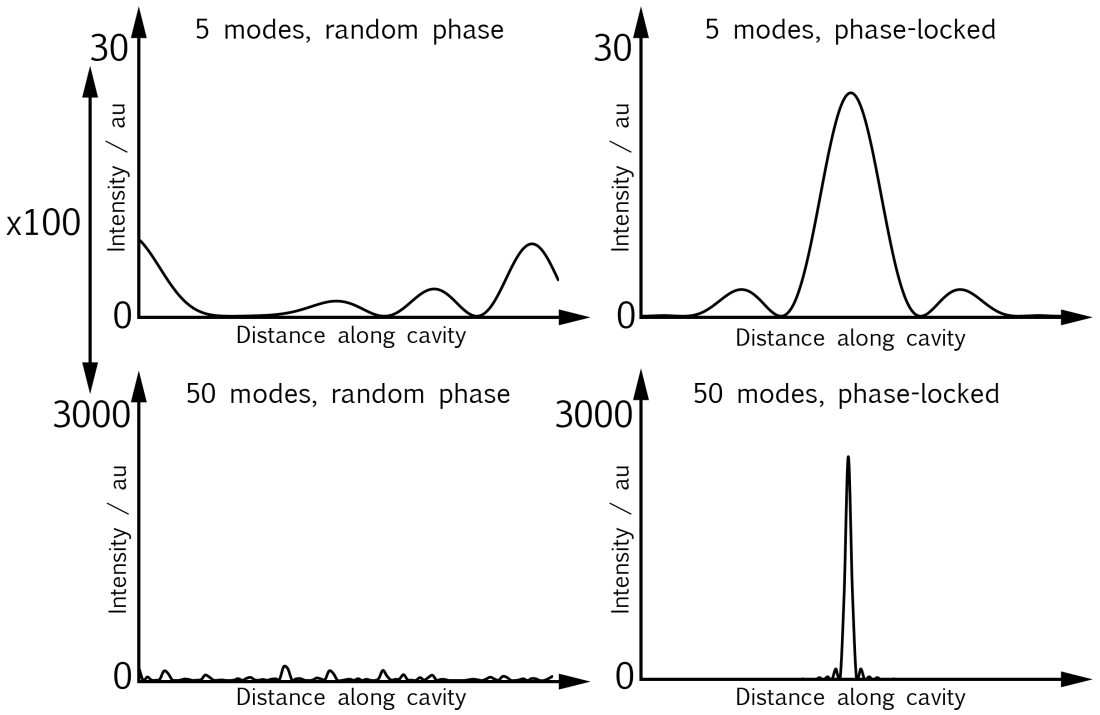

Figure 2.1: Comparison of the light intensity in a laser cavity with 5 or 50 random-phase or phase-locked modes present. Locking a large number of modes produces a narrow, intense pulse, as indicated by the difference in y-axis scales.

lection of the desired output wavelength in the control software. Both lasers were pumped using the 532 nm output of a neodymium-doped yttrium orthovanadate (Nd:YVO_4) laser (Verdi, Coherent).

The dwell time between consecutive laser pulses determines the duration of fluorescence decays measured using the TCSPC technique. The Mira 900F produces 200 fs pulses with a repetition rate of 76 MHz, allowing the first 13.2 ns of the fluorescence decay to be measured post-excitation. To increase this time for studies of NADH and NADPH in solution, the repetition rate was reduced to 3.8 MHz using a pulse picker (PulseSelect, APE). In this apparatus, the laser beam is passed through an acousto-optic modulator. The refractive index of this material is varied at the desired output frequency using a piezoelectric transducer (Svelto, 2010). This deflects a certain proportion of pulses, in this case one in 20. The path of undeflected pulses is blocked while the path of the deflected beam is left unobstructed, producing an output of decreased repetition rate.

2.2 Time correlated single photon counting

Pulsed laser sources allow the rapidly repeated excitation of a sample. The technique of TCSPC takes advantage of this for the accurate measurement of fluorescence decays,

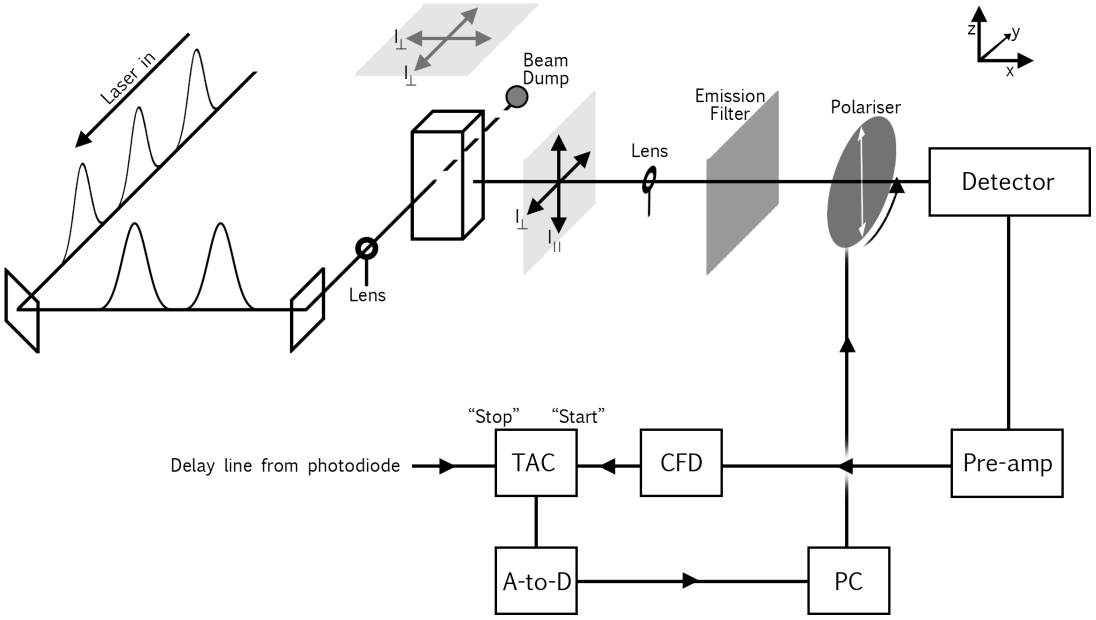

Figure 2.2: Experimental setup for TCSPC experiments used in this work with illumination along the y-axis and detection along the x-axis.

building them up on a photon-by-photon basis. Upon the detection of a single fluorescence photon, the time delay between excitation and emission is recorded in a histogram. After many excitation-emission events, this histogram will resemble the exponential population decay of the fluorophore under analysis. Subsequent fitting to an appropriate model reveals the fluorescence lifetimes present in the sample (Valeur, 2001).

A detector sensitive to single photons is required for TCSPC such as a photomultiplier tube (PMT). Here, the energy of a single photon is sufficient to cause the ejection of electrons from a photoelectric material. These electrons are then multiplied by acceleration through a large voltage and collisions with a series of dynodes. Upon each collision, the kinetic energy gained from the externally applied electric field causes the ejection of further electrons. This cascade forms the output current of the PMT, indicating the detection of a photon (Lakowicz, 2006).

The essentially random amplification process taking place in a PMT causes the amplitudes of the signals output from the detector to vary greatly, even though each spike corresponds to the detection of a single photon (Becker, 2012). In order to ensure that the time measured between excitation and emission is not affected by the different shapes of the detector signals, the output of the detector is passed through a constant fraction discriminator, or CFD. This outputs a trigger current when the detector signal reaches a particular fraction of its overall height (Lakowicz, 2006).

The output from the CFD is used to start a high speed stopwatch, known as the time to amplitude converter, or TAC. This generates an increasing voltage by charging a capacitor until a stop signal is received. The stop signal used is the next incoming laser pulse, measured by splitting a small fraction (∼5%) of the incident light onto a photodiode. The TAC therefore produces a voltage proportional to the time delay between emission and the next excitation. The time between excitation and emission can then be calculated using the known time period between excitation pulses. This is known as the reversed start-stop principle (Becker, 2012).

In TCSPC, the power incident on the sample is reduced such that, on average, one emitted photon is detected every 100 excitation pulses, achieved in this work by the introduction of neutral density filter wheels. As a rule of thumb, the probability of multiple emission events being detected in a single dwell period between pulses is reduced to insignificance under these conditions (Valeur, 2001). Pulse pile-up such as this would bias the measured fluorescence decay towards shorter lifetimes. Implementation of the reversed start-stop principle is advantageous as it requires the TCSPC electronics to work at the photon detection rate, not at the 100-fold higher repetition rate of the laser (Becker, 2012). The registration of a single photon emission event is completed when the output of the TAC enters an analogue to digital converter. This translates the TAC voltage into a photon detection time and the corresponding time-bin of a histogram stored in computer memory is incremented.

In this work, the modular TCSPC system used (Ortec) contained 512 time-bins of width 0.053 ns. Single-photon emission events were registered by a Hamamatsu MCP-PMT detector (R3809U). The laser beam was focussed onto the sample by a 10 cm focal length lens and fluorescence was focussed onto the detector with a 6.3cm focal length lens (both Melles Griot). Background noise was minimised by the construction of a black wooden casing around the apparatus, with blackout curtains keeping ambient light to a minimum.

Photophysical studies of NADH and NADPH in solution were performed using the 90° excitation-detection geometry shown in figure 2.2. Following excitation by vertically (z) polarised pulses, fluorescence will be emitted in all directions. Resolving into components polarised parallel ($I_{||}$) and perpendicular ($I_{\perp}$) to the polarisation of the incident beam, a detector placed along the x-axis will record the signal $I_x = I_{\perp} + I_{||}$. Cylindrical symmetry about the z-axis means a detector placed along the y-axis also records $I_x = I_y = I_{\perp} + I_{||}$.

However, as light propagates in a direction perpendicular to its plane of polarisation, a detector placed along the z axis will observe $I_z = I_\perp + I_\perp$. The total fluorescence intensity emitted by the sample is therefore given by (Valeur, 2001),

$$I_{\text{total}} = I_x + I_y + I_z = 2I_{||} + 4I_\perp \tag{2.2}$$

For a detector placed along the x-axis, as in figure 2.2, measuring a signal representative of the fluorescence emitted in all directions therefore requires it to be twice as sensitive to fluorescence polarised along the y-axis than the z-axis. This can be achieved by setting the transmission axis of an emission polariser such that it makes an angle of 54.7° (the so-called "magic angle") with the z-axis (Lakowicz, 2006). However, for the measurement of fluorescence decays in chapters 3 and 4 of this work, a stepper motor was used to alternately transmit vertically and horizontally polarised emission every 10 seconds for 30 minutes and the polarised decays $I_{||}(t)$ and $I_\perp(t)$ were stored separately in computer memory. An intensity proportional to the total emission was then reconstructed using,

$$I_{\text{total}}(t) = I_{||}(t) + 2I_\perp(t) \tag{2.3}$$

This method was preferred over the magic angle technique as $I_{||}(t)$ and $I_\perp(t)$ can subsequently be combined in a different manner to produce the fluorescence anisotropy decay of the solution for the study of rotational dynamics, described in section 2.4. As the sum $I_{||} + 2I_\perp$ detects I_x, I_y and I_z with the same efficiency, the effects of rotational diffusion on the fluorescence decay are eliminated (Becker, 2012).

Applying equation 2.3 requires that y- and z-polarised light is detected along the x-axis with the same efficiency. This was confirmed by rotating the direction of polarisation of the incident light by 90° using a half-wave plate and observing that the detected fluorescence intensity of a reference sample was equal with the analysing polariser set in both directions.

2.3 Fluorescence decay fitting

Following TCSPC, the histogram of excitation-emission delay times represents the fluorescence decay of the NAD(P)H solution under investigation. The fluorescence lifetime parameters of the decay were obtained by fitting an exponential decay model to this data using a least-squares algorithm in MATLAB. In this technique, a sum is formed of the squared

differences between the measured fluorescence decay and the model curve at each time point. The software then varies the model parameters until this sum is minimised (Lakowicz, 2006).

The number of photon counts contained in each bin of a TCSPC histogram is affected by noise. This occurs because, despite occurring at an average rate controlled by the fluorescence lifetime of the fluorophore, electronic relaxation is an inherently random process. The statistics of random events occurring at a known average rate are described by the Poisson distribution. This states that the expected standard deviation of the Poisson noise σ affecting a bin containing N counts is $\sqrt{N}$ (Valeur, 2001). It can therefore be expected that the absolute difference between the model prediction and the measured data is largest in the bins containing the most signal. This can be accounted for in the fitting process by using the reduced chi-squared (χ_r^2) statistic as the minimisation parameter, defined as,

$$\chi_r^2 = \frac{1}{n-l} \sum_{k=1}^{n} \frac{1}{\sigma_k^2} \left[N_{\text{measured}}\left(t_k\right) - N_{\text{model}}\left(t_k\right) \right]^2 \tag{2.4}$$

where n is the total number of datapoints and l is the number of free parameters. The term in square brackets gives the difference between the decay model and the measured data at each time point t_k. Dividing this term by σ_k gives the so-called weighted residual of the data point. For a fluorescence decay undergoing Poisson noise, $\sigma_k^2 = N_{\text{measured}}\left(t_k\right)$.

In this work, NAD(P)H fluorescence decays were fit to functions of the form,

$$I_{\text{total}}\left(t\right) = Z + I\left(0\right) \sum_{i=1}^{n} \alpha_i \exp\left(-\frac{t}{\tau_i}\right) \tag{2.5}$$

The number of decay components n was increased until the addition of further lifetimes no longer caused an improvement in χ_r^2. Based on equation 2.4, optimised fits between model and data give a χ_r^2 value close to 1.

Typically, the TCSPC histogram is not a pure multiexponential decay but a convolution with the instrument response function (IRF) of the system. The IRF describes the distribution of possible delay times between fluorescence emission and TAC output, resulting largely from the random amplification process in the detector (Lakowicz, 2006). The convolution measured using TCSPC is represented in figure 2.3 as the initiation of a fluorescence decay at each point of the IRF. The intensity of each fluorescence decay is proportional to the height of the IRF at the point at which it was initiated. The value of

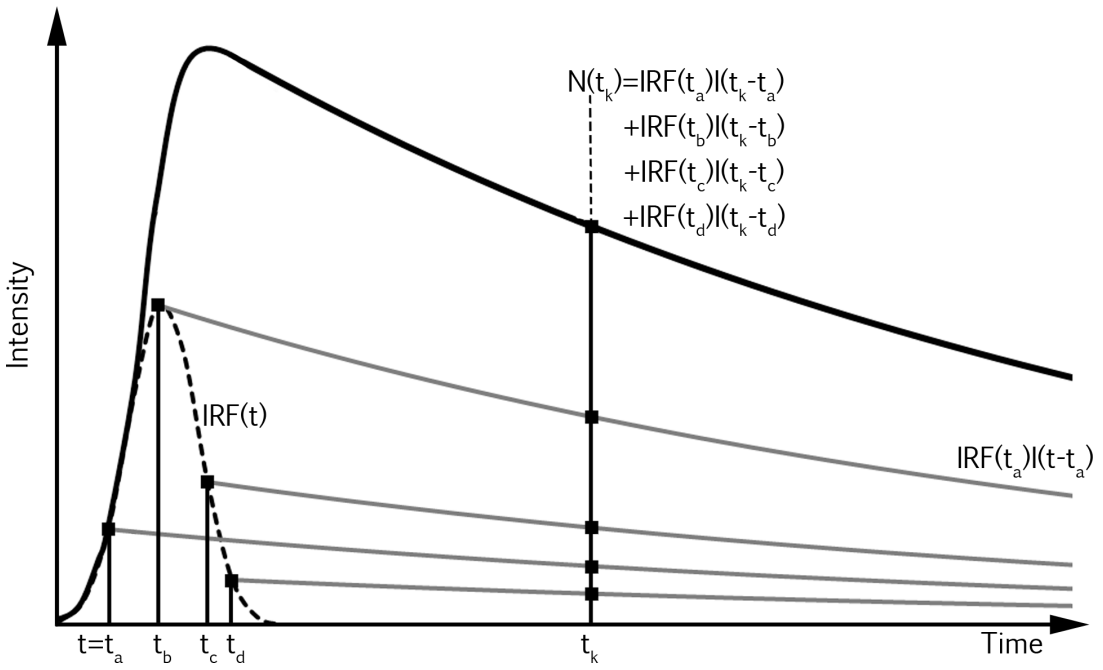

Figure 2.3: The instrument response function introduces a temporal spread in delay times between fluorescence emission and histogram incrementation, causing a convolution of the IRF with the fluorescence decay of the sample.

the convolution measured at time t_k, $N\left(t_k\right)$, is then the sum of all decays present at t_k. Mathematically, this is written,

$$N\left(t_k\right) = \sum_{t=0}^{t_k} \mathrm{IRF}\left(t\right) I_{\mathrm{total}}\left(t_k - t\right) \tag{2.6}$$

To account for the convolution during fitting, a measurement of the IRF of the system is convolved with the decay model during each iteration of the curve fitting algorithm. The IRF is measured using TCSPC by replacing the fluorophore with a sample with an effectively zero fluorescence lifetime, such as a scatterer. This iterative reconvolution approach was employed in this work during the pixel-by-pixel decay fitting of FLIM images. However, the width of the instrument response function of the TCSPC setup used for photophysical studies in solution was approximately the same as the bin width (~0.05 ns). Equation 2.6 shows that if the IRF is contained in a single bin, the measured decay will reduce to a direct measurement of the fluorescence decay. Under these circumstances, decay models were fit directly to the histogram, a faster method known as tail-fitting.

2.4 Fluorescence anisotropy measurements

In the TCSPC experiments described above, the vertically polarised incident laser light will preferentially excite molecules oriented in a particular direction in space (Valeur, 2001).

This direction is defined by the absorption transition moment of the molecule. The single-photon excitation probability for a molecule whose absorption transition moment is oriented at an angle θ to the direction of linear polarisation is proportional to $\cos^2\theta$ (Lakowicz, 2006). In a solution where the orientation of the fluorophores is initially random, an ordered array of excited state molecules is created, a process known as photoselection.

Fluorescence emission from a molecule is polarised in the direction defined by its emission transition moment (Valeur, 2001). Fluorescence emitted immediately after linearly polarised photoselection therefore has a net polarisation. This is described mathematically by the fluorescence anisotropy R, defined as,

$$R = \frac{I_{||} - I_{\perp}}{I_{||} + 2I_{\perp}} \tag{2.7}$$

If the absorption and emission transition moments are collinear, the initial anisotropy will be at its positive maximum. If they are perpendicular, the initial anisotropy will be maximised negatively. This allows the fluorescence anisotropy immediately after excitation $R(0)$ to be used to calculate the angle between the absorption and emission transition moments ϕ. It can be shown (Lakowicz, 2006) that $R(0)$ varies with ϕ according to,

$$R(0) = \frac{2}{5}\left(\frac{3\cos^2\phi - 1}{2}\right) \tag{2.8}$$

Rotational diffusion of the excited state population will decrease the fluorescence anisotropy. Over time, the rotational diffusion of excited molecules will cause the anisotropy to decay to zero as the initially aligned population of emitting fluorophores is randomised by collisions with the environment. The rate of depolarisation will be proportional to the rate of rotational diffusion of the fluorophore. Time-resolved anisotropy decays can therefore be used to measure the rotational diffusion dynamics of a fluorescent molecule. For small-step (Debye) diffusion (Berne and Pecora, 1976), the fluorescence anisotropy decays as an exponential (Munro et al., 1979) with rotational correlation time τ_{rot},

$$R(t) = R(0)\exp\left(-\frac{t}{\tau_{\text{rot}}}\right) \tag{2.9}$$

Multiexponential fluorescence decays of NAD(P)H suggest the presence of a number of species with distinct fluorescence lifetimes and rotational correlation times. In this situ-

ation, the overall anisotropy decay becomes the sum of the anisotropy decays of the component species. However, if the species have different fluorescence lifetimes, their contribution to the overall fluorescence intensity will change with time (Lakowicz, 2006). The sum of the individual anisotropy decays must therefore be weighted by the corresponding time-varying intensity contribution (Ko et al., 2009) given by,

$$f_i(t) = \frac{\alpha_i \exp\left(-\frac{t}{\tau_i}\right)}{\sum_{j=1}^{n} \alpha_j \exp\left(-\frac{t}{\tau_j}\right)} \tag{2.10}$$

The combined anisotropy decay is then written,

$$R(t) = \frac{\sum_{i=1}^{n} R_i(0)\,\alpha_i \exp\left(-\frac{t}{\tau_i}\right) \exp\left(-\frac{t}{\tau_{\text{rot},i}}\right)}{\sum_{i=1}^{n} \alpha_i \exp\left(-\frac{t}{\tau_i}\right)} \tag{2.11}$$

where α_i is the fraction of the excited state population consisting of species i with lifetime τ_i, rotational correlation time $\tau_{\text{rot},i}$ and initial anisotropy $R_i(0)$. In chapters 3 and 4 of this work, the fluorescence anisotropy decays of NADH and NADPH solutions were constructed by combining the polarised fluorescence decays measured using TCSPC according to equation 2.7. Equation 2.11 was then fit to this data to recover the initial anisotropy and rotational correlation time of each component. Previously determined fluorescence lifetimes were held constant in the fit to reduce the number of free parameters. Fitting was performed in MATLAB using a least-squares algorithm to minimise χ_r^2. As the composite decays are a ratio of combined Poisson processes given by equation 2.7, propagation of error causes the value of σ_k^2 in the calculation of χ_r^2 using equation 2.4 to become the more complex function (appendix B),

$$\sigma_k^2 = \frac{\left[I_{||}(t_k) + 4I_{\perp}(t_k)\right] R^2(t_k) - 2\left[I_{||}(t_k) - 2I_{\perp}(t_k)\right] R(t_k) + \left[I_{||}(t_k) + I_{\perp}(t_k)\right]}{I_{\text{total}}^2(t_k)} \tag{2.12}$$

2.5 NAD(P)H fluorescence decay modelling

A basic computational scheme was devised to better understand how changes in the distribution of enzyme-bound NAD(P)H species are reflected in the simplified two-component fluorescence decays measured in live cells and tissues. Artificial fluorescence decays were

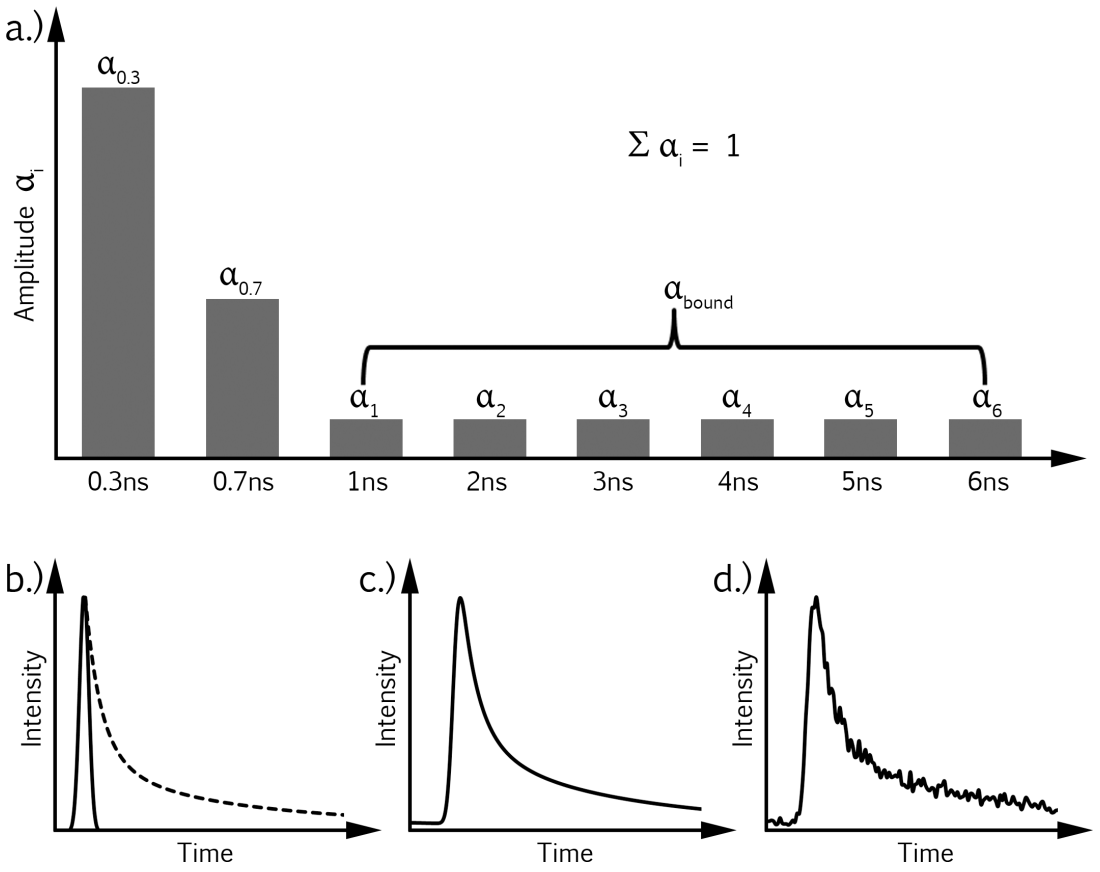

Figure 2.4: NAD(P)H fluorescence decays are produced using the distribution of lifetimes shown in (a). (c) Convolution and (d) the addition of noise simulates the conditions of measurement in a FLIM experiment.

generated containing a defined set of lifetime components. These input parameters were then compared to those output upon the fitting of a decay model to the simulated data.

Multiexponential decay functions containing a distribution of lifetimes were produced in MATLAB. The distribution, shown in figure 2.4a, contained 0.3 ns and 0.7 ns components to represent the two lifetimes observed for NAD(P)H in solution (Visser and Hoek, 1981), along with six evenly spaced lifetimes between 1 ns and 6 ns to represent the enzyme-bound lifetimes reported in literature (table 1.1). The multiexponential decays were binned at 0.0488 ns intervals and convolved with a Gaussian IRF with FWHM 0.1 ns to represent the operating parameters of the lifetime imaging system used in this work. The convolved decay was then scaled such that a predefined number of counts were present in the peak bin and a baseline of 10 counts was added as uncorrelated background noise. Finally, Poisson noise was added to each bin using the `poissrnd()` MATLAB function. The construction of these artificial NAD(P)H fluorescence decays is shown schematically in figure 2.4b-d.

The creation of an artificial NAD(P)H fluorescence decay based on the input of a peak

bin count and weightings for each component of the lifetime distribution was written into the single MATLAB function `simulate_data()`. The raw code for this function, called repeatedly in the subsequent experiments, is contained in appendix A. The generated data were fit to fluorescence decay models using the `FLUOFIT` iterative reconvolution package written for MATLAB by Enderlein and Erdmann (1997). The parameters input into the `simulate_data()` function were compared with those output by `FLUOFIT`. Inputs were varied to observe how modifications to the distribution of NAD(P)H species present in the decay and the number of photon counts in the peak bin are reflected by the lifetime parameters obtained during fitting of FLIM data.

2.6 Cell culture techniques

A number of different immortalised cell lines were used to investigate the effect of metabolic perturbation on the fluorescence decay of NAD(P)H in live biological samples. A cell line is a population of cells derived from a common source capable of being grown *in vitro*. An immortalised cell line can be grown for an indefinite number of generations using the sterile techniques of cell culture (Bryan and Reddel, 1997).

Cells are maintained in a liquid medium designed to provide an environment close to that experienced *in vivo* (Whitaker, 1972). Unless otherwise stated, all cell lines used in this work were grown in 10 ml Advanced Dulbecco's Modified Eagle Medium (DMEM, Gibco) containing 25 mM glucose and 1 mM pyruvate as metabolic substrates in addition to salts, vitamins and amino acids. This was supplemented by the addition of 10% foetal bovine serum (FBS) and 2 mM GlutaMAX (Invitrogen), a stable precursor to the mitochondrial substrate glutamine.

Cells were grown as monolayers in sterile 75 cm^2 tissue culture flasks (EasYFlask, Thermo Scientific Nunc) and were incubated at 37 °C. A 5% CO_2 level was maintained in the incubator to permit the buffering of the growth medium by bicarbonate. The inclusion of phenol red in Advanced DMEM allows pH to be monitored by eye, with medium replaced upon its acidification, indicated by a colour change from red to yellow.

Culture flasks were inspected daily using a benchtop phase contrast inverted microscope (Nikon). If the culture had grown to 70-80% confluence, medium was removed from the flask and the cell monolayer was dissociated by incubation with 3 ml trypsin. Upon dispersal of all cell aggregates, the trypsin was inactivated by the addition of 5 ml growth medium. The contents of the flask were then transferred to a 15 ml conical Falcon tube

Cell Line	Split Interval	Ratio
HeLa	4/5 days	1:10
HEK293	4/5 days	1:6
MSC1H	7-10 days	1:2
MSC2H	6/7 days	1:4
MSC4H	4/5 days	1:4
MSC5H	4/5 days	1:10
NADK+	4/5 days	1:6
NADK–	4/5 days	1:3

Table 2.1: Ratios and intervals required to split the cell lines used in this work at 70-80% confluence.

(BD Biosciences) and centrifuged at 1100 rpm for five minutes, resulting in the formation of a pellet of cells. The supernatant was removed and the pellet resuspended in 5 ml Advanced DMEM. A fraction of this resuspension was then added to a new flask containing 10 ml fresh growth medium. The precise dilution was governed by the growth rate of the different cells, with cultures ideally requiring splitting again in four to five days. The split ratios of the different cell lines used in this project are summarised in table 2.1.

At all times when working with cell lines, contamination was avoided by the addition of antibiotics to the growth medium (100 units ml^{-1} penicillin and 100 μg ml^{-1} streptomycin, Invitrogen) and by performing all procedures using aseptic technique in a laminar flow hood. All items placed under the hood were first sprayed with 70% ethanol and all liquids were transferred to and from the culture flask using sterile glass pipettes.

During the periods in which cells were not required for experiments, cell line stocks were stored in a –80 °C freezer. Once trypsinised and centrifuged, the pellet was resuspended in a freezing medium consisting of FBS and 10% dimethyl sulfoxide (DMSO, Sigma-Aldrich) and then added to cryovials (Thermo Scientific Nunc) for freezing. 1.5 ml of the resuspension was added to each vial at the usual split ratio of the cell line being frozen. To restart the culture of a frozen cell line, vials were thawed in a 37 °C water bath and slowly pipetted into a Falcon tube of warmed growth media. This was then centrifuged to remove DMSO and the pellet was resuspended in 10 ml of Advanced DMEM before being added to a new culture flask.

To prepare cells for experiments, a sterile (autoclaved) 22 mm glass coverslip was placed in each well of a six-well plate (Thermo Scientific Nunc). As published FLIM studies have shown that NAD(P)H fluorescence lifetimes are sensitive to cell number (Ghukasyan and Kao, 2009), the number of cells added to each well was controlled by counting

their concentration in the resuspension using a haemocytometer. By diluting accordingly, 300,000 cells were added to each well and the plates were incubated overnight to allow adherence to the coverslips.

2.7 Fluorescence microscopy

For live-cell imaging, coverslip cultures were held at the microscope stage in a metal ring and bathed in a modified DMEM solution. This was produced using DMEM base powder (Sigma Aldrich) containing no glucose, pyruvate, glutamine, bicarbonate buffer or phenol red. Substrates could then be added as required by the particular experiment to allow their effect on NAD(P)H fluorescence lifetimes to be studied. 10 mM HEPES was added to permit buffering at atmospheric CO_2 concentrations and the solution was adjusted to pH 7.4, measured using an electronic pH meter (Mettler Toledo). These recording solutions were then sterile filtered and warmed to 37 °C before use. Pharmacological perturbations to metabolism were applied by the dropwise addition of working concentrations of each compound, diluted from stock solutions in a suitable DMEM recording medium.

Measurement of NAD(P)H fluorescence intensity in response to metabolic perturbation was performed on an inverted LSM 510 laser scanning confocal microscope (Carl Zeiss). Illumination was provided by the 351 nm output of an argon ion laser (Enterprise UV, Coherent) and NAD(P)H fluorescence was observed using a 460($\pm$25) nm band pass emission filter. A quartz objective (40x oil immersion, 1.3 N.A.) was used to ensure efficient transmission of the ultraviolet illumination. For time series measurements, 12-bit 512x512 images were obtained with a pixel dwell time of 1.6 μs at one minute intervals. To reduce noise, the image recorded at each time point was a mean of four consecutive scans. Intensity traces were extracted using ImageJ (NIH).

FLIM was performed on an upright Zeiss LSM 510 microscope with a 1.0 N.A. 40x water-dipping objective. Two-photon excitation was provided by a Chameleon (Coherent) Ti:sapphire laser; tunable from 690 nm to 1020 nm, producing 140 fs pulses with a repetition rate of 80 MHz. A heated stage maintained the cells at 37 °C. This microscope was adapted for lifetime imaging by installing an external detector (HPM-100, Becker & Hickl) into an exit port of the microscope. This detector is sensitive to single photons, combining a gallium arsenide cathode with a PMT tube (R10467-40, Hamamatsu). Unlike the setup used for measurements in solution, performing TCSPC with excitation and detection through a high numerical aperture confocal microscope objective requires no emission

polariser as the magic angle decreases to 45° (Fisz, 2007; Becker, 2012). The output of the detector was connected to a TCSPC electronics module (SPC-830, Becker & Hickl) contained on a PCI board in a desktop computer. The operating principles for obtaining fluorescence lifetime images by TCSPC are identical to those described in section 2.2, only the x-y coordinates of the microscope scan heads are recorded by the electronics module along with the excitation-emission delay time of each photon detected. This allows separate fluorescence decays to be built up at each pixel of the image, with scanning performed continuously for four minutes with a pixel dwell time of 1.6 μs.

On-sample power for FLIM was set to 10 mW, measured by an optical power meter (Coherent FieldMate). This is well below the threshold for cell damage of 50 mW observed by Ridsdale and Webb (1993) with seven minutes of continuous scanning of rat basophilic leukemia cells. Previously, Tiede and Nichols (2006) observed the generation of highly fluorescent lesions at the onset of cellular damage when imaging NAD(P)H with two-photon microscopy. The authors observed such damage after three minutes of imaging at 20 mW. A similar effect was not observed at the lower imaging powers applied here.

In a two-photon microscope, dichroic beam splitters acting in reverse to those used with single-photon excitation are required. Light with a wavelength longer than the threshold of the dichroic must be directed to the sample, while the fluorescence emitted at a shorter wavelength to the excitation must reach the detector. A 650 nm short pass dichroic was used in this work. As with the standard confocal microscopy, NAD(P)H emission was observed during FLIM using a 460(±25) nm band pass filter.

To separate the NAD(P)H lifetime images into mitochondrial and cytosolic regions of interest, the mitochondrially-targeted fluorescent dye tetramethylrhodamine methyl ester (TMRM) was added to the recording medium 20 minutes prior to imaging at a final concentration of 25 nM. TMRM fluorescence was collected for a 10 s burst using a 610(±30) nm band pass emission filter. Excitation was provided at the same wavelength as NAD(P)H to avoid the possibility of chromatic aberration causing the TMRM and NAD(P)H images to be collected from different focal planes. The 585(±15) nm emission spectrum of TMRM ensures none of its fluorescence contaminates the NAD(P)H FLIM images (Scaduto Jr and Grotyohann, 1999).

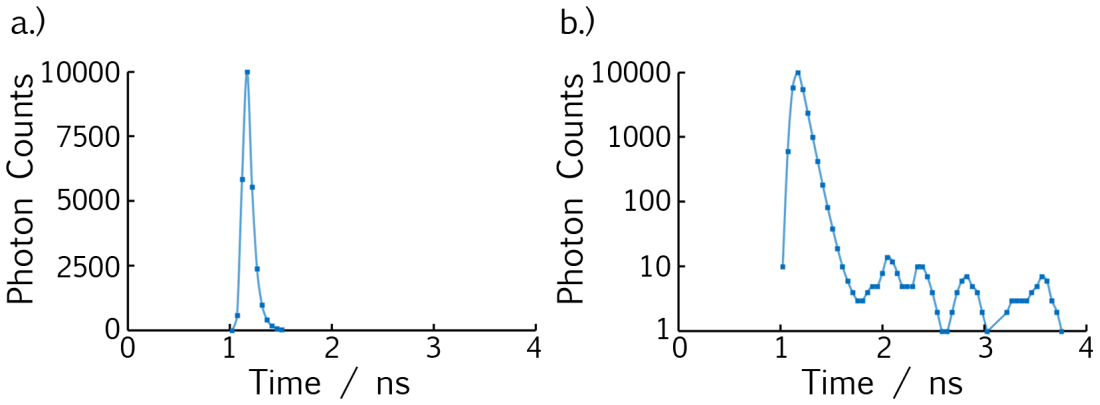

Figure 2.5: Instrument response function of the FLIM detector used in this work plotted on (a) linear and (b) log scale.

2.8 FLIM data analysis

Files containing the raw fluorescence decay data of a 256x256 FLIM image are more than 30 MB in size. Extracting fluorescence lifetime parameters from these requires the sequential fitting of 65536 fluorescence decay curves. This was performed using the software SPCImage (Becker & Hickl), where applying the iterative reconvolution fitting method on a pixel-by-pixel basis takes around eight minutes for a single image on a laptop computer. In all circumstances, a two-component exponential decay was sufficient to give a good fit at each pixel of the FLIM images obtained. A measurement of the IRF of the FLIM system was required for this process. This was obtained by measuring the fluorescence decay of second harmonic generation by a potassium dihydrogen phosphate (KDP) crystal at 920 nm. Crystals were grown by leaving a molar solution of KDP in water on a coverslip to evapourate. The measured IRF is shown in figure 2.5

As the tools available in SPCImage for processing fluorescence lifetime images post-fitting are crude, a method was developed to import the data into ImageJ for further analysis. Matrices of the fit parameters τ_{free}, τ_{bound} and α_{bound}, along with the total photons counted at each pixel, were exported from SPCImage. The MATLAB algorithm `lifetimes_to_grayscale()` was then applied to these matrices, the source code of which is contained in appendix A. This produced a 16-bit grayscale image for each parameter matrix where the intensity of each pixel was proportional to the parameter value at that location. ImageJ could then be used to measure the grayscale intensity in regions of the parameter images and the values obtained converted back to parameter values using the scaling factors applied in their production. By importing images of the TMRM distribution in the cell taken prior to lifetime imaging, masks identifying the location of mitochondrial

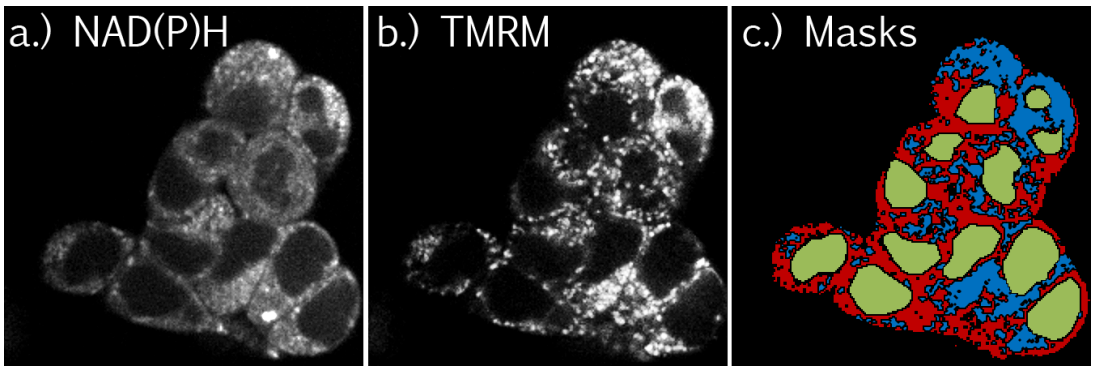

Figure 2.6: Averaging of fluorescence decay parameters based on subcellular location using masks created with the use of TMRM staining.

and cytosolic pixels could be created and a nuclear mask could be defined by hand, as shown in figure 2.6. The parameters describing the fluorescence decay of NAD(P)H in each of these regions could then be extracted separately.

2.9 Statistics and error propagation

NAD(P)H fluorescence lifetime parameters obtained using FLIM are reported as a mean over multiple regions of at least three coverslips. Uncertainties in these values are taken as the standard deviation of the measurements. Differences between the lifetime parameters measured under different conditions were tested for statistical significance ($P<0.05$) using a two-tailed Student's t-test. Uncertainties in values obtained from curve fits were taken as the 95% confidence intervals output by the fitting software. For the calculation of dependent quantities, uncertainties were propagated using the standard formula (Hughes and Hase, 2010) for the calculation of the error σ_z^2 in an arbitrary function $Z = Z(A, B, C...)$,

$$\sigma_z^2 = \left(\frac{\partial Z}{\partial A}\right)^2 \sigma_A^2 + \left(\frac{\partial Z}{\partial B}\right)^2 \sigma_B^2 + \left(\frac{\partial Z}{\partial C}\right)^2 \sigma_C^2 + ... \tag{2.13}$$

Chapter 3

Activated barrier crossing dynamics in the non-radiative decay of NADH and NADPH

The results presented in this chapter have been published as:

Blacker, T.S., Marsh, R.J., Duchen, M.R., Bain, A.J. (2013). Activated barrier crossing dynamics in the non-radiative decay of NADH and NADPH. *Chemical Physics*, In Press.

3.1 Kramers models of barrier crossing

The non-radiative rate of excited state decay in NAD(P)H is around 50 times greater than the radiative rate, causing its small (2%, Scott et al., 1970) quantum yield. As shown in section 1.12, the increased quantum yield, and therefore fluorescence lifetime, of enzyme bound NAD(P)H must be caused by the non-radiative decay pathway being restricted upon binding. However, the non-radiative decay mechanism has never been identified.

A number of studies (Gafni and Brand, 1976; Couprie et al., 1994; Zelent et al., 2007) have shown the fluorescence lifetimes of NAD(P)H increasing with increased solvent viscosity and decreasing with increased temperature. These correlations are hallmarks of fluorophores in which the non-radiative decay pathway constitutes a conformational relaxation of the molecule (Voth and Hochstrasser, 1996). In this process, motion of the molecule induces an overlap of the ground and excited state potential energy surfaces leading to ground state return via internal conversion. This can be described phenomenologically by Kramers theory (Kramers, 1940), in which the non-radiative decay results from the Brownian escape of the molecule over an intramolecular energy barrier.

The use of Kramers theory to describe conformational relaxation by barrier crossing was first proposed by McCaskill and Gilbert (1979) and later developed by Hochstrasser

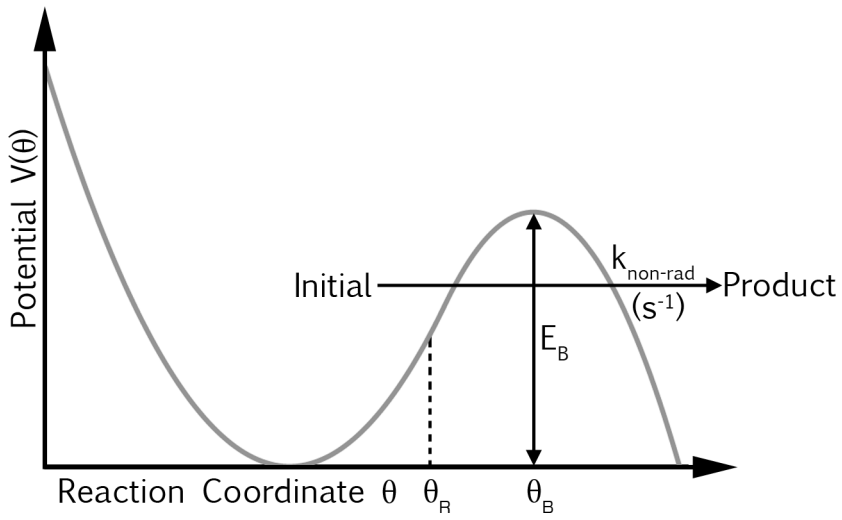

Figure 3.1: Kramers theory models non-radiative decay as the escape of a molecule over a potential energy barrier from an initial well to a product well.

(1980). The model was first applied experimentally by Velsko et al. (1983) and Lee et al. (1986) to the study of isomerisations. The Kramers model describes the escape of the excited state molecule across a potential energy barrier from an initial well to a product well with the variation in intramolecular potential V with reaction coordinate θ described by,

$$V(\theta) = \begin{cases} \frac{1}{4} I \omega_A^2 \theta^2 & (\theta < \theta_R) \\ E_B - \frac{1}{4} I \omega_B^2 \left(\theta - \theta_B\right)^2 & (\theta \geq \theta_R) \end{cases} \tag{3.1}$$

where I is the moment of inertia of the molecule about the axis of conformational change, ω_A and ω_B are the frequencies of the initial and product molecular configurations, respectively, and θ_R is the inflection point where the two piecewise potentials join (Lee et al., 1986). E_B is the height of the energy barrier located at point θ_B, as shown in figure 3.1. The positions of the turning points are related to the other parameters by,

$$\theta_B = 2\sqrt{\left(\frac{\omega_A^2 + \omega_B^2}{\omega_A^2 \omega_B^2}\right)\frac{E_B}{I}} \tag{3.2}$$

$$\theta_R = \left(\frac{\omega_B^2}{\omega_A^2 + \omega_B^2}\right)\theta_B \tag{3.3}$$

In Kramers's model, the rate at which electronic excitations decay non-radiatively, $k_{\text{non-rad}}$, is the rate at which the molecule crosses the energy barrier. This rate is dependent on the parameters describing the shape of the intramolecular potential, the thermal energy

available from the environment $k_B T$ and the correlation frequency β,

$$k_{\text{non-rad}} = \frac{\beta}{4\pi}\frac{\omega_A}{\omega_B}\left\{\left[1+\left(\frac{2\omega_B}{\beta}\right)^2\right]^{1/2}-1\right\}\exp\left(-E_B/k_B T\right) \tag{3.4}$$

The correlation frequency is the ratio of the friction coefficient between the molecule and the environment, ζ, to the moment of inertia of the induced motion,

$$\beta = \frac{\zeta}{I} \tag{3.5}$$

Both increased friction between the molecule and the environment and a decrease in I can increase the correlation frequency. As a direct measure of the friction coefficient is not possible, it is necessary to make an approximation of the friction experienced by the molecule during the conformational relaxation. The typical assumption made is that this friction is directly proportional to the viscosity of the environment η (Velsko et al., 1983),

$$\beta = p\frac{\eta}{I} \tag{3.6}$$

Substituting into equation 3.4 and introducing the parameters,

$$A = \frac{\omega_A}{2\pi}\exp\left(-E_B/k_B T\right) \tag{3.7}$$

$$B = \frac{2\omega_B I}{p} \tag{3.8}$$

gives,

$$k_{\text{non-rad}} = \eta\frac{A}{B}\left\{\left[1+\left(\frac{B}{\eta}\right)^2\right]^{1/2}-1\right\} \tag{3.9}$$

This is the hydrodynamic Kramers equation. Assuming the radiative rate remains constant, measurements of the fluorescence lifetimes of NADH and NADPH as a function of viscosity, combined with the relationship between fluorescence lifetime and non-radiative rate (equation 1.12), will allow $k_{\text{non-rad}}(\eta)$ to be plotted. A good fit of equation 3.13 to this data would suggest that conformational relaxation by barrier crossing plays a role in the non-radiative decay of excited NAD(P)H, yielding values for the intramolecular poten-

tial parameters A and B.

An alternative approach often used when the proportionality between the friction experienced by the fluorophore during conformational relaxation and the solvent viscosity does not appear to hold is to assume that ζ is proportional to the friction experienced by the molecule during rotational diffusion, ζ_{rot} (Lee et al., 1986). This is given by the Einstein relation,

$$\zeta_{\text{rot}} = \frac{k_B T}{D} \tag{3.10}$$

where D is the rotational diffusion coefficient. D is related to the rotational correlation time of the molecule τ_{rot} by (Tao, 1969),

$$D = \frac{1}{6\tau_{\text{rot}}} \tag{3.11}$$

Combining equations 3.10 and 3.11 with equation 3.6 gives the so-called Hubbard relation for the correlation frequency,

$$\beta = \frac{\zeta}{I} = \frac{q\zeta_{\text{rot}}}{I} = \frac{6qk_B T}{I}\tau_{\text{rot}} \tag{3.12}$$

where q is a constant of proportionality. Substitution of this expression into equation 3.4 yields the Kramers-Hubbard equation (Lee et al., 1986) in terms of τ_{rot},

$$k_{\text{non-rad}} = \tau_{\text{rot}}\frac{A}{C}\left\{\left[1+\left(\frac{C}{\tau_{\text{rot}}}\right)^2\right]^{1/2} - 1\right\} \tag{3.13}$$

with the parameter C defined by,

$$C = \frac{\omega_B I}{3qk_B T} \tag{3.14}$$

Activated barrier crossing can thus be studied by fitting equation 3.13 to plots of $k_{\text{non-rad}}$ against the rotational correlation time τ_{rot}. This quantity is obtained from the measurements of the fluorescence anisotropy decay of the molecules.

Solutions of NADH and NADPH were produced at varying viscosities to investigate the possibility of activated barrier crossing dynamics in the non-radiative decay of these molecules. Seven solvents were produced by mixing glycerol with 100 mM HEPES buffer

in differing proportions. These ranged in viscosity from 0.001 N s m^{-2} (100% HEPES, least viscous) to 1.4 N s m^{-2} (100% glycerol, most viscous), with the viscosity of each solvent calculated by the parameterisation provided by Cheng (2008).

By choosing to alter the viscosity of the NAD(P)H solutions using mixtures of two different solvents, consideration must be given to the effect that a varying refractive index will have on the measured fluorescence lifetimes. The Strickler-Berg relation (Strickler and Berg, 1962) shows that k_{rad} is proportional to the square of the refractive index of the surrounding medium. The refractive index of the solvents used here will vary between that of pure water (n =1.33303) to that of pure glycerol (n =1.47399) (Hoyt, 1934). As calculated in section 1.12, k_{rad} for NAD(P)H in aqueous solution is approximately 4 x 10^7 s^{-1}. This value should therefore increase to 4.9 x 10^7 s^{-1} in glycerol. The difference in the non-radiative rates calculated from a measured fluorescence lifetime τ_f in glycerol for these two radiative decay limits is given by,

$$\frac{k_{\text{non-rad}}^{\text{Glycerol}}}{k_{\text{non-rad}}^{\text{Water}}} = \frac{1-\tau_f k_{\text{rad}}^{\text{Glycerol}}}{1-\tau_f k_{\text{rad}}^{\text{Water}}} \tag{3.15}$$

For short fluorescence lifetimes the ratio is close to unity. The fluorescence lifetime of NAD(P)H in glycerol is of the order of 2 ns (Gafni and Brand, 1976) and the corresponding ratio is 0.98. The true value of the non-radiative decay rate is thus overestimated by only 2% by not accounting for the increase in the radiative rate between pure water and glycerol environments. Refractive index changes across the range of water-glycerol mixtures measured can therefore be safely neglected.

3.2 Variation of fluorescence decay with viscosity

1 mM solutions of NADH and NADPH (Sigma Aldrich) were produced at each viscosity and added to an optical cuvette (Hellma) for TCSPC experiments using the apparatus described in section 2.2 with 360 nm excitation and a 435 nm long-pass filter to eliminate laser breakthrough. The fluorescence intensity decays of these solutions were reconstructed from the measured $I_{||}(t)$ and $I_{\perp}(t)$ using equation 2.3. Fluorescence lifetimes and population fractions were then extracted by tail-fitting to equation 2.5, with good fits obtained at all viscosities with $n = 2$ components.

The fluorescence decays of NADH and NADPH are displayed at three representative viscosities in figures 3.2a and 3.2b, with the decay parameters summarised in table 3.1.

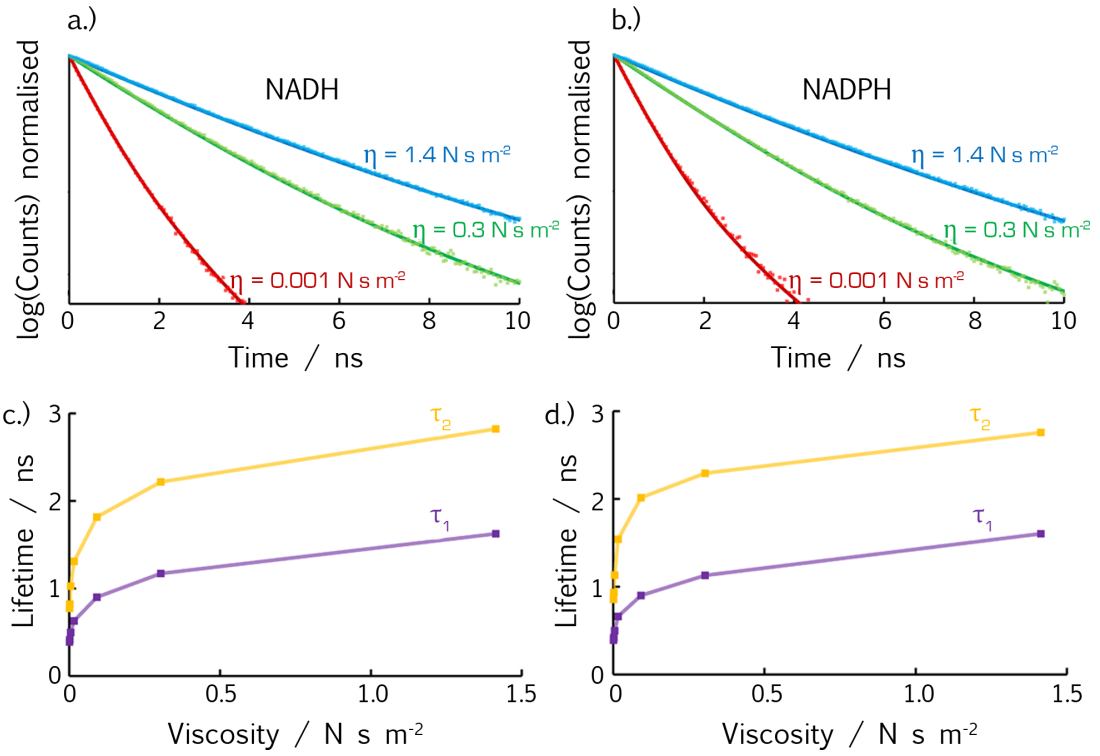

Figure 3.2: Fluorescence decays and lifetimes of NADH and NADPH as a function of viscosity.

The observed biexponential decay kinetics of freely diffusing NAD(P)H are in agreement with previous work (Visser and Hoek, 1981; Couprie et al., 1994).

The variation with solvent viscosity of the two fluorescence decay components of NADH and NADPH are shown in figures 3.2c and 3.2d. Both the short and long lifetimes are observed to increase with solvent viscosity, with the rate of increase becoming smaller and a lifetime threshold viscosity being approached at higher viscosities. The lifetime variation with viscosity is identical for NADH and NADPH, suggesting that the presence of the additional phosphate group in NADPH plays little part in the decay kinetics, with the electronic rearrangement of the transition largely localised over the nicotinamide ring in both molecules. This is in agreement with previous theoretical work (De Ruyck et al., 2007).

As seen in table 3.1, at high viscosity, the fraction of short lifetime species of NAD(P)H is significantly lower at around 70% from the maximum value of more than 90%. This behaviour was also observed by Gafni and Brand (1976), showing that a greater friction between the molecule and its environment, induced by greater solvent viscosity, inhibits the population of short lifetime NAD(P)H states. A decrease in the fraction of the short-lived species with decreasing temperature was observed by Couprie et al. (1994). The relative population of short and long lifetime species in both systems is therefore dependent on

NADH				
Viscosity / N s m^{-2}	α_1 / %	τ_1 / ns	τ_2 / ns	χ_r^2
0.001	86.6	0.39 (±0.01)	0.77 (±0.01)	1.7
0.002	83.4	0.41 (±0.01)	0.82 (±0.01)	1.5
0.005	88.7	0.50 (±0.01)	1.03 (±0.02)	1.2
0.016	90.9	0.63 (±0.01)	1.31 (±0.02)	1.9
0.092	91.4	0.90 (±0.01)	1.82 (±0.03)	1.7
0.304	87.2	1.17 (±0.01)	2.22 (±0.04)	1.9
1.414	72.0	1.62 (±0.02)	2.82 (±0.04)	2.7
NADPH				
Viscosity / N s m^{-2}	α_1 / %	τ_1 / ns	τ_2 / ns	χ_r^2
0.001	89.5	0.39 (±0.01)	0.86 (±0.02)	1.5
0.002	89.8	0.42 (±0.01)	0.93 (±0.01)	2.3
0.005	91.4	0.50 (±0.01)	1.13 (±0.02)	1.9
0.016	94	0.66 (±0.01)	1.54 (±0.03)	1.9
0.092	93.4	0.90 (±0.01)	2.01 (±0.04)	1.6
0.304	91.0	1.13 (±0.01)	2.29 (±0.04)	2.0
1.414	69.4	1.6 (±0.02)	2.76 (±0.04)	1.9

Table 3.1: Lifetime parameters recovered from biexponential fits to measured fluorescence decays of NADH and NADPH.

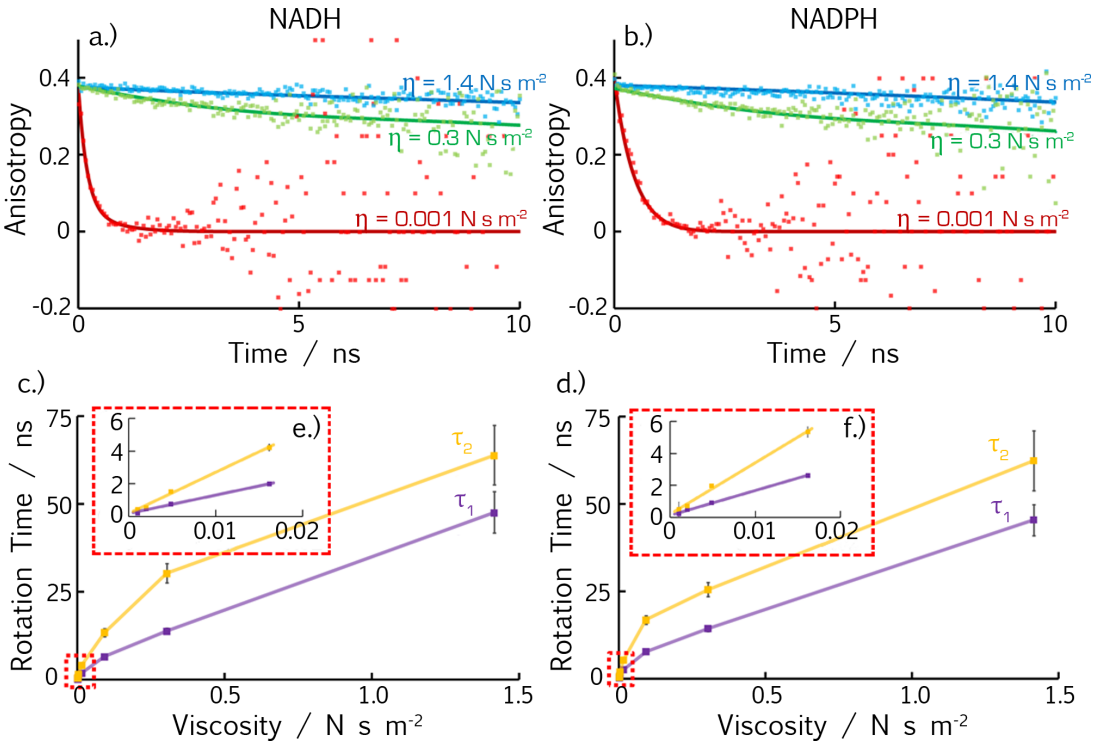

Figure 3.3: Fluorescence anisotropy decays and rotational correlation times of NADH and NADPH as a function of viscosity.

the thermal energy of the environment and solvent friction, with population of the short lifetime species promoted by an increase in thermal energy and opposed by solvent friction.

3.3 Rotational dynamics of NAD(P)H

The fluorescence anisotropy decays of the NADH and NADPH solutions were reconstructed from the polarised fluorescence decays using equation 2.7. Holding the previously-obtained fluorescence lifetimes and population fractions constant, rotational correlation times and initial anisotropies were extracted for each species by fitting to equation 2.11 with two components ($n = 2$).

Figures 3.3a and 3.3b show the anisotropy decays of NADH and NADPH, respectively, at three representative viscosities. The parameters defining the best-fit curves are detailed in table 3.2. Initial anisotropies close to the theoretical maximum of 0.4 suggest nearly collinear absorption and emission transition moments. The inclusion of additional decay components as found in the rotational dynamics of more flexible chromophores exhibiting restricted local motion moderated by overall rotational diffusion (Lipari and Szabo, 1980; Chadborn et al., 1999; Ko et al., 2009) did not improve χ_r^2.

The rotational correlation times obtained for the two emitting states of NADH and

NADH					
Viscosity / N s m^{-2}	$R_1(0)$	$\tau_{rot,1}$ / ns	$R_2(0)$	$\tau_{rot,2}$ / ns	χ_r^2
0.001	0.37 (±0.01)	0.20 (±0.01)	0.40 (±0.01)	0.45 (±0.03)	1.2
0.002	0.40 (±0.01)	0.46 (±0.01)	0.40 (±0.01)	0.55 (±0.04)	1.3
0.005	0.40 (±0.01)	0.75 (±0.02)	0.40 (±0.01)	1.53 (±0.08)	1.4
0.016	0.36 (±0.01)	1.99 (±0.05)	0.40 (±0.01)	4.2 (±0.2)	1.3
0.092	0.37 (±0.01)	6.6 (±0.3)	0.40 (±0.01)	13 (±1)	1.2
0.304	0.38 (±0.01)	13.9 (±0.8)	0.40 (±0.01)	30 (±3)	1.0
1.414	0.37 (±0.01)	48 (±6)	0.40 (±0.01)	64 (±8)	1.4
NADPH					
Viscosity / N s m^{-2}	$R_1(0)$	$\tau_{rot,1}$ / ns	$R_2(0)$	$\tau_{rot,2}$ / ns	χ_r^2
0.001	0.40 (±0.01)	0.22 (±0.05)	0.40 (±0.01)	0.5 (±0.4)	1.8
0.002	0.40 (±0.01)	0.50 (±0.01)	0.40 (±0.01)	0.71 (±0.04)	1.6
0.005	0.35 (±0.01)	0.91 (±0.02)	0.40 (±0.01)	1.97 (±0.09)	1.7
0.016	0.37 (±0.01)	2.62 (±0.08)	0.40 (±0.01)	5.4 (±0.3)	1.5
0.092	0.37 (±0.01)	7.7 (±0.3)	0.40 (±0.01)	17 (±1)	1.1
0.304	0.37 (±0.01)	14.4 (±0.8)	0.40 (±0.01)	26 (±2)	1.2
1.414	0.35 (±0.01)	45 (±4)	0.40 (±0.01)	62 (±9)	1.4

Table 3.2: Anisotropy decay parameters recovered from fits of equation 2.11 to polarised fluorescence decays of NADH and NADPH.

NADPH are displayed as a function of viscosity in figures 3.3c and 3.3d. Both show an initial linear increase with viscosity (up to η =0.016 N s m^{-2} as shown in figures 3.3e and 3.3f), as described by the generalised Stokes-Einstein-Debye equation (Lee et al., 1986; Kubinyi et al., 2006),

$$\tau_{\text{rot}} = f\kappa\frac{V_h\eta}{k_BT} + \tau_0 \tag{3.16}$$

Here, V_h is the van der Waals volume of the molecule and f is the form factor used to take account of the molecule's shape. Modelled as a spheroid, f is defined as the ratio of the equatorial diameter to the length of the polar axis. f equal to 1 indicates a spherical molecule, with deviations from this value indicating an increasingly non-spherical shape, either oblate ($f > 1$) or prolate ($f < 1$) (Koenig, 1975; Mannekutla et al., 2007). The parameter κ describes the boundary conditions of the molecular rotation in the solvent. For "stick" boundary conditions, where the first solvation shell rotates with the molecule, κ is equal to one. As the interaction between the solvent and solute decreases, κ decreases, reaching zero for the complete "slip" boundary condition. The parameter τ_0 has been suggested to represent the free rotor correlation time of the molecule (Lee et al., 1986), defined using the moment of inertia about the rotational axis under consideration I_{rot} as,

$$\tau_0 = \sqrt{\left(\frac{I_{\text{rot}}}{k_BT}\right)} \tag{3.17}$$

The deviation from Stokes-Einstein-Debye behaviour, as shown in figures 3.3c and 3.3d, is not uncommon (Rice and Kenney-Wallace, 1980; Lee et al., 1986; Megens et al., 1997) and results from the decreased interaction between solute and solvent causing a breakdown of the "stick" boundary condition. This effectively decreases the parameter κ in equation 3.16, causing the molecule to rotate more quickly at larger viscosities than would be predicted from simple Stokes-Einstein-Debye behaviour.

Fits to the linear portions of τ_{rot} vs. η data are shown in figures 3.3e and 3.3f. Equations 3.16 and 3.17 suggest the y-intercepts of these plots are proportional to the square root of the moment of inertia of each species. Using a routine written in MATLAB (contained in appendix A), the moment of inertia about the centre of mass of the NADH structure contained in entry 1I10 of the RCSB Protein Data Bank (Read et al., 2001) was calculated as 4 x 10^{-43} kg m^2, corresponding to a τ_0 value of 0.01 ns, at the limit of the temporal

resolution of the TCSPC setup used in this work. The y-intercepts of the lines of best fit in figures 3.3e and 3.3f are each similar, with an average value of 0.16(±0.02) ns, suggesting moments of inertia at least two orders of magnitude larger than the calculated value. Similar discrepancies between τ_0 and the calculated free rotor correlation time are widely reported (Evans and Kivelson, 1986; Dutt et al., 1990; Megens et al., 1997; Nguyen et al., 2012).

The gradients of the straight lines in figures 3.3e and 3.3f were 1.13(±0.06) x 10^{-7} m^2 N^{-1} and 2.5(±0.1) x 10^{-7} m^2 N^{-1} for the short and long lifetime species of NADH respectively, with these values increasing to 1.55(±0.06) x 10^{-7} m^2 N^{-1} and 3.2(±0.2) x 10^{-7} m^2 N^{-1} for NADPH. As the laboratory temperature was maintained at 19°C and assuming that the stick boundary condition holds ($\kappa = 1$) over this linear region, the differences in these gradients must result from differences in the product fV_h in equation 3.16. These parameters describe the shape of the molecule, supporting the view that the two fluorescence lifetimes observed result from structurally different NAD(P)H species, rather than two competing excited-state processes (Visser and Hoek, 1981; Couprie et al., 1994).

Using equation 3.16, the linear gradients in figures 3.3e and 3.3f correspond to fV_h values of 460(±30) Å^3 and 1020(±30) Å^3 for the short and long lifetime species of NADH, respectively, increasing to 630(±20) Å^3 and 1300(±60) Å^3 for NADPH. The short lifetime NADH value is similar to the theoretically calculated solvation volume for NADH of 493 Å^3 (Zheng et al., 2010). Whether these volumes correspond to folded and extended NAD(P)H remains to be seen. As the structures of folded (2BKJ, Tanner et al., 1999) and extended (1I10, Read et al., 2001) NADH are available from the RCSB Protein Data Bank, molecular dynamics simulations could be used to calculate the solvation volumes and form factors of the two configurations for comparison with these results.

The linearity of the relationship between rotational correlation time and viscosity described by the generalised Stokes-Einstein-Debye equation will break down when the "stick" boundary condition is no longer applicable. The point at which this occurs is often attributed to the length of the solvents becoming comparable to the length of the solutes (Dutt, 2005). This can be the case for studies in which the viscosity is increased by using a homologous series of linear chain alkanes, such as in the work by Lee et al. (1986). However, here viscosity was varied by changing the proportions of water and glycerol, both of which are much smaller than NAD(P)H. As will be seen in section 3.4, in contrast to

	NADH		NADPH	
Hydrodynamic	Short lifetime	Long lifetime	Short lifetime	Long lifetime
	A=2.5	A=1.3	A=2.5	A=1.1
	(±0.1)	(±0.1)	(±0.1)	(±0.1)
	B=0.029	B=0.024	B=0.026	B=0.022
	(±0.007)	(±0.007)	(±0.006)	(±0.006)
Kramers-Hubbard	Short lifetime	Long lifetime	Short lifetime	Long lifetime
	A=2.6	A=1.29	A=2.6	A=1.15
	(±0.1)	(±0.07)	(±0.1)	(±0.05)
	C=3.3	C=6	C=4.0	C=7
	(±0.7)	(±1)	(±0.6)	(±1)

Table 3.3: Summary of Kramers fit parameters to low-viscosity datapoints. Units of A are ns^{-1}, B are N s m^{-2} and C are ns.

previous work (Lee et al., 1986) where the Kramers-Hubbard approach remains a valid description of barrier crossing dynamics when Stokes-Einstein-Debye diffusion no longer holds, these results show that both barrier crossing models underestimate the non-radiative decay rate in this regime.

3.4 Barrier crossing in NAD(P)H

Up to viscosities of 0.016 N s m^{-2}, the non-radiative decay rates of NADH and NADPH are both well described by the Kramers and Kramers-Hubbard models, as shown by the fits of equations 3.9 and 3.13 to figures 3.4c and 3.4d and figures 3.5c and 3.5d respectively. The best fit parameters are shown in table 3.3. For both NADH and NADPH, the parameter A is significantly smaller for the long lifetime species than the short lifetime species. Arrhenius plots constructed by Couprie et al. (1994) show that the energy barrier heights of the two species are equal at 0.065 eV, approximately 2.6 $k_B T$. Combining this result with equation 3.7, the initial well frequencies of the short and long lifetime species of NAD(P)H are 7.2(±0.3) cm^{-1} and 3.4(±0.3) cm^{-1} respectively. These small values suggest the conformational relaxation involves small, rather than large-scale, molecular motion, as for example ring puckering (Colegrove and Laane, 1991; Fischer and Cao, 1999; Kuhlman et al., 2012), known to occur in the nicotinamide ring of NAD(P)H (Hurley and Hammes-Schiffer, 1997).

Table 3.3 shows that the values of A obtained by the Kramers-Hubbard approach are in agreement with those obtained from the hydrodynamic Kramers model. The values of the parameter B in the hydrodynamic Kramers fits remain constant across all species of NADH and NADPH, while the equivalent parameter in the Kramers-Hubbard model, C, varies.

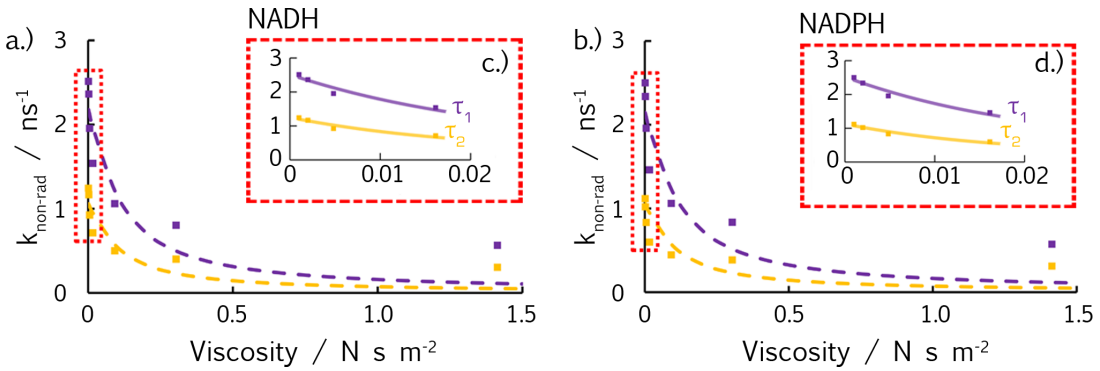

Figure 3.4: Non-radiative decay rate of NADH and NADPH as a function of viscosity. The hydrodynamic Kramers equation fits to the data up to $\eta = 0.016$ N s m^{-2} where hydrodynamics breaks down.

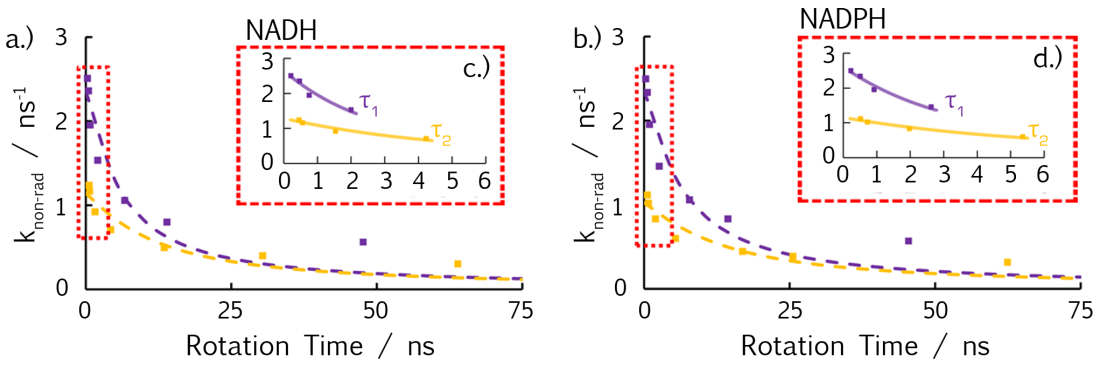

Figure 3.5: Non-radiative decay rate of NADH and NADPH as a function of rotational correlation time. The Kramers-Hubbard equation fits to the data up to $\eta = 0.016$ N s m^{-2} where rotational diffusion begins to occur at much slower timescales than barrier crossing.

The constant value for B indicates that the product $\omega_B I$ is equal for all species. The varying values of C observed suggest the ratios of the friction experienced during conformational relaxation and during rotation of the molecule are different for the short and long lifetime species of NADH and NADPH. Specifically, the value of q in the long lifetime species is 1.8 times that of the short lifetime species for both molecules.

In water-glycerol mixtures with viscosities between 0.001 N s m^{-2} and 0.016 N s m^{-2} in which the hydrodynamic Kramers and Kramers-Hubbard models provide good fits of the non-radiative decay rates of NAD(P)H, Stokes-Einstein-Debye rotational dynamics are also a good description of the anisotropy decays, as seen in figures 3.3e and 3.3f. At larger viscosities, corresponding to solutions containing 80-100% glycerol by volume, all three models of the excited state dynamics break down. Kramers and Kramers-Hubbard theory both underestimate the non-radiative decay rates and the observed rotational diffusion dynamics are significantly faster than predicted by Stokes-Einstein-Debye behaviour (equation 3.16).

The results presented here are in contrast to previous studies by Lee et al. (1986) on viscosity dependent non-radiative decay. Firstly, hydrodynamic Kramers and Stokes-Einstein-Debye dynamics are observed over a significantly larger viscosity range in this work on NAD(P)H. For example, in the work of Lee et al., viscosity variation was achieved using a series of alkane solvents with a maximum viscosity of only 0.004 N s m^{-2} in n-hexadecane. Secondly, in their work, barrier-crossing dynamics in the non-hydrodynamic regime were well described by the Kramers-Hubbard approach. In the studies of NAD(P)H presented here, the break down in hydrodynamics leads to a failure of both barrier-crossing models; behaviour previously observed by Velsko et al. (1983).

The standard Kramers model relies on the hydrodynamic assumption that the friction experienced during conformational relaxation is proportional to the viscosity of the solvent. Upon the breakdown of hydrodynamics, indicated by the deviation from linear Stokes-Einstein-Debye rotational dynamics at viscosities above 0.016 N s m^{-2}, the Kramers model will no longer apply. Hydrodynamic break down in water-glycerol mixtures has previously been observed by Mikosch et al. (1994) at viscosities above 0.025 N s m^{-2} for solutes with volumes between 10^2 and 10^3 $Å^3$, similar to those of NADH and NADPH. The authors attributed this behaviour to the formation of transient cavities in the water-glycerol mixture with relaxation times much larger than the rotational correlation time of the so-

lute (Dux and Dorfmuller, 1979). Recent molecular dynamics studies have confirmed the appearance of a glycerol hydrogen bonding network in water-glycerol mixtures of similar concentration (Egorov et al., 2011). This would allow conformational relaxation to occur relatively unimpeded inside a glycerol "cage" (Rice and Kenney-Wallace, 1980), permitting faster barrier crossing times than could be predicted from the viscosity of the solvent.

The discrepancy between Kramers-Hubbard theory and the measured non-radiative decay rates at viscosities larger than 0.016 N s m^{-2} implies that the friction experienced during the overall tumbling of NAD(P)H is no longer proportional to that experienced by the part of the molecule in which the barrier crossing is taking place. In the work of Lee et al., the product $k_{\mathrm{non-rad}}\tau_{\mathrm{rot}}$ in each solvent is approximately 0.4. This indicates that the time scale of rotational diffusion remains two to three times faster than the time scale of barrier crossing across the whole range of viscosities studied. In the NAD(P)H results presented here, a similar degree of proportionality between $k_{\mathrm{non-rad}}$ and τ_{rot} does not hold as can be seen in table 3.4. In the hydrodynamic region, $k_{\mathrm{non-rad}}\tau_{\mathrm{rot}}$ increases with viscosity from approximately 0.5 to 3. Rotational diffusion therefore takes place around three times slower than barrier crossing at the onset of non-hydrodynamic behaviour. This product increases to between 20 and 30 in pure glycerol (η =1.41 N s m^{-2}). It appears likely that the significant change in local structure of the solvent at high glycerol concentrations affects the friction experienced during rotational diffusion of the entire NAD(P)H molecule to a greater extent than the friction experienced by the nicotinamide moiety during conformational relaxation. This leads the Kramers-Hubbard model to overestimate the friction experienced during barrier crossing at these viscosities, resulting in the theoretical barrier crossing rates being lower than those measured experimentally.

Many studies (Velsko et al., 1983; Jas et al., 2000; Litvinenko et al., 2003; Wohl and Kuciauskas, 2005; Harris et al., 2006; Stsiapura et al., 2008; Cheng et al., 2009; Jee et al., 2010; Gangamallaiah and Dutt, 2011) have shown good fits of the non-radiative decay rates across the whole viscosity range using the phenomenological function,

$$k_{\mathrm{non-rad}} = \frac{D}{\eta^{\alpha}} \tag{3.18}$$

The parameter α has been suggested to relate to the volume of solvent displaced during the conformational relaxation (Velsko et al., 1983) while the parameter D is inversely proportional to the time scale over which the motion takes place (Gangamallaiah and Dutt,

	Short Lifetime			Long Lifetime		
Viscosity / N s m^{-2}	$k_{\mathrm{non-rad}}$ / ns^{-1}	τ_{rot} / ns	$k_{\mathrm{non-rad}}\tau_{\mathrm{rot}}$	$k_{\mathrm{non-rad}}$ / ns^{-1}	τ_{rot} / ns	$k_{\mathrm{non-rad}}\tau_{\mathrm{rot}}$
NADH						
0.001	2.5	0.2	0.51	1.2	0.45	0.56
0.002	2.4	0.46	1.1	1.2	0.55	0.64
0.005	2	0.75	1.5	0.92	1.5	1.4
0.016	1.5	2	3.1	0.71	4.2	3
0.092	1.1	6.6	7	0.5	13	6.7
0.3	0.8	14	11	0.4	30	12
1.4	0.57	48	27	0.3	64	19
NADPH						
0.001	2.5	0.22	0.54	1.1	0.5	0.56
0.002	2.3	0.5	1.2	1	0.71	0.73
0.005	2	0.91	1.8	0.83	2	1.6
0.016	1.5	2.6	3.8	0.6	5.4	3.2
0.092	1.1	7.8	8.2	0.45	17	7.5
0.3	0.84	14	12	0.39	26	9.9
1.4	0.57	45	26	0.31	62	20

Table 3.4: Barrier crossing rates and rotational correlation times of the short and long lifetime species of NADH and NADPH. The disproportionate increase of the rotational correlation time with viscosity is evident from the product $k_{\mathrm{non-rad}}\tau_{\mathrm{rot}}$.

2011). A value of $\alpha = 1$ will indicate behaviour in agreement with the inverse viscosity dependence of Stokes-Einstein-Debye hydrodynamics, with smaller values suggesting the conformational relaxation is less affected by friction than Stokes-Einstein-Debye hydrodynamics would predict (Harris et al., 2006; Stsiapura et al., 2008). Values of α less than one can indicate the presence of multidimensionality of time-dependent friction in the barrier-crossing dynamics of the molecule (Jee et al., 2010), as well as the breakdown of the simple hydrodynamic assumptions.

The excellent fit of equation 3.18 to the data is shown in figure 3.6. For the short and long lifetime of both NADH and NADPH, the exponents α were equal at 0.20($\pm$0.01). This value is much lower than the range of 0.5 to 0.8 expected when the non-radiative decay takes place via isomerisation (Biswas and Bagchi, 1996; Jee et al., 2010). The common value of α suggests that the motion responsible for internal conversion is the same for both configurations in NADH and NADPH. It should be noted that the timescale of the non-radiative decay is different between the two emitting populations in NAD(P)H with D =0.31($\pm$0.01) s^{-1} and D =0.66($\pm$0.03) s^{-1} for the long and short lifetime species respectively. The common values for α and D in NADH and NADPH indicate that the conformational relaxation motion in both molecules is not affected by the presence of the

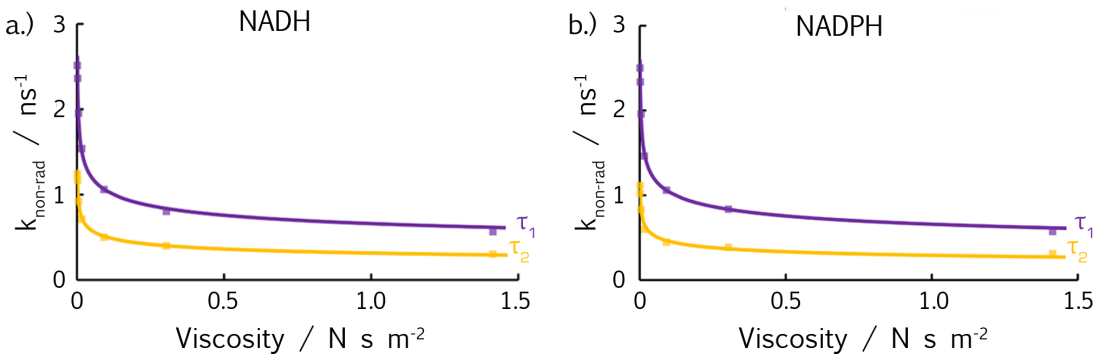

Figure 3.6: The variation of the non-radiative decay rates of NADH and NADPH as a function of viscosity fit to the power-law defined by equation 3.18.

additional phosphate group in NADPH.

3.5 Conclusions

By conforming to the Kramers and Kramers-Hubbard models, it can be concluded that the non-radiative decay of NAD(P)H is described by activated barrier crossing dynamics. However, this does not reveal the specific molecular motions involved. The low values of the initial well frequencies for NADH and NADPH suggest the involvement of small scale motions such as ring puckering (Colegrove and Laane, 1991; Fischer and Cao, 1999; Kuhlman et al., 2012). Puckering of the nicotinamide ring of NADH is known to change upon enzyme binding (Meijers et al., 2001). Establishing whether this is the cause of the fluorescence lifetime changes of NAD(P)H when bound to different enzymes could be investigated by correlating the lifetime of NAD(P)H when bound to a particular enzyme with its known configuration in the binding site. This would require use of the large number of crystal structures available of enzyme-bound NADH and NADPH. Any enzymes causing a significantly large increase in the fluorescence lifetime of bound NAD(P)H could indicate an increased restriction of the conformational relaxation of the nicotinamide ring caused by the presence of a unique structural motif.

The Kramers fits performed in this study indicate that the initial well frequency for the short lifetime species of NAD(P)H is double that of the long lifetime species. With the fits in figure 3.6 suggesting that the relaxation motion is identical in all species and the hydrodynamic Kramers fits suggesting that the product well frequency is the same for all species, the difference in the time scale of non-radiative decay in the short and long lifetime species must be due to the difference in their initial well frequencies. The envisioned potential is sketched in figure 3.7. The varied hydrodynamic volumes observed in the rotational corre-

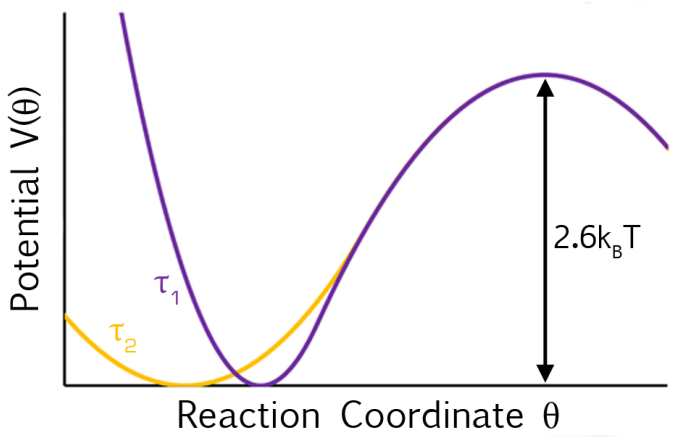

Figure 3.7: Hypothetical potential energy surfaces for conformational relaxation of the short (τ_1) and long (τ_2) lifetime NAD(P)H species based on the differences in initial well frequencies determined from Kramers theory. The barrier height was provided by Couprie et al. (1994).

lation times of the different NAD(P)H species suggest that structural distinctions give rise to the different initial well frequencies. However, it remains uncertain as to whether these distinct configurations are the folded and extended conformations of NAD(P)H observed in crystal structures, particularly in light of the fluorescence excitation transfer spectroscopy experiments performed by Hull et al. (2001) suggesting that the populations of free and folded species in room temperature aqueous solutions are more equal in size than the amplitudes observed in this work would indicate.

Chapter 4

Two-photon spectroscopy of NADH and NADPH

4.1 Two-photon absorption

The requirement of a pulsed laser source for both TCSPC and multiphoton imaging means laboratories frequently combine two-photon excitation microscopy and FLIM into the same system (Becker, 2012). A large number of published NAD(P)H FLIM experiments therefore employ two-photon excitation, using incident wavelengths ranging from 730 nm to 800 nm (Vishwasrao et al., 2005; Skala et al., 2007b; Gehlsen et al., 2012). However, previous studies of NADH in solution suggest its two-photon cross section is maximum between 700 nm and 720 nm (Huang et al., 2002; Kasischke et al., 2004). As measurements of the two-photon cross section of NADPH have never been reported, this chapter investigates the two-photon absorption properties of both cofactors.

The excitation of a molecule upon the simultaneous absorption of two photons was first proposed theoretically by Maria Goeppert-Mayer in 1931. The phenomenon was not experimentally realised until the 1960's upon the development of short-pulsed laser sources able to provide the large incident photon flux required (Larijani et al., 2006). For pulses with energy E_{pulse}, the probability of a two-photon transition taking place is related to the incident photon flux by,

$$P_{2PA} = \frac{g_p}{2w}\left(\frac{E_{\text{pulse}}}{Ahv}\right)^2 \sigma_{2P} \tag{4.1}$$

where g_p is a dimensionless quantity dependent on the temporal profile of the laser pulses (0.664 for Gaussian pulses, Xu and Webb, 1996) of duration (FWHM) w, incident over an area A. The photon flux to which the sample is exposed is given by the fraction

$E_{\text{pulse}}/Ah\upsilon$. The constant σ_{2P} is the two-photon cross section of the molecule with units cm^4 s photon^{-1}, typically in the range of 10^{-51} to 10^{-48} (Larijani et al., 2006). For convenience, two-photon cross sections are frequently quoted in the units of Goeppert-Mayer (GM) where 1 GM $= 10^{-50}$ cm^4 s photon^{-1}.

The small typical values for σ_{2P} suggest that two-photon excitation is a low probability event. However, P_{2PA} is directly proportional to the square of the pulse energy and inversely proportional to the square of the illumination area. Significant two-photon absorption can therefore be achieved by focusing high-energy pulses, such as those output by a Ti:sapphire laser, with a high numerical aperture lens. This allows two-photon excitation microscopy, described in section 1.10, to be a viable experimental technique.

In single-photon excitation, the rate of transition between ground and excited state is proportional to the projection of the polarisation vector of the incident light onto the absorption transition dipole moment of the molecule under investigation (Lakowicz, 2006). This leads to the initial $\cos^2\theta$ distribution of the excited state population with single photon photoselection. For two-photon excitation, the transition rate becomes proportional to a double projection of polarisation vectors. The absorption transition dipole moment is therefore replaced by the two-photon transition tensor $\mathbf{S}$ (Lakowicz, 1997), leading to,

$$\text{transition rate} \propto \left|\hat{\mu}_\mathbf{1} \cdot \mathbf{S} \cdot \hat{\mu}_\mathbf{2}\right|^2 \tag{4.2}$$

where $\hat{\mu}_\mathbf{1}$ and $\hat{\mu}_\mathbf{2}$ are unit vectors defining the directions of polarisation of the two incident photons in the molecular frame of reference. The product can be expanded as,

$$\begin{aligned}
\begin{pmatrix} \mu_{1,x} & \mu_{1,y} & \mu_{1,z} \end{pmatrix} \begin{pmatrix} S_{xx} & S_{xy} & S_{xz} \\ S_{yx} & S_{yy} & S_{yz} \\ S_{zx} & S_{zy} & S_{zz} \end{pmatrix} \begin{pmatrix} \mu_{2,x} \\ \mu_{2,y} \\ \mu_{2,z} \end{pmatrix} & \\
= S_{xx}\mu_{1,x}\mu_{2,x} + S_{xy}\mu_{1,x}\mu_{2,y} + S_{xz}\mu_{1,x}\mu_{2,z} + & \\
S_{yx}\mu_{1,y}\mu_{2,x} + S_{yy}\mu_{1,y}\mu_{2,y} + S_{yz}\mu_{1,y}\mu_{2,z} + & \\
S_{zx}\mu_{1,z}\mu_{2,x} + S_{zy}\mu_{1,z}\mu_{2,y} + S_{zz}\mu_{1,z}\mu_{2,z} &
\end{aligned} \tag{4.3}$$

For identical photons, $\hat{\mu}_\mathbf{1} = \hat{\mu}_\mathbf{2}$ and $\mathbf{S}$ becomes symmetric (Larijani et al., 2006). For molecules in which the electronic rearrangement upon excitation is constrained to a plane, as can be expected in the nicotinamide moiety of NAD(P)H (Kierdaszuk et al., 1996;

De Ruyck et al., 2007), the two-photon transition tensor reduces to two-dimensions. **S** can then be further simplified by introducing the parameters $D = S_{xy}/S_{xx}$ and $S = S_{yy}/S_{xx}$, giving,

$$\mathbf{S} = \begin{pmatrix} S_{xx} & S_{xy} \\ S_{xy} & S_{yy} \end{pmatrix} = S_{xx} \begin{pmatrix} 1 & D \\ D & S \end{pmatrix} \tag{4.4}$$

In single photon photoselection, the initial fluorescence anisotropy $R(0)$ is defined by the angle between the emission and absorption transition dipole moments. Similarly, for two-photon photoselection, the initial anisotropy depends on the orientation of the two-photon transition tensor relative to the emission dipole moment. If this is defined to be along the x-axis, the initial anisotropy can be written in terms of the tensor components as (Lakowicz, 1997),

$$R_{\text{lin}}(0) = \frac{1}{7} \frac{2(1+S)^2 + (1-S)^2 + 4D^2 + 9\left(1-S^2\right)}{2(1+S)^2 + (1-S)^2 + 4D^2} \tag{4.5}$$

Excitation with circularly polarised light yields a different initial anisotropy, defined by,

$$R_{\text{circ}}(0) = \frac{1}{7} \frac{3(1-S)^2 - (1+S)^2 + 12D^2 + 6\left(1-S^2\right)}{(1+S)^2 + 3(1-S)^2 + 12D^2} \tag{4.6}$$

The ratio between the time-averaged total fluorescence intensities emitted with circularly and linearly polarised excitation, Ω, is also related to D and S by,

$$\Omega = \frac{\left\langle I_{\text{total}}^{\text{circ}} \right\rangle}{\left\langle I_{\text{total}}^{\text{lin}} \right\rangle} = \frac{1}{2} \frac{(1+S)^2 + 3(1-S)^2 + 12D^2}{2(1+S)^2 + (1-S)^2 + 4D^2} \tag{4.7}$$

As S and D are molecular parameters, whereas the fluorescence observables are measured in the laboratory frame of reference, equations 4.5 to 4.7 are calculated by averaging over all possible molecular orientations (Wan and Johnson, 1994), a valid approach for liquid samples, such as those under investigation here, in which no long-range order is present. Given these expressions, the shape of the two-photon transition tensor of a molecule can be determined by experimental determination of $R_{\text{lin}}(0)$, $R_{\text{circ}}(0)$ and Ω. These measurements can be performed simultaneously to those for determining the wavelength-dependence of two-photon absorption in NADH and NADPH.

4.2 NAD(P)H cross section spectra

Upon two-photon excitation by a pulsed laser source at a wavelength λ, the time-averaged total fluorescence intensity collected from a sample by a detector is given by,

$$\langle I_{total}(t)\rangle = \frac{4}{\pi}\left(\frac{g_p}{fw\lambda}\right) nC\Phi\varepsilon\sigma_{2P}\langle P(t)\rangle^2 \tag{4.8}$$

where Φ is the quantum yield of the fluorophore present at a concentration C in a medium of refractive index n (Xu and Webb, 1996). $\langle P(t)\rangle$ is the time-averaged on-sample power of the illumination pulses with repetition rate f (Yu and Heikal, 2009). Fluorescence will be emitted across the distribution of wavelengths defined by the emission spectrum of the fluorophore. However, less than 100% of the emission spectrum will be included in the total light collected due to the presence of wavelength-dependent transmission efficiencies in the detector and the emission filters. This is accounted for in equation 4.8 by the parameter ε, calculated as

$$\varepsilon = \frac{\int_{\lambda_{min}}^{\lambda_{max}} E(\lambda)F(\lambda)G(\lambda)d\lambda}{\int_{\lambda_{min}}^{\lambda_{max}} E(\lambda)d\lambda} \tag{4.9}$$

where $E(\lambda)$ is the emission spectrum of the fluorophore and F and G are the fractional transmission efficiencies of the emission filter and detector, respectively, at wavelength λ.

Equation 4.8 allows the two-photon cross section of a sample to be calculated directly. However, this would require the accurate measurement of the temporal profile of the laser pulses within the excitation volume. This can be avoided by comparing the fluorescence emitted by the sample under analysis with that emitted under identical illumination conditions by a reference sample with a known two-photon cross section. When the ratio of the fluorescence intensity emitted by the two samples is compared, the temporal properties of the incident pulses cancel, giving,

$$\frac{\langle I_{\text{total}}(t)\rangle_{\text{sample}}}{\langle I_{\text{total}}(t)\rangle_{\text{ref}}} = \frac{n_{\text{sample}}C_{\text{sample}}\Phi_{\text{sample}}\varepsilon_{\text{sample}}\sigma_{\text{2P,sample}}}{n_{\text{ref}}C_{\text{ref}}\Phi_{\text{ref}}\varepsilon_{\text{ref}}\sigma_{\text{2P,ref}}}\frac{\langle P(t)\rangle^2_{\text{sample}}}{\langle P(t)\rangle^2_{\text{ref}}} \tag{4.10}$$

This can then be rearranged to allow the calculation of the two-photon cross section of the molecule under investigation by comparison of its emission intensity with that of the

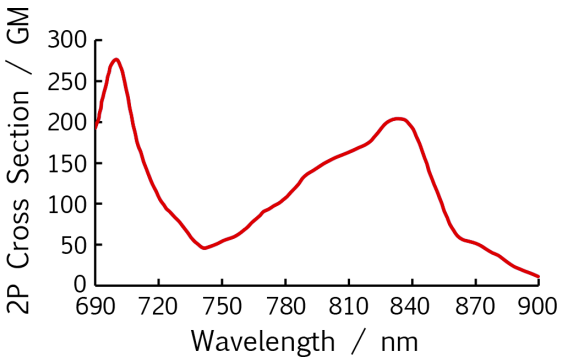

Figure 4.1: Two-photon absorption cross section spectrum of rhodamine B in methanol used as a reference for NAD(P)H cross section measurements, downloaded from DRBIO.

reference standard,

$$\sigma_{2P,sample} = \sigma_{2P,ref} \frac{n_{ref} C_{ref} \Phi_{ref} \varepsilon_{ref}}{n_{sample} C_{sample} \Phi_{sample} \varepsilon_{sample}} \frac{\langle P(t) \rangle^2_{ref}}{\langle P(t) \rangle^2_{sample}} \frac{\langle I_{total}(t) \rangle_{sample}}{\langle I_{total}(t) \rangle_{ref}} \tag{4.11}$$

Given the wavelength range in which two-photon excitation of NADH has previously been achieved, a 10 μM solution of rhodamine B in methanol was used as the reference standard in these experiments. Its two-photon cross section spectrum in the wavelength range 690 nm to 900 nm, shown in figure 4.1, was downloaded from DRBIO (Developmental Resource for Biophysical Imaging Optoelectronics, Cornell University). 1 mM solutions of NADH or NADPH in HEPES or glycerol were added to an optical cuvette and placed in the optical apparatus described in section 2.2. Incident illumination was provided by a Ti:sapphire laser (Mira 900F, Coherent) with readings taken at wavelengths of 690 nm upwards at approximately 5 nm intervals. On-sample powers were measured using an optical power meter (Thorlabs). A 600 nm short-pass emission filter was used to eliminate laser break through and the emission polariser was set to the magic angle. Fluorescence intensities were read from the analogue count-rate display of the modular TCSPC system.

For each solvent, the average quantum yield of NAD(P)H was input into equation 4.11, calculated using equation 1.15 with the radiative rate of 4 x 10^7 s^{-1} approximated in section 1.12 and the amplitude-weighted average of the lifetimes taken from table 3.1. This gave quantum yields of 0.018 and 0.078 for NAD(P)H in HEPES and glycerol respectively. The quantum yield of rhodamine B was taken as 0.8 (Bindhu et al., 1996). For the calculation of ε for each fluorophore, emission spectra were obtained from Du et al. (1998) and Patterson et al. (2000). The detection efficiency of the MCP-PMT was provided by the

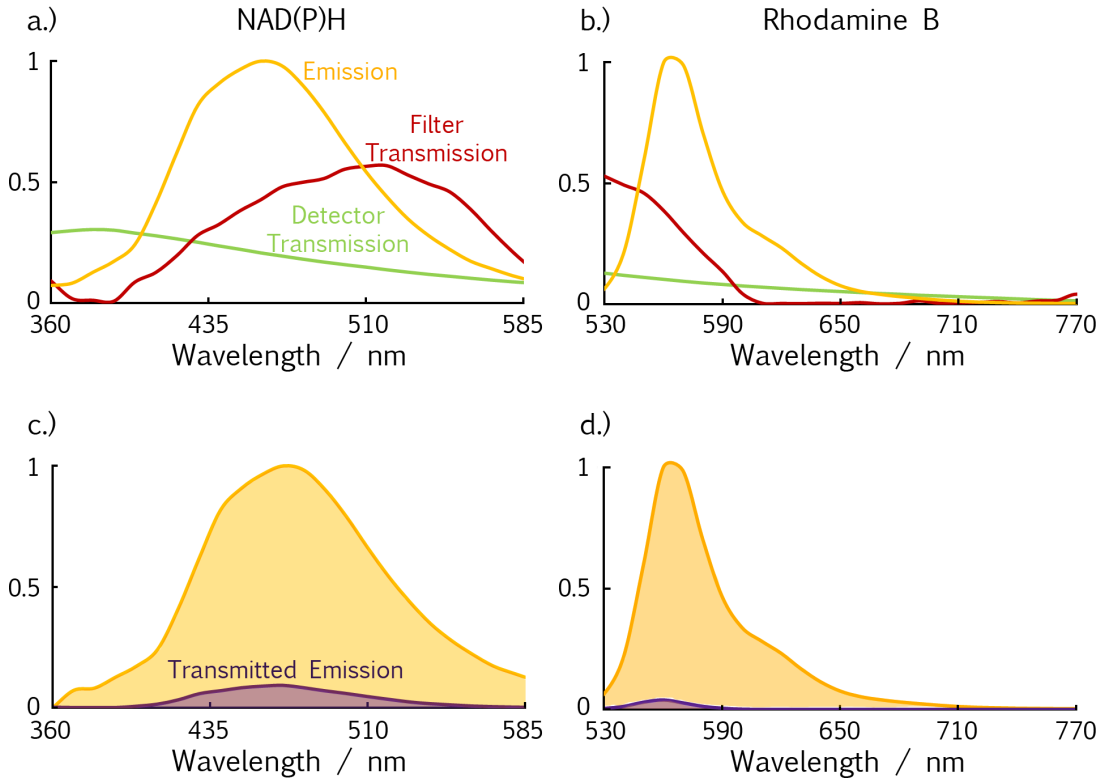

Figure 4.2: Emission spectra of NAD(P)H and rhodamine B alongside the transmission efficiencies of the emission filter and detector at the appropriate wavelengths, used for calculation of the correction factors ε. The product of the three curves in (a) and (b) give the purple transmitted emission spectra in (c) and (d) respectively. ε is the ratio of the areas under the purple and yellow curves.

manufacturer. The transmission curve of the emission filter was obtained by measuring its spectral absorption of a white light source using a USB spectrometer (OceanOptics). These distributions are shown in figure 4.2. Using equation 4.9, $\varepsilon_{\text{sample}}$ is calculated as 0.072 and ε_{ref} is 0.025.

The measured two-photon cross section spectra of NADH and NADPH in HEPES and glycerol are shown in figure 4.3. The absorption maximum occurs at approximately 700 nm in each case, with the peak cross section of around 4 GM agreeing with previously published measurements (Huang et al., 2002; Kasischke et al., 2004). This value is 100- to 1000-fold smaller than chromophores that have been specifically designed for two-photon excitation (Katan et al., 2007). However, comparable absorption cross sections are found in conventional fluorescent dyes used previously for cellular imaging with two-photon excitation microscopy such as DAPI and indo-1 (Xu and Webb, 1996; Hell et al., 1998; Wilms et al., 2006), confirming the viability of NAD(P)H as a fluorescent target for two-photon excitation microscopy.

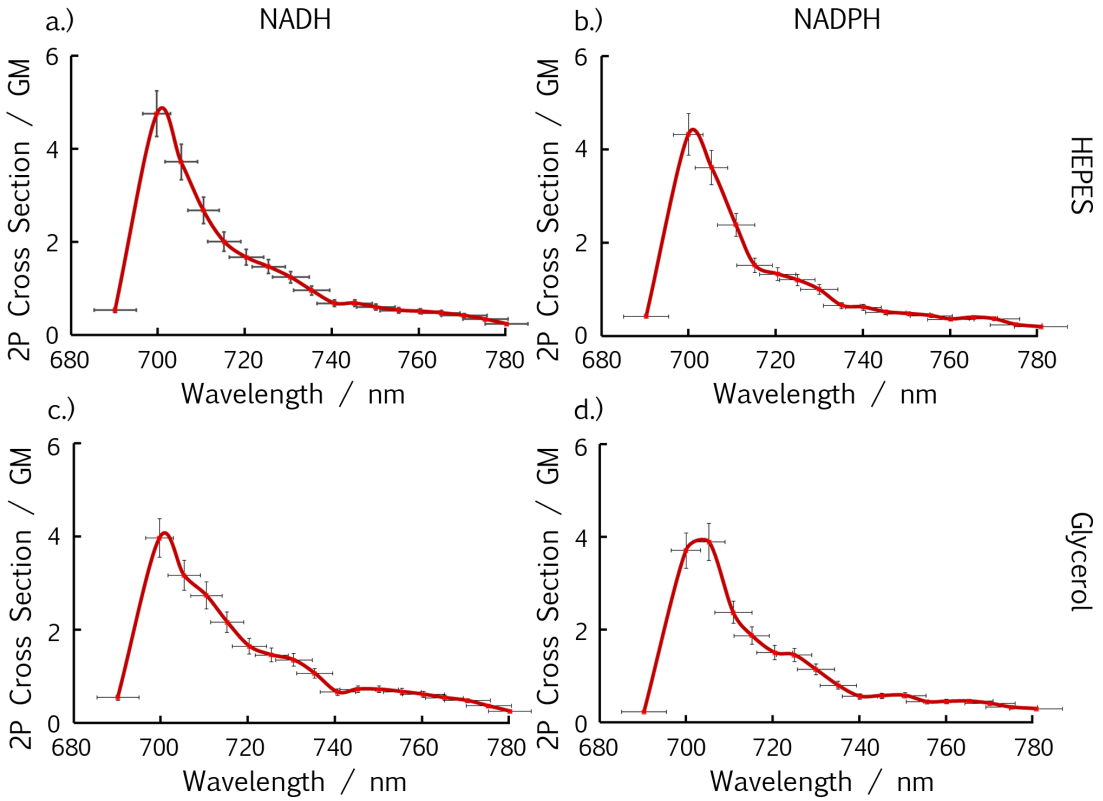

Figure 4.3: Two-photon absorption cross section spectra for NADH and NADPH in HEPES and glycerol.

4.3 Two-photon transition tensors

Measuring the time-resolved fluorescence anisotropy decay of the solutions produced for the previous section under linearly and circularly polarised two-photon excitation allows determination of $R_{\text{lin}}(0)$ and $R_{\text{circ}}(0)$ for the fluorescent species of NADH and NADPH. The time-averaged total fluorescent intensities at each incident polarisation setting determines Ω, allowing the tensor elements D and S to be determined for the molecules using equations 4.5 to 4.7. This data was obtained at illumination wavelengths between 705 nm and 765 nm at 10 nm intervals. The apparatus used was as in figure 2.2 with an adjustable phase retardation plate (Alphalas) introduced into the beam path to produce circularly polarised illumination. Circular polarisation was confirmed by observing that the power transmitted through a linear analysing polariser remained constant throughout its 360° rotation. Anisotropy decays were reconstructed from the measured $I_{||}(t)$ and $I_{\perp}(t)$ differently depending on whether linearly or circularly polarised excitation was used. Linearly polarised fluorescence anisotropy decays were calculated by equation 2.7. However, with excitation polarised circularly in the x-z plane, the y-axis becomes the axis of symmetry for the distribution of excited state molecular orientations. The total fluorescence intensity is

therefore given by $I_\perp + 2I_{||}$ and the magic angle becomes 35.3°, both still measured relative to the z-axis (Valeur, 2001). The fluorescence anisotropy for circularly polarised excitation is therefore,

$$R_{\text{circ}}(t) = \frac{I_{||}(t) - I_\perp(t)}{I_\perp(t) + 2I_{||}(t)} \tag{4.12}$$

Fits to the circularly-excited anisotropy decays must then be weighted according to (appendix B),

$$\sigma_k^2 = \frac{\left[4I_{||}(t_k) + I_\perp(t_k)\right] R^2(t_k) - 2\left[2I_{||}(t_k) - I_\perp(t_k)\right] R(t_k) + \left[I_{||}(t_k) + I_\perp(t_k)\right]}{I_{\text{total}}^2(t_k)} \tag{4.13}$$

in contrast to the use of equation 2.12 for the calculation of χ_r^2 (equation 2.4) in the linearly-excited case.

As in section 3.3, a two-component anisotropy decay model (equation 2.11) was fit to the data, allowing the recovery of initial anisotropy values $R_1(0)$ and $R_2(0)$ for both NAD(P)H species present. Fluorescence lifetimes τ_i and population fractions α_i were held constant in the anisotropy decay fits after tail-fitting of equation 2.5 to the total fluorescence decays of the solutions under linearly- and circularly-polarised excitation. In the majority of cases, a two-component model gave the best fits. However, at four wavelengths (435 nm to 465 nm), the fluorescence decay of NADH in HEPES required an additional component for a good fit across the entire 26 ns measurement range. The weighting of this component was extremely small, averaging 0.0014(±0.0008). However, its fluorescence lifetime of 6(±2) ns was long relative to the typical NAD(P)H lifetimes. As such, its contribution to the total fluorescence signal at delay times of 6 ns or more was more than 90%. A species with similar characteristics has previously been observed in the fluorescence decay of aqueous NADH (Couprie et al., 1994), suggesting it to be a decomposition product rather than a contaminant. Here, the decays requiring this long component to be fit were those with more than 70,000 counts in the peak bin. It is likely that the presence of this species is masked by background noise in the measurements at lower signal levels. The negligible amplitude of this component ensures that values of α_i and τ_i for the two primary NAD(P)H species are unaffected by its presence, with similar values in each measurement regardless of whether a two-component or three-component model is required for a good fit. In all

measurements, the lifetimes and rotational diffusion times were similar to those obtained with single-photon excitation.

The time-averaged total fluorescence emission intensity was recorded from the analogue count-rate display of the TCSPC system under the corresponding magic angle detection conditions for each illumination polarisation. The separate intensities emitted by each NAD(P)H species were then calculated by multiplying the measured intensity by the fractional contribution of each species to the total fluorescence, given by (Lakowicz, 2006),

$$f_i = \frac{\alpha_i \tau_i}{\alpha_1 \tau_1 + \alpha_2 \tau_2} \tag{4.14}$$

where the parameters α_i and τ_i were obtained from the total fluorescence decay measurements at the respective incident polarisation, neglecting the small (approximately 1%) contribution from the presence of a third decay component. 10 intensity measurements were made at alternate polarisation settings, giving five estimates of the ratio Ω, defined for each NAD(P)H species as,

$$\Omega_i = \frac{f_{i,\mathrm{circ}} I_{\mathrm{total,circ}}}{f_{i,\mathrm{lin}} I_{\mathrm{total,lin}}} \tag{4.15}$$

The mean values of Ω_i in each solvent, along with their initial anisotropies $R_{i,\mathrm{lin}}(0)$ and $R_{i,\mathrm{circ}}(0)$, are displayed in figures 4.4 and 4.5. The initial anisotropies are similar across each NADH and NADPH species in both HEPES and glycerol, with average values of $R_{\mathrm{lin}}(0) = 0.55(\pm 0.01)$ and $R_{\mathrm{circ}}(0) = 0.26(\pm 0.01)$. Larger anisotropies than the limit of 0.4 imposed by single-photon excitation are possible with two-photon excitation due to $\cos^4\theta$, rather than $\cos^2\theta$, photoselection (Lakowicz, 1997)

While the initial anisotropies are similar, the values of Ω differ significantly between the two NAD(P)H species. The mean value of Ω_1 across all measurements is $0.7(\pm 0.1)$ while Ω_2 is larger at $1.0(\pm 0.2)$. By inspection of the mean fluorescence decay fit parameters contained in table 4.1, the difference in Ω values of the two species results from linearly polarised excitation creating an excited state population with a larger fraction of the short lifetime NAD(P)H species than with circularly polarised excitation. The fraction of the time-averaged fluorescence intensity due to the short lifetime species is therefore larger for linearly polarised excitation than circularly polarised excitation, resulting in a smaller value of Ω_1 than Ω_2. Averaging the NADH and NADPH results, the excited state population

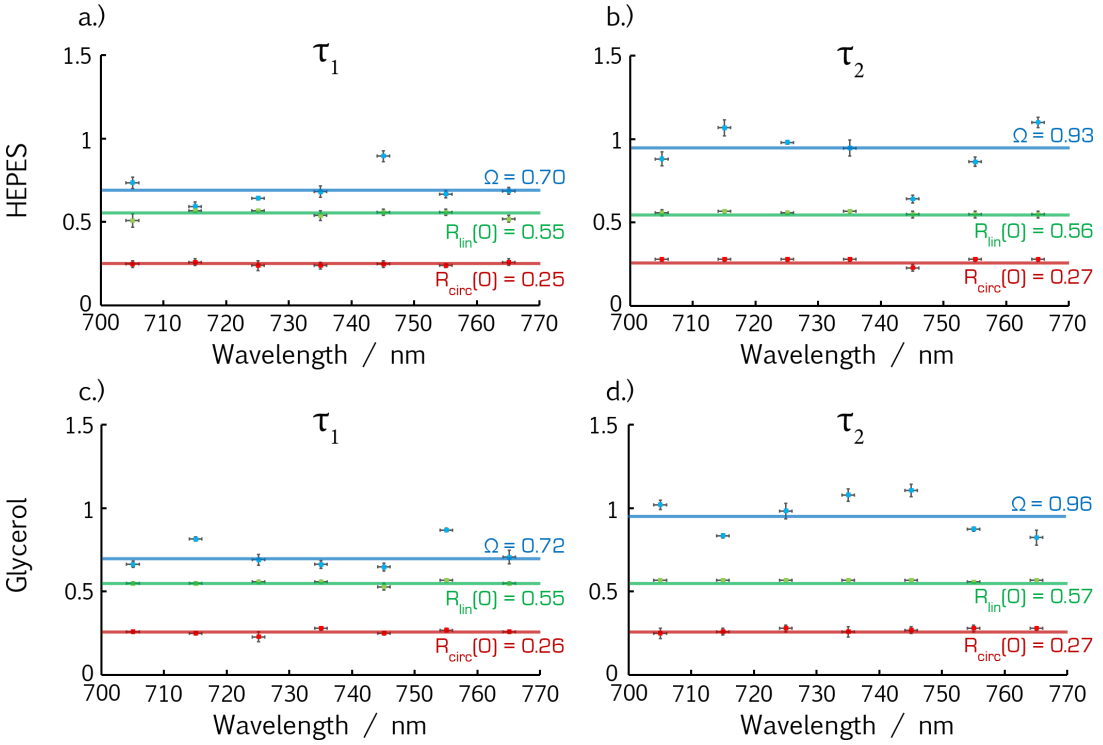

Figure 4.4: Initial anisotropies and relative emission intensities of NADH under circularly and linearly polarised two-photon excitation as a function of wavelength.

created with linearly polarised excitation consists of 78(±4)% and 70(±3)% of the short lifetime species in HEPES and glycerol respectively. With circularly polarised excitation, these values decrease to 72(±6)% and 65(±4)%. The value of α_1 measured in glycerol with linearly polarised two-photon excitation is similar to its value measured with single-photon excitation in the previous chapter. However, in HEPES, α_1 is significantly smaller in the two-photon case at 78% compared to 88%.

As $R_{i,\mathrm{lin}}(0)$, $R_{i,\mathrm{circ}}(0)$ and Ω_i appear to be independent of excitation wavelength, their mean values were taken for calculation of the tensor elements D and S for the two species of NADH and NADPH in each solvent. Given these measurements, equations 4.5 to 4.7 form three non-linear equations in two unknowns. The system is therefore overdetermined, allowing the optimal values of D and S to be found using a Levenberg-Marquard-Fletcher least-squares algorithm (Fletcher, 1971) contained in MATLAB (LMFnlsq.m). Uncertainties in the output parameters were judged by using the optimised values of D and S to recalculate corresponding values of $R_{\mathrm{lin}}(0)$, $R_{\mathrm{circ}}(0)$ and Ω and comparing them to those measured experimentally. These results are shown in table 4.2.

In all cases, values of S are close or equal to zero, indicating that excitation cannot take place upon the incidence of two photons polarised parallel to the y-axis of the co-ordinate

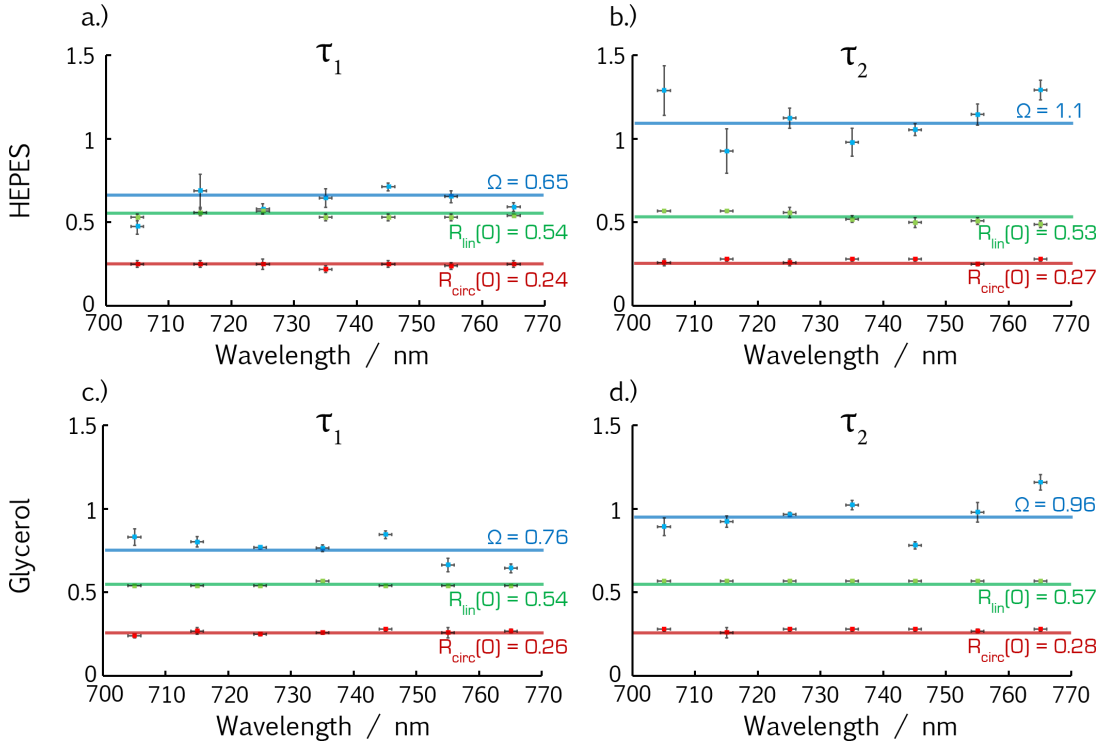

Figure 4.5: Initial anisotropies and relative emission intensities of NADPH under circularly and linearly polarised two-photon excitation as a function of wavelength.

	α_1	τ_1/ns	τ_2/ns	f_1	f_2
			NADH in HEPES		
Linear	0.75 (±0.05)	0.36 (±0.02)	0.70 (±0.05)	0.61 (±0.07)	0.39 (±0.07)
Circular	0.71 (±0.06)	0.33 (±0.03)	0.69 (±0.05)	0.55 (±0.08)	0.45 (±0.08)
			NADH in Glycerol		
Linear	0.71 (±0.02)	1.6 (±0.1)	3.2 (±0.3)	0.55 (±0.04)	0.45 (±0.04)
Circular	0.66 (±0.05)	1.5 (±0.1)	3.1 (±0.2)	0.48 (±0.06)	0.52 (±0.06)
			NADPH in HEPES		
Linear	0.81 (±0.03)	0.37 (±0.02)	0.79 (±0.06)	0.67 (±0.04)	0.33 (±0.04)
Circular	0.72 (±0.06)	0.31 (±0.02)	0.73 (±0.04)	0.53 (±0.08)	0.47 (±0.08)
			NADPH in Glycerol		
Linear	0.69 (±0.05)	1.6 (±0.1)	3.1 (±0.2)	0.53 (±0.05)	0.47 (±0.05)
Circular	0.64 (±0.02)	1.5 (±0.1)	3.0 (±0.2)	0.47 (±0.03)	0.53 (±0.03)

Table 4.1: Fluorescence decay parameters of NADH and NADPH with linearly or circularly polarised excitation averaged across all illumination wavelengths.

	Short Lifetime τ_1			Long Lifetime τ_2		
	D	S	Uncertainty	D	S	Uncertainty
			NADH			
HEPES	0.23	0.02	2.9%	0.54	0	14%
Glycerol	0.22	0	2.0%	0.57	0	15%
			NADPH			
HEPES	0.21	0.06	3.9%	0.75	0	20%
Glycerol	0.3	0	2.2%	0.57	0	16%

Table 4.2: Mean tensor elements for the short and long lifetime species of NADH and NADPH.

system in which the matrix **S** is defined. Equations 4.5 to 4.7 are derived for a co-ordinate system in which the x-axis lies along the emission transition dipole of the molecule (Wan and Johnson, 1994). Interpretation of the shapes of the two-photon transition tensors can be facilitated by diagonalising the matrices (Lakowicz, 1997). Geometrically, this corresponds to rotating the coordinate system until the xy elements of the matrix become zero. This was performed by computation of the eigenvalues and eigenvectors of the matrices in MATLAB. The matrix of eigenvalues is then the diagonal form of **S**, produced by similarity transformation with the rotation matrix defined by the eigenvectors (Weber and Arfken, 2004). The diagonal forms of the two-photon transition tensors of NAD(P)H are shown in table 4.3.

The direction of polarisation at which light is maximally absorbed defines the x-axis in the diagonal forms of the two-photon transition tensors. The absorption amplitude of light polarised in the y-direction, S_{yy}, is negligible for the short lifetime species, with its amplitude measured relative to that of the x-component averaging –0.03($\pm$0.04) across all experiments. However, this perpendicular element becomes significant for the long lifetime species, increasing in magnitude to –0.22($\pm$0.04).

For these diagonal tensors, the transition amplitude in equation 4.2 reduces to,

$$\hat{\mu} \cdot \mathbf{S} \cdot \hat{\mu} = S_{xx}\mu_x^2 + S_{yy}\mu_y^2 \tag{4.16}$$

The shapes defined by **S** can therefore be visualised in spherical polar surface plots in which equation 4.16 defines the distance from the origin to the surface. From equation 4.2, the two-photon transition rate for photons polarised in each direction is then the square of this distance. The MATLAB algorithm `plot_2p_tensor()`, included in appendix A, was

	Short Lifetime τ_1	Long Lifetime τ_2
	NADH in HEPES	
Original	$\begin{pmatrix} 1 & 0.23 \\ 0.23 & 0.02 \end{pmatrix}$	$\begin{pmatrix} 1 & 0.54 \\ 0.54 & 0 \end{pmatrix}$
Rotation Matrix	$\begin{pmatrix} -0.98 & 0.22 \\ -0.22 & -0.98 \end{pmatrix}$	$\begin{pmatrix} -0.92 & 0.40 \\ -0.40 & -0.92 \end{pmatrix}$
Rotation Angle	12.5°	23.7°
Diagonal	$\begin{pmatrix} 1.05 & 0 \\ 0 & -0.03 \end{pmatrix}$	$\begin{pmatrix} 1.24 & 0 \\ 0 & -0.24 \end{pmatrix}$
Scaled	$\begin{pmatrix} 1 & 0 \\ 0 & -0.03 \end{pmatrix}$	$\begin{pmatrix} 1 & 0 \\ 0 & -0.19 \end{pmatrix}$
	NADH in Glycerol	
Original	$\begin{pmatrix} 1 & 0.22 \\ 0.22 & 0 \end{pmatrix}$	$\begin{pmatrix} 1 & 0.57 \\ 0.57 & 0 \end{pmatrix}$
Rotation Matrix	$\begin{pmatrix} -0.98 & 0.21 \\ -0.21 & -0.98 \end{pmatrix}$	$\begin{pmatrix} -0.91 & 0.41 \\ -0.41 & -0.91 \end{pmatrix}$
Rotation Angle	12.0°	24.3°
Diagonal	$\begin{pmatrix} 1.05 & 0 \\ 0 & -0.05 \end{pmatrix}$	$\begin{pmatrix} 1.26 & 0 \\ 0 & -0.26 \end{pmatrix}$
Scaled	$\begin{pmatrix} 1 & 0 \\ 0 & -0.05 \end{pmatrix}$	$\begin{pmatrix} 1 & 0 \\ 0 & -0.20 \end{pmatrix}$
	NADPH in HEPES	
Original	$\begin{pmatrix} 1 & 0.21 \\ 0.21 & 0.06 \end{pmatrix}$	$\begin{pmatrix} 1 & 0.75 \\ 0.75 & 0 \end{pmatrix}$
Rotation Matrix	$\begin{pmatrix} -0.98 & 0.21 \\ -0.21 & -0.98 \end{pmatrix}$	$\begin{pmatrix} -0.88 & 0.47 \\ -0.47 & -0.88 \end{pmatrix}$
Rotation Angle	12.0°	28.1°
Diagonal	$\begin{pmatrix} 1.04 & 0 \\ 0 & 0.02 \end{pmatrix}$	$\begin{pmatrix} 1.40 & 0 \\ 0 & -0.40 \end{pmatrix}$
Scaled	$\begin{pmatrix} 1 & 0 \\ 0 & 0.02 \end{pmatrix}$	$\begin{pmatrix} 1 & 0 \\ 0 & -0.29 \end{pmatrix}$
	NADPH in Glycerol	
Original	$\begin{pmatrix} 1 & 0.30 \\ 0.30 & 0 \end{pmatrix}$	$\begin{pmatrix} 1 & 0.57 \\ 0.57 & 0 \end{pmatrix}$
Rotation Matrix	$\begin{pmatrix} -0.96 & 0.27 \\ -0.27 & -0.96 \end{pmatrix}$	$\begin{pmatrix} -0.91 & 0.41 \\ -0.41 & -0.91 \end{pmatrix}$
Rotation Angle	15.4°	24.3°
Diagonal	$\begin{pmatrix} 1.08 & 0 \\ 0 & -0.08 \end{pmatrix}$	$\begin{pmatrix} 1.26 & 0 \\ 0 & -0.26 \end{pmatrix}$
Scaled	$\begin{pmatrix} 1 & 0 \\ 0 & -0.08 \end{pmatrix}$	$\begin{pmatrix} 1 & 0 \\ 0 & -0.20 \end{pmatrix}$

Table 4.3: Calculation of the diagonal forms of the two-photon transition tensors of the two species of NADH and NADPH.

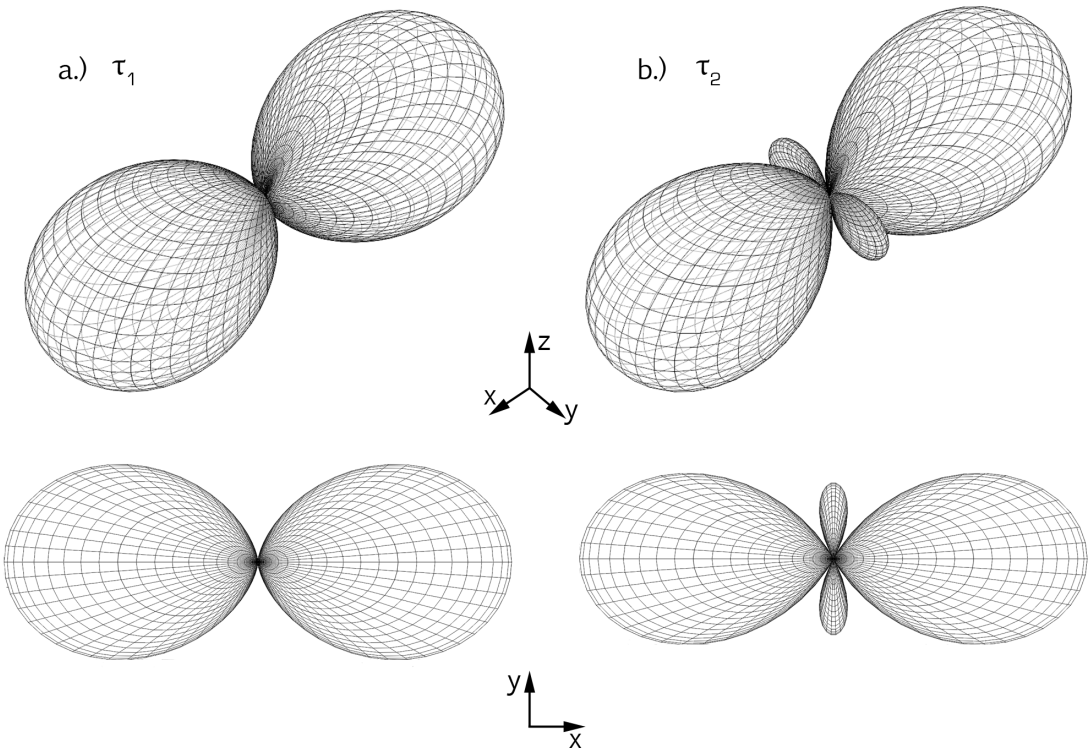

Figure 4.6: Spherical polar surfaces displaying the polarisation dependence of two-photon absorption in the short and long lifetime species of NAD(P)H.

written to produce these plots for the short and long lifetime two-photon transition tensors of NAD(P)H. These are shown in figure 4.6.

In figure 4.6b, it is clear that the transition tensor of the long lifetime species permits two-photon absorption of light polarised perpendicularly to the primary axis. Such a distribution has previously been computationally predicted for the nicotinamide moiety by Kierdaszuk et al. (1996). Their work found the corresponding x-axis of this diagonalised form to point from the oxygen to the ring nitrogen, with the transition accompanied by charge transfer from the nitrogen to the amide group. However, as seen in figure 4.6a, these perpendicular lobes appear to be reduced to insignificance in the short lifetime species. This is comparable to behaviour observed by Callis (1993) in the ^1L_b absorption band of indole, the moiety responsible for fluorescence of the amino acid tryptophan (Albinsson and Norden, 1992; Sobolewski and Domcke, 1999). In their work, similar negative lobes are present in the two-photon transition tensor of pure indole, which are then reduced significantly upon the addition of a single methyl group to the pyrole ring.

The difference in the two-photon transition tensors of the short and long lifetime species of NAD(P)H cannot be attributed by the presence of additional chemical groups. However, alternate configurations of the amide group on the nicotinamide ring could con-

tribute to their separate absorption properties. This group is known to favour the cis conformation displayed in figure 1.4 (Kumar et al., 2010). However, by overcoming an energy barrier of approximately 0.3 eV, a trans conformation can be produced in which the amide group is rotated by 180° (Wu and Houk, 1993). The two fluorescent species of NAD(P)H could therefore correspond to separate cis-trans geometries of the amide group, causing the average angle of 13(±2)° formed by the principle axis of the lobeless short lifetime tensor with the emission dipole increasing to 25(±2)° in the long lifetime species. The computational studies of Kierdaszuk et al. would need to be repeated with both conformations of nicotinamide to confirm whether this is the case.

4.4 Conclusions

The two-photon spectroscopy performed here indicates that two-photon excitation of NAD(P)H is maximised at approximately 700 nm. These results suggest the illumination wavelengths applied in previously published NAD(P)H FLIM studies are sub-optimal, with the emitted fluorescence intensity reduced by 71(±5)% at 730 nm and 94(±2)% at 800 nm, relative to the 700 nm cross section and assuming constant power. Perhaps the use of these inefficient excitation wavelengths is justified by poor stability of the laser sources at the shorter, more suitable, wavelengths. However, maintaining NAD(P)H fluorescence intensity while switching from 700 nm excitation to 730 nm would require the incident power to be almost doubled, with a further doubling of power required at 800 nm. Based on a parameterisation provided by Hopt and Neher (2001), these increased powers will cause cell damage four times sooner at 730 nm than at 700 nm, increasing to 26-times sooner at 800 nm. As maintaining the biological integrity of the model under investigation is crucial, two-photon excitation of NAD(P)H at its optimal wavelength should be encouraged.

One caveat to the use of 700 nm excitation for NAD(P)H is if other molecules are present with overlapping two-photon absorption spectra. In addition to NADH and NADPH, a number of other intrinsic fluorophores are present in tissue (Prasad, 2004) including elastin, collagen and lipofuscin (Billinton and Knight, 2001). However, the only other significant contributor to the autofluorescence of live cells is flavin (Aubin, 1979), an alternative intracellular redox carrier. The absorption cross section spectrum of flavin also peaks at 700 nm and extends further to around 1000 nm. However, emission takes place at longer wavelengths than in NAD(P)H, around 530 (±30) nm (Huang et al., 2002).

An indication of the relative brightness of two fluorophores under two-photon exci-

tation is given by the product of the quantum yield and the two-photon absorption cross section, known as the two-photon action cross section (Xu et al., 1996). At 700 nm, the two-photon action cross section of flavin is measured to be approximately 0.1 GM (Huang et al., 2002). The results presented here suggest a two-photon action cross section for free NAD(P)H at 700 nm of 0.08 GM. Using the emission spectra reported by Patterson et al. (2000) and Huang et al. (2002), and neglecting wavelength-dependent detector efficiencies, the 460(±25) nm band-pass emission filter used in the two-photon excitation microscopy performed in this work will allow capture of approximately 57% of the total NAD(P)H emission and rejection of 95% of the flavin fluorescence. With these excitation and detection conditions and the slightly larger two-photon action cross section of flavin at 700 nm, use of equation 4.10 shows that 90% of the fluorescence collected will be due to NAD(P)H if equal concentrations of the two intrinsic fluorophores are present in the tissue. However, live cells contain a larger concentration of NAD(P)H than flavin by a factor of approximately seven (Yu and Heikal, 2009; Heikal, 2010). Therefore, by illuminating a sample at the two-photon absorption maximum of NAD(P)H, the emission filtering employed in the two-photon excitation microscopy performed in this work will ensure that the detection of fluorescence from NADH and NADPH outweighs that of flavin by at least 99 to one.

Chapter 5

NAD(P)H fluorescence decay in oxidative and glycolytic cells

5.1 NAD(P)H intensity time-series

In the NAD(P)H FLIM literature, it is frequently suggested that changes in the fluorescence decay of NAD(P)H in live tissue are induced by variations in the balance of aerobic and anaerobic respiration (Skala et al., 2007a; Ghukasyan and Kao, 2009; Stringari et al., 2012a). This is based on the decreased reliance on oxidative phosphorylation known to occur in tumours (Warburg, 1956) and observation of differences in the NAD(P)H fluorescence decay arising from healthy and cancerous tissue. However, this hypothesis has never been systematically verified and no mechanism has been proposed. The experiments described in this chapter attempt to address this issue.

As a first investigation into the biochemical origin of variations in the fluorescence lifetime of NAD(P)H in live cells, FLIM was used to measure the fluorescence decay parameters of the cofactor in response to the application of treatments with known effects on energy metabolism in HeLa cells. To prepare for these experiments, the perturbations were first applied during time-series measurements of the NAD(P)H fluorescence intensity using standard confocal microscopy as described in section 2.7. This allowed the time taken for the intensity to reach a new steady state to be measured, indicating the uptake of, and response to, the applied treatment.

The treatments used in these experiments were chosen for their ability to alter the balance between mitochondrial and cytosolic NADH production. 10μM rotenone and 1μM FCCP will both decrease ATP production in the mitochondria (Duchen et al., 2003). As described in section 1.8, the mitochondrial NAD(P)H fluorescence intensity will be max-

imised or minimised by rotenone or FCCP, respectively. To alter cytosolic metabolism, the standard glucose-containing recording medium was removed from the cells and replaced by a modified version in which the glucose was replaced by 10 mM deoxyglucose, inhibiting hexokinase and therefore ATP production in the cytosol by glycolysis (Tower, 1958). 1 mM pyruvate or 10 mM lactate were then present as metabolic substrates (concentrations based on Dumollard et al. 2007).

The intensity of NAD(P)H fluorescence in response to treatment with rotenone, FCCP, pyruvate and lactate is shown in figure 5.1. Each trace is the average of three separate experiments with the perturbation applied after two minutes. In all cases, the time scale for response to the treatments is of the order of 10 minutes, evident from the observed change in the fluorescence intensity.

Also plotted in figure 5.1 is the standard deviation of the distribution of pixel intensities in response to the treatments. In these images, the brightest pixels were the punctate regions of mitochondrial fluorescence, with the lowest intensities measured in the nuclei. Rotenone treatment did not affect the spread of the distribution of pixel intensities, suggesting increased cytosolic and nuclear fluorescence intensity in addition to the expected increase in the mitochondria. FCCP did induce a change in the spread of intensity values present, with the observed decrease in the standard deviation to mean ratio expected if the oxidation of the NAD^+/NADH pool is primarily localised to the mitochondria. Smaller (10%) decreases in this ratio were induced by the inhibition of glycolysis. If the sole effect of this treatment was to decrease the rate of reduction of NAD^+ in the cytosol while maintaining a constant rate of metabolism in the mitochondria, an increase in this quantity would be expected. However, the measured decrease must indicate a lowering of mitochondrial NAD(P)H fluorescence alongside that of the cytosol, suggesting a decreased supply of citric acid cycle substrates upon transition from recording medium containing 25 mM glucose to analogues containing lower concentrations of pyruvate and lactate.

5.2 Simulations of live-cell NAD(P)H fluorescence decays

As discussed in section 1.13, published FLIM studies in live cells and tissues typically resolve two components in the fluorescence decay of NAD(P)H. With the fluorescence from freely-diffusing NAD(P)H alone decaying biexponentially and its lifetime increasing by various factors upon binding to different enzymes (table 1.1), the true distribution of species present in live tissue is likely to be more heterogeneous. To understand how changes in

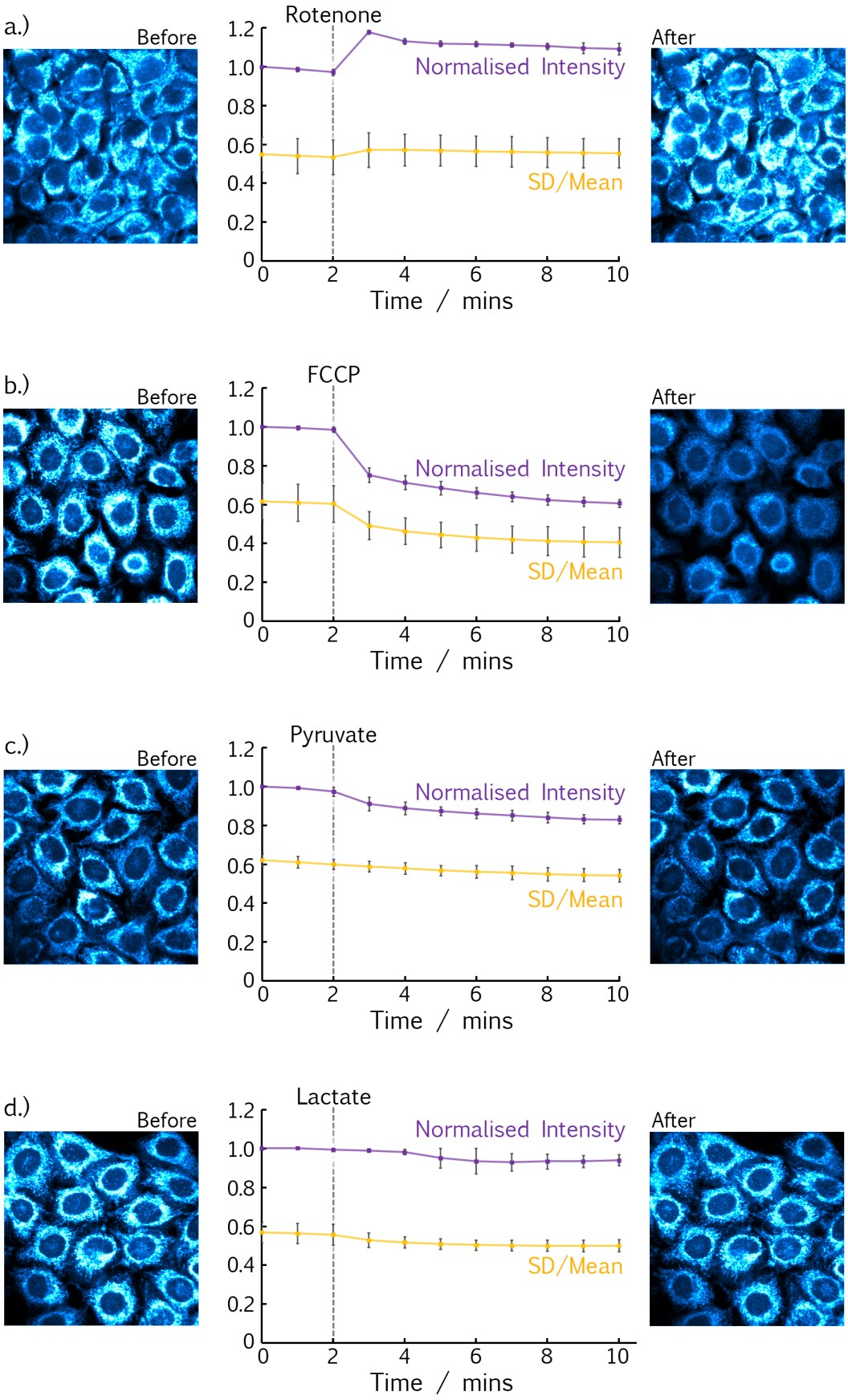

Figure 5.1: Time-series measurements of the NAD(P)H fluorescence intensity at one minute intervals following metabolic perturbation of HeLa cells. The standard deviation of the distribution of pixel intensities within the cells relative to its mean is also plotted.

the underlying distribution of species is reflected in the simplified fluorescence decays measured using FLIM, computational simulations were performed using the methods described in section 2.5 prior to making experimental measurements of NAD(P)H fluorescence lifetimes in live cells.

As the signal to noise ratio of a photon counting experiment scales as the square root of the number of photons counted, the quality of fits to NAD(P)H fluorescence decays were investigated as a function of the amount of signal collected. Fluorescence decays were generated based on the distribution shown in figure 2.4. From the results of Skala et al. (2007a), α_{bound} was taken as 0.3. Each bound species (1 ns to 6 ns) was present in equal proportion and the relative 0.3 ns and 0.7 ns amplitudes were based on those measured in the previous chapter, giving $\alpha_{0.3} = 0.7\left(1 - \alpha_{\text{bound}}\right)$, $\alpha_{0.7} = 0.3\left(1 - \alpha_{\text{bound}}\right)$.

In these simulations, the signal level is input as the desired number of photon counts in the peak bin, I_0. This value is related to the total number of photons counted by,

$$I_{\text{total}} = I_0 \sum_{i=0}^{255} \sum_{j} \alpha_j \exp\left(-\frac{i\,\Delta t}{\tau_j}\right) \tag{5.1}$$

where j represents each species and Δt is the spacing between each of the 256 time bins of the TCSPC setup used for FLIM in this work. For an excitation laser with repetition rate 80 MHz, the maximum count rate permissible for TCSPC is 800 kHz. This corresponds to an average count rate of 12 counts per pixel per second for a 256x256 image. The double-sum term in equation 5.1 is equal to 27 for the lifetime distribution applied here. I_0 at each pixel, assuming the maximum possible count rate, is therefore equal to the total imaging time in seconds multiplied by 0.46. Thus, acquisition times of the order of minutes will measure fluorescence decays at each pixel with 10^1 to 10^2 counts in the peak bin. As this is insufficient signal for the accurate fitting of decay curves (Moger et al., 2006; Becker, 2012), the fluorescence decay at a given pixel in a FLIM experiment is frequently composed of the sum with all surrounding pixels (Skala et al., 2007a; Becker, 2012). This is known as binning, and amounts to increasing the time accuracy of the experiment at the expense of spatial resolution. The counts in the peak bin of the fluorescence decays at each pixel will be increased by an order of magnitude by binning direct neighbours. Peak bin levels were therefore varied between 100 and 1000 in these simulations.

Figure 5.2a shows an attempt to fit a single exponential decay to a simulated NAD(P)H fluorescence decay with a signal level of 1000 peak bin counts. It is clear from the residual

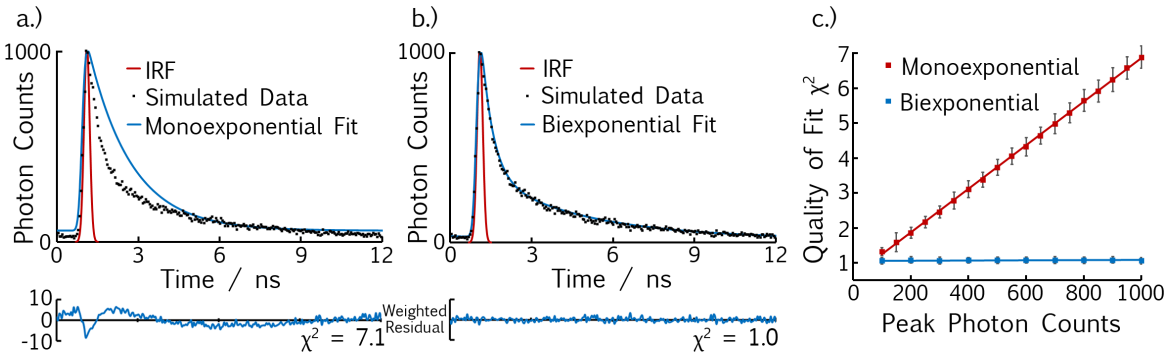

Figure 5.2: Fits of a monoexponential (a) and biexponential (b) model to a single simulated fluorescence decay. Repeating this process 100 times at each signal level illustrates the dependence of fit quality on I_0 for the two models (c).

trace that this model is a poor fit for the data. Increasing the number of lifetime components to two, shown in figure 5.2b, improved the quality-of-fit parameter χ_r^2 from 7.1 to 1.0. Any differences between the data and a biexponential model are therefore attributable to Poisson noise, indicating a perfect fit. This fitting process was repeated on datasets with peak count values of between 100 and 1000 at 100-count intervals. 100 unique decays were generated at each signal level. As can be seen in figure 5.2c, a monoexponential model becomes a poorer description of the data as the signal level is increased. However, across the whole range of signal levels possible by imaging at the maximum possible count rate with realistic acquisition times (0.5 to 4 minutes), a biexponential model is a good fit. Addition of more lifetime components would not improve the quality of the biexponential fits further within this range, explaining why only two lifetime components are typically resolved in the pixel-wise NAD(P)H fluorescence decays measured using FLIM.

The decay parameters recovered from the series of signal-dependent biexponential fits are shown in figure 5.3a. The mean values of τ_{free} and τ_{bound} extracted from the fits to the simulated fluorescence decays remain close to the α-weighted mean values of the free and enzyme-bound lifetime components of the synthetic data, 0.42 ns and 3.5 ns respectively. However, in figure 5.3b it can be seen that, at the lowest signal levels, the standard deviation of the 100 lifetime values extracted increases dramatically, despite each simulated fluorescence decay being based on the same underlying distribution of species. This demonstrates the significant influence of Poisson noise in the fluorescence decays at these low signal levels. These results show that taking a mean across a region of interest, rather than taking values from the fluorescence decay at a single pixel, provides a reliable measure of the true free and enzyme-bound lifetime components in an NAD(P)H FLIM

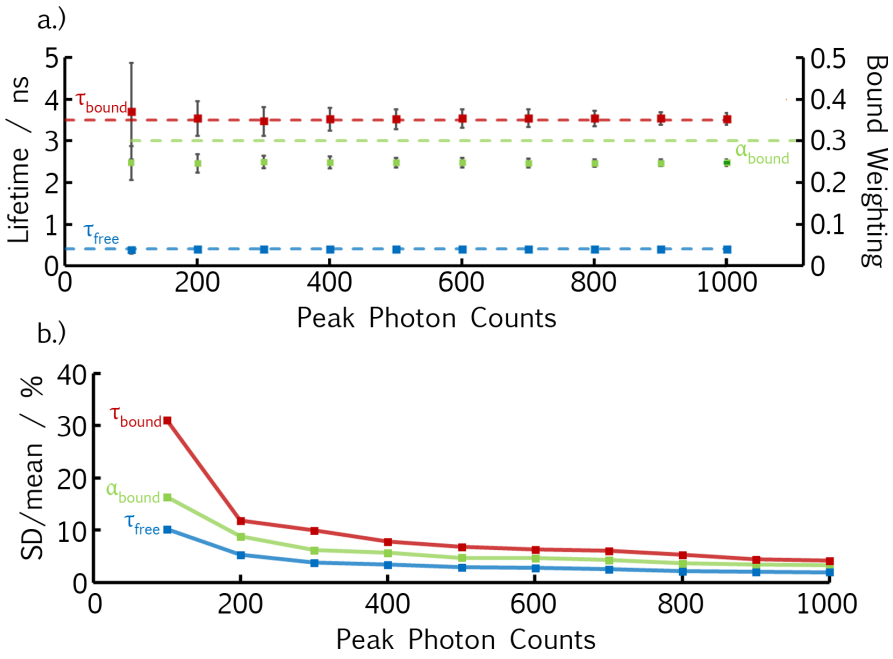

Figure 5.3: (a) Variation in the best-fit parameters of NAD(P)H fluorescence decays simulated at signal levels accessible using FLIM. Blue and red dashed lines represent the α-weighted mean values of the free and enzyme-bound species respectively. The green dashed line lies at the true α_{bound} value of the lifetime distribution. (b) A larger spread of values is obtained for each parameter as the signal level is decreased.

experiment.

While the two lifetimes fit to the simulated NAD(P)H fluorescence decays agree with the α-weighted means of the free and enzyme-bound species present, confirming the validity of labelling these components τ_{free} and τ_{bound}, the values of α_{bound} consistently underestimate the true fraction of bound species input into the lifetime distribution. The mean value of the fits across the signal levels is 0.25, whereas the true value in the distribution of species is 0.3. In light of this underestimation by the fitting process, α_{bound} should not be used as an exact measure of the fraction of NAD(P)H bound to an enzyme for drawing biochemical conclusions.

To investigate how a change in the distribution of the bound lifetime species present in the simulated data is manifested in the measured τ_{bound}, simulations were performed in which the amplitudes of the 2 ns and 5 ns components, α_{short} and α_{long} respectively, were varied with respect to one-another at a series of fixed α_{bound} values. A schematic diagram of this modified distribution is shown in figure 5.4a. Again, 100 simulations were performed for each set of parameters. As shown in figure 5.4b, the measured τ_{bound} decreases linearly as α_{short} is increased from zero to α_{bound}. By assigning the minimum and maximum lifetimes measured for each α_{bound} value as τ_{short} and τ_{long}, the equation for these straight

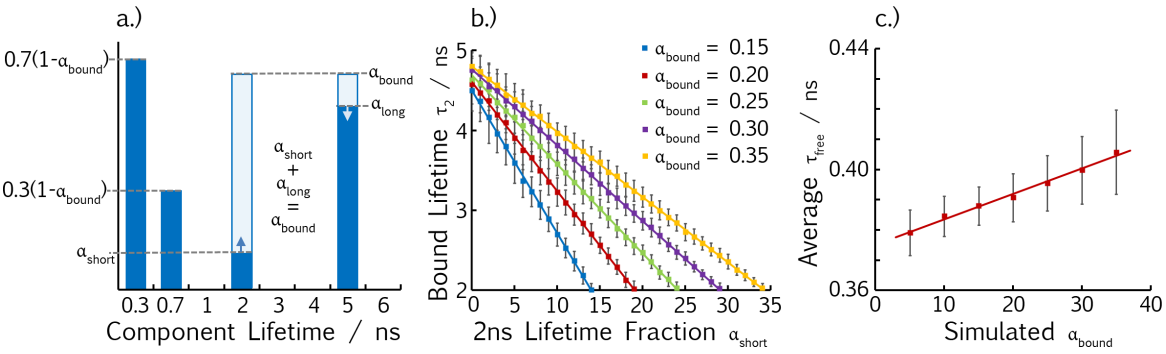

Figure 5.4: Increasing the presence of the 2 ns bound component at the expense of the 5 ns bound component in the distribution of NAD(P)H species, as shown in (a), decreases the measured enzyme-bound lifetime linearly (b). A positive correlation can be identified between the α_{bound} input into the simulations and the value of τ_{free} extracted through fitting (c).

lines can be written,

$$\tau_{\text{bound}} = \left(\frac{\tau_{\text{short}} - \tau_{\text{long}}}{\alpha_{\text{bound}}} \right) \alpha_{\text{short}} + \tau_{\text{long}} \tag{5.2}$$

Knowledge of τ_{short} and τ_{long} can therefore be used to calculate the ratio $\alpha_{\text{short}}/\alpha_{\text{bound}}$ given a measurement of τ_{bound}.

While analysing the effect of varying the weightings of the bound NAD(P)H species in the simulated data on the measured values of τ_{bound}, it was observed that changes in α_{bound} were positively correlated with the observed values of τ_{free}. The mean τ_{free} value, averaged across all α_{short} and α_{long} values at constant α_{bound}, increased as the proportion of the total NAD(P)H fluorescence consisting of enzyme-bound species was increased, as shown in figure 5.4c. This suggests that part of the fluorescence arising from the 2 ns and 5 ns components is being assigned to the shorter component of the biexponential fit. This perhaps explains why α_{bound} underestimates the true fraction of bound species present. It is likely that these effects would be enhanced if intracellular conditions caused the 0.7 ns free NAD(P)H species to be present in a larger proportion than in aqueous solution.

5.3 NAD(P)H fluorescence decay in subcellular compartments

To investigate whether shifts between cytosolic and mitochondrial catabolism affect the NAD(P)H fluorescence lifetimes measured in live cells, fluorescence lifetime images of NAD(P)H in HeLa cells were taken under control conditions and following the same treatments as in section 5.1. In accordance with the results displayed in figure 5.1, imaging was performed at least 10 minutes after the addition of each treatment.

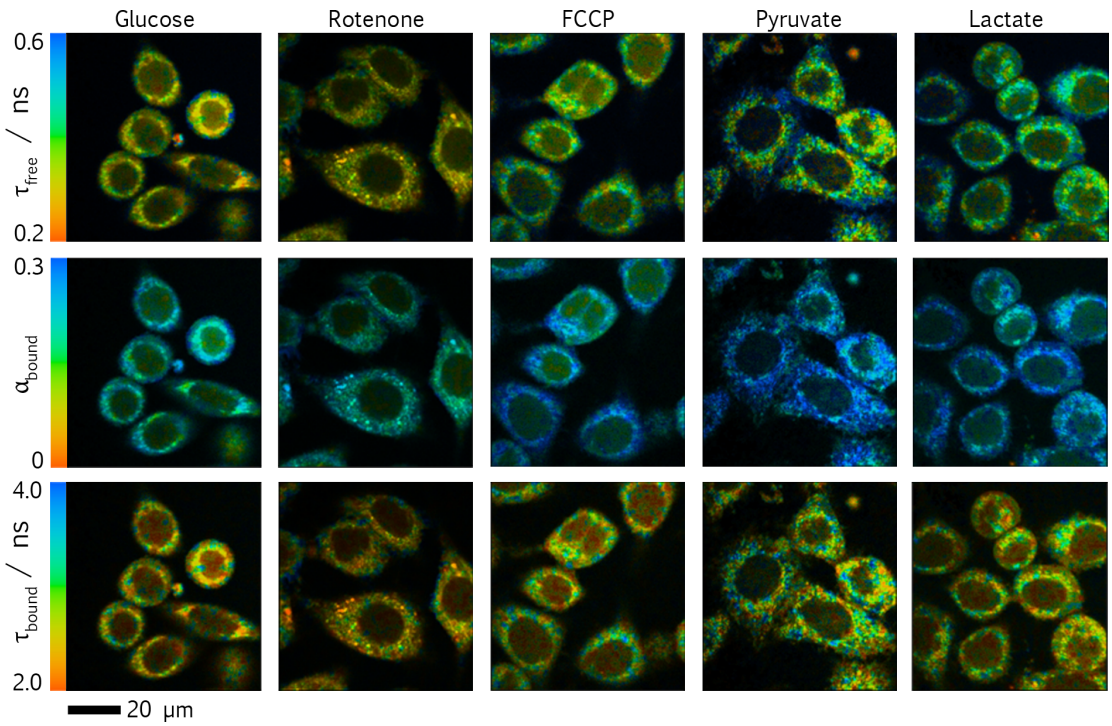

Figure 5.5: Typical NAD(P)H FLIM images of HeLa cells in response to treatments chosen to perturb ATP production.

Upon loading the FLIM images acquired into SPCImage, it was observed that binning photon counts of the eight surrounding pixels resulted in only 50 to 75 counts in the peak bin of fluorescence decays within the darkest regions of the cell (the nuclei). Based on the results of the previous section, such regions have insufficient signal for the accurate fitting of the two-component fluorescence decays fit to the rest of the image. Binning was therefore increased to 24 surrounding pixels (five by five square) across the whole image. This resulted in a more suitable 150 to 200 counts in the peak bin of dark regions and 500 to 600 in the brightest regions. These settings were applied to all subsequent FLIM experiments.

After fitting a biexponential decay at each pixel, the average χ_r^2 value was 1.2, compared to 3.9 for a monoexponential, justifying the use of this model. The mean values of the parameters τ_{free}, α_{bound} and τ_{bound} in each image were extracted separately for NAD(P)H fluorescence arising from mitochondrial, cytosolic or nuclear regions using the masking technique described in section 2.8. This would allow the identification of any characteristic differences that exist between the fluorescence decay of NAD(P)H in each subcellular compartment in response to the applied treatments. The results are shown in figures 5.5 and 5.6 and detailed in table 5.1.

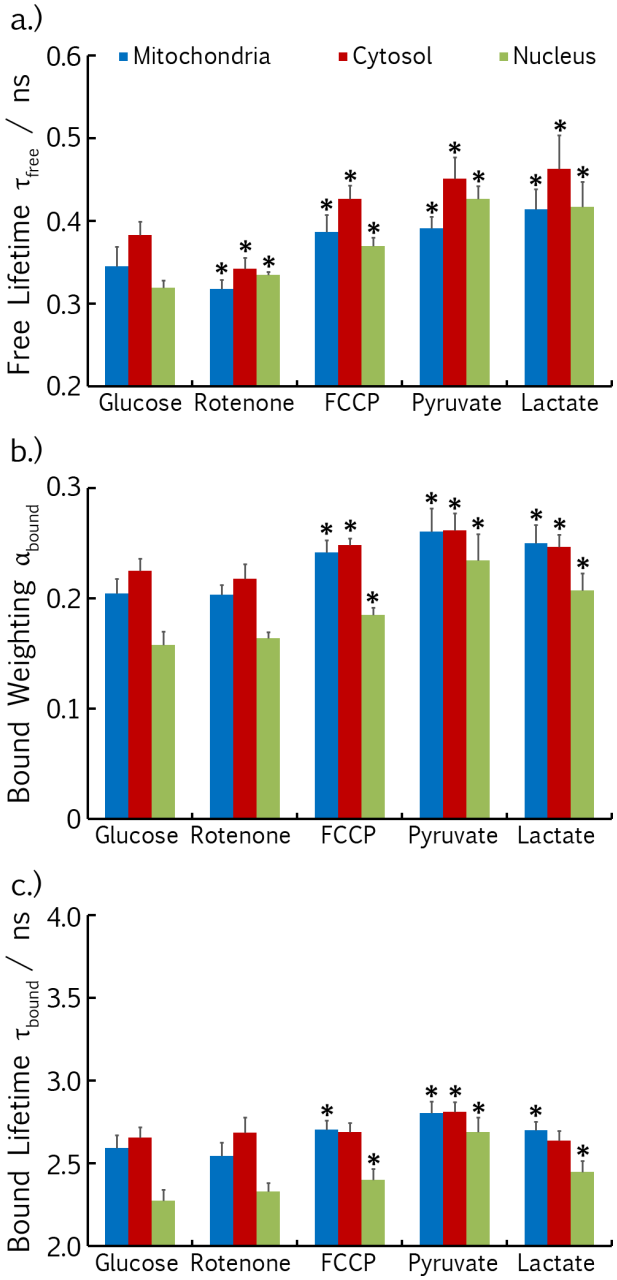

Figure 5.6: Values of the NAD(P)H fluorescence decay parameters (a) τ_{free}, (b) α_{bound} and (c) τ_{bound} measured in the mitochondrial (blue bars), cytosolic (red bars) and nuclear (green bars) compartments of HeLa cells in response to treatments chosen to perturb ATP production. Stars indicate statistically significant (P<0.05) differences relative to the corresponding compartment under control (glucose) conditions.

	τ_{free}/ns			α_{bound}			τ_{bound}/ns			$\langle I_{total} \rangle$/au			C_{free}/au			C_{bound}/au		
	M	C	N	M	C	N	M	C	N	M	C	N	M	C	N	M	C	N
Glucose	0.34	0.38	0.32	0.20	0.22	0.16	2.59	2.66	2.27	1.7	1.0	1.0	2.0	1.0	1.5	0.5	0.3	0.3
±	0.02	0.02	0.01	0.01	0.01	0.01	0.08	0.06	0.07	0.3	0.2	0.1	0.3	0.2	0.2	0.4	0.2	0.2
Rotenone	0.32	0.34	0.33	0.20	0.22	0.16	2.54	2.7	2.33	2.2	1.3	0.9	2.6	1.4	1.3	0.7	0.4	0.3
±	0.01	0.01	0.01	0.01	0.01	0.01	0.08	0.1	0.04	0.3	0.2	0.2	0.3	0.2	0.2	0.4	0.2	0.2
FCCP	0.39	0.43	0.37	0.24	0.25	0.18	2.70	2.69	2.40	1.1	0.7	0.59	1.0	0.6	0.74	0.3	0.2	0.2
±	0.02	0.02	0.01	0.01	0.01	0.01	0.05	0.03	0.06	0.2	0.1	0.07	0.2	0.1	0.09	0.2	0.1	0.1
Pyruvate	0.39	0.45	0.43	0.26	0.26	0.23	2.80	2.81	2.7	0.9	0.43	0.39	0.78	0.34	0.36	0.3	0.12	0.11
±	0.01	0.03	0.02	0.02	0.02	0.02	0.07	0.06	0.1	0.1	0.09	0.09	0.09	0.07	0.08	0.1	0.07	0.09
Lactate	0.41	0.46	0.42	0.25	0.25	0.21	2.70	2.64	2.45	1.3	0.6	0.51	1.1	0.6	0.6	0.4	0.2	0.2
±	0.02	0.04	0.03	0.02	0.01	0.02	0.04	0.04	0.07	0.3	0.2	0.09	0.2	0.2	0.1	0.2	0.2	0.1

Table 5.1: Average NAD(P)H fluorescence decay parameters in subcellular compartments of HeLa cells in response to treatments chosen to perturb ATP production. Values are averages from at least three separate regions of three separate coverslips. Concentrations are calculated from the measured parameters using equations 5.4 and 5.5.

Under control conditions, there are significant differences in the values of τ_{free} and α_{bound} in the mitochondria, cytosol and nucleus of HeLa cells. Both parameters are largest in the cytosol, at 0.38(±0.02) ns and 0.22(±0.01) respectively, and smallest in the nucleus, at 0.32(±0.01) ns and 0.16(±0.01). The average fluorescence lifetime of enzyme-bound species is the same in the mitochondria and cytosol, averaging 2.60(±0.10) ns. However, τ_{bound} is significantly smaller in the nucleus, at 2.27(±0.07) ns.

Both rotenone and FCCP treatment represent methods for decreasing ATP production in the mitochondria. However, the NAD(P)H fluorescence decay parameters respond in opposing manners following their application to the cells. Rotenone caused small (0.03 ns) decreases in τ_{free} in the mitochondria and cytosol relative to their values under control conditions, while α_{bound} and τ_{bound} remained constant. In contrast, treatment with FCCP caused τ_{free} and α_{bound} to increase slightly in each compartment, averaging 0.05(±0.01) ns and 0.03(±0.01) respectively. 0.1 ns increases in τ_{bound} were also observed in the mitochondria and nucleus. These contrasting responses to two distinct methods for perturbing mitochondrial metabolism (electron transport chain inhibition and uncoupling) suggests that changes in the fluorescence decay of NAD(P)H in diseased tissue are mechanism-specific, and do not generically represent a downregulation of mitochondrial ATP production.

Replacement of the control recording medium with one containing deoxyglucose allowed measurement of the fluorescence decay of NAD(P)H upon the inhibition of cytosolic ATP production. Pyruvate or lactate was provided to maintain mitochondrial ATP synthesis. Pyruvate caused both τ_{free} and α_{bound} to increase significantly, with the largest increases observed in the nucleus. In the presence of lactate rather than pyruvate, similar increases in τ_{free} were observed across all compartments. Although of a smaller magnitude than those caused by pyruvate, increases in α_{bound} were also observed, suggesting a correlation between inhibition of cytosolic ATP production and increased values of τ_{free} and α_{bound}. The enzyme-bound lifetimes in the presence of lactate were smaller than those induced by the supply of pyruvate. The largest changes in τ_{bound} for both substrates are observed in the nucleus, increasing by 0.17 ns and 0.41 ns to 2.45(±0.07) ns and 2.69(±0.09) ns with lactate and pyruvate respectively. In the cytosol, supply of lactate left τ_{bound} unchanged. However, pyruvate caused its value to increase by 0.2 ns to 2.80(±0.10) ns relative to control. Outside the mitochondria, these two substrates have opposing redox effects on

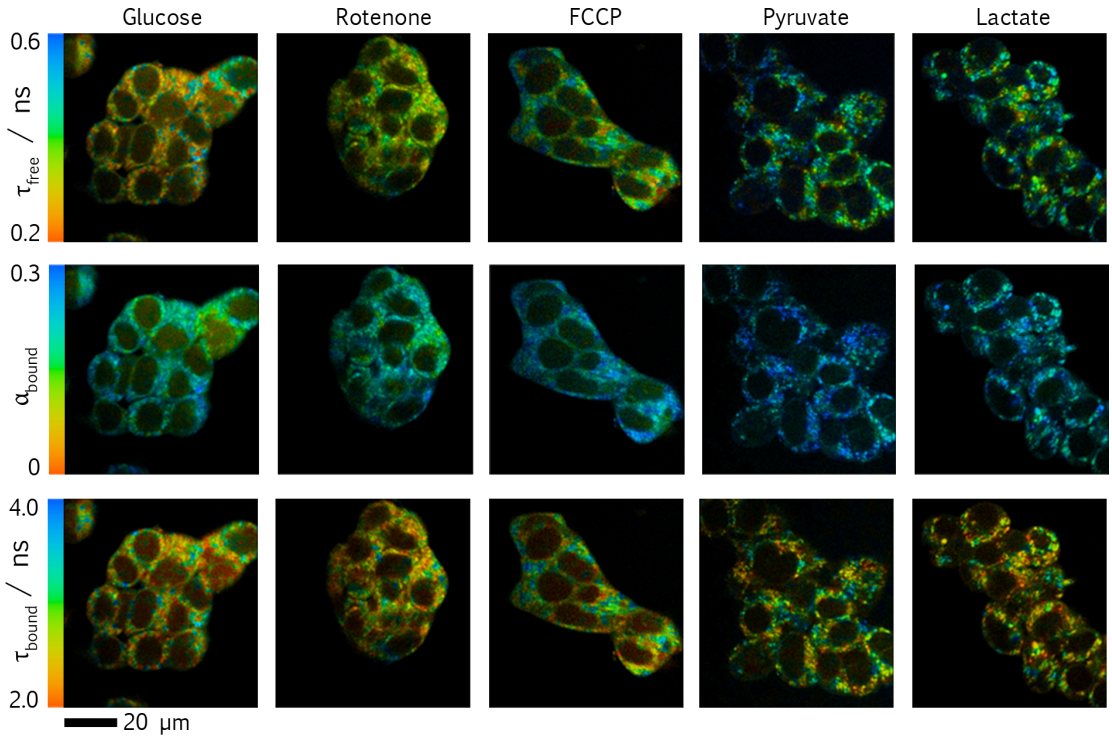

Figure 5.7: Typical NAD(P)H FLIM images of HEK293 cells in response to treatments chosen to perturb ATP production.

the NAD^+/NADH pool. In the absence of glycolysis, this is determined by the direction of the reaction catalysed by lactate dehydrogenase. Lactate will cause reduction of the pool, whereas pyruvate will cause its oxidation. These results could therefore indicate a positive correlation between τ_{bound} and the NAD^+ to NADH ratio.

To examine whether the observed differences between the NAD(P)H fluorescence decay parameters are typical responses to each treatment or are specific to HeLa cells, the experiment was repeated using HEK293 cells. The results are shown in figures 5.7 and 5.8 and table 5.2. Under control conditions, only one difference in the compartmentalised NAD(P)H fluorescence decay parameters between HEK293 cells and HeLa cells is observed. This is the significantly lower cytosolic value of α_{bound} in the HEK293's, at 0.18($\pm$0.01) compared to 0.22($\pm$0.01). In contrast to HeLa cells, no difference is observed between τ_{free}, α_{bound} and τ_{bound} in the mitochondria and cytosol of HEK293 cells. This implies that the slight differences in the parameters measured previously are characteristic of the HeLa cell type and do not, therefore, represent inherent differences in the fluorescence decay of mitochondrial and cytosolic NAD(P)H. One feature common to both HeLa and HEK293 cells is in the fluorescence decay of nuclear NAD(P)H. Again, the values of α_{bound} and τ_{bound} are significantly lower in this region than in the other compartments.

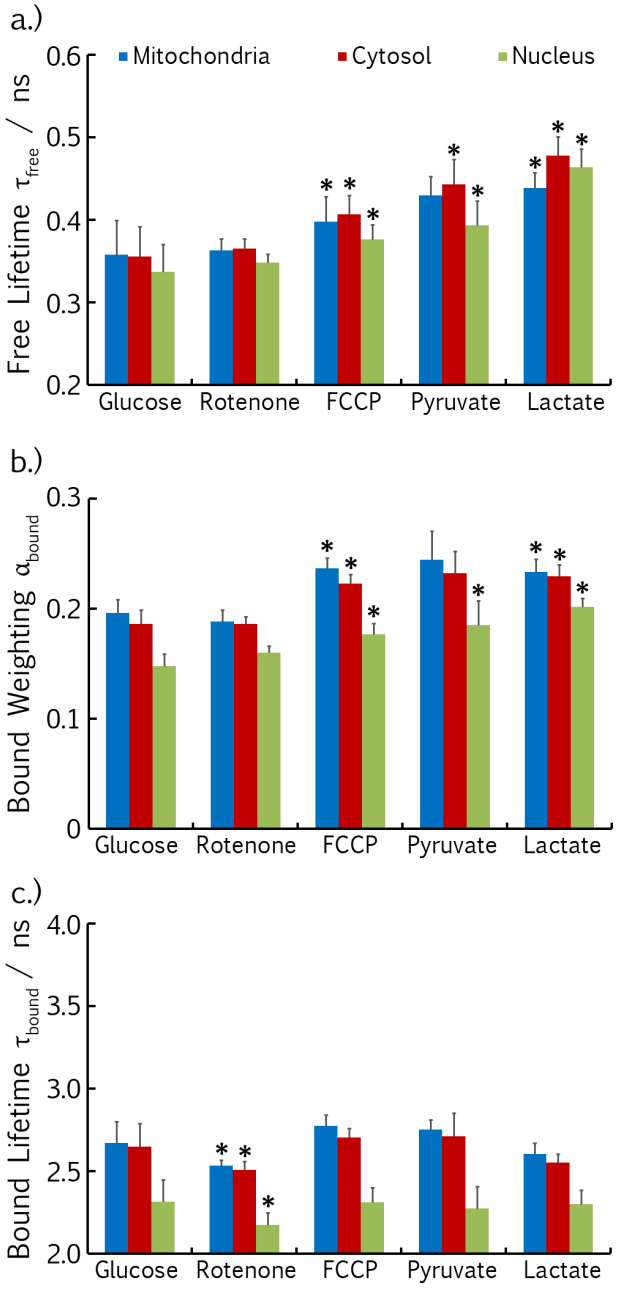

Figure 5.8: NAD(P)H fluorescence decay parameters of HEK293 cells in response to treatments chosen to perturb ATP production.

	τ_{free}/ns			α_{bound}			τ_{bound}/ns			$\langle I_{\text{total}} \rangle$/au			C_{free}/au			C_{bound}/au		
	M	C	N	M	C	N	M	C	N	M	C	N	M	C	N	M	C	N
Glucose	0.36	0.36	0.34	0.19	0.19	0.15	2.7	2.7	2.3	1.6	1.0	0.7	1.5	1.0	0.9	0.4	0.2	0.2
±	0.04	0.04	0.03	0.01	0.01	0.01	0.2	0.1	0.2	0.3	0.3	0.2	0.3	0.3	0.3	0.4	0.3	0.3
Rotenone	0.36	0.36	0.35	0.19	0.19	0.16	2.53	2.51	2.17	1.1	0.63	0.36	1.2	0.6	0.45	0.3	0.2	0.09
±	0.01	0.01	0.01	0.01	0.01	0.01	0.03	0.05	0.07	0.2	0.09	0.06	0.2	0.1	0.07	0.2	0.1	0.08
FCCP	0.40	0.41	0.38	0.24	0.22	0.18	2.77	2.70	2.31	0.8	0.38	0.26	0.6	0.31	0.28	0.2	0.09	0.06
±	0.03	0.02	0.02	0.01	0.01	0.01	0.07	0.05	0.09	0.2	0.07	0.04	0.1	0.05	0.05	0.1	0.06	0.05
Pyruvate	0.43	0.44	0.39	0.24	0.23	0.18	2.75	2.7	2.3	0.47	0.17	0.09	0.34	0.13	0.09	0.11	0.04	0.02
±	0.02	0.03	0.03	0.03	0.02	0.02	0.06	0.1	0.1	0.03	0.04	0.02	0.03	0.03	0.02	0.03	0.04	0.03
Lactate	0.44	0.48	0.46	0.23	0.23	0.20	2.60	2.55	2.30	0.71	0.25	0.14	0.6	0.20	0.12	0.17	0.06	0.03
±	0.02	0.02	0.02	0.01	0.01	0.01	0.07	0.05	0.08	0.14	0.05	0.02	0.1	0.04	0.02	0.11	0.04	0.02

Table 5.2: Average NAD(P)H fluorescence decay parameters in subcellular compartments of HEK293 cells in response to treatments chosen to perturb ATP production.

Under the same metabolic perturbations, the significant responses in τ_{bound} are inverted in the HEK293 cells relative to those present in the HeLa cells. In HeLa cells, treatment with FCCP, pyruvate and lactate caused τ_{bound} to increase in the majority of subcellular compartments and rotenone caused no change in this parameter. In HEK293 cells, however, rotenone is the only treatment causing a change in τ_{bound}, inducing a decrease of 0.14(±0.01) ns, averaged across all compartments. As rotenone causes the reduction of the mitochondrial NAD^+/NADH pool, this response supports the hypothesis that τ_{bound} is somehow proportional to the NAD^+ to NADH ratio. However, the other treatments would also cause variations in this quantity, yet the change in τ_{bound} induced by rotenone is the only one observed.

The specific values of τ_{free}, α_{bound} and τ_{bound} in response to each treatment are similar in the two cell types, with the parameter values differing by under 10% in most compartments. These differences are similar in magnitude to the uncertainties in the values themselves. The only exception to this is in the nuclear response to pyruvate. In HEK293 cells, α_{bound} increases from 0.15(±0.01) to 0.18(±0.02) and τ_{bound} remains constant at 2.3(±0.1) ns. In contrast, HeLa cells show a larger increase of α_{bound} from 0.16(±0.01) to 0.23(±0.02), accompanied by a significant increase in τ_{bound} from 2.27(±0.07) ns to 2.69(±0.09) ns. The primary goal of this research is to be able to draw conclusions regarding metabolic differences between the two cell types from variations such as these. However, the lack of obvious systematic change in the parameters describing the fluorescence decay of NAD(P)H in response to perturbation of the oxidative and glycolytic pathways makes forming an explanatory framework not possible from this data alone.

The interpretation of fluorescence lifetime data can be aided by the incorporation of fluorescence intensity data into the analysis (Vishwasrao et al., 2005; Yu and Heikal, 2009). The time-averaged fluorescence intensity in response to the treatments can easily be recovered from the fluorescence decays at each pixel by integration in the absence of binning. This data, shown in tables 5.1 and 5.2, displays a correlation between the intensity changes and the parameters τ_{free} and α_{bound}. In response to FCCP, pyruvate and lactate, the general trend across both cell types was for τ_{free} and α_{bound} to increase. These treatments are also those that cause a decrease in the fluorescence intensity. To investigate this association, the fluorescence intensities and α_{bound} values in response to the treatments were used to calculate the implied changes in the absolute concentrations of each NAD(P)H species, C_{free}

and C_{bound}. The fraction of bound species present is related to these concentrations by,

$$\alpha_{\text{bound}} = \frac{C_{\text{bound}}}{C_{\text{free}} + C_{\text{bound}}} = \frac{1}{1 + \frac{C_{\text{free}}}{C_{\text{bound}}}} \tag{5.3}$$

Variations in α_{bound} in response to a treatment therefore depend on the relative changes in the concentrations of free and bound NAD(P)H species; an increase in α_{bound} can be induced by both an increase in C_{bound} or a decrease in C_{free}. Equation 4.14 allows the detected intensity to be separated into the contributions from the free and bound lifetime components based on the measured τ_{free}, α_{bound} and τ_{bound} values. Substituting this into equation 4.8, the concentrations of each species in a compartment can be calculated by,

$$C_{\text{free}} = k \frac{\left(1 - \alpha_{\text{bound}}\right) \left\langle I_{\text{total}} \right\rangle}{\left(1 - \alpha_{\text{bound}}\right) \tau_{\text{free}} + \alpha_{\text{bound}} \tau_{\text{bound}}} \tag{5.4}$$

$$C_{\text{bound}} = k \frac{\alpha_{\text{bound}} \left\langle I_{\text{total}} \right\rangle}{\left(1 - \alpha_{\text{bound}}\right) \tau_{\text{free}} + \alpha_{\text{bound}} \tau_{\text{bound}}} \tag{5.5}$$

The calculated values of C_{free} and C_{bound} are shown in tables 5.1 and 5.2 where the proportionality constant k was chosen for each cell type such that the concentration of free NAD(P)H in the cytosol under control conditions is 1 au. The assumption that the value of k is the same in all measurements is only valid if the excitation and detection conditions, such as laser power and acquisition time, are held constant (Yu and Heikal, 2009), as they were here.

In response to treatments causing the overall NAD(P)H fluorescence intensity to decrease, the percentage changes in C_{free} are larger than those in C_{bound}, typically by 5-10%. The association between decreases in the fluorescence intensity and increases in α_{bound} could therefore result from the concentration of free NAD(P)H species varying to a greater extent upon the application of a treatment than the concentration of bound species. Perhaps the concentration of NAD(P)H-binding enzymes remains relatively constant while the concentration of free NAD(P)H is able to change significantly over the time scale at which these perturbations take effect. This interpretation partially supports the previous suggestion that α_{bound} is proportional to the redox ratio of the total NAD(P)+/NAD(P)H pool (Bird et al., 2005). If the concentration of free NAD(P)H changes in response to acute perturbation to a greater extent than the concentration of bound NAD(P)H, the direction of change of α_{bound} will indicate the direction of change of the NAD(P)+/NAD(P)H redox

ratio. However, this interpretation would not be applicable for comparing the redox ratio in different cell types or different regions of the same cell where the concentrations of NAD(P)H-binding enzymes and total sizes of the NAD(P)+/NAD(P)H pools may vary.

Each significant change in the value of α_{bound} measured so far is accompanied by a proportional change in τ_{free}. The computational simulations of the biexponential fitting process in NAD(P)H FLIM experiments showed that this apparent dependence could result from fitting error rather than it reflecting a change in a biochemical characteristic of the system being studied. The changes in τ_{free} observed experimentally were larger than those seen in the simulations. However, this could be due to the absence of enzyme-bound lifetime components shorter than 2ns being present in that part of the simulation work. The presence of enzyme-bound components closer in lifetime to the free species, as have been shown to exist in live tissue by fluorescence anisotropy microscopy studies (Vishwasrao et al., 2005), is likely to enhance the dependence of τ_{free} on α_{bound}.

Given that the fraction of enzyme-bound NAD(P)H species appears to vary proportionally to the NAD(P)+/NAD(P)H redox ratio upon acute application of perturbations to NAD(P)H metabolism, a decrease in α_{bound} would be expected upon treatment with an electron transport chain inhibitor such as rotenone. Indeed, this is seen in other work (Ye et al., 2007; Gehlsen et al., 2012). However, no change was observed upon application of rotenone to the cells here. It is likely that this is a side effect of the experimental protocol, devised for measurement of the fluorescence decay parameters with high accuracy. Allowing 10 minutes after application of the drug before the first image was taken and imaging each coverslip at least three times with four minute collection times meant that some images were taken after the cells had been exposed to rotenone for more than 30 minutes. Nonspecific damage could therefore occur to the cells as chronic exposure to rotenone is known to cause increased production of reactive oxygen species (Li et al., 2003). This is particularly likely to have occurred in the HEK293 cells where the concentrations of both free and bound NAD(P)H species are calculated to have decreased during the delay between treatment and imaging. In the next section, therefore, a more subtle approach to switching between oxidative and glycolytic metabolism is introduced, permitting further investigation into the characteristics of NAD(P)H fluorescence decay in live cells in which these separate pathways are utilised.

5.4 NAD(P)H FLIM response to forced oxidative metabolism

Immortalised cell lines typically display an extreme dependence on ATP production by the breakdown of glucose to lactate in glycolysis, bypassing the possibility of further processing in the mitochondria (Marroquin et al., 2007). In HeLa cells, at least 80% of the glucose present in the growth medium is metabolised to lactate, with only 5% entering the citric acid cycle (Reitzer et al., 1979). This inhibition of aerobic respiration by enhanced cytosolic glucose metabolism, known as the Crabtree effect (Ibsen, 1961), can be reversed by instead choosing galactose as the primary sugar source in the growth medium (Gohil et al., 2010). Although galactose can enter glycolysis and the pentose phosphate pathway by conversion to glucose 6-phosphate in the LeLoir pathway (Berg et al., 2011), cells grown in medium where glucose has been replaced by galactose exhibit decreased lactate release and an increased rate of oxygen consumption (Gohil et al., 2010), fueled by increased uptake of glutamine into the citric acid cycle (Reitzer et al., 1979). ATP production rates in galactose-fed cells display enhanced susceptibility to rotenone and FCCP (Marroquin et al., 2007), providing further evidence for their increased dependence on mitochondrial metabolism. Separate cell lines fed glucose or galactose therefore represent an ideal model for the comparison of NAD(P)H fluorescence decay parameters in aerobically and anaerobically respiring cells.

HeLa cells were cultured in normal growth medium as in the previous experiments before being grown on coverslips in a six-well plate. Here, the normal growth medium was replaced by one of two custom-made equivalents. These were produced using DMEM base powder containing the same components as the normal growth medium with the exception of sugars. Half of the coverslips were grown in the presence of 25 mM glucose, with the other half grown in medium containing 10 mM galactose. The cells were incubated under these conditions for at least 24 hours before imaging, in accordance with the protocol of Gohil et al. (2010). At the microscope, the growth medium was replaced by recording media containing the same sugar substrate but with FBS removed and the bicarbonate buffer replaced by HEPES. The NAD(P)H FLIM parameters measured under these distinct conditions are shown in figures 5.9 and 5.10 and table 5.3.

The concentrations of free and bound NAD(P)H calculated using equations 5.4 and 5.5 are smaller in all compartments when metabolising galactose rather than glucose, as shown in table 5.3. With decreased cytosolic glucose breakdown and increased electron

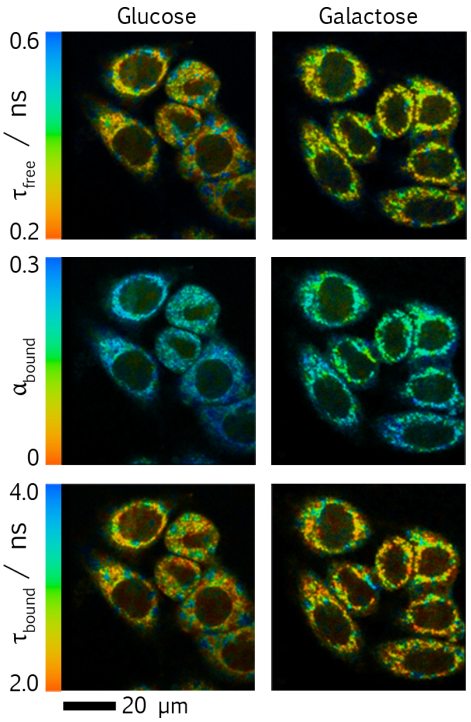

Figure 5.9: Typical NAD(P)H FLIM images of HeLa cells grown in glucose or galactose.

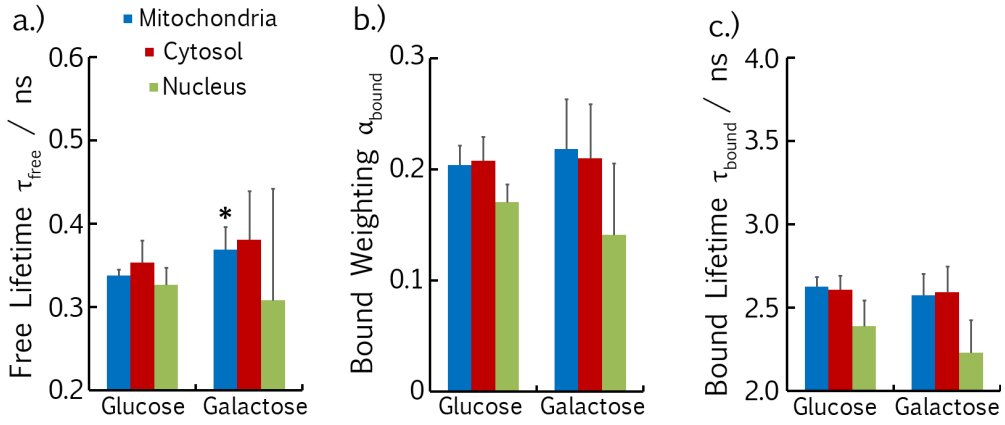

Figure 5.10: NAD(P)H fluorescence decay parameters of HeLa cells grown in glucose or galactose.

		Glucose	±	Galactose	±
τ_{free}/ns	M	0.34	0.01	0.37	0.03
	C	0.35	0.03	0.38	0.06
	N	0.33	0.02	0.3	0.1
α_{bound}	M	0.20	0.02	0.22	0.04
	C	0.21	0.02	0.21	0.05
	N	0.17	0.02	0.14	0.06
τ_{bound}/ns	M	2.63	0.06	2.6	0.1
	C	2.61	0.09	2.6	0.2
	N	2.4	0.2	2.2	0.2
$\langle I_{\text{total}} \rangle$/au	M	1.8	0.5	0.8	0.4
	C	1.0	0.3	0.4	0.3
	N	0.7	0.3	0.3	0.2
C_{free}/au	M	1.8	0.6	0.8	0.5
	C	1.0	0.4	0.5	0.3
	N	1.0	0.5	0.5	0.3
C_{bound}/au	M	0.5	0.1	0.2	0.1
	C	0.25	0.08	0.11	0.07
	N	0.19	0.07	0.07	0.04

Table 5.3: Average NAD(P)H fluorescence decay parameters in subcellular compartments of HeLa cells grown in glucose or galactose.

transport chain activity, this is to be expected. However, there is no associated response in α_{bound} and τ_{bound}. The only difference between the fluorescence decay parameters is an increased value of τ_{free} in the mitochondria of galactose-treated cells, although this is small at 0.03 ns.

The absence of differences between the fluorescence decay parameters in glucose- and galactose-fed HeLa cell lines suggests that NAD(P)H fluorescence lifetimes are not sensitive to changes in the balance of anaerobic and aerobic metabolism. This contradicts suggestions in the literature that differences between the fluorescence decay parameters of NAD(P)H in healthy tissue and tumours are due to the Warburg effect (Skala et al., 2007a). However, in the investigations performed thus far, shifts between aerobic and anaerobic metabolism have been forced with externally applied treatments. Shifts in metabolism during carcinogenesis are known to result from a complex interplay of environmental and genetic factors (Dang, 2012). The effect on the NAD(P)H fluorescence lifetimes of a genetically-determined shift between glycolytic and oxidative metabolic states will therefore be investigated next.

5.5 NAD(P)H lifetime imaging of stem cell carcinogenesis

The transformation of healthy tissue into cancerous tissue is controlled by oncogenes; genes coding for products that disrupt the balance between cell proliferation and cell death. A tumour develops in response to the gradual accumulation of oncogenes within a cell (Ruddon, 2007). For example, for a colorectal tumour to become metastatic, at least six "hits" must be accumulated over time (Knudson, 2001). This mechanism is used to explain the correlation between cancer risk and age (DePinho, 2000). The enhanced proliferation induced by oncogenes comes with a metabolic burden; replication of the contents of a cell requires a doubling of nucleotides, lipids and amino acids, in addition to the energy necessary to perform mitosis (Vander Heiden et al., 2009). For this reason, cancer progression is associated with shifts in metabolic pathways to fulfill the increased bioenergetic demands of rapid proliferation. In differentiated cells, this requirement is manifested in the Warburg effect.

In the last decade, greater emphasis has been placed on the role of stem cells in carcinogenesis (Reya et al., 2001; Ricci-Vitiani et al., 2007). These cells are responsible for differentiating into the specialised cell types of an organism (Alberts et al., 2007). Differentiation into a daughter cell is accompanied by the replacement of the mother cell, providing the population of stem cells with self-renewal properties (Shenghui et al., 2009). Self-renewing is also observed in a subset of the cells contained within a tumour (Pardal et al., 2003), suggesting that cancers either originate from oncogenically-transformed stem cells or that tumours utilise the self-renewal instructions present in the genome to enhance proliferation. Due to the recent discovery of these cancer stem cells, changes in the metabolic pathways utilised during their oncogenesis were originally poorly understood relative to the widely-studied metabolic properties of the bulk tumour.

In 2007, Funes et al. published a study into changes in energy metabolism during stem cell transformation. This work produced a sequence of mesenchymal stem cell lines expressing a steadily increasing number of oncogenes. The cells were labelled 1-hit (1H), 3-hit (3H), 4-hit (4H) and 5-hit (5H) based on the number of oncogenes introduced. The hTERT gene was introduced into the 1H cells, expressing the catalytic subunit of telomerase, allowing the cell to avoid senescence by maintaining the protective caps at the ends of its chromosomes (Hiyama and Hiyama, 2007). 3H cells were produced from the 1H cells by introducing genes from human papillomavirus coding for the E6 and E7 oncoproteins.

E6 and E7 cause inactivation of tumour suppressor proteins (p53 and pRb respectively, Scheffner et al. 1993; Slebos et al. 1994). In 4H cells, the small t antigen from simian virus 40 was introduced. This acts as an oncoprotein by inactivating an enzyme (protein phosphatase 2A) responsible for degrading a transcription factor (c-Myc, Yeh et al. 2004) controlling a number of cell proliferation genes. Finally, 5H cells were produced upon the addition of the oncogenic allele of H-Ras, a regulator of cell division (Chin et al., 1999), to the 4H cells.

Funes et al. observed that the carcinogenesis of mesenchymal stem cells is accompanied by increased oxidative phosphorylation and decreased glycolysis. This appears to show that, unlike the bulk tumour, cancer stem cells follow a reverse of the Warburg effect. However, this result could also indicate that the Warburg effect results from adaptation to the hypoxic microenvironment of the tumour rather than a process under direct control of the oncogenes. Regardless of the interpretation of this result, the well characterised gradual shift in metabolism of these cells represents an ideal model in which to study the response of the NAD(P)H fluorescence decay parameters to genetically-induced shifts between anaerobic and aerobic respiration.

The cell lines 1H through 5H were obtained from the laboratory of Prof. Chris Boshoff at the UCL Cancer Institute. Mesenchymal stem cells were cultured identically to the HeLa and HEK293 cells. The influence of the increased expression of oncogenes was evident in the drastic difference in growth rates of the cell lines. 1H cells required splitting only once per week at a ratio of 1:2, whereas 5H cells were split twice per week at a ratio of 1:10. After plating onto coverslips, FLIM images of these cell lines were obtained as before. The resulting NAD(P)H fluorescence decay parameters are shown in figures 5.11 and 5.12 and table 5.4.

Carcinogenesis in mesenchymal stem cells is accompanied by a steady decrease in the NAD(P)H fluorescence intensity in all cellular compartments. As in the previous experiments, τ_{free} increases in response to this decreased intensity. However, while this was previously attributed to a parameter interdependency observed in computational models of the fitting process, this cannot be the cause here as no differences in α_{bound} values are evident between the transformed cell lines. Significantly lower values of τ_{bound} are observed in the mitochondria and cytosol of 4H and 5H cells relative to the 1H cells. A similar decrease has previously been observed in bulk tumour relative to healthy tissue by Skala

	τ_{free}/ns			α_{bound}			τ_{bound}/ns			$\langle I_{total} \rangle$/au			C_{free}/au			C_{bound}/au		
	M	C	N	M	C	N	M	C	N	M	C	N	M	C	N	M	C	N
1H	0.32	0.32	0.31	0.19	0.19	0.16	2.63	2.61	2.45	1.6	1.0	0.9	1.6	1.0	1.1	0.4	0.2	0.21
±	0.02	0.01	0.02	0.01	0.01	0.02	0.08	0.08	0.1	0.7	0.4	0.3	0.6	0.4	0.4	0.2	0.1	0.06
3H	0.35	0.35	0.35	0.18	0.18	0.15	2.57	2.56	2.37	1.0	0.5	0.4	1.0	0.5	0.5	0.22	0.12	0.08
±	0.01	0.02	0.01	0.01	0.01	0.01	0.05	0.06	0.05	0.3	0.1	0.1	0.3	0.2	0.1	0.07	0.03	0.02
4H	0.37	0.39	0.39	0.18	0.18	0.17	2.52	2.51	2.36	0.8	0.4	0.27	0.8	0.4	0.29	0.18	0.08	0.06
±	0.02	0.03	0.02	0.01	0.01	0.01	0.07	0.04	0.05	0.2	0.1	0.06	0.2	0.1	0.08	0.04	0.02	0.01
5H	0.39	0.40	0.36	0.18	0.19	0.16	2.48	2.46	2.13	0.34	0.21	0.14	0.33	0.20	0.17	0.08	0.05	0.03
±	0.01	0.02	0.01	0.01	0.01	0.01	0.08	0.12	0.10	0.09	0.04	0.03	0.08	0.03	0.02	0.02	0.01	0.01

Table 5.4: Average fluorescence decay parameters in subcellular compartments of mesenchymal stem cells expressing a steadily increasing number of oncogenes.

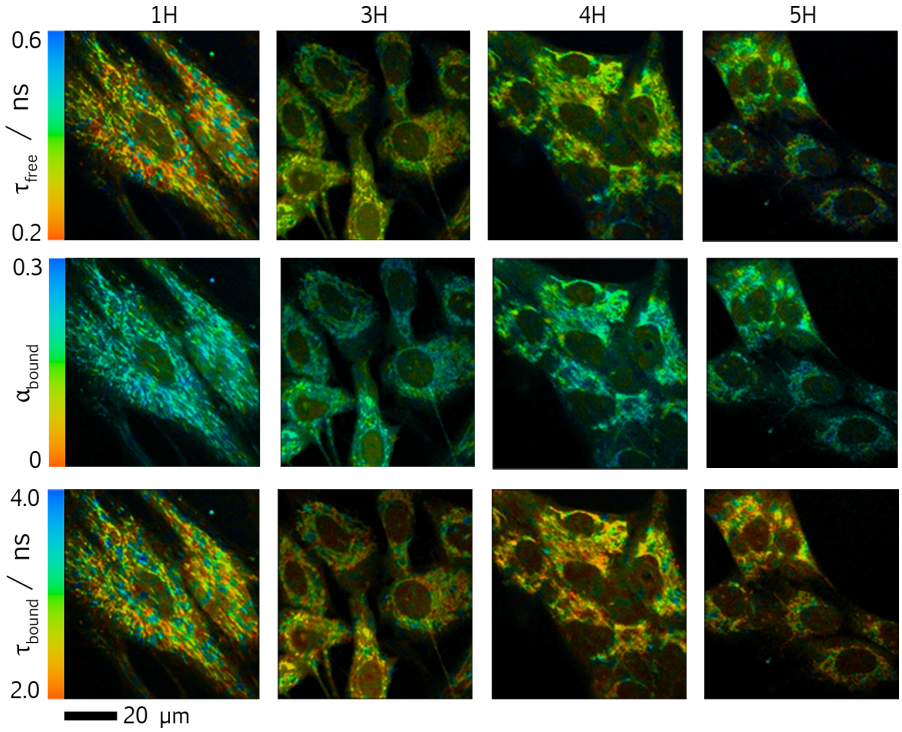

Figure 5.11: Typical NAD(P)H FLIM images of mesenchymal stem cells expressing a steadily increasing number of oncogenes.

et al., where the change in value was attributed to increased glycolysis in the tumour. However, in this work, the smaller enzyme bound NAD(P)H fluorescence lifetime components are observed in the most oxidative of the transformed cell lines. This disagreement again suggests that variations in τ_{bound} are not the direct result of shifts between oxidative and glycolytic metabolism.

5.6 Conclusions

In this chapter, a number of experimental models have been used to investigate the presence of unique characteristics in the fluorescence decay of NAD(P)H in oxidative and glycolytic cells. No intrinsic differences were observed between the fluorescence decay parameters of NAD(P)H in the distinct regions of the cell where aerobic and anaerobic respiration take place; the mitochondria and cytosol respectively. It is unlikely that this is an artifact of the binning process as the bin area of 25 pixels is small relative to the total areas of each compartment (~0.1%). Cytosolic and mitochondrial regions remain identifiable by eye upon application of the same procedure to the intensity images, as shown in figure 5.13.

The absence of NAD(P)H fluorescence lifetime differences between the mitochondria and the cytosol is notable because these two regions present distinct microenvironments for NAD(P)H due to the presence of different sets of metabolic enzymes (Berg et al., 2011)

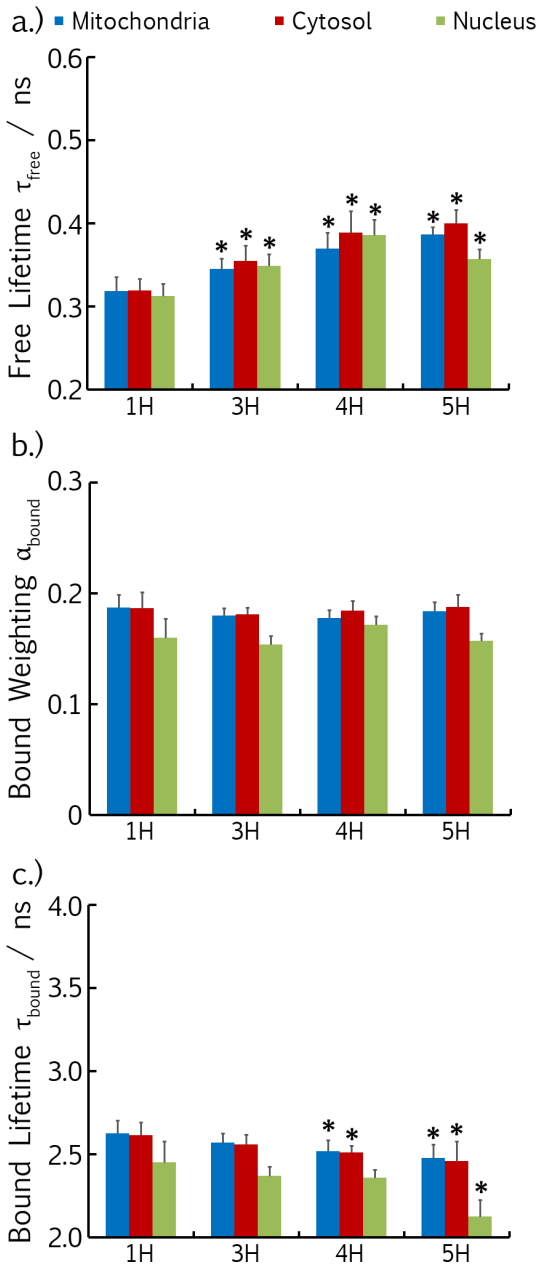

Figure 5.12: NAD(P)H fluorescence decay parameters of mesenchymal stem cells expressing a steadily increasing number of oncogenes.

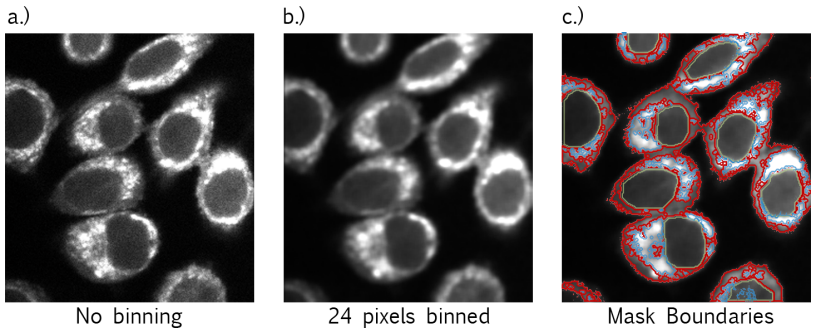

Figure 5.13: Binning the 24 surrounding pixels causes a slight blurring of the boundary between fluorescence arising from the mitochondria and cytosol (b). However, the five by five area binned is small relative to the total area of each subcellular region. The areas defined by the masks therefore remain representative of the fluorescence arising from each compartment, as shown by the fluorescence intensity within their perimeters (c).

and different local viscosities. The presence of high concentrations of macromolecules means the cytosol constitutes a gel-like environment (Alberts et al., 2007) with a viscosity of around 0.01 N s m^{-2} (Dix and Verkman, 1990). The mitochondrial matrix is three-times more viscous still, with proteins reaching the close-packing limit (Scalettar et al., 1991). The results presented in chapter 3 suggest this viscosity difference would cause the average fluorescence lifetime of NAD(P)H diffusing freely in the mitochondrial matrix to be 20% larger than in the cytosol. However, the intracellular rotational correlation time of NAD(P)H has been previously measured as 0.3 ns (Vishwasrao et al., 2005), similar to its value in aqueous solution. Perhaps, therefore, small molecules such as free NAD(P)H exist in aqueous microdomains within the intracellular milieu, causing the absence of intrinsic fluorescence lifetime differences between the subcellular compartments. Across all cell lines under control conditions, the NAD(P)H fluorescence intensity is 75% higher in the mitochondria than the cytosol. As the measurements reported in this chapter indicate no significant quantum yield differences between mitochondrial and cytosolic NAD(P)H, the intensity difference must be due to elevated concentrations of NAD(P)H in the mitochondria rather than the presence of a larger population of bound species.

The most consistent correlation between the fluorescence decay parameters and the metabolic perturbations applied was an inverse proportionality between the total intensity of NAD(P)H fluorescence and the fluorescence lifetime of freely-diffusing species. As the free NAD(P)H lifetime lies close to the time resolution of the FLIM setup, an obvious explanation for this relationship would be to attribute it as an artifact in the least-squares fitting of the fluorescence decays induced by a decrease in signal levels. However, the computa-

tional simulations performed here suggest that this cannot be the case, with only the spread in specific values of τ_{free} extracted increasing with decreasing signal, not the mean values. A preferential oxidation of the short lifetime species of free NAD(P)H upon increases in the NAD(P)$^+$/NAD(P)H redox ratio would explain this phenomenon. However, without knowledge of the configurational differences between the two species, proposing a mechanism of how this could be so is not possible.

An interesting feature of the results reported in this chapter is the similarity between the changes in the measured parameters in all subcellular compartments, regardless of the perceived compartment-specific effects of each treatment. For example, a decrease in the concentration of free and bound NAD(P)H is measured in the cytosol and nucleus upon application of FCCP to both HeLa and HEK cells, in addition to its expected effect within the mitochondria. All compartments then respond with an increase in τ_{free} and α_{bound}. Alterations in mitochondrial morphology over the four minutes of imaging may cause a blurring of the boundaries between mitochondria and cytosol in the final FLIM images. However, these images show consistently higher NAD(P)H fluorescence in the regions identified by TMRM staining, suggesting the technique applied here is largely successful in segmenting pixel locations as mitochondria or cytosol. In addition, the similar responses of parameters are also observed in the nuclear regions, which are easily segmented by eye. This phenomenon suggests that changes in redox state, whether induced by pharmacological, substrate-supply or genetic means, are not compartment-specific but are partially propagated throughout the cell. Perhaps this results from the action of the malate-aspartate shuttle and diffusion of NAD(P)H through the nuclear pores (Zhang et al., 2002). Despite the similar changes in values between compartments, the absolute values of α_{bound} and τ_{bound} remain smaller in the nucleus relative to the rest of the cell.

A recent trend has emerged in the NAD(P)H FLIM literature to interpret α_{bound} as a direct reporter of the balance between glycolytic and oxidative metabolism (Stringari et al., 2012a,c,b). The logic of this approach follows Bird et al.'s 2005 observation that α_{bound} varies in proportion to the NAD$^+$/NADH redox ratio in response to serum starvation and inhibition of the electron transport chain. Anaerobic respiration is assumed to cause reduction of the cellular NAD$^+$/NADH pool while aerobic respiration is assumed to cause its oxidation (Stringari et al., 2012a). An interpretation of α_{bound} as proportional to the balance of oxidative phosphorylation to glycolysis then follows. The results obtained

in this chapter are in disagreement with this scheme. Shifts from glycolytic to oxidative metabolism induced by both substrate supply in HeLa cells and genetic transformation in mesenchymal stem cells are accompanied by no change in α_{bound}. It is likely that α_{bound} is a function of the concentration of NAD(P)H-binding enzymes present, the total concentration of the NAD(P)$^+$/NAD(P)H pool and its redox ratio. In addition, the changes in redox ratio during transitions between oxidative and glycolytic metabolism may not necessarily be those assumed in this interpretation of α_{bound}. For example, increased glycolysis will only cause net reduction of the NAD$^+$/NADH pool if there is no compensatory change in the activity of the malate-aspartate shuttle or the lactate dehydrogenase enzyme. Likewise, termination of aerobic ATP production may result either in a reduction or an oxidation of the NAD$^+$/NADH pool based on whether this takes place in response to electron transport chain inhibition or by uncoupling. Modelling these two processes in HeLa and HEK293 cells by rotenone and FCCP treatment caused different changes in α_{bound} due to their contrasting effects on the concentration of NAD(P)H, despite them both causing a decrease in mitochondrial ATP output relative to glycolysis.

In the NAD(P)H FLIM literature, the balance between glycolytic and oxidative metabolism has also been suggested to be indicated by changes in τ_{bound}, following observation that τ_{bound} is lower in tumours relative to healthy tissue (Skala et al., 2007a). Based on the Warburg hypothesis, this suggests that τ_{bound} decreases with increased reliance on anaerobic metabolism. The results obtained in this chapter again disagree with this interpretation. This parameter does increase upon inhibition of glycolysis in HeLa cells. However, a similar increase can be induced by terminating mitochondrial ATP production with the uncoupler FCCP. In addition, these results could not be repeated in HEK293 cells. Perhaps most significantly, τ_{bound} did not differ between HeLa cells grown in glucose and galactose and also displayed a decrease in response to an increased reliance on oxidative metabolism in 4H and 5H transformed mesenchymal stem cells. The metabolic significance of the changes in this parameter observed in disease models therefore remains to be determined. One avenue for investigation is offered by the results of Funes et al., who observed decreased pentose phosphate pathway activity in the 4H and 5H cell lines in which the decreased values of τ_{bound} were measured. Perhaps, therefore, NADPH levels play a role in the value of τ_{bound} measured in a live cell.

Chapter 6

Separation of NADH and NADPH fluorescence in live tissue using FLIM

6.1 NAD kinase influence on NAD(P)H fluorescence decay

Simply in response to increasing the number of cells on a coverslip, the NAD(P)H fluorescence decay parameter τ_{bound} has been observed to decrease from 3.1($\pm$0.1) ns to 1.72($\pm$0.02) ns (Bird et al., 2005). This was attributed to the increased cell confluence decreasing the availability of oxygen, downregulating aerobic metabolism. However, such large differences in τ_{bound} could not be reproduced in the four separate experiments of the previous chapter, designed to measure the fluorescence decay of NAD(P)H in response to perturbation of the glycolytic and oxidative ATP-production pathways.

While chapter 3 showed that the fluorescence decays of NADH and NADPH in solution are equal, no investigations have been made into whether the lifetime characteristics of these two cofactors differ in the cellular environment. In published NAD(P)H FLIM studies, the contribution of NADPH to the total fluorescence is typically assumed to be negligible (Vishwasrao et al., 2005; Skala et al., 2007a; Ghukasyan and Kao, 2009; Yu and Heikal, 2009). For example, a recent study into the fluorescence decay of NADH in live rat brains by Yaseen et al. (2013) declares "NADPH is widely believed to contribute minimally to the fluorescence signal, due to its much lower concentration in brain tissue, low quantum yield and insensitivity to metabolic perturbation". This is despite the NADPH to NADH ratio in the brain being previously measured as approximately 0.30($\pm$0.05) (Klaidman et al., 1995), the quantum yield of the two cofactors being identical in solution (Patterson et al., 2000) and NADPH playing a crucial role in intracellular metabolism (Ying, 2008).

To investigate the contribution of NADPH to the NAD(P)H fluorescence decay, two ge-

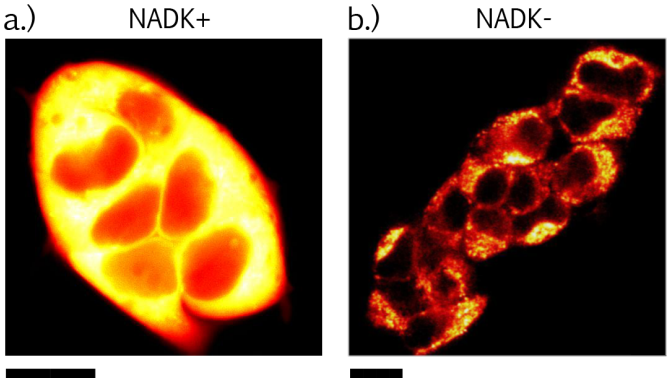

Figure 6.1: Confocal microscopy images of NAD(P)H fluorescence in NADK+ and NADK– cells. Scale bars are 20 μm.

netically modified HEK293 cell lines containing different NADPH concentrations were imaged using FLIM. In these cell lines, obtained from the laboratory of Prof. Mathias Ziegler at the Department of Molecular Biology, University of Bergen, the enzyme NAD kinase is stably overexpressed (NADK+) or knocked down (NADK–). As NAD kinase is the sole enzyme responsible for converting NAD^+ to $NADP^+$ and the $NADP^+$/NADPH pool is maintained in a highly reduced state, the concentration of NADPH is approximately five times higher in the NADK+ cells than the NADK– cells (Pollak et al., 2007b).

NADK+ and NADK– cells were cultured identically to wild-type HEK293 cells with the addition of 0.1 mg ml^{-1} G-418 to the culture medium. This compound is an antibiotic, resistance to which is encoded in the plasmids used to introduce the genes necessary to express or knock down NAD kinase. Its presence therefore selects for cells expressing the genetic modifications. Knock down was achieved in the NADK– cells by RNA interference (Hannon, 2002). Upon imaging with standard confocal microscopy, distinct patterns of NAD(P)H fluorescence were evident, as shown in figure 6.1. While the NADK– cells appeared similar to wild-type HEK293 cells, NADK+ cells exhibited bright NAD(P)H fluorescence throughout the cytosol.

NAD(P)H FLIM images of NADK+ and NADK– cells were obtained as previously, with the cells bathed in standard glucose-containing recording medium. It is immediately clear from inspection of the NAD(P)H fluorescence lifetime parameters extracted, displayed in figures 6.2 and 6.3 and detailed in table 6.1, that the measured fluorescence decays differ significantly between the two cell lines. While τ_{free} and α_{bound} were both significantly smaller in the NADK+ cells compared to the NADK– cells, the most dramatic difference between the fluorescence decay of NAD(P)H in the two cell lines is in the enzyme bound

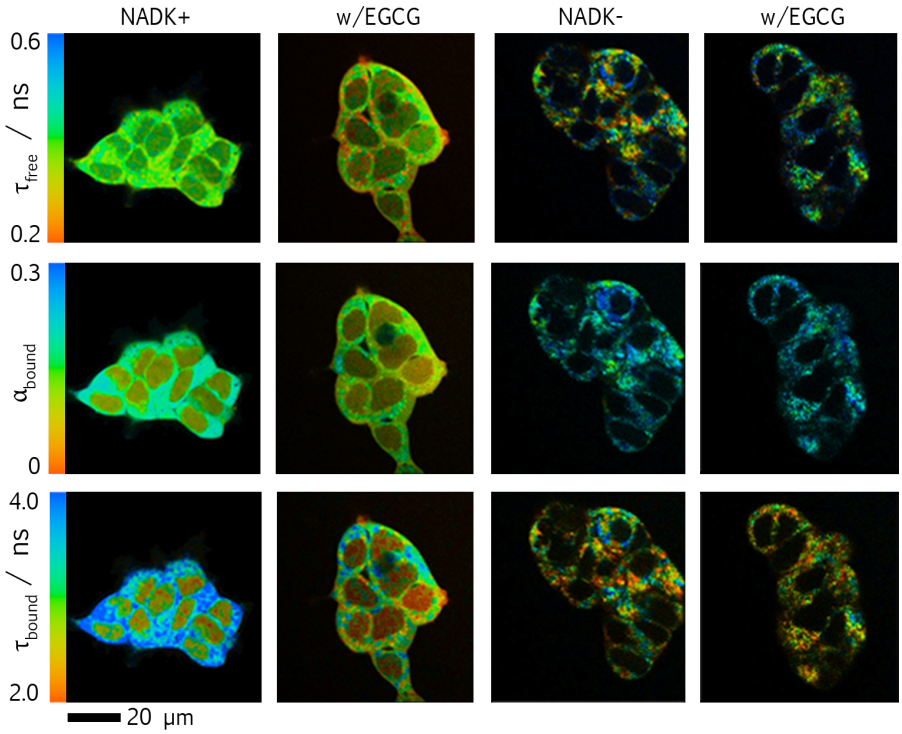

Figure 6.2: Typical NAD(P)H FLIM images of NADK+ and NADK– cells under control conditions and in response to EGCG treatment.

fluorescence lifetime values. The longest enzyme bound fluorescence lifetime measured previously was 2.8(±0.1) ns in the mitochondria and cytosol of HeLa cells provided with pyruvate in the absence of glucose. τ_{bound} is much larger than this in the mitochondria of NADK+ cells at 3.6(±0.2) ns and larger still in their cytosol at 3.8(±0.2) ns. τ_{bound} in the mitochondria and cytosol of NADK– cells is 2.7(±0.1) ns, closer to the values typically measured in these compartments of the cell lines in chapter 5. The trend observed in the previous chapter for lower α_{bound} and τ_{bound} values in the nucleus is maintained in both of these cell lines.

As NADPH concentrations are greatly increased in the NADK+ cells relative to the NADK– cells, it was hypothesised that a larger enzyme bound NAD(P)H lifetime could be an intrinsic property of intracellular NADPH fluorescence compared to intracellular NADH fluorescence. To investigate this, the NAD(P)H fluorescence decay parameters in both cell types were measured in response to treatment with the compound epigallocatechin gallate (EGCG). Computational screening and enzyme kinetic assays have been used to show that this compound is a potent inhibitor of the NADPH-producing enzymes of the pentose phosphate pathway, causing 50% reduction in activity of glucose 6-phosphate dehydrogenase at only 250 nM (Shin et al., 2008). EGCG was found to compete with NADPH for its binding

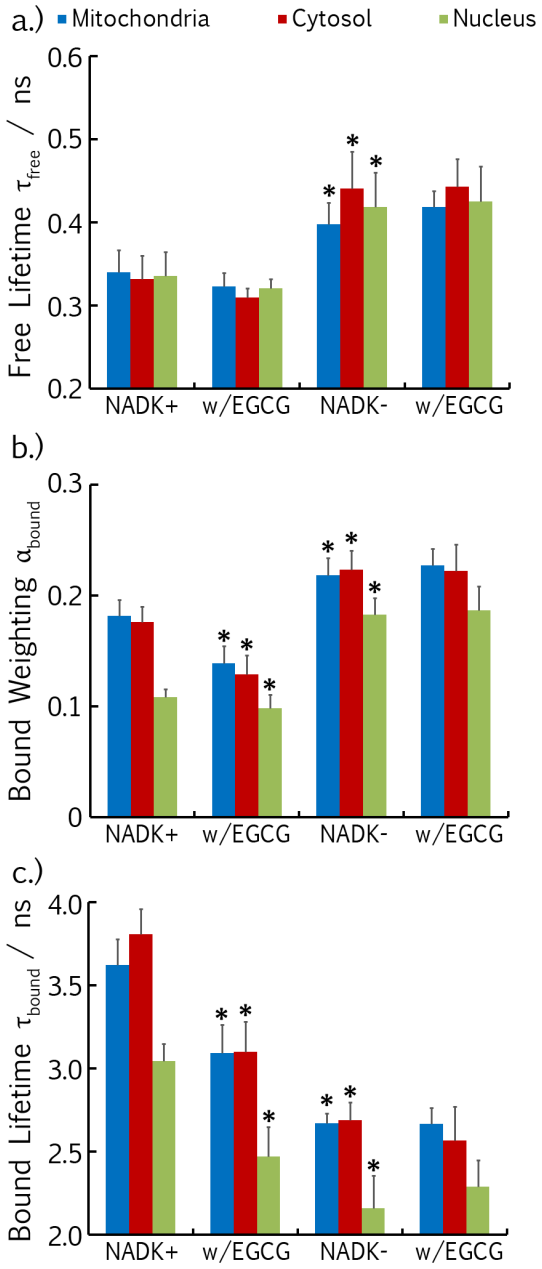

Figure 6.3: NAD(P)H fluorescence decay parameters of NADK+ and NADK– cells under control conditions and in response to EGCG treatment. Stars above NADK– bars under control conditions indicate statistically significant differences relative to the untreated NADK+ cells. Changes upon EGCG treatment are relative to the respective cell line under control conditions.

	τ_{free}/ns			α_{bound}			τ_{bound}/ns		
	M	C	N	M	C	N	M	C	N
NADK+	0.34	0.33	0.34	0.18	0.18	0.11	3.6	3.8	3.0
±	0.03	0.03	0.03	0.01	0.01	0.01	0.2	0.2	0.1
w/EGCG	0.32	0.31	0.32	0.14	0.13	0.10	3.1	3.1	2.5
±	0.02	0.01	0.01	0.02	0.02	0.01	0.2	0.2	0.2
NADK–	0.40	0.44	0.42	0.22	0.22	0.18	2.67	2.7	2.2
±	0.03	0.04	0.04	0.02	0.02	0.02	0.06	0.1	0.2
w/EGCG	0.42	0.44	0.42	0.23	0.22	0.19	2.7	2.6	2.3
±	0.02	0.03	0.04	0.02	0.02	0.02	0.1	0.2	0.2
wtHEK	0.36	0.36	0.34	0.20	0.19	0.15	2.7	2.7	2.3
±	0.04	0.04	0.03	0.01	0.01	0.01	0.2	0.1	0.2
w/EGCG	0.35	0.34	0.34	0.18	0.17	0.16	2.46	2.4	2.03
±	0.02	0.02	0.02	0.01	0.01	0.01	0.08	0.1	0.08

Table 6.1: Average NAD(P)H fluorescence decay parameters in subcellular compartments of wild-type and genetically modified HEK293 cells under control conditions and in response to treatment with EGCG.

site on these enzymes, a phenomenon previously observed in the enzyme fatty acid synthase (Wang et al., 2003). A search of the BRENDA database (Schomburg et al., 2002) revealed no similar effects of this compound on the NADH-dependent enzymes of glycolysis and oxidative phosphorylation. As shown in the computational simulations of the previous chapter, τ_{bound} represents a weighted average of the lifetimes of the enzyme-bound NAD(P)H species present. If bound NADPH is characterised by an increased fluorescence lifetime relative to bound NADH and EGCG competes for NADPH, but not NADH, binding sites, its application to live cells should cause τ_{bound} to decrease.

FLIM images of NADK+ and NADK– cells were obtained at least 10 minutes after addition of 100 μM EGCG (Sigma Aldrich) to their recording medium. Addition of EGCG to NADK+ cells caused τ_{bound} to decrease to 3.1(±0.2) ns in the mitochondria and cytosol and to 2.5 (±0.2) ns in the nucleus. This result is consistent with the increased enzyme bound NAD(P)H fluorescence lifetime in these cells being caused by an increased ratio of bound NADPH to NADH.

Given the results of Pollak et al. (2007b), the ratio of NADPH to NADH fluorescence in the total NAD(P)H emission will be larger in NADK+ cells than in NADK– cells. If application of EGCG causes competition for NADPH binding sites but not NADH binding sites, the bound NADPH population will decrease while the bound NADH population remains constant. This suggests that the value of α_{bound} will be more sensitive to EGCG treatment

in NADK+ cells than in NADK– cells, as bound NADPH will form a greater fraction of the total population of enzyme bound NAD(P)H species. This expected contrast in responses was observed here, with α_{bound} decreasing significantly upon EGCG treatment in NADK+ cells but remaining constant in NADK– cells.

Interestingly, there is also no change in τ_{bound} upon EGCG application to NADK– cells. This suggests that the magnitude of the response of τ_{bound} to EGCG treatment is proportional to the initial ratio of NADPH to NADH present in the cells. If this is the case, τ_{bound} in wild-type HEK293 cells, containing an intermediate concentration of NADPH between cells in which NAD kinase is overexpressed or knocked down, should respond in an intermediate manner. This is exactly what was observed when the experiment was performed, as seen in figures 6.4 and 6.5 and table 6.1. EGCG caused a decrease in τ_{bound} in wild-type HEK293 cells that, while significant, was smaller than that observed in the NADK+ cells, decreasing by approximately 10% in all compartments compared to 17% when NAD kinase is overexpressed. A response in α_{bound} that is proportional to the relative concentration of NADPH and NADH present is to be expected, based on the relative abundance of the two cofactors in the enzyme bound populations. However, similar behaviour in τ_{bound} is less trivial and represents a phenomenon that must be explainable by any valid interpretive model for this parameter.

6.2 A simple model for τ_{bound}

The experiments of the previous section suggested that, within the environment of the cell, NADPH is associated with a larger enzyme bound fluorescence lifetime than NADH. Computational simulations of the biexponential fitting process in NAD(P)H FLIM showed that the enzyme bound fluorescence lifetime contained in an NAD(P)H fluorescence decay will vary linearly from a minimum value τ_{short} to a maximum value τ_{long} as the proportion of the total enzyme-bound population consisting of the longer-lifetime species increases from 0% to 100%. This model could therefore be a valid description of the dependence of τ_{bound} on varying concentrations of NADPH, with enzyme-bound NADH species represented by a fluorescence lifetime τ_{NADH} and enzyme-bound NADPH species represented by a longer fluorescence lifetime τ_{NADPH}. Equation 5.2 can be rearranged and written in terms of the concentrations of NADH and NADPH present to give,

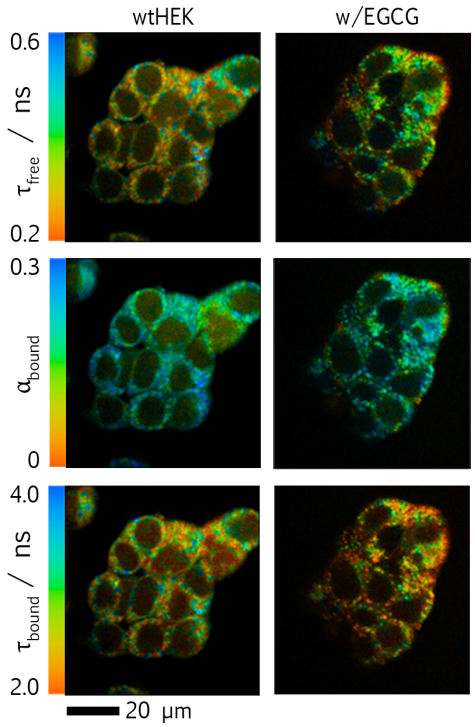

Figure 6.4: Typical NAD(P)H FLIM images of wild-type HEK293 cells under control conditions and in response to EGCG treatment.

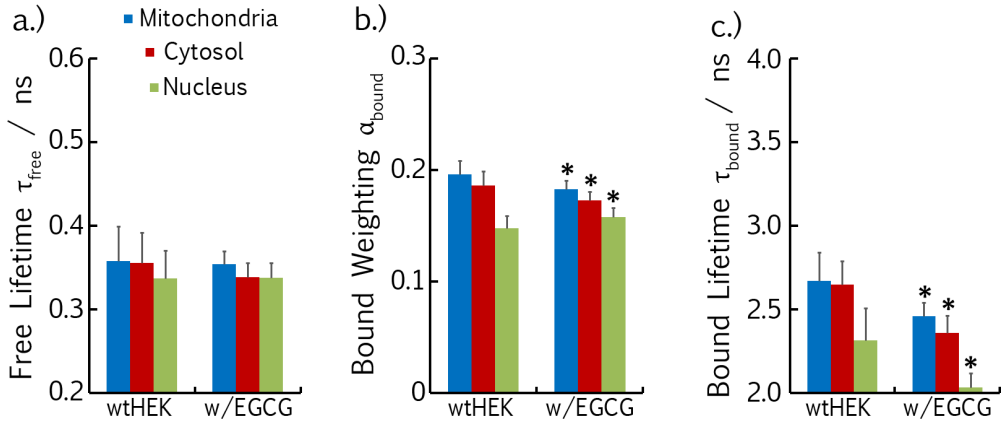

Figure 6.5: NAD(P)H fluorescence decay parameters of wild-type HEK293 cells under control conditions and in response to EGCG treatment.

$$\frac{\alpha_{\text{NADPH}}}{\alpha_{\text{bound}}} = \frac{\tau_{\text{bound}} - \tau_{\text{NADH}}}{\tau_{\text{NADPH}} - \tau_{\text{NADH}}} = \frac{[\text{NADPH}]_{\text{bound}}}{[\text{NADH}]_{\text{bound}} + [\text{NADPH}]_{\text{bound}}} \tag{6.1}$$

where the total fraction of enzyme-bound species present in an NAD(P)H fluorescence decay has been split into separate weightings due to enzyme-bound NADH and enzyme-bound NADPH ($\alpha_{\text{bound}} = \alpha_{\text{NADH}} + \alpha_{\text{NADPH}}$). This expression can then be rearranged to calculate the dependence of τ_{bound} on the distinct lifetimes of enzyme-bound NADH and NADPH and the concentrations of bound NADH and NADPH present, giving,

$$\tau_{\text{bound}} = (\tau_{\text{NADPH}} - \tau_{\text{NADH}}) \frac{[\text{NADPH}]_{\text{bound}}}{[\text{NADH}]_{\text{bound}} + [\text{NADPH}]_{\text{bound}}} + \tau_{\text{NADH}} \tag{6.2}$$

As the concentrations of NADH and NADPH in the NADK+ and NADK– cells are known (Pollak et al., 2007b), the measurements of τ_{bound} made in the previous section can be used to approximate values of τ_{NADH} and τ_{NADPH}. However, as there is no *a priori* knowledge of the fraction of bound NAD(P)H consisting of NADH or NADPH, the approximation must be made that the fractions of NADH and NADPH present in the enzyme bound population are similar to the overall proportions of each cofactor present in the cell, thus,

$$\tau_{\text{bound}} = (\tau_{\text{NADPH}} - \tau_{\text{NADH}}) \frac{[\text{NADPH}]}{[\text{NADH}] + [\text{NADPH}]} + \tau_{\text{NADH}} \tag{6.3}$$

This equation describes the behaviour expected if intracellular NADPH is associated with a larger enzyme bound fluorescence lifetime than NADH; τ_{bound} goes to τ_{NADPH} as the NADH concentration goes to zero, and τ_{bound} goes to τ_{NADH} if all NADPH is removed. If the ratio of NADPH to NADH in the NADK+ and NADK– cells respectively is written as R^+ and R^-, with associated enzyme-bound fluorescence lifetimes in these cells measured as τ^+_{bound} and τ^-_{bound}, equation 6.3 can be used to derive expressions for the NADH- and NADPH-associated enzyme-bound fluorescence lifetimes as,

$$\tau_{\text{NADH}} = \frac{\tau^-_{\text{bound}} R^+ (1 + R^-) - \tau^+_{\text{bound}} R^- (1 + R^+)}{(R^+ - R^-)} \tag{6.4}$$

$$\tau_{\text{NADPH}} = \frac{\tau^+_{\text{bound}} (1 + R^+) - \tau^-_{\text{bound}} (1 + R^-)}{(R^+ - R^-)} \tag{6.5}$$

Values of τ_{bound} differ between mitochondrial, cytosolic and nuclear compartments. However, measurements of the cofactor concentrations are only available for the cell as a

whole. To account for this, τ^{+}_{bound} and τ^{-}_{bound} must be replaced in equations 6.4 and 6.5 by effective enzyme-bound fluorescence lifetimes $\tau^{+,\text{eff}}_{\text{bound}}$ and $\tau^{-,\text{eff}}_{\text{bound}}$. The whole-cell R values would then be calculated by,

$$R = \frac{[\text{NADPH}]}{[\text{NADH}]} = \frac{\tau^{\text{eff}}_{\text{bound}} - \tau_{\text{NADH}}}{\tau_{\text{NADPH}} - \tau^{\text{eff}}_{\text{bound}}} \tag{6.6}$$

where this expression is obtained by rearranging equation 6.3.

To calculate the effective enzyme-bound fluorescence lifetime of a cell in terms of its compartmentalised parameters, the ratio of NADPH to NADH for the whole cell is first expressed in terms of its mitochondrial, cytosolic and nuclear values and the concentrations of NADH in these compartments,

$$R = \frac{[\text{NADPH}]_{\text{total}}}{[\text{NADH}]_{\text{total}}} = \frac{A_{\text{M}}R_{\text{M}}[\text{NADH}]_{\text{M}} + A_{\text{C}}R_{\text{C}}[\text{NADH}]_{\text{C}} + A_{\text{N}}R_{\text{N}}[\text{NADH}]_{\text{N}}}{A_{\text{M}}[\text{NADH}]_{\text{M}} + A_{\text{C}}[\text{NADH}]_{\text{C}} + A_{\text{N}}[\text{NADH}]_{\text{N}}} \tag{6.7}$$

where A_{M}, A_{C} and A_{N} are fractional areas of the images occupied by mitochondria, cytosol and nucleus respectively. Substitution of equation 6.3 for the concentrations of NADH in each compartment, writing the total NAD(P)H concentration as C_{total}, gives,

$$R = \frac{A_{\text{M}}C_{\text{tot,M}}R_{\text{M}}\left(\tau_{\text{NADPH}} - \tau_{\text{bound,M}}\right) + A_{\text{C}}C_{\text{tot,C}}R_{\text{C}}\left(\tau_{\text{NADPH}} - \tau_{\text{bound,C}}\right) + A_{\text{N}}C_{\text{tot,N}}R_{\text{N}}\left(\tau_{\text{NADPH}} - \tau_{\text{bound,N}}\right)}{A_{\text{M}}C_{\text{tot,M}}\left(\tau_{\text{NADPH}} - \tau_{\text{bound,M}}\right) + A_{\text{C}}C_{\text{tot,C}}\left(\tau_{\text{NADPH}} - \tau_{\text{bound,C}}\right) + A_{\text{N}}C_{\text{tot,N}}\left(\tau_{\text{NADPH}} - \tau_{\text{bound,N}}\right)} \tag{6.8}$$

The R-terms in the numerator can be eliminated by substitution of equation 6.6 for each compartment. Multiplying out the brackets and then rearranging gives,

$$R = \frac{\left(\frac{A_{\text{M}}C_{\text{tot,M}}\tau_{\text{bound,M}} + A_{\text{C}}C_{\text{tot,C}}\tau_{\text{bound,C}} + A_{\text{N}}C_{\text{tot,N}}\tau_{\text{bound,N}}}{A_{\text{M}}C_{\text{tot,M}} + A_{\text{C}}C_{\text{tot,C}} + A_{\text{N}}C_{\text{tot,N}}}\right) - \tau_{\text{NADH}}}{\tau_{\text{NADPH}} - \left(\frac{A_{\text{M}}C_{\text{tot,M}}\tau_{\text{bound,M}} + A_{\text{C}}C_{\text{tot,C}}\tau_{\text{bound,C}} + A_{\text{N}}C_{\text{tot,N}}\tau_{\text{bound,N}}}{A_{\text{M}}C_{\text{tot,M}} + A_{\text{C}}C_{\text{tot,C}} + A_{\text{N}}C_{\text{tot,N}}}\right)} \tag{6.9}$$

Comparison with equation 6.6 shows that the effective enzyme-bound fluorescence lifetime for purposes of calculating R^{+} and R^{-} is given by,

$$\tau^{\text{eff}}_{\text{bound}} = \frac{A_{\text{M}}C_{\text{tot,M}}\tau_{\text{bound,M}} + A_{\text{C}}C_{\text{tot,C}}\tau_{\text{bound,C}} + A_{\text{N}}C_{\text{tot,N}}\tau_{\text{bound,N}}}{A_{\text{M}}C_{\text{tot,M}} + A_{\text{C}}C_{\text{tot,C}} + A_{\text{N}}C_{\text{tot,N}}} \tag{6.10}$$

This represents a sum of the average fluorescence lifetime of enzyme bound NAD(P)H in each of the compartments weighted by the proportional sizes of the NAD(P)H pools in

each subcellular location.

The areas occupied by mitochondria, cytosol or nucleus were measured from the segmentation masks for each image using ImageJ. Calculating the total concentration of NAD(P)H in each compartment using equations 5.4 and 5.5 then gives average values of $\tau_{\text{bound}}^{+,\text{eff}}$= 3.5(±0.1) ns and $\tau_{\text{bound}}^{-,\text{eff}}$= 2.61(±0.08) ns. From the high performance liquid chromatography (HPLC) studies of the NADK+ and NADK– cells presented by Pollak et al., the ratios of NADPH to NADH in the two cell lines are R^{+}=2.3 and R^{-}=0.6 respectively. Substituting these values into equations 6.4 and 6.5 then gives τ_{NADH}= 1.5(±0.2) ns and τ_{NADPH}= 4.4(±0.2) ns.

Given a measurement of τ_{bound}, the model developed here predicts the corresponding ratio of NADPH to NADH as,

$$\frac{[\text{NADPH}]}{[\text{NADH}]} = \frac{\tau_{\text{bound}} - \tau_{\text{NADH}}}{\tau_{\text{NADPH}} - \tau_{\text{bound}}} = \frac{\tau_{\text{bound}}\,(\text{ns}) - 1.5}{4.4 - \tau_{\text{bound}}\,(\text{ns})} \tag{6.11}$$

This relationship demonstrates that τ_{bound} depends nonlinearly on the relative concentrations of NADPH and NADH present. As can be seen in figure 6.6a, τ_{bound} is less sensitive to changes in the ratio of NADPH to NADH when this ratio is top-heavy or bottom-heavy. This explains the contrasting behaviour of τ_{bound} in NADK+ and NADK– cells in response to application of EGCG; the change in τ_{bound} observed upon treatment with this compound was proportional to the initial concentration of NADPH relative to NADH. In figure 6.6b, the change in τ_{bound} upon removal of 10%, 50% and 90% of the bound NADPH population is calculated as a function of initial ratio of bound NADPH to bound NADH. It can be seen that τ_{bound} is most sensitive to decreases in the bound NADPH population when the bound NADH population is of a similar size. When the presence of one cofactor outweighs the other, decreasing the bound NADPH population, such as with EGCG treatment, does not significantly perturb τ_{bound}. This behaviour was observed in the NADK– cells, where the NADPH to NADH ratio is around five times smaller than in the NADK+ cells. The inherence of this behaviour in this model supports the validity of its use in describing the dependence of τ_{bound} on the relative abundance of NADH and NADPH.

Based on the data contained in table 6.1, this model suggests that the wild-type HEK293 cells contain the same ratio of NADPH to NADH as HEK293 cells in which NAD kinase has been knocked down. Given that the wild-type cells are of a separate lineage to those used to produce the genetically modified cell lines, this is unsurprising. However,

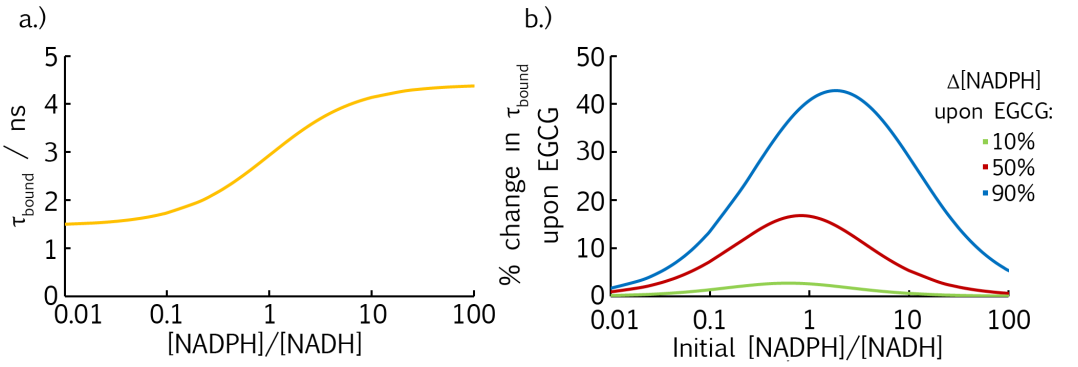

Figure 6.6: Non-linear dependence of the enzyme-bound fluorescence lifetime on the NADPH to NADH ratio (a) causes the change in τ_{bound} expected upon application of EGCG (b) to vary depending on the initial [NADPH]/[NADH] ratio.

despite the initial NADPH to NADH ratio being the same, the two cell lines respond to the same concentration of EGCG in a different manner; no decrease in τ_{bound} is observed in the NADK– cells, whereas a 0.26($\pm$ 0.04) ns decrease, averaged across all compartments, is evident in the wild-type HEK293 cells. Given the behaviour of τ_{bound} observed in figure 6.6b, this apparent anomaly is attributable to an increased percentage decrease in bound NADPH in the wild-type cells induced by the same concentration of EGCG. The precise reduction in binding will be determined by the absolute concentration of bound NADPH in the tissue relative to the concentration of EGCG present (Bisswanger, 2008). This result therefore implies that genetic drift (Hughes et al., 2007) in the wild type cells has caused a lowering of the absolute concentration of NAD(P)H present relative to the lineage from which the genetically modified HEK293 cells are derived.

6.3 NAD(P)H FLIM in the mammalian cochlea

The results presented in this chapter suggest that the NAD(P)H fluorescence decay parameter τ_{bound} can be used to measure the relative abundance of NADPH and NADH in live cells. This ratio can, of course, be measured by traditional biochemical means such as HPLC (Klaidman et al., 1995; Pollak et al., 2007b). However, a microscopy-based method for determining this property has the advantage of making its measurement possible in complex tissue preparations containing diverse networks of different cell types. To demonstrate this, the metabolism of the mammalian cochlea was investigated using NAD(P)H FLIM.

The cochlea is a coiled, fluid-filled duct of the inner ear (Ashmore, 2008). Sound waves passing through the cochlea stimulate sensory cells known as hair cells. These cells convert the mechanical auditory stimulus into a nerve impulse for interpretation by the

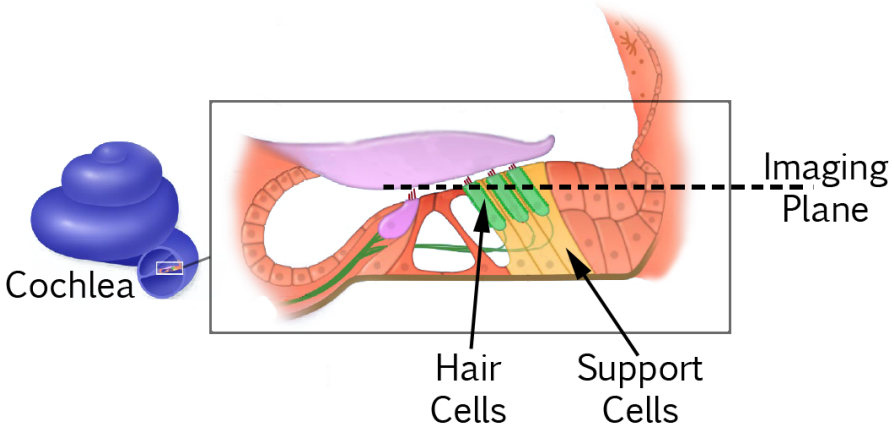

Figure 6.7: Schematic diagram of the mammalian cochlea, adapted from Ashmore (2008).

brain. The hair cells are present in a region of the cochlea known as the Organ of Corti, where they are held in place by a network of support cells, as shown in figure 6.7. This formation is akin to the support role that glial cells provide for neurons in the brain (Allen and Barres, 2009).

Cochlea explant cultures were provided by Dr. Jonathan Gale at the UCL Ear Institute. These were isolated from P2 rats as described by Lahne and Gale (2008). For imaging, explants were adhered to glass coverslips and bathed in HEPES-buffered HBSS (Hanks and Wallace, 1949) containing 5 mM glucose. The cultures appeared as full or partial turns of a flat white coil, occupying a disc of approximately 3 mm in width. FLIM images of NAD(P)H were taken identically as for cell cultures. However, as different cell types exist at increasing depth into the tissue, images were taken at 5 μm z-intervals.

Five separate cochlea explant cultures were imaged, producing a total of 19 FLIM images. Following fitting of a two-component model to the NAD(P)H fluorescence decays at each pixel, the parameters τ_{free} and α_{bound} were observed to be homogeneous across the images at 0.40($\pm$0.01) ns and 0.26($\pm$0.01) respectively. However, τ_{bound} differed between cell type, with one particular group of cells exhibiting an extended fluorescence lifetime of 3.5($\pm$0.1) ns. These were identified as support cells, with the mean value of τ_{bound} measured in hair cells lower at 2.9($\pm$0.1) ns. This partitioning of enzyme-bound fluorescence lifetimes can be observed in the typical images included in figure 6.8, where each cell is colour coded for its mean τ_{bound} value.

The different values of τ_{bound} measured in the hair and support cells of the mammalian cochlea are similar in magnitude to those measured in NADK– and NADK+ cells. To investigate whether the variation of this parameter between the cell types is caused by

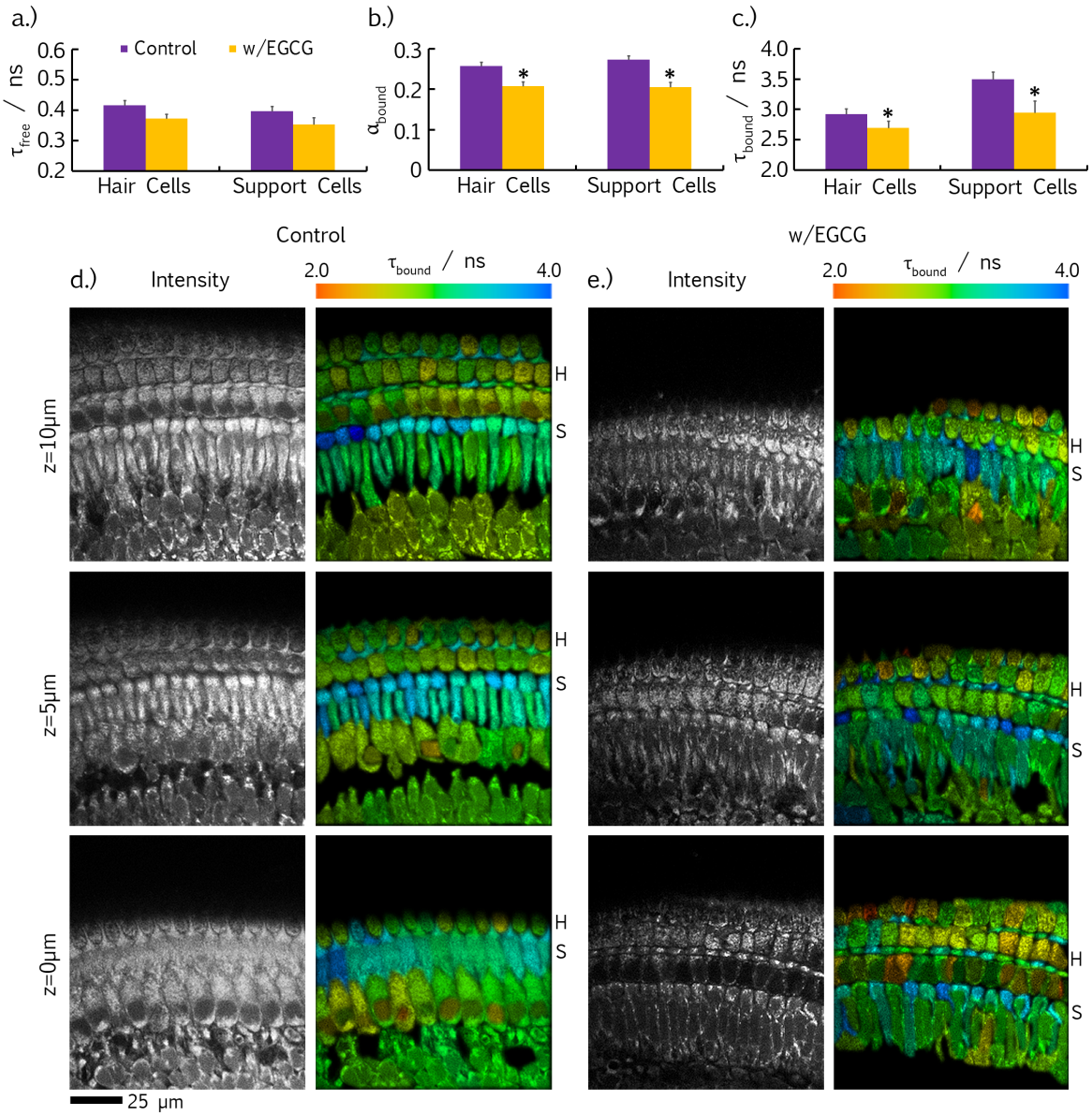

Figure 6.8: Typical values of (a) τ_{free}, (b) α_{bound} and (c) τ_{bound}, measured in hair cells and support cells of the mammalian cochlea under control conditions and upon treatment with EGCG. A row of hair and support cells are labelled in each image as **H** and **S** respectively. In the FLIM images colour-coded for τ_{bound} (d), support cells are seen to exhibit a longer fluorescence lifetime than hair cells, which is decreased upon EGCG treatment (e).

differences in NADPH levels, as in the genetically modified cell lines, three of the cochlea explant cultures were treated with EGCG for 15 minutes and imaged in a neighbouring but separate region from where the control images were taken. The EGCG concentration was increased to 200 μM to account for an expected decrease in the permeability of the thick tissue sample. The results, shown in figure 6.8, indicate that preferential unbinding of NADPH upon the application of EGCG to the cultures is accompanied by a decrease in τ_{bound}. The increased τ_{bound} values measured in the support cells are therefore attributable to increased levels of NADPH, relative to NADH, in this cell type in comparison to the rest of the tissue.

6.4 Conclusions

The experiments discussed in this chapter suggest that the value of τ_{bound} measured in an NAD(P)H FLIM experiment is directly proportional to the fraction of the total bound NAD(P)H pool consisting of NADPH. As this parameter was not consistently affected by changes in the balance of aerobic and anaerobic respiration in the previous chapter, these results suggest that variations in the enzyme bound fluorescence lifetime reported in the NAD(P)H FLIM literature are caused by changes in the relative concentrations of NADPH and NADH in these models.

The simple mathematical model for the dependence on τ_{bound} on the NADPH to NADH ratio developed in this chapter is able to explain the contrasting responses of this parameter in NADK+ and NADK– cells treated with the compound EGCG. This behaviour is caused by τ_{bound} reaching limiting values when the ratio of NADPH to NADH is top- or bottom-heavy. Using this model, the proportion of each cofactor contributing to the NAD(P)H fluorescence intensity can be calculated. This could therefore represent the first method for separating NADPH and NADH fluorescence emission in live cells.

Genetically-encoded probes for NADH and NAD^+ have recently been developed based on resonant energy transfer between fluorescent proteins (Hung et al., 2011; Zhao et al., 2011). It is inevitable, therefore, that an NADPH sensor will follow, allowing variations in the relative abundance of the cofactors to be measured optically without the need for FLIM. The advantage of the approach introduced in this chapter is its applicability to complex tissue models where transfection may be difficult. This was demonstrated here by using NAD(P)H FLIM to observe increased NADPH levels in the support cells of the cochlea. As NADPH is a regulator of biosynthetic pathways, this finding could imply a trophic, as

well as structural, support role for these cells. Such metabolic support is provided by the glia to the neurons in the brain (Allen and Barres, 2009). As NADPH is responsible for maintaining the glutathione defence against reactive oxygen species, perhaps support cells have an increased requirement for protection against oxidative stress. It is obvious that further experiments would be required to investigate the significance of this finding in terms of the physiology of the inner ear. However, the results reported here demonstrate the potential of NAD(P)H FLIM to be a standard tool in the arsenal of imaging approaches to the study of metabolism.

Chapter 7

Discussion and future directions

Explaining the origin of changes in the fluorescence lifetime of NAD(P)H in live cells and tissues is a long standing problem (Schneckenburger and Koenig, 1992; Pradhan et al., 1995; Paul and Schneckenburger, 1996). A large catalogue of work exists demonstrating that the fluorescence decay of NAD(P)H varies between metabolically distinct tissue types (Bird et al., 2005; Evans et al., 2005; Skala et al., 2007a; Ghukasyan and Kao, 2009; Stringari et al., 2012a). However, relatively little is understood about the underlying causes of these changes, both in terms of the biochemical pathways and photophysical phenomena involved.

In this work, the fluorescence decay of NAD(P)H was measured in live cells in response to alterations in energy metabolism. No consistent correlation was found between the parameters describing the NAD(P)H fluorescence decay and shifts between aerobic and anaerobic ATP production. However, the fluorescence lifetime of enzyme bound species was found to increase significantly in the presence of increased concentrations of the cofactor NADPH relative to NADH. Based on computational simulations of the behaviour of τ_{bound}, a model was proposed in which this parameter can be used to calculate the ratio of concentrations of NADPH and NADH present in a cell or subcellular compartment.

The mathematical model developed in chapter 6 for the dependence of τ_{bound} on the NADPH to NADH ratio represents a simple first attempt at quantifying the biochemical determinants of the NAD(P)H fluorescence decay. A concrete test of its validity would be to perform measurements of the concentrations of NADH and NADPH present in a number of cell models using standard laboratory techniques (Klaidman et al., 1995) and compare the results with those predicted by NAD(P)H FLIM. The assumptions inherent in this simple model should then be questioned if its predictions for the NADPH to NADH ratio are found not to reflect measurements made by more traditional means.

In lieu of such experiments, an insight into the effectiveness of the interpretation of τ_{bound} developed in this thesis can be obtained by comparing its implications with the known biochemistry of the models investigated both in this work and in the existing NAD(P)H FLIM literature. To do this, it will be useful to be able to calculate absolute concentrations of NADPH and NADH from the relative measure τ_{bound}. Chapter 5 applied a technique first introduced by Vishwasrao et al. (2005) in which intensity change data is combined with the relative parameter α_{bound} to calculate absolute changes in the free and enzyme-bound populations of a cell. Similarly, from equations 5.4, 5.5 and 6.11, the abundances of NADH and NADPH can be written in terms of the NAD(P)H fluorescence parameters as,

$$[\text{NADH}] = k\left(\frac{\tau_{\text{NADPH}} - \tau_{\text{bound}}}{\tau_{\text{NADPH}} - \tau_{\text{NADH}}}\right)\frac{\langle I_{\text{total}}\rangle}{(1-\alpha_{\text{bound}})\,\tau_{\text{free}} + \alpha_{\text{bound}}\tau_{\text{bound}}} \tag{7.1}$$

$$[\text{NADPH}] = k\left(\frac{\tau_{\text{bound}} - \tau_{\text{NADH}}}{\tau_{\text{NADPH}} - \tau_{\text{NADH}}}\right)\frac{\langle I_{\text{total}}\rangle}{(1-\alpha_{\text{bound}})\,\tau_{\text{free}} + \alpha_{\text{bound}}\tau_{\text{bound}}} \tag{7.2}$$

Calculating these quantities for the NADK+ cells gives concentrations of NADH in the mitochondria, cytosol and nucleus as 1.6(±0.7) au, 1.0(±0.5) au and 2.0(±0.8) au respectively, where k has been chosen such that all measurements are relative to the cytosolic concentration of NADH. The NADPH concentrations in the mitochondria and cytosol are significantly higher, both at 4(±1) au. However, the NADPH and NADH concentrations in the nucleus of these cells are equal. After treatment with EGCG, the NADPH concentrations in all three compartments decrease by an average of 60(±20)%. However, concentrations of NADH remain relatively constant, at 1.5(±0.5) au, 1.2(±0.4) au and 1.6(±0.6) au in the mitochondria, cytosol and nucleus. As these measurements are sensitive to the bound NAD(P)H population only, this result supports the literature demonstrating that EGCG preferentially competes for NADPH binding sites over those of NADH (Wang et al., 2003; Shin et al., 2008).

It is trivial to test the validity of the interpretation of τ_{bound} developed in this thesis in the cells used to parameterise the model. A more informative assessment would be provided by examining the concentrations of NADH and NADPH implied in the cell types of the cochlea using the NAD(P)H FLIM images obtained in this work. In this instance, making comparisons between separate images is not valid due to the variation in detected fluores-

cence intensity with increased depth into the sample. However, relative measurements can be made within each image by setting the value of k such that the concentration of NADH in the hair cells is 1 au.

Applying equations 7.1 and 7.2, the summed concentrations of NADH and NADPH are equal in the hair cells and support cells under control conditions. In the hair cells, the concentration of NADPH is 1.0(±0.2) au and therefore equal to the concentration of NADH in this region. However, in the support cells, the concentration of NADPH is significantly larger at 1.4(±0.3) au with a smaller concentration of NADH at 0.7(±0.2) au. Following EGCG treatment, the concentrations of NADPH in the hair and support cells decrease significantly to 0.8(±0.2) au and 0.9(±0.3) au. The NADH concentration in the support cells following EGCG application remained in the same proportion to the hair cells as under control conditions. As these measurements are made relative to the concentration of NADH in the hair cells, this result again demonstrates the preferential action of this compound on the NADPH binding site.

Despite the apparent dependence of τ_{bound} on the concentration of NADH present relative to the concentration of NADPH, treatments designed to perturb the redox ratio of the NAD^+/NADH pool in the subcellular compartments of HeLa and HEK293 cell lines had relatively little effect on this parameter. If the sole action of a treatment was to oxidise (or reduce) the NADH pool, an associated increase (or decrease) in τ_{bound} would be expected. Small increases in τ_{bound} were observed in HeLa cells treated with the mitochondrial uncoupler FCCP or upon inhibition of glycolysis in the cytosol with deoxyglucose. Applying equations 7.1 and 7.2 to this data shows the intensity, amplitude and lifetime changes correspond to significant decreases in the concentrations of both NADH and NADPH in all compartments.

Removal of glucose and replacement with deoxyglucose will inhibit the pentose phosphate pathway as well as glycolysis. This explains why switching substrates to pyruvate caused a 56(±5)% decrease in NADPH concentration in HeLa cells in addition to a 69(±8)% decrease in NADH. At 49(±12)%, the decrease in NADH concentration was smaller when replacing glucose with lactate, indicating the ability of this substrate to reduce NAD^+ to NADH through lactate dehydrogenase. The corresponding decrease in NADPH of 42(±9)% was also smaller when glucose was replaced by lactate than pyruvate, perhaps indicating the action of malic enzyme using pyruvate to oxidise NADPH in the latter case

(Stickland, 1959).

While increased oxidation of the mitochondrial NAD^+/NADH pool would be expected upon addition of the uncoupler FCCP, the changes in the NAD(P)H fluorescence intensity and decay parameters suggest oxidation of both the NAD^+/NADH and $NADP^+$/NADPH pools. This is likely caused by the action of the mitochondrial transhydrogenase. This enzyme is located on the inner mitochondrial membrane and is able to transfer hydride from NADH to $NADP^+$ or from NADPH to NAD^+. Generation of NADPH is favoured during normal mitochondrial function, powered by translocation of protons from the intermembrane space to the mitochondrial matrix (Huxley et al., 2011). However, upon uncoupling, NADPH is oxidised and the hydride is passed to NAD^+ to produce NADH (Enander and Rydstrom, 1982). The interpretation of NAD(P)H FLIM data developed in this thesis implies the oxidation of both the NAD^+/NADH and $NADP^+$/NADPH pools propagates to all subcellular compartments upon FCCP treatment. NADPH concentrations decreased by an average of 39(±3)% and NADH by 47(±7)%. While the malate-aspartate shuttle is known to facilitate redox transmission of the NAD^+/NADH pool between the mitochondria and cytosol (LaNoue and Williamson, 1971; Barron et al., 1998), these results suggest that the $NADP^+$/NADPH redox state can also be shuttled across the mitochondrial inner membrane.

As with FCCP, changes in the intensity and decay of NAD(P)H fluorescence propagated to all compartments in the majority of attempts to perturb the balance of aerobic and anaerobic metabolism. Despite this, values of τ_{bound} consistently remained smaller in the nucleus compared to the rest of the cell. This feature was common to all cell lines measured. Based on the results of this work, this suggests that the nucleus contains a lower concentration of NADPH relative to NADH than the other subcellular regions. As it can be assumed that NAD^+, $NADP^+$, NADH and NADPH can freely diffuse through the nuclear pores (Zhang et al., 2002), these results indicate that the separate populations of cytosolic and nuclear enzymes maintain the NAD^+/NADH and $NADP^+$/NADPH pools in differing redox states. An enzyme localisation search of the BRENDA database indicates that glyceraldehyde 3-phosphate dehydrogenase (EC 1.2.1.12), the NADH-producing enzyme of the glycolytic pathway, can be found in the nucleus. However, the NADPH-producing enzymes of the pentose phosphate pathway, glucose 6-phosphate dehydrogenase (EC 1.1.1.49) and 6-phosphogluconate dehydrogenase (EC 1.1.1.44), are only found in the cytosol. Decreased production of NADPH in the nucleus is surprising, giving its role in ROS defence and nu-

cleotide synthesis (Berg et al., 2011). However, the BRENDA database findings can explain the lower abundance of NADPH relative to NADH in the nucleus predicted by the interpretation of NAD(P)H FLIM results developed in this thesis.

Further insight into the biological significance of previously published NAD(P)H FLIM studies can be gained in view of the results obtained in this work. For example, a 2009 study by Ogikubo et al. observed a steady increase in the amplitude-weighted mean fluorescence lifetime of NAD(P)H in HeLa cells with decreasing intracellular pH. As the authors measured relatively little pH-induced change of the fluorescence lifetime of NADH in solution, the interpretation of this finding based on the work of this thesis would be the $NADP^+$/NADPH pool becoming more reduced or the NAD^+/NADH pool becoming more oxidised in acidic conditions. In red blood cells, the flux of glucose through glycolysis or the pentose phosphate pathway has been shown to be pH-dependent, with the pentose phosphate pathway favoured in acidic conditions and glycolysis favoured in alkali conditions (Albrecht et al., 1971). Perhaps, therefore, the inverse proportionality between pH and $\left\langle \tau_{NAD(P)H} \right\rangle$ observed by Ogikubo et al. is caused by a shift from NADPH production by the pentose phosphate pathway to NADH production by glycolysis with increasing pH.

In 2008, Niesner et al. performed a novel study on the decay of NAD(P)H fluorescence in granulocytes exposed to *Aspergillus fumigatus* fungus. Granulocytes are white blood cells capable of enveloping invading pathogens by phagocytosis (Alberts et al., 2007). The contents of the subsequent vacuole are neutralised by the action of the enzyme NADPH oxidase. This multisubunit complex is assembled on the vacuolar membrane where it uses NADPH to reduce molecular oxygen. The molar concentration of superoxide, O_2^-, produced inside the vacuole by this "respiratory burst" initiates the breakdown of the pathogen (Segal, 2005). Niesner et al. observed the parameter τ_{bound} to be approximately 2 ns within the majority of the granulocytes. However, localised regions of the cytosol in contact with the fungus displayed τ_{bound} values of 3.7 ns. The authors attributed this to a unique fluorescence lifetime of NADPH when bound to NADPH oxidase.

The computational simulations performed in chapter 5 of this work showed that τ_{bound} represents a weighted average of the fluorescence lifetimes of the enzyme bound NAD(P)H species present. For NADPH oxidase alone to cause an increase in τ_{bound} as significant as that observed in the granulocytes would require this enzyme to be present in a greater concentration than the NADH-binding enzymes of the cytosol. A search of the Model Or-

ganism Protein Expression Database (MOPED, Kolker et al., 2012) within the GeneCards human gene compendium (Rebhan et al., 1997) shows that expression of glyceraldehyde 3-phosphate dehydrogenase outweighs that of the NADPH-binding subunit of NADPH oxidase (neutrophil cytosolic factor 2, Shatwell and Segal, 1996) by around 100 to one in white blood cells. It is therefore more likely that the NAD(P)H fluorescence lifetime observed in the regions of the cytosol where NADPH oxidase is activated is, as implied by the results of chapter 6, due to increased local NADPH production. Production of large quantities of superoxide by NADPH oxidase requires plentiful supply of NADPH. Activation of this enzyme therefore causes increased flux of glucose through the pentose phosphate pathway (Iyer et al., 1961). This association between the respiratory burst and upregulated NADPH production could have been predicted by combining the results of Niesner et al. and the interpretation of NAD(P)H fluorescence decays developed in this thesis.

A significant driving force in the original development of fluorescence lifetime imaging of NAD(P)H was its potential as a tool for the clinical diagnosis of cancer. Suggestions of this application were based on the logic that the local environment of the fluorescent metabolic cofactors should be altered during the metabolic shifts associated with tumour progression. Correlations between carcinogenesis and NAD(P)H fluorescence lifetime changes have been reported many times (for example Pradhan et al., 1995; Bird et al., 2005; Skala et al., 2007a) and diagnostic instruments based on these measurements have been constructed as a result (for example Mycek et al., 1998; Colasanti et al., 2000; Butte et al., 2005; Sud et al., 2006). While a belief exists that these NAD(P)H fluorescence decay changes are somehow caused by the Warburg effect, no mechanism has yet been proposed.

In the work of Bird et al. (2005) and Skala et al. (2007a), the Warburg effect was suggested to be manifest in a decreased value of τ_{bound} in cancerous tissue relative to healthy tissue. The behaviour of this parameter revealed in this thesis could be used to explain such a response. The hypoxic environment of the tumour will cause the rate of NADH oxidation by the electron transport chain to decrease while the NADPH concentration remains constant (Shigemori et al., 1996). This will increase the NADH to NADPH ratio, thereby decreasing τ_{bound}. This interpretation assumes that the upregulation of glycolysis in response to the selective pressure of the hypoxic tumour microenvironment is the only metabolic difference between the two tissue types. However, since the Warburg hypothesis was first proposed, shifts in metabolism during carcinogenesis have been shown to be more

complex than this (Vander Heiden et al., 2009; Gottlieb and Vousden, 2010). For example, the tumour suppressor gene p53 has been shown to have a direct inhibitory effect on glucose 6-phosphate dehydrogenase, preventing entry of glucose into the pentose phosphate pathway (Jiang et al., 2011). Mutation of p53 therefore permits an increase in the level of NADPH, a necessary step to fulfill the increased demand for synthesis of lipids and nucleic acids in a rapidly proliferating cell population (Gottlieb, 2011).

Despite inactivation of p53 in the transformed mesenchymal stem cell lines investigated in chapter 5 of this work, the presence of additional oncogenes has been shown to cause the pentose phosphate pathway to be downregulated in the 4H and 5H cell lines (Funes et al., 2007). This could have been implied from the lower value of τ_{bound} in these cell lines relative to the 1H and 3H cells. As demonstrated by these cell lines, the continuous interplay of genetic and metabolic changes during carcinogenesis will cause variations in the concentrations of NADH and NADPH throughout the gradual transformation from healthy tissue into aggressive tumour. Therefore, in order for the viability of detection and prognosis by autofluorescence lifetime approaches to be assessed, further work must be performed to correlate cancer progression with the abundance of these cofactors. Cancer could not be diagnosed based on the ratio of NADPH to NADH alone. However, NAD(P)H FLIM could be combined with other spectroscopic techniques, such as Raman spectroscopy (Almond et al., 2012), as part of a multimodal biophotonic diagnostic device for the staging of accessible tumours (Periasamy and Clegg, 2010).

The above discussion demonstrates that the relationship between τ_{bound} and the intracellular levels of NADPH and NADH revealed in this thesis is consistent with the known biochemistry of the models investigated in this work and reported in the NAD(P)H FLIM literature. Further work is required to confirm whether the quantification of this relationship, performed with the simple mathematical model developed in chapter 6, provides an accurate representation of the precise NADPH and NADH levels within a cell. Nevertheless, the discovered relationship suggests that enzyme bound NADH and enzyme bound NADPH possess distinct fluorescence lifetimes inside the cell. In chapter 6 it was predicted that these two lifetimes were 1.5($\pm$0.2) ns and 4.4($\pm$0.2) ns respectively. The reductionist stance would dictate that these contrasting fluorescence lifetimes require a photophysical explanation before NAD(P)H FLIM can be accepted as a standard laboratory technique for quantifying the relative abundance of the two cofactors. However, why, inside the environ-

ment of the cell, enzyme-bound NADPH should be associated with a significantly longer fluorescence lifetime than enzyme-bound NADH is not obvious. In chapter 3 of this work, it was demonstrated that the non-radiative decay of NADH and NADPH can be described by one-dimensional activated barrier crossing, suggesting that the large non-radiative rates of NADH and NADPH are due to an internal conversion process based on conformational relaxation. Differences in the fluorescence lifetime of NADH and NADPH when bound to their respective enzymes should therefore be caused by variations in the level of conformational restriction of the cofactors in their corresponding binding sites. However, significantly greater conformational restriction of the nicotinamide moiety within the NADPH binding site relative to the NADH binding site is unlikely as the nicotinamide-binding regions are similar in both structures. Discrimination between the two cofactors is realised at the adenine end of the molecule (Scrutton et al., 1990).

In table 1.1 it can be seen that previously reported values of the fluorescence lifetime of NADH and NADPH bound to enzymes in solution are of the order of 1.6($\pm$0.7) ns, similar to the value of τ_{NADH} predicted in this work. It is only upon the binding of a substrate in addition to the cofactor that the observed fluorescence lifetimes become large enough to account for the intracellular value of τ_{NADPH} inferred here. A molecular-level explanation for the contrasting fluorescence lifetimes of enzyme bound NADH and NADPH may therefore require a mechanism in which NADPH is more likely to be bound to an enzyme upon which a substrate is simultaneously present, and NADH more likely to be bound to an otherwise unoccupied enzyme. Perhaps a mechanism such as this must be linked to the canonical redox reactions that the two cofactors are involved in, with NADPH donating reducing equivalents for reductive biosynthesis and NADH produced after receiving reducing equivalents from catabolic processes.

A large number of crystal structures of NADH and NADPH bound to various enzymes in the presence and absence of additional substrates are available on the RCSB Protein Data Bank (Bernstein et al., 1977). These could be studied in order to understand conformational restriction of the nicotinamide moiety in different NAD(P)H binding configurations. Relating the findings of this work back to the corresponding fluorescence lifetimes of the cofactors would require a knowledge of which bonds play a role in the conformational freedom, and therefore non-radiative rate, of NAD(P)H. This could be provided by measuring the fluorescence lifetimes of chemically-synthesised NAD(P)H analogues in which

the fluorescent moiety is made more rigid by restricting specific internal motions. Such experiments may also elucidate the origins of the biexponential decay of NADH and NADPH when free in solution. The work of this thesis demonstrated that the two fluorescent species correspond to different molecular configurations, perhaps with alternate cis/trans geometries of the amide group of the nicotinamide moiety. However, more precise details of these configurations remain unknown.

Evidently, many questions remain to be answered regarding the molecular mechanism and range of validity of the biochemical interpretation of the fluorescence decay of intracellular NAD(P)H developed in this thesis. However, the results presented here represent a first step towards remedying the lack of interpretive theories amongst the vast range of published NAD(P)H FLIM studies. NAD(P)H FLIM shows promise as the first method for separating the fluorescence emission of NADH and NADPH in live biological samples. As such, the technique could find widespread use, given the importance of NADH and NADPH in processes ranging from development (Dumollard et al., 2007) to ageing (Brandes et al., 2013). Before becoming a standard laboratory technique, the arduous nature of the data analysis process would have to be remedied to improve user-friendliness, perhaps by replacing the notoriously slow pixel-by-pixel iterative reconvolution with a more novel approach (Digman et al., 2008; Stringari et al., 2012b). Nevertheless, within this work, the potential has been demonstrated for NAD(P)H FLIM to be used to study variation between the cell types of complex tissues in the most fundamental of metabolic pathways. Such measurements would be inaccessible using traditional biochemical methods.

Bibliography

Alberts, B., Johnson, A., Lewis, J., Raff, M., Roberts, K., and Walter, P. (2007). *Molecular Biology of the Cell*. Garland Science, fifth edition.

Albinsson, B. and Norden, B. (1992). Excited-state properties of the indole chromophore: electronic transition moment directions from linear dichroism measurements: effect of methyl and methoxy substituents. *The Journal of Physical Chemistry*, 96(15):6204–6212.

Albrecht, V., Roigas, H., Schultze, M., Jacobasch, G., and Rapoport, S. (1971). The influence of pH and methylene blue on the pathways of glucose utilization and lactate formation in erythrocytes of man. *European Journal of Biochemistry*, 20(1):44–50.

Allen, N. J. and Barres, B. A. (2009). Neuroscience: Glia - more than just brain glue. *Nature*, 457(7230):675–677.

Almond, L. M., Hutchings, J., Kendall, C., Day, J. C. C., Stevens, O. A. C., Lloyd, G. R., Shepherd, N. A., Barr, H., and Stone, N. (2012). Assessment of a custom-built Raman spectroscopic probe for diagnosis of early oesophageal neoplasia. *Journal of Biomedical Optics*, 17(8):081421–1.

Ashmore, J. (2008). Cochlear outer hair cell motility. *Physiological Reviews*, 88(1):173–210.

Atkins, P. and De Paula, J. (2010). *Atkins' Physical Chemistry*. Oxford University Press.

Atkins, P. and Friedman, R. (2010). *Molecular Quantum Mechanics*. OUP Oxford.

Aubin, J. E. (1979). Autofluorescence of viable cultured mammalian cells. *J Histochem Cytochem*, 27(1):36–43.

Barron, J. T., Gu, L., and Parrillo, J. E. (1998). Malate-aspartate shuttle, cytoplasmic NADH redox potential, and energetics in vascular smooth muscle. *Journal of Molecular and Cellular Cardiology*, 30(8):1571–1579.

Becker, W. (2012). *The bh TCSPC Handbook*. Becker & Hickl, fifth edition.

Berg, J., Tymoczko, J., and Stryer, L. (2011). *Biochemistry*. W.H. Freeman, international seventh edition.

Berger, F., Ramirez-Hernandez, M. H., and Ziegler, M. (2004). The new life of a centenarian: signalling functions of NAD(P). *Trends Biochem Sci*, 29(3):111–118.

Berne, B. and Pecora, R. (1976). *Dynamic Light Scattering: With Applications to Chemistry, Biology, and Physics*. Dover Books on Physics Series. Dover Publications.

Bernstein, F. C., Koetzle, T. F., Williams, G. J. B., Meyer Jr, E. F., Brice, M. D., Rodgers, J. R., Kennard, O., Shimanouchi, T., and Tasumi, M. (1977). The protein data bank: A computer-based archival file for macromolecular structures. *Journal of Molecular Biology*, 112(3):535–542.

Billinton, N. and Knight, A. W. (2001). Seeing the wood through the trees: A review of techniques for distinguishing green fluorescent protein from endogenous autofluorescence. *Analytical Biochemistry*, 291(2):175–197.

Bindhu, C., Harilal, S., Varier, G., Issac, R., Nampoori, V., and Vallabhan, C. (1996). Measurement of the absolute fluorescence quantum yield of rhodamine B solution using a dual-beam thermal lens technique. *Journal of Physics D: Applied Physics*, 29(4):1074.

Bird, D. K., Yan, L., Vrotsos, K. M., Eliceiri, K. W., Vaughan, E. M., Keely, P. J., White, J. G., and Ramanujam, N. (2005). Metabolic mapping of MCF10A human breast cells via multiphoton fluorescence lifetime imaging of the coenzyme NADH. *Cancer Research*, 65(19):8766–8773.

Bisswanger, H. (2008). *Enzyme Kinetics*. Wiley.

Biswas, R. and Bagchi, B. (1996). Activated barrier crossing dynamics in slow, viscous liquids. *The Journal of Chemical Physics*, 105(17):7543–7549.

Blacker, T. S., Marsh, R. J., Duchen, M. R., and Bain, A. J. (2013). Activated barrier crossing dynamics in the non-radiative decay of NADH and NADPH. *Chemical Physics*, In Press.

Blinova, K., Carroll, S., Bose, S., Smirnov, A. V., Harvey, J. J., Knutson, J. R., and Balaban, R. S. (2005). Distribution of mitochondrial NADH fluorescence lifetimes: Steady-state kinetics of matrix NADH interactions. *Biochemistry*, 44(7):2585–2594.

Bogaerts, A. and Gijbels, R. (1998). Argon and copper optical emission spectra in a grimm glow discharge source: mathematical simulations and comparison with experiment. *Journal of Analytical Atomic Spectrometry*, 13(8):721–726.

Brand, M. D., Affourtit, C., Esteves, T. C., Green, K., Lambert, A. J., Miwa, S., Pakay, J. L., and Parker, N. (2004). Mitochondrial superoxide: production, biological effects, and activation of uncoupling proteins. *Free Radical Biology and Medicine*, 37(6):755–767.

Brandes, N., Tienson, H., Lindemann, A., Vitvitsky, V., Reichmann, D., Banerjee, R., and Jakob, U. (2013). Time line of redox events in aging postmitotic cells. *eLife*, 2.

Brochon, J. C., Wahl, P., Jallon, J. M., and Iwatsubo, M. (1976). Pulse fluorimetry study of beef liver glutamate dehydrogenase-reduced nicotinamide adenine dinucleotide phosphate complexes. *Biochemistry*, 15(15):3259–3265.

Bryan, T. M. and Reddel, R. R. (1997). Telomere dynamics and telomerase activity in in vitro immortalised human cells. *European Journal of Cancer*, 33(5):767–773.

Butte, P. V., Pikul, B. K., Hever, A., Yong, W. H., Black, K. L., and Marcu, L. (2005). Diagnosis of meningioma by time-resolved fluorescence spectroscopy. *Journal of Biomedical Optics*, 10(6):064026–9.

Callis, P. R. (1993). On the theory of two-photon induced fluorescence anisotropy with application to indoles. *The Journal of Chemical Physics*, 99(1):27–37.

Capiod, T., Shuba, Y., Skryma, R., and Prevarskaya, N. (2007). Calcium signalling and cancer cell growth. *Subcell Biochem*, 45:405–27.

Carew, J. S. and Huang, P. (2002). Mitochondrial defects in cancer. *Mol Cancer*, 1(9):9.

Chadborn, N., Bryant, J., Bain, A. J., and O'Shea, P. (1999). Ligand-dependent conformational equilibria of serum albumin revealed by tryptophan fluorescence quenching. *Biophys J*, 76(4):2198–207.

Chance, B., Cohen, P., Jobsis, F., and Schoener, B. (1962). Intracellular oxidation-reduction states in vivo. *Science*, 137:499–508.

Cheng, N.-S. (2008). Formula for the viscosity of a glycerol-water mixture. *Industrial & Engineering Chemistry Research*, 47(9):3285–3288.

Cheng, R. R., Uzawa, T., Plaxco, K. W., and Makarov, D. E. (2009). The rate of intramolecular loop formation in DNA and polypeptides: The absence of the diffusion-controlled limit and fractional power-law viscosity dependence. *The Journal of Physical Chemistry B*, 113(42):14026–14034.

Chin, L., Tam, A., Pomerantz, J., Wong, M., Holash, J., Bardeesy, N., Shen, Q., O'Hagan, R., Pantginis, J., Zhou, H., Horner, J. W., Cordon-Cardo, C., Yancopoulos, G. D., and DePinho, R. A. (1999). Essential role for oncogenic Ras in tumour maintenance. *Nature*, 400(6743):468–472.

Clasquin, M., Melamud, E., Singer, A., Gooding, J., Xu, X., Dong, A., Cui, H., Campagna, S., Savchenko, A., Yakunin, A., Rabinowitz, J., and Caudy, A. (2011). Riboneogenesis in yeast. *Cell*, 145(6):969–980.

Coherent (2013). *Mira Optima 900-F Laser Operator's Manual*.

Colasanti, A., Kisslinger, A., Fabbrocini, G., Liuzzi, R., Quarto, M., Riccio, P., Roberti, G., and Villani, F. (2000). MS-2 fibrosarcoma characterization by laser induced autofluorescence. *Lasers in Surgery and Medicine*, 26(5):441–448.

Cole, M. J., Siegel, J., Webb, S. E. D., Jones, R., Dowling, K., Dayel, M. J., Parsons-Karavassilis, D., French, P. M. W., Lever, M. J., Sucharov, L. O. D., Neil, M. A. A., Juskaitis, R., and Wilson, T. (2001). Time-domain whole-field fluorescence lifetime imaging with optical sectioning. *Journal of Microscopy*, 203(3):246–257.

Colegrove, L. F. and Laane, J. (1991). Vibrational spectra, ring-puckering potential energy function, and conformation of 1,3-disilacyclopent-4-ene. *The Journal of Physical Chemistry*, 95(17):6494–6499.

Couprie, M. E., Merola, F., Tauc, P., Garzella, D., Delboulbe, A., Hara, T., and Billardon, M. (1994). First use of the UV super-ACO free-electron laser: Fluorescence decays and rotational dynamics of the NADH coenzyme. *Review of Scientific Instruments*, 65(5):1485–1495.

Cross, A. J. and Fleming, G. R. (1984). Analysis of time-resolved fluorescence anisotropy decays. *Biophys J*, 46(1):45–56.

Dang, C. V. (2012). Links between metabolism and cancer. *Genes Dev*, 26(9):877–90.

Davidson, S. M., Yellon, D. M., Murphy, M. P., and Duchen, M. R. (2012). Slow calcium waves and redox changes precede mitochondrial permeability transition pore opening in the intact heart during hypoxia and reoxygenation. *Cardiovascular Research*, 93(3):445–453.

De Beule, P. A., Dunsby, C., Galletly, N. P., Stamp, G. W., Chu, A. C., Anand, U., Anand, P., Benham, C. D., Naylor, A., and French, P. M. (2007). A hyperspectral fluorescence lifetime probe for skin cancer diagnosis. *Rev Sci Instrum*, 78(12):123101.

De Ruyck, J., Fameree, M., Wouters, J., Perpete, E. A., Preat, J., and Jacquemin, D. (2007). Towards the understanding of the absorption spectra of NAD(P)H/NAD(P)+ as a common indicator of dehydrogenase enzymatic activity. *Chemical Physics Letters*, 450(1-3):119–122.

Denk, W., Strickler, J. H., and Webb, W. W. (1990). Two-photon laser scanning fluorescence microscopy. *Science*, 248(4951):73–76.

DePinho, R. A. (2000). The age of cancer. *Nature*, 408(6809):248–54.

Digman, M. A., Caiolfa, V. R., Zamai, M., and Gratton, E. (2008). The phasor approach to fluorescence lifetime imaging analysis. *Biophys J*, 94(2):L14–6.

Dix, J. A. and Verkman, A. S. (1990). Mapping of fluorescence anisotropy in living cells by ratio imaging. application to cytoplasmic viscosity. *Biophysical Journal*, 57(2):231–240.

Du, H., Fuh, R. C. A., Li, J., Corkan, L. A., and Lindsey, J. S. (1998). PhotochemCAD: A computer-aided design and research tool in photochemistry. *Photochemistry and Photobiology*, 68(2):141–142.

Duchen, M. R. (2004). Mitochondria in health and disease: perspectives on a new mitochondrial biology. *Mol Aspects Med*, 25(4):365–451.

Duchen, M. R., Surin, A., and Jacobson, J. (2003). Imaging mitochondrial function in intact cells. *Methods Enzymol*, 361:353–89.

Dumollard, R., Ward, Z., Carroll, J., and Duchen, M. R. (2007). Regulation of redox metabolism in the mouse oocyte and embryo. *Development*, 134(3):455–65.

Dutt, G. B. (2005). Molecular rotation as a tool for exploring specific solute-solvent interactions. *Chemphyschem*, 6(3):413–8.

Dutt, G. B., Doraiswamy, S., Periasamy, N., and Venkataraman, B. (1990). Rotational reorientation dynamics of polar dye molecular probes by picosecond laser spectroscopic technique. *The Journal of Chemical Physics*, 93(12):8498–8513.

Dux, H. and Dorfmuller, T. (1979). Reorientation in associated liquids: I glycerol. *Chemical Physics*, 40:219 – 227.

Efremov, R. G., Baradaran, R., and Sazanov, L. A. (2010). The architecture of respiratory complex I. *Nature*, 465(7297):441–445.

Egorov, A. V., Lyubartsev, A. P., and Laaksonen, A. (2011). Molecular dynamics simulation study of glycerol-water liquid mixtures. *The Journal of Physical Chemistry B*, 115(49):14572–14581.

Enander, K. and Rydstrom, J. (1982). Energy-linked nicotinamide nucleotide transhydrogenase. kinetics and regulation of purified and reconstituted transhydrogenase from beef heart mitochondria. *Journal of Biological Chemistry*, 257(24):14760–14766.

Enderlein, J. and Erdmann, R. (1997). Fast fitting of multi-exponential decay curves. *Optics Communications*, 134(1-6):371–378.

Evans, G. T. and Kivelson, D. (1986). The orientational-correlation time intercept in liquids. *The Journal of Chemical Physics*, 84(1):385–390.

Evans, N. D., Gnudi, L., Rolinski, O. J., Birch, D. J. S., and Pickup, J. C. (2005). Glucose-dependent changes in NAD(P)H-related fluorescence lifetime of adipocytes and fibroblasts in vitro: Potential for non-invasive glucose sensing in diabetes mellitus. *Journal of Photochemistry and Photobiology B: Biology*, 80(2):122–129.

Ferguson, S. J. (2010). ATP synthase: From sequence to ring size to the p/o ratio. *Proceedings of the National Academy of Sciences*, 107(39):16755–16756.

Feynman, R. P. (1970). *Feynman lectures on physics*. Addison Wesley Longman.

Fischer, G. and Cao, X. (1999). Vibrational analysis and ring-puckering inversion barrier of perfluorocyclopentene. *The Journal of Physical Chemistry A*, 103(19):3726–3731.

Fisz, J. J. (2007). Another look at magic-angle-detected fluorescence and emission anisotropy decays in fluorescence microscopy. *The Journal of Physical Chemistry A*, 111(50):12867–12870.

Fletcher, R. (1971). *A Modified Marquardt Subroutine for Non-linear Least Squares*. Theoretical Physics Division, Atomic Energy Research Establishment.

Funes, J. M., Quintero, M., Henderson, S., Martinez, D., Qureshi, U., Westwood, C., Clements, M. O., Bourboulia, D., Pedley, R. B., Moncada, S., and Boshoff, C. (2007). Transformation of human mesenchymal stem cells increases their dependency on oxidative phosphorylation for energy production. *Proceedings of the National Academy of Sciences*, 104(15):6223–6228.

Gafni, A. and Brand, L. (1976). Fluorescence decay studies of reduced nicotinamide adenine dinucleotide in solution and bound to liver alcohol dehydrogenase. *Biochemistry*, 15(15):3165–3171.

Gangamallaiah, V. and Dutt, G. B. (2011). Photoisomerization dynamics of 3,3'-diethyloxadicarbocyanine iodide in ionic liquids: Breakdown of hydrodynamic kramers model. *The Journal of Chemical Physics*, 135(17):174505–7.

Gehlsen, U., Oetke, A., Szaszak, M., Koop, N., Paulsen, F., Gebert, A., Huettmann, G., and Steven, P. (2012). Two-photon fluorescence lifetime imaging monitors metabolic changes during wound healing of corneal epithelial cells in vitro. *Graefe's Archive for Clinical and Experimental Ophthalmology*, 250(9):1293–1302.

Ghukasyan, V. V. and Kao, F.-J. (2009). Monitoring cellular metabolism with fluorescence lifetime of reduced nicotinamide adenine dinucleotide. *The Journal of Physical Chemistry C*, 113(27):11532–11540.

Goeppert-Mayer, M. (1931). Elementary processes with two quantum transitions. *Annalen der Physik*, 401(3):273–294.

Gohil, V. M., Sheth, S. A., Nilsson, R., Wojtovich, A. P., Lee, J. H., Perocchi, F., Chen, W., Clish, C. B., Ayata, C., Brookes, P. S., and Mootha, V. K. (2010). Nutrient-sensitized screening for drugs that shift energy metabolism from mitochondrial respiration to glycolysis. *Nat Biotech*, 28(3):249–255.

Gottlieb, E. (2011). p53 guards the metabolic pathway less travelled. *Nat Cell Biol*, 13(3):195–197.

Gottlieb, E. and Vousden, K. H. (2010). p53 regulation of metabolic pathways. *Cold Spring Harb Perspect Biol*, 2(4):a001040.

Gray, M. W. (2012). Mitochondrial evolution. *Cold Spring Harbor Perspectives in Biology*, 4(9).

Griesinger, C. B., Richards, C. D., and Ashmore, J. F. (2005). Fast vesicle replenishment allows indefatigable signalling at the first auditory synapse. *Nature*, 435(7039):212–215.

Hanks, J. H. and Wallace, R. E. (1949). Relation of oxygen and temperature in the preservation of tissues by refrigeration. *Proceedings of the Society for Experimental Biology and Medicine. Society for Experimental Biology and Medicine (New York, N.Y.)*, 71(2):196–200.

Hannon, G. J. (2002). RNA interference. *Nature*, 418(6894):244–251.

Harris, D. A., Orozco, M. B., and Sension, R. J. (2006). Solvent dependent conformational relaxation of cis-1,3,5-hexatriene. *The Journal of Physical Chemistry A*, 110(30):9325–9333.

Hecht, E. and Zajac, A. (1974). *Optics*. Addison Wesley.

Heikal, A. A. (2010). Intracellular coenzymes as natural biomarkers for metabolic activities and mitochondrial anomalies. *Biomarkers in Medicine*, 4(2):241–263.

Hell, S. W., Booth, M., Wilms, S., Schnetter, C. M., Kirsch, A. K., Arndt-Jovin, D. J., and Jovin, T. M. (1998). Two-photon near- and far-field fluorescence microscopy with continuous-wave excitation. *Opt. Lett.*, 23(15):1238–1240.

Helmchen, F. and Denk, W. (2005). Deep tissue two-photon microscopy. *Nat Meth*, 2(12):932–940.

Herzig, S., Raemy, E., Montessuit, S., Veuthey, J.-L., Zamboni, N., Westermann, B., Kunji, E. R. S., and Martinou, J.-C. (2012). Identification and functional expression of the mitochondrial pyruvate carrier. *Science*, 337(6090):93–96.

Hiyama, E. and Hiyama, K. (2007). Telomere and telomerase in stem cells. *Br J Cancer*, 96(7):1020–1024.

Hochstrasser, R. M. (1980). Picosecond processes in the isomerism of stilbenes. *Pure & Applied Chemistry*, 52(12):2683–2691.

Hopt, A. and Neher, E. (2001). Highly nonlinear photodamage in two-photon fluorescence microscopy. *Biophysical Journal*, 80(4):2029–2036.

Hoyt, L. F. (1934). New table of the refractive index of pure glycerol at 20c. *Industrial & Engineering Chemistry*, 26(3):329–332.

Huang, S., Heikal, A. A., and Webb, W. W. (2002). Two-photon fluorescence spectroscopy and microscopy of NAD(P)H and flavoprotein. *Biophys J*, 82(5):2811–25.

Hughes, I. and Hase, T. (2010). *Measurements and Their Uncertainties: A Practical Guide to Modern Error Analysis*. OUP Oxford.

Hughes, P., Marshall, D., Reid, Y., Parkes, H., and Gelber, C. (2007). The costs of using unauthenticated, over-passaged cell lines: how much more data do we need? *Biotechniques*, 43(5):575.

Hull, R. V., Conger, P. S., and Hoobler, R. J. (2001). Conformation of NADH studied by fluorescence excitation transfer spectroscopy. *Biophys Chem*, 90(1):9–16.

Hung, Y., Albeck, J., Tantama, M., and Yellen, G. (2011). Imaging cytosolic NADH-NAD+ redox state with a genetically encoded fluorescent biosensor. *Cell Metabolism*, 14(4):545–554.

Hurley, M. M. and Hammes-Schiffer, S. (1997). Development of a potential surface for simulation of proton and hydride transfer reactions in solution: Application to NADH hydride transfer. *The Journal of Physical Chemistry A*, 101(21):3977–3989.

Huxley, L., Quirk, P. G., Cotton, N. P. J., White, S. A., and Jackson, J. B. (2011). The specificity of proton-translocating transhydrogenase for nicotinamide nucleotides. *Biochimica et Biophysica Acta (BBA) - Bioenergetics*, 1807(1):85–94.

Ibsen, K. H. (1961). The Crabtree effect: A review. *Cancer Research*, 21(7):829–841.

Iyer, G. Y. N., Islam, M. F., and Quastel, J. H. (1961). Biochemical aspects of phagocytosis. *Nature*, 192(4802):535–541.

Jas, G. S., Eaton, W. A., and Hofrichter, J. (2000). Effect of viscosity on the kinetics of helix and hairpin formation. *The Journal of Physical Chemistry B*, 105(1):261–272.

Jee, A.-Y., Bae, E., and Lee, M. (2010). Internal motion of an electronically excited molecule in viscoelastic media. *The Journal of Chemical Physics*, 133(1):014507–8.

Jiang, P., Du, W., Wang, X., Mancuso, A., Gao, X., Wu, M., and Yang, X. (2011). p53 regulates biosynthesis through direct inactivation of glucose-6-phosphate dehydrogenase. *Nat Cell Biol*, 13(3):310–316.

Johnson, I. and Spence, M. (2010). *Molecular Probes Handbook, A Guide to Fluorescent Probes and Labeling Technologies*. Invitrogen, 11th edition.

Kasischke, K. A., Vishwasrao, H. D., Fisher, P. J., Zipfel, W. R., and Webb, W. W. (2004). Neural activity triggers neuronal oxidative metabolism followed by astrocytic glycolysis. *Science*, 305(5680):99–103.

Katan, C., Tretiak, S., Werts, M. H. V., Bain, A. J., Marsh, R. J., Leonczek, N., Nicolaou, N., Badaeva, E., Mongin, O., and Blanchard-Desce, M. (2007). Two-photon transitions in quadrupolar and branched chromophores: Experiment and theory. *The Journal of Physical Chemistry B*, 111(32):9468–9483.

Kierdaszuk, B., Malak, H., Gryczynski, I., Callis, P., and Lakowicz, J. R. (1996). Fluorescence of reduced nicotinamides using one- and two-photon excitation. *Biophysical Chemistry*, 62(1-3):1–13.

Kitano, H. (2002). Systems biology: A brief overview. *Science*, 295(5560):1662–1664.

Klaidman, L. K., Leung, A. C., and Adams, J. D. (1995). High-performance liquid chromatography analysis of oxidized and reduced pyridine dinucleotides in specific brain regions. *Analytical Biochemistry*, 228(2):312–317.

Knudson, A. G. (2001). Two genetic hits (more or less) to cancer. *Nat Rev Cancer*, 1(2):157–162.

Ko, C. W., Wei, Z., Marsh, R. J., Armoogum, D. A., Nicolaou, N., Bain, A. J., Zhou, A., and Ying, L. (2009). Probing nanosecond motions of plasminogen activator inhibitor-1 by time-resolved fluorescence anisotropy. *Molecular BioSystems*, 5(9):1025–1031.

Koenig, S. H. (1975). Brownian motion of an ellipsoid. a correction to Perrin's results. *Biopolymers*, 14(11):2421–2423.

Kolker, E., Higdon, R., Haynes, W., Welch, D., Broomall, W., Lancet, D., Stanberry, L., and Kolker, N. (2012). MOPED: Model organism protein expression database. *Nucleic Acids Res*, 40(Database issue):D1093–9.

Konig, K., Berns, M. W., and Tromberg, B. J. (1997). Time-resolved and steady-state fluorescence measurements of beta-nicotinamide adenine dinucleotide-alcohol dehydrogenase complex during UVA exposure. *J Photochem Photobiol B*, 37(1-2):91–5.

Konig, K. and Riemann, I. (2003). High-resolution multiphoton tomography of human skin with subcellular spatial resolution and picosecond time resolution. *Journal of Biomedical Optics*, 8(3):432–439.

Kramers, H. (1940). Brownian motion in a field of force and the diffusion model of chemical reactions. *Physica*, 7(4):284–304.

Krishnamoorthy, G., Periasamy, N., and Venkataraman, B. (1987). On the origin of heterogeneity of fluorescence decay kinetics of reduced nicotinamide adenine dinucleotide. *Biochem Biophys Res Commun*, 144(1):387–92.

Kubinyi, M., Grofcsik, A., Karpati, T., and Jones, W. J. (2006). Rotational reorientation dynamics of ionic dye solutes in polar solvents with the application of a general model for the solvation shell. *Chemical Physics*, 322(3):247–253.

Kuhlman, T. S., Solling, T. I., and Moller, K. B. (2012). Coherent motion reveals non-ergodic nature of internal conversion between excited states. *Chemphyschem*, 13(3):820–7.

Kumar, M., Jaiswal, S., Singh, R., Srivastav, G., Singh, P., Yadav, T. N., and Yadav, R. A. (2010). Ab initio studies of molecular structures, conformers and vibrational spectra of heterocyclic organics: I. nicotinamide and its n-oxide. *Spectrochimica Acta Part A: Molecular and Biomolecular Spectroscopy*, 75(1):281–292.

Ladokhin, A. and Brand, L. (1995). Evidence for an excited-state reaction contributing to NADH fluorescence. *Journal of Fluorescence*, 5:99–106.

Lahne, M. and Gale, J. E. (2008). Damage-induced activation of ERK1/2 in cochlear supporting cells is a hair cell death-promoting signal that depends on extracellular ATP and calcium. *J Neurosci*, 28(19):4918–28.

Lakowicz, J. (1992). *Techniques*, volume 1 of *Topics in Fluorescence Spectroscopy*. Springer.

Lakowicz, J. (1997). *Nonlinear and Two-photon-induced Fluorescence*, volume 5 of *Topics in Fluorescence Spectroscopy*. Springer.

Lakowicz, J. (2006). *Principles of Fluorescence Spectroscopy*. Springer, third edition.

Lakowicz, J. R. and Berndt, K. W. (1991). Lifetime-selective fluorescence imaging using an RF phase-sensitive camera. *Review of Scientific Instruments*, 62(7):1727–1734.

Lakowicz, J. R., Szmacinski, H., Nowaczyk, K., and Johnson, M. L. (1992). Fluorescence lifetime imaging of free and protein-bound NADH. *Proceedings of the National Academy of Sciences of the United States of America*, 89(4):1271–1275.

Lane, N. (2002). *Oxygen: The Molecule That Made the World*. Popular Science. Oxford University Press.

Lane, N., Allen, J. F., and Martin, W. (2010). How did LUCA make a living? Chemiosmosis in the origin of life. *Bioessays*, 32(4):271–80.

Lane, N. and Martin, W. (2010). The energetics of genome complexity. *Nature*, 467(7318):929–934.

LaNoue, K. F. and Williamson, J. R. (1971). Interrelationships between malate-aspartate shuttle and citric acid cycle in rat heart mitochondria. *Metabolism*, 20(2):119–140.

Larijani, B., Rosser, C., and Woscholski, R. (2006). *Chemical biology: applications and techniques*. John Wiley & Sons.

Lee, M., Bain, A. J., McCarthy, P. J., Han, C. H., Haseltine, J. N., Smith III, A. B., and Hochstrasser, R. M. (1986). Picosecond photoisomerization and rotational reorientation dynamics in solution. *The Journal of Chemical Physics*, 85(8):4341–4347.

Li, N., Ragheb, K., Lawler, G., Sturgis, J., Rajwa, B., Melendez, J. A., and Robinson, J. P. (2003). Mitochondrial complex I inhibitor rotenone induces apoptosis through enhanc-

ing mitochondrial reactive oxygen species production. *The Journal of Biological Chemistry*, 278(10):8516–8525.

Lichtman, J. W. and Conchello, J.-A. (2005). Fluorescence microscopy. *Nat Meth*, 2(12):910–919.

Lipari, G. and Szabo, A. (1980). Effect of librational motion on fluorescence depolarization and nuclear magnetic resonance relaxation in macromolecules and membranes. *Biophysical journal*, 30(3):489–506.

Litvinenko, K. L., Webber, N. M., and Meech, S. R. (2003). Internal conversion in the chromophore of the green fluorescent protein: Temperature dependence and isoviscosity analysis. *The Journal of Physical Chemistry A*, 107(15):2616–2623.

Mann, Z. F., Duchen, M. R., and Gale, J. E. (2009). Mitochondria modulate the spatiotemporal properties of intra- and intercellular Ca2+ signals in cochlear supporting cells. *Cell Calcium*, 46(2):136–146.

Mannekutla, J. R., Ramamurthy, P., Mulimani, B. G., and Inamdar, S. R. (2007). Rotational dynamics of UVITEX-OB in alkanes, alcohols and binary mixtures. *Chemical Physics*, 340:149–157.

Marroquin, L. D., Hynes, J., Dykens, J. A., Jamieson, J. D., and Will, Y. (2007). Circumventing the Crabtree effect: Replacing media glucose with galactose increases susceptibility of HepG2 cells to mitochondrial toxicants. *Toxicological Sciences*, 97(2):539–547.

McCaskill, J. S. and Gilbert, R. G. (1979). Fokker-Planck interpretation of picosecond intramolecular dynamics in solutions. *Chemical Physics*, 44(3):389–402.

Megens, M., Sprik, R., Wegdam, G. H., and Lagendijk, A. (1997). Orientational relaxation times of rhodamine 700 in glycerol-water mixtures. *The Journal of Chemical Physics*, 107(2):493–498.

Meijers, R., Morris, R. J., Adolph, H. W., Merli, A., Lamzin, V. S., and Cedergren-Zeppezauer, E. S. (2001). On the enzymatic activation of NADH. *J Biol Chem*, 276(12):9316–21.

Mikosch, W., Dorfmuller, T., and Eimer, W. (1994). Rotational motion of charged molecules in aqueous solutions. a change in the diffusion mechanism. *The Journal of Chemical Physics*, 101(12):11044–11051.

Mitchell, P. (1961). Coupling of phosphorylation to electron and hydrogen transfer by a chemi-osmotic type of mechanism. *Nature*, 191(4784):144–148.

Moger, J., Gribbon, P., Sewing, A., and Winlove, C. P. (2006). The application of fluorescence lifetime readouts in high-throughput screening. *Journal of Biomolecular Screening*, 11(7):765–772.

Munro, I., Pecht, I., and Stryer, L. (1979). Subnanosecond motions of tryptophan residues in proteins. *Proc Natl Acad Sci U S A*, 76(1):56–60.

Murphy, M. P. (2009). How mitochondria produce reactive oxygen species. *Biochem J*, 417(1):1–13.

Mycek, M.-A., Schomacker, K. T., and Nishioka, N. S. (1998). Colonic polyp differentiation using time-resolved autofluorescence spectroscopy. *Gastrointestinal Endoscopy*, 48(4):390–394.

Nakamoto, R. K., Baylis Scanlon, J. A., and Al-Shawi, M. K. (2008). The rotary mechanism of the ATP synthase. *Arch Biochem Biophys*, 476(1):43–50.

Nelson, P., Radosavljević, M., and Bromberg, S. (2007). *Biological Physics: Energy, Information, Life*. W.H. Freeman and Company.

Nguyen, S. C., Lomont, J. P., and Harris, C. B. (2012). Mass effect on rotational diffusion of small solutes in solution. *Chemical Physics*, In Press.

Nicholls, D. and Ferguson, S. (2013). *Bioenergetics*. Elsevier Science.

Niesner, R., Narang, P., Spiecker, H., Andresen, V., Gericke, K. H., and Gunzer, M. (2008). Selective detection of NADPH oxidase in polymorphonuclear cells by means of NAD(P)H-based fluorescence lifetime imaging. *J Biophys*, 2008(16):602639.

Ogikubo, S., Nakabayashi, T., Adachi, T., Islam, M. S., Yoshizawa, T., Kinjo, M., and Ohta, N. (2009). Intracellular pH sensing using autofluorescence lifetime microscopy. *The Journal of Physical Chemistry B*, 115(34):10385–10390.

Osellame, L., Blacker, T., and Duchen, M. (2012). Cellular and molecular mechanisms of mitochondrial function. *Best Practice & Research Clinical Endocrinology & Metabolism*, 26(6):711–723.

Pardal, R., Clarke, M. F., and Morrison, S. J. (2003). Applying the principles of stem-cell biology to cancer. *Nat Rev Cancer*, 3(12):895–902.

Patterson, G. H., Knobel, S. M., Arkhammar, P., Thastrup, O., and Piston, D. W. (2000). Separation of the glucose-stimulated cytoplasmic and mitochondrial NAD(P)H responses in pancreatic islet beta cells. *Proc Natl Acad Sci U S A*, 97(10):5203–7.

Paul, R. J. and Schneckenburger, H. (1996). Oxygen concentration and the oxidation-reduction state of yeast: Determination of free/bound NADH and flavins by time-resolved spectroscopy. *Naturwissenschaften*, 83(1):32–35.

Pawley, J. (2006). *Handbook of Biological Confocal Microscopy*. Springer, third edition.

Pedrotti, F. L., Pedrotti, L. M., and Pedrotti, L. S. (1993). *Introduction to Optics (2nd Edition)*. Prentice Hall, third edition.

Periasamy, A. and Clegg, R. M. (2010). *FLIM Microscopy in Biology and Medicine*. CRC Press.

Pogue, B. W., Pitts, J. D., Mycek, M. A., Sloboda, R. D., Wilmot, C. M., Brandsema, J. F., and O'Hara, J. A. (2001). In vivo NADH fluorescence monitoring as an assay for cellular damage in photodynamic therapy. *Photochemistry and Photobiology*, 74(6):817–824.

Pollak, N., Dolle, C., and Ziegler, M. (2007a). The power to reduce: pyridine nucleotides–small molecules with a multitude of functions. *Biochem J*, 402(2):205–18.

Pollak, N., Niere, M., and Ziegler, M. (2007b). NAD kinase levels control the NADPH concentration in human cells. *J Biol Chem*, 282(46):33562–71.

Pradhan, A., Pal, P., Durocher, G., Villeneuve, L., Balassy, A., Babai, F., Gaboury, L., and Blanchard, L. (1995). Steady state and time-resolved fluorescence properties of metastatic and non-metastatic malignant cells from different species. *Journal of Photochemistry and Photobiology B-Biology*, 31(3):101–112.

Prasad, P. (2004). *Introduction to Biophotonics*. Wiley.

Ramanujam, N. (2000). Fluorescence spectroscopy of neoplastic and non-neoplastic tissues. *Neoplasia*, 2(1-2):89–117.

Read, J. A., Winter, V. J., Eszes, C. M., Sessions, R. B., and Brady, R. L. (2001). Structural basis for altered activity of m- and h-isozyme forms of human lactate dehydrogenase. *Proteins*, 43(2):175–85.

Rebhan, M., Chalifa-Caspi, V., Prilusky, J., and Lancet, D. (1997). Genecards: integrating information about genes, proteins and diseases. *Trends Genet*, 13(4):163.

Reitzer, L. J., Wice, B. M., and Kennell, D. (1979). Evidence that glutamine, not sugar, is the major energy source for cultured HeLa cells. *J Biol Chem*, 254(8):2669–76.

Reya, T., Morrison, S. J., Clarke, M. F., and Weissman, I. L. (2001). Stem cells, cancer, and cancer stem cells. *Nature*, 414(6859):105–111.

Ricci-Vitiani, L., Lombardi, D. G., Pilozzi, E., Biffoni, M., Todaro, M., Peschle, C., and De Maria, R. (2007). Identification and expansion of human colon-cancer-initiating cells. *Nature*, 445(7123):111–5.

Rice, S. A. and Kenney-Wallace, G. A. (1980). Time-resolved fluorescence depolarization studies of rotational relaxation in viscous media. *Chemical Physics*, 47(2):161–170.

Rich, P. (2003). Chemiosmotic coupling: The cost of living. *Nature*, 421(6923):583–583.

Ridsdale, J. A. and Webb, W. W. (1993). The viability of cultured cells under two-photon laser scanning microscopy. *Biophysical Journal*, 64:A109.

Romano, A. H. and Conway, T. (1996). Evolution of carbohydrate metabolic pathways. *Research in Microbiology*, 147(6):448–455.

Rose, S. (1999). *The Chemistry of Life*. Penguin Books Limited.

Ruddon, R. (2007). *Cancer Biology*. Oxford University Press, USA.

Sanchez, W. Y., Prow, T. W., Sanchez, W. H., Grice, J. E., and Roberts, M. S. (2010). Analysis of the metabolic deterioration of ex vivo skin from ischemic necrosis through the imaging of intracellular NAD(P)H by multiphoton tomography and fluorescence lifetime imaging microscopy. *Journal of Biomedical Optics*, 15(4):046008–11.

Scaduto Jr, R. C. and Grotyohann, L. W. (1999). Measurement of mitochondrial membrane potential using fluorescent rhodamine derivatives. *Biophysical Journal*, 76(1):469–477.

Scalettar, B. A., Abney, J. R., and Hackenbrock, C. R. (1991). Dynamics, structure, and function are coupled in the mitochondrial matrix. *Proc Natl Acad Sci U S A*, 88(18):8057–61.

Scheffner, M., Huibregtse, J. M., Vierstra, R. D., and Howley, P. M. (1993). The HPV-16 E6 and E6-AP complex functions as a ubiquitin-protein ligase in the ubiquitination of p53. *Cell*, 75(3):495–505.

Schneckenburger, H. and Koenig, K. (1992). Fluorescence decay kinetics and imaging of NAD(P)H and flavins as metabolic indicators. *Optical Engineering*, 31(7):1447–1451.

Schneckenburger, H., Wagner, M., Weber, P., Strauss, W. S. L., and Sailer, R. (2004). Autofluorescence lifetime imaging of cultivated cells using a UV picosecond laser diode. *Journal of Fluorescence*, 14(5):649–654.

Schomburg, I., Chang, A., Hofmann, O., Ebeling, C., Ehrentreich, F., and Schomburg, D. (2002). BRENDA: a resource for enzyme data and metabolic information. *Trends in Biochemical Sciences*, 27(1):54–56.

Schroeder, D. (2000). *An Introduction To Thermal Physics*. Addison Wesley.

Scott, T. G., Spencer, R. D., Leonard, N. J., and Weber, G. (1970). Synthetic spectroscopic models related to coenzymes and base pairs, V: Emission properties of NADH. studies of fluorescence lifetimes and quantum efficiencies of NADH, AcPyADH, [reduced acetylpyridineadenine dinucleotide] and simplified synthetic models. *Journal of the American Chemical Society*, 92(3):687–695.

Scrutton, N. S., Berry, A., and Perham, R. N. (1990). Redesign of the coenzyme specificity of a dehydrogenase by protein engineering. *Nature*, 343(6253):38–43.

Segal, A. W. (2005). How neutrophils kill microbes. *Annu Rev Immunol*, 23:197–223.

Shatwell, K. P. and Segal, A. W. (1996). NADPH oxidase. *The International Journal of Biochemistry & Cell Biology*, 28(11):1191–1195.

Shenghui, H., Nakada, D., and Morrison, S. J. (2009). Mechanisms of stem cell self-renewal. *Annual Review of Cell and Developmental Biology*, 25(1):377–406.

Shigemori, K., Ishizaki, T., Matsukawa, S., Sakai, A., Nakai, T., and Miyabo, S. (1996). Adenine nucleotides via activation of ATP-sensitive K+ channels modulate hypoxic response in rat pulmonary artery. *American Journal of Physiology - Lung Cellular and Molecular Physiology*, 270(5):L803–L809.

Shin, E. S., Park, J., Shin, J.-M., Cho, D., Cho, S. Y., Shin, D. W., Ham, M., Kim, J. B., and Lee, T. R. (2008). Catechin gallates are NADP+-competitive inhibitors of glucose-6-phosphate dehydrogenase and other enzymes that employ NADP+ as a coenzyme. *Bioorganic & Medicinal Chemistry*, 16(7):3580–3586.

Skala, M. C., Riching, K. M., Bird, D. K., Gendron-Fitzpatrick, A., Eickhoff, J., Eliceiri, K. W., Keely, P. J., and Ramanujam, N. (2007a). In vivo multiphoton fluorescence lifetime imaging of protein-bound and free nicotinamide adenine dinucleotide in normal and precancerous epithelia. *J Biomed Opt*, 12(2):024014.

Skala, M. C., Riching, K. M., Gendron-Fitzpatrick, A., Eickhoff, J., Eliceiri, K. W., White, J. G., and Ramanujam, N. (2007b). In vivo multiphoton microscopy of NADH and FAD redox states, fluorescence lifetimes, and cellular morphology in precancerous epithelia. *Proceedings of the National Academy of Sciences*, 104(49):19494–19499.

Slebos, R. J., Lee, M. H., Plunkett, B. S., Kessis, T. D., Williams, B. O., Jacks, T., Hedrick, L., Kastan, M. B., and Cho, K. R. (1994). p53-dependent G1 arrest involves pRB-related proteins and is disrupted by the human papillomavirus 16 E7 oncoprotein. *Proc Natl Acad Sci U S A*, 91(12):5320–4.

Sobolewski, A. L. and Domcke, W. (1999). Ab initio investigations on the photophysics of indole. *Chemical Physics Letters*, 315:293–298.

Spiegel, M., Lipschutz, S., and Liu, J. (2008). *Schaum's Outline of Mathematical Handbook of Formulas and Tables*. McGraw-Hill Education, third edition.

Stickland, R. G. (1959). Some properties of the malic enzyme of pigeon liver. 2. synthesis of malate from pyruvate. *Biochem J*, 73:654–9.

Strickler, S. J. and Berg, R. A. (1962). Relationship between absorption intensity and fluorescence lifetime of molecules. *The Journal of Chemical Physics*, 37(4):814–822.

Stringari, C., Edwards, R. A., Pate, K. T., Waterman, M. L., Donovan, P. J., and Gratton, E. (2012a). Metabolic trajectory of cellular differentiation in small intestine by phasor fluorescence lifetime microscopy of NADH. *Sci. Rep.*, 2.

Stringari, C., Nourse, J. L., Flanagan, L. A., and Gratton, E. (2012b). Phasor fluorescence lifetime microscopy of free and protein-bound NADH reveals neural stem cell differentiation potential. *PLoS ONE*, 7(11):e48014.

Stringari, C., Sierra, R., Donovan, P. J., and Gratton, E. (2012c). Label-free separation of human embryonic stem cells and their differentiating progenies by phasor fluorescence lifetime microscopy. *Journal of Biomedical Optics*, 17(4):046012–046012.

Stsiapura, V. I., Maskevich, A. A., Kuzmitsky, V. A., Uversky, V. N., Kuznetsova, I. M., and Turoverov, K. K. (2008). Thioflavin T as a molecular rotor: fluorescent properties of thioflavin T in solvents with different viscosity. *J Phys Chem B*, 112(49):15893–902.

Sud, D., Zhong, W., Beer, D. G., and Mycek, M. A. (2006). Time-resolved optical imaging provides a molecular snapshot of altered metabolic function in living human cancer cell models. *Optics Express*, 14(10):4412–4426.

Sun, F., Dai, C., Xie, J., and Hu, X. (2012). Biochemical issues in estimation of cytosolic free NAD/NADH ratio. *PLoS ONE*, 7(5):e34525.

Sun, Y., Phipps, J., Elson, D. S., Stoy, H., Tinling, S., Meier, J., Poirier, B., Chuang, F. S., Farwell, D. G., and Marcu, L. (2009). Fluorescence lifetime imaging microscopy: in vivo application to diagnosis of oral carcinoma. *Opt. Lett.*, 34(13):2081–2083.

Svelto, O. (2010). *Principles of Lasers*. Springer, fifth edition.

Tadrous, P. J., Siegel, J., French, P. M., Shousha, S., Lalani, E.-N., and Stamp, G. W. (2003). Fluorescence lifetime imaging of unstained tissues: early results in human breast cancer. *J Pathol*, 199(3):309–17.

Tanner, J. J., Tu, S. C., Barbour, L. J., Barnes, C. L., and Krause, K. L. (1999). Unusual folded conformation of nicotinamide adenine dinucleotide bound to flavin reductase p. *Protein Sci*, 8(9):1725–32.

Tao, T. (1969). Time-dependent fluorescence depolarization and Brownian rotational diffusion coefficients of macromolecules. *Biopolymers*, 8(5):609–632.

Thorens, B. and Mueckler, M. (2010). Glucose transporters in the 21st century. *American Journal of Physiology-Endocrinology and Metabolism*, 298(2):E141–E145.

Tiede, L. M. and Nichols, M. G. (2006). Photobleaching of reduced nicotinamide adenine dinucleotide and the development of highly fluorescent lesions in rat basophilic leukemia cells during multiphoton microscopy. *Photochem Photobiol*, 82(3):656–64.

Tower, D. B. (1958). The effects of 2-deoxy-d-glucose on metabolism of slices of cerebral cortex incubated in vitro. *Journal of Neurochemistry*, 3(2):185–205.

Valeur, B. (2001). *Molecular Fluorescence: Principles and Applications*. Wiley-VCH.

Vander Heiden, M. G., Cantley, L. C., and Thompson, C. B. (2009). Understanding the Warburg effect: The metabolic requirements of cell proliferation. *Science*, 324(5930):1029–1033.

Velsko, S. P., Waldeck, D. H., and Fleming, G. R. (1983). Breakdown of Kramers theory description of photochemical isomerization and the possible involvement of frequency dependent friction. *The Journal of Chemical Physics*, 78(1):249–258.

Vishwasrao, H. D., Heikal, A. A., Kasischke, K. A., and Webb, W. W. (2005). Conformational dependence of intracellular NADH on metabolic state revealed by associated fluorescence anisotropy. *Journal of Biological Chemistry*, 280(26):25119–25126.

Visser, A. J. W. G. and Hoek, A. v. (1981). The fluorescence decay of reduced nicotinamides in aqueous solution after excitation with a UV-mode locked locked Ar ion laser. *Photochem Photobiol*, 33(1):35–40.

Voth, G. A. and Hochstrasser, R. M. (1996). Transition state dynamics and relaxation processes in solutions: A frontier of physical chemistry. *The Journal of Physical Chemistry*, 100(31):13034–13049.

Wakita, M., Nishimura, G., and Tamura, M. (1995). Some characteristics of the fluorescence lifetime of reduced pyridine-nucleotides in isolated-mitochondria, isolated hepatocytes, and perfused-rat-liver in-situ. *Journal of Biochemistry*, 118(6):1151–1160.

Wall, K. and Sanchez, A. (1990). Titanium sapphire lasers. *The Lincoln Laboratory Journal*, 3(3):447–462.

Wan, C. and Johnson, C. K. (1994). Time-resolved anisotropic two-photon spectroscopy. *Chemical Physics*, 179(3):513–531.

Wang, H. W., Gukassyan, V., Chen, C. T., Wei, Y. H., Guo, H. W., Yu, J. S., and Kao, F. J. (2008). Differentiation of apoptosis from necrosis by dynamic changes of reduced nicotinamide adenine dinucleotide fluorescence lifetime in live cells. *Journal of Biomedical Optics*, 13(5):9.

Wang, X., Song, K. S., Guo, Q. X., and Tian, W. X. (2003). The galloyl moiety of green tea catechins is the critical structural feature to inhibit fatty-acid synthase. *Biochem Pharmacol*, 66(10):2039–47.

Warburg, O. (1956). On the origin of cancer cells. *Science*, 123(3191):309–314.

Weber, H. and Arfken, G. (2004). *Essential Mathematical Methods for Physicists*. Academic Press.

Whitaker, A. (1972). *Tissue and cell culture*. Laboratory monographs. Baillière Tindall.

Willock, D. (2009). *Molecular Symmetry*. John Wiley & Sons.

Wilms, C. D., Schmidt, H., and Eilers, J. (2006). Quantitative two-photon Ca2+ imaging via fluorescence lifetime analysis. *Cell Calcium*, 40(1):73–9.

Wohl, C. J. and Kuciauskas, D. (2005). Isomerization dynamics of photochromic spiropyran molecular switches in phospholipid bilayers. *The Journal of Physical Chemistry B*, 109(46):21893–21899.

Wu, Y. D. and Houk, K. N. (1993). Theoretical study of conformational features of nad+ and nadh analogs: protonated nicotinamide and 1,4-dihydronicotinamide. *The Journal of Organic Chemistry*, 58(8):2043–2045.

Xu, C. and Webb, W. W. (1996). Measurement of two-photon excitation cross sections of molecular fluorophores with data from 690 to 1050 nm. *J. Opt. Soc. Am. B*, 13(3):481–491.

Xu, C., Williams, R. M., Zipfel, W., and Webb, W. W. (1996). Multiphoton excitation cross-sections of molecular fluorophores. *Bioimaging*, 4(3):198–207.

Yaseen, M. A., Sakadzic, S., Wu, W., Becker, W., Kasischke, K. A., and Boas, D. A. (2013). In vivo imaging of cerebral energy metabolism with two-photon fluorescence lifetime microscopy of NADH. *Biomed Opt Express*, 4(2):307–21.

Ye, Y., Yanfang, L., Cameron, B. D., and Relue, P. (2007). Fluorescence anisotropy of cellular NADH as a tool to study different metabolic properties of human melanocytes and melanoma cells. *Selected Topics in Quantum Electronics, IEEE Journal of*, 13(6):1671–1679.

Yeh, E., Cunningham, M., Arnold, H., Chasse, D., Monteith, T., Ivaldi, G., Hahn, W. C., Stukenberg, P. T., Shenolikar, S., Uchida, T., Counter, C. M., Nevins, J. R., Means, A. R., and Sears, R. (2004). A signalling pathway controlling c-myc degradation that impacts oncogenic transformation of human cells. *Nat Cell Biol*, 6(4):308–318.

Ying, W. (2008). NAD+/NADH and NADP+/NADPH in cellular functions and cell death: regulation and biological consequences. *Antioxid Redox Signal*, 10(2):179–206.

Young, H. and Freedman, R. (2004). *University Physics with Modern Physics*. Pearson Education, Limited, 11th edition.

Yu, J.-S., Guo, H.-W., Wang, C.-H., Wei, Y.-H., and Wang, H.-W. (2011). Increase of reduced nicotinamide adenine dinucleotide fluorescence lifetime precedes mitochondrial dysfunction in staurosporine-induced apoptosis of HeLa cells. *Journal of Biomedical Optics*, 16(3):036008–036008.

Yu, Q. and Heikal, A. A. (2009). Two-photon autofluorescence dynamics imaging reveals sensitivity of intracellular NADH concentration and conformation to cell physiology at the single-cell level. *Journal of Photochemistry and Photobiology B: Biology*, 95(1):46–57.

Zelent, B., Troxler, T., and Vanderkooi, J. M. (2007). Temperature dependence for fluorescence of beta-NADH in glycerol/water solution and in trehalose/sucrose glass. *Journal of Fluorescence*, 17(1):37–42.

Zhang, Q., Piston, D. W., and Goodman, R. H. (2002). Regulation of corepressor function by nuclear NADH. *Science*, 295(5561):1895–7.

Zhao, Y., Jin, J., Hu, Q., Zhou, H.-M., Yi, J., Yu, Z., Xu, L., Wang, X., Yang, Y., and Loscalzo,

J. (2011). Genetically encoded fluorescent sensors for intracellular NADH detection. *Cell Metabolism*, 14(4):555–566.

Zheng, W., Li, D., and Qu, J. Y. (2010). Monitoring changes of cellular metabolism and microviscosity in vitro based on time-resolved endogenous fluorescence and its anisotropy decay dynamics. *Journal of Biomedical Optics*, 15(3):037013–11.

Zollner, H. (1999). *Handbook of enzyme inhibitors*. New York.

Appendix A

MATLAB data analysis algorithms

```
function [simulateddata] = ...
    simulate_data(irf,I0,a03,a06,a1,a2,a3,a4,a5,a6)

    timeunit=12.5/256;  %12.5ns period with 256 bins
    Z=10;  %background noise

    for i=1:256  %generate exponential decay
        pure_decay(i,1)=1000000*(a03*exp(-(i-1)*timeunit/0.3) ...
            +a06*exp(-(i-1)*timeunit/0.6) ...
            +a1*exp(-(i-1)*timeunit/1) ...
            +a2*exp(-(i-1)*timeunit/2) ...
            +a3*exp(-(i-1)*timeunit/3) ...
            +a4*exp(-(i-1)*timeunit/4) ...
            +a5*exp(-(i-1)*timeunit/5) +a6*exp(-(i-1)*timeunit/6));
    end

    model=Convol(irf,pure_decay);  %convolve irf with decay

    for i=1:256
        scalemodel(i,1)=(model(i,1)*(I0-Z)/max(model))+Z;  ...
            %scale the data to I0 and add background
    end

    simulateddata=arrayfun(@(x) poissrnd(x), scalemodel);  ...
        %apply poisson noise
end
```

```
function[]=lifetimes_to_grayscale(path)

    j=1;
    cd(path);
    [files]=read_folder_of_lifetime_matrices(path);  %creates ...
       array of the file names of FLIM matrices exported from ...
       SPCImage contained in the folder 'path', labelling them ...
       according the image and NAD(P)H lifetime decay parameter ...
       to which they correspond

    %import files in MATLAB workspace
    for i=1:length(files)
        if strcmp(files(i).type,'OTHER')==0
            datasets{j,1}=files(i).id;
            j=j+1;
            varname=[files(i).id,'_',files(i).type];
            command1=[varname,'=importdata('];
            singlequote='''';
            command2=files(i).name;
            command3=');';
            eval([command1, singlequote, command2, singlequote, ...
                command3])
        end
    end
    datasets=unique(datasets);  %remove any duplicate copies ...
       that sneaked through

    %loop over all FLIM images
    for i=1:length(datasets);

        %assign each parameter matrix for this image to a variable
        datasetname=char(datasets(i,1));
        command=['a1matrix=',datasetname,'_a1;'];
        eval(command);
        command=['a2matrixpre=',datasetname,'_a2;'];
        eval(command);
        command=['t1matrix=',datasetname,'_t1;'];
        eval(command);
        command=['t2matrix=',datasetname,'_t2;'];
```

```
34          eval(command);
35          command=['photonsmatrix=',datasetname,'_I;'];
36          eval(command);
37
38          %scale a2 between 0 and 1
39          [rows,columns]=size(a1matrix);
40          for i=1:rows
41              for j=1:columns
42                  a2matrix(i,j)=a2matrixpre(i,j)*1/(a1matrix(i,j) ...
                        +a2matrixpre(i,j));
43              end
44          end
45
46          %ignore any negative values that sneaked through
47          a2matrix_mod=a2matrix;
48          t1matrix_mod=t1matrix;
49          t2matrix_mod=t2matrix;
50
51          %find maximum value of each parameter
52          maxa2=max(max(a2matrix_mod));
53          maxt1=max(max(t1matrix_mod));
54          maxt2=max(max(t2matrix_mod));
55          maxint=3000; %arbitrary
56
57          %find minimum value of each parameter
58          mina2=min(min(a2matrix_mod));
59          mint1=min(min(t1matrix_mod));
60          mint2=min(min(t2matrix_mod));
61          minint=min(min(photonsmatrix));
62
63          %calculate grayscale value for each pixel in each image
64          for i=1:rows
65              for j=1:columns
66                  if a2matrix(i,j)==0
67                      a2image(i,j)=0;
68                  else
69                      a2image(i,j)=((a2matrix(i,j)-mina2)*65534/ ...
                            (maxa2-mina2))+1;
70                  end
71                  if t1matrix(i,j)==0
```

```
72                      t1image(i,j)=0;
73                  else
74                      t1image(i,j)=((t1matrix(i,j)-mint1)*65534/ ...
                            (maxt1-mint1))+1;
75                  end
76                  if t2matrix(i,j)==0
77                      t2image(i,j)=0;
78                  else
79                      t2image(i,j)=((t2matrix(i,j)-mint2)*65534/ ...
                            (maxt2-mint2))+1;
80                  end
81                  intimage(i,j)=(photonsmatrix(i,j)-minint)*65535/ ...
                        (maxint-minint);
82              end
83          end
84
85          %convert images to png format
86          a2image=uint16(a2image);
87          t1image=uint16(t1image);
88          t2image=uint16(t2image);
89          intimage=uint16(intimage);
90
91          %create file names
92          a2filename=[datasetname, '_a2_', num2str(mina2), '_', ...
                num2str(maxa2), '.png'];
93          t1filename=[datasetname, '_t1_', num2str(mint1), '_', ...
                num2str(maxt1), '.png'];
94          t2filename=[datasetname, '_t2_', num2str(mint2), '_', ...
                num2str(maxt2), '.png'];
95          intfilename=[datasetname, '_int.png'];
96
97          %write files
98          imwrite(a2image,a2filename,'png');
99          imwrite(t1image,t1filename,'png');
100         imwrite(t2image,t2filename,'png');
101         imwrite(intimage,intfilename,'png');
102
103     end
104 end
```

```
function[files]=read_folder_of_lifetime_matrices(path)

    cd(path);
    files = dir('*'); %import file structure from path folder
    files=rmfield(files, ...
        [{'date'},{'bytes'},{'isdir'},{'datenum'}]); %ignore ...
        file info we don't need

    %loop over all files in the folder
    for i=1:length(files)
        if strcmp(strtok(files(i).name),'Amp1')==1
            files(i).type='a1';  %assign correct parameter ...
                label to this file
            [token, remain] = strtok(files(i).name);  %extract ...
                the dataset id from the filename
            [token, remain] = strtok(remain);
            files(i).id=strtok(remain);
        elseif strcmp(strtok(files(i).name),'Amp2')==1
            files(i).type='a2';
            [token, remain] = strtok(files(i).name);
            [token, remain] = strtok(remain);
            files(i).id=strtok(remain);
        elseif strcmp(strtok(files(i).name),'Photons')==1
            files(i).type='I';
            [token, remain] = strtok(files(i).name);
            [token, remain] = strtok(remain);
            files(i).id=strtok(remain);
        elseif strcmp(strtok(files(i).name),'Tau1')==1
            files(i).type='t1';
            [token, remain] = strtok(files(i).name);
            [token, remain] = strtok(remain);
            files(i).id=strtok(remain);
        elseif strcmp(strtok(files(i).name),'Tau2')==1
            files(i).type='t2';
            [token, remain] = strtok(files(i).name);
            [token, remain] = strtok(remain);
            files(i).id=strtok(remain);
        else
            files(i).type='OTHER';  %ignore anything other than ...
```

```
                SPCImage exports that might be in the folder
36              files(i).id='OTHER';
37          end
38      end
39
40  end
```

```
1   function [I]=moment_of_inertia(molecule)
2
3       [atoms, width]=size(molecule)  %measure number of atoms in ...
            the structure file 'molecule'
4
5       cx=0;
6       cy=0;
7       cz=0;
8
9       for i=1:atoms
10          cx=cx+molecule(i,1)*molecule(i,4);  %add x co-ord ...
                multiplied by mass of atom
11          cy=cy+molecule(i,2)*molecule(i,4);  %add y co-ord ...
                multiplied by mass of atom
12          cz=cz+molecule(i,3)*molecule(i,4);  %add z co-ord ...
                multiplied by mass of atom
13      end
14
15      %divide cx, cy, cz by total mass to get centre of mass ...
            components
16      cx=cx/sum(molecule(:,4));
17      cy=cy/sum(molecule(:,4));
18      cz=cz/sum(molecule(:,4));
19
20      I=0;
21
22      for i=1:atoms
23          xdistance=molecule(i,1)-cx;  %moment of inertia ...
                relative to centre of mass
24          ydistance=molecule(i,2)-cy;
25          zdistance=molecule(i,3)-cz;
```

```
26          %I=sum of mass times r-squared
27          I=I +molecule(i,4)*(xdistance*xdistance ...
                +ydistance*ydistance +zdistance*zdistance);
28      end
29
30      %print results
31      ['Centre of mass: x=',num2str(cx),' y=',num2str(cy),' ...
            z=',num2str(cz)]
32      I
33  end
```

```
1   function plot_2p_tensor(Sxx,Syy,res,viewpoint)
2
3       %resolution determines number of elevation and azimuth ...
            angles r is calculated at
4       Ntheta=res;
5       Nphi=(2*res)-1;
6
7       %loop over all spherical polar angles
8       for i=1:Ntheta
9           for j=1:Nphi
10              theta=(i-1)*pi/(res-1);
11              phi=(j-1)*pi/(res-1);
12              r=Sxx*sin(theta)*sin(theta)*cos(phi)*cos(phi) ...
                    +Syy*sin(theta)*sin(theta)*sin(phi)*sin(phi); ...
                    %spherical polar form of amplitude calculation
13
14              %convert spherical polars back to cartesians for ...
                    plotting
15              x(i,j) = r*sin(theta)*cos(phi);
16              y(i,j) = r*sin(theta)*sin(phi);
17              z(i,j) = r*cos(theta);
18          end
19      end
20
21      %some nice viewpoints
22      if viewpoint==2
23          az=0;
```

```
24          el=20;
25          zoomfactor=2.4;
26      elseif viewpoint==3
27          az=-180;
28          el=90;
29          zoomfactor=2.4;
30      else
31          az=-40;
32          el=50;
33          zoomfactor=1.6;
34      end
35
36      %plot
37      figure('Color',[1 1 1]);
38      plot=surf(x,y,z);
39      set(plot,'LineWidth',1.1,'LineSmoothing','on')
40      alpha(0.5)
41      colormap([1 1 1]);
42      set(gca,'DataAspectRatio',[1 1 1]);
43      axis equal;
44      grid off;
45      view(az,el);
46      zoom(zoomfactor);
47
48  end
```

Appendix B

Anisotropy variance

Calculation of the variance of the fluorescence anisotropies reconstructed from the measured $I_{||}(t)$ and $I_{\perp}(t)$ is most easily performed by separating the ratio into its numerator and denominator (Cross and Fleming, 1984), thus,

$$R = \frac{I_{||} - I_{\perp}}{I_{||} + 2I_{\perp}} = \frac{D}{S} \tag{B.1}$$

S and D are clearly interdependent as any change in $I_{||}$ or $I_{\perp}$ will induce a change in both parameters. An extended form of equation 2.13 must therefore be used to calculate the variance of R, in which the covariance of S and D is taken into account (Hughes and Hase, 2010), thus,

$$\sigma_R^2 = \left(\frac{\partial R}{\partial D}\right)^2 \sigma_D^2 + \left(\frac{\partial R}{\partial S}\right)^2 \sigma_S^2 + 2\left(\frac{\partial R}{\partial D}\right)\left(\frac{\partial R}{\partial S}\right) \mathrm{cov}\,[D,S] \tag{B.2}$$

Calculating the first term,

$$D = I_{||} - I_{\perp} \tag{B.3}$$

$$\frac{\partial R}{\partial D} = \frac{1}{S} \tag{B.4}$$

$$\sigma_D^2 = \left(\frac{\partial D}{\partial I_{||}}\right)^2 \sigma_{||}^2 + \left(\frac{\partial D}{\partial I_{\perp}}\right)^2 \sigma_{\perp}^2 = I_{||} + I_{\perp} \tag{B.5}$$

where the intrinsic property of the Poisson processes governing $I_{||}$ and $I_{\perp}$ ($\sigma = \sqrt{I}$) has been applied. Similarly, for the second term,

$$S = I_{||} + 2I_{\perp} \tag{B.6}$$

$$\frac{\partial R}{\partial S} = -\frac{D}{S^2} \tag{B.7}$$

$$\sigma_S^2 = \left(\frac{\partial S}{\partial I_{||}}\right)^2 \sigma_{||}^2 + \left(\frac{\partial S}{\partial I_{\perp}}\right)^2 \sigma_{\perp}^2 = I_{||} + 4I_{\perp} \tag{B.8}$$

Calculation of the third term in equation B.2 is aided by the use of the identity (Spiegel et al., 2008),

$$\mathrm{cov}\left[ax + by, cx + dy\right] = ac\sigma_x^2 + bd\sigma_y^2 + ad\mathrm{cov}\left[x, y\right] + bc\mathrm{cov}\left[y, x\right] \tag{B.9}$$

If $x = I_{||}$ and $y = I_{\perp}$, the covariance of S and D can be calculated by taking $a = c = 1$, $b = -1$ and $d = 2$. As $I_{||}$ and $I_{\perp}$ are uncorrelated with each other, the last two terms in equation B.9 will disappear, giving,

$$\mathrm{cov}\left[D, S\right] = I_{||} - 2I_{\perp} \tag{B.10}$$

Substituting equations B.3 to B.8 and equation B.10 back into equation B.2 and writing $S = I_{\mathrm{total}}$ gives,

$$\sigma_R^2 = \frac{\left(I_{||} + 4I_{\perp}\right)R^2 - 2\left(I_{||} - 2I_{\perp}\right)R + I_{||} + I_{\perp}}{I_{\mathrm{total}}^2} \tag{B.11}$$

For circularly polarised illumination, $S = I_{\mathrm{total}} = I_{\perp} + 2I_{||}$. Repeating the above process with this expression for S then leads to equation 4.13.